XMCD investigations on new hard magnetic systems

Von der Fakultät Mathematik und Physik der Universität Stuttgart
zur Erlangung der Würde eines Doktors der Naturwissenschaften
(Dr. rer. nat.) genehmigte Abhandlung

Dissertation vorgelegt von *Yu-Chun Chen*

aus Taipei, Taiwan

Hauptberichter: PD Dr. Eberhard Goering

Mitberichter: Prof. Dr. Sebastian Loth

Tag der mündlichen Prüfung: 9. März 2018

Max-Planck-Institut für Intelligente Systeme, Stuttgart

2018

Table of contents

1. Introduction

1.1. Clean Energy and the Rare-Earth Crisis

New energy concepts are required for the future of our industrial society to improve the efficiency of electricity transmission due to current climate change and limited energy resources. Although biofuels and hydrogen can replace fossil fuels for use in internal combustion engines, hybrid electric motors or all electric vehicles are generally considered as the primary technologies capable of reducing dependence on petroleum for the transportation sector.[1] It was said that just a 1% improvement in efficiency would result in the savings of hundreds of millions of dollars and a reduction in CO_2 emissions of nearly 2.2 million metric tons of carbon equivalent.[2] Therefore, it is really worthy to take effort on improvement in energy efficiency for electric motors from now on, which will have a large economical and environmental savings in future. However, most of people ignore the importance of magnetic materials, but they indeed play a crucial role in improving the efficiency and performance of the electric power generator and conversion systems. Moreover, many functions in modern vehicles and household appliances would not be possible without advanced magnetic materials: they are used in safety features, engines, freezers, braking, fans, pumps, wipers, and so on.[1]

For practical applications, the criterion of permanent-magnet alloys in performances is: (1) anisotropy (K), (2) Curie temperature (T_c), and (3) magnetization (M). According to this principle, rare-earth (RE) based materials have dominated permanent magnet (PM) applications since the discovery of $SmCo_5$ in the sixties and $Nd_2Fe_{14}B$ in the eighties. Among all commercial materials, commercial $Nd_2Fe_{14}B$-based magnets exhibit the highest magnetic performance (saturation magnetization ($\mu_0 M_s$) of 1.6 T and maximum energy product of 56 MGOe),[3, 4] which makes it become the preferred choice for high-efficiency sustainable energy applications worldwide. Although the $\mu_0 M_s$ of SmCo-based magnets is slightly lower (~1.2 T), it has extraordinary temperature coefficient of intrinsic coercivity (β) and higher Curie temperature (T_c) compared to other magnetic

compounds. Therefore, Nd-Fe-B and Sm-Co magnets are in general utilized at room and high temperatures, respectively.

Although RE permanent magnets are widely exploited at the moment, the availability of critical materials for permanent magnets is a growing concern. "Worldwide demand for rare earths is expected to exceed supply by some 40,000 tons annually by the end of this decade," said Larry Allard, a researcher in ORNL's Materials Science and Technology Division. His remark indicates that there will be a growing global shortage of rare earth materials in near future. In reality, the cost of these materials has increased dramatically since China government announced that it would begin to curtail its export of the rare earths (ex. Eu, Tb, and Dy) in 2009.[1] The rise of selected RE oxide prices can be seen in Figure 1.1.[5] It was reported that most easily-exploitable ores are found in China, and the current rare-earth

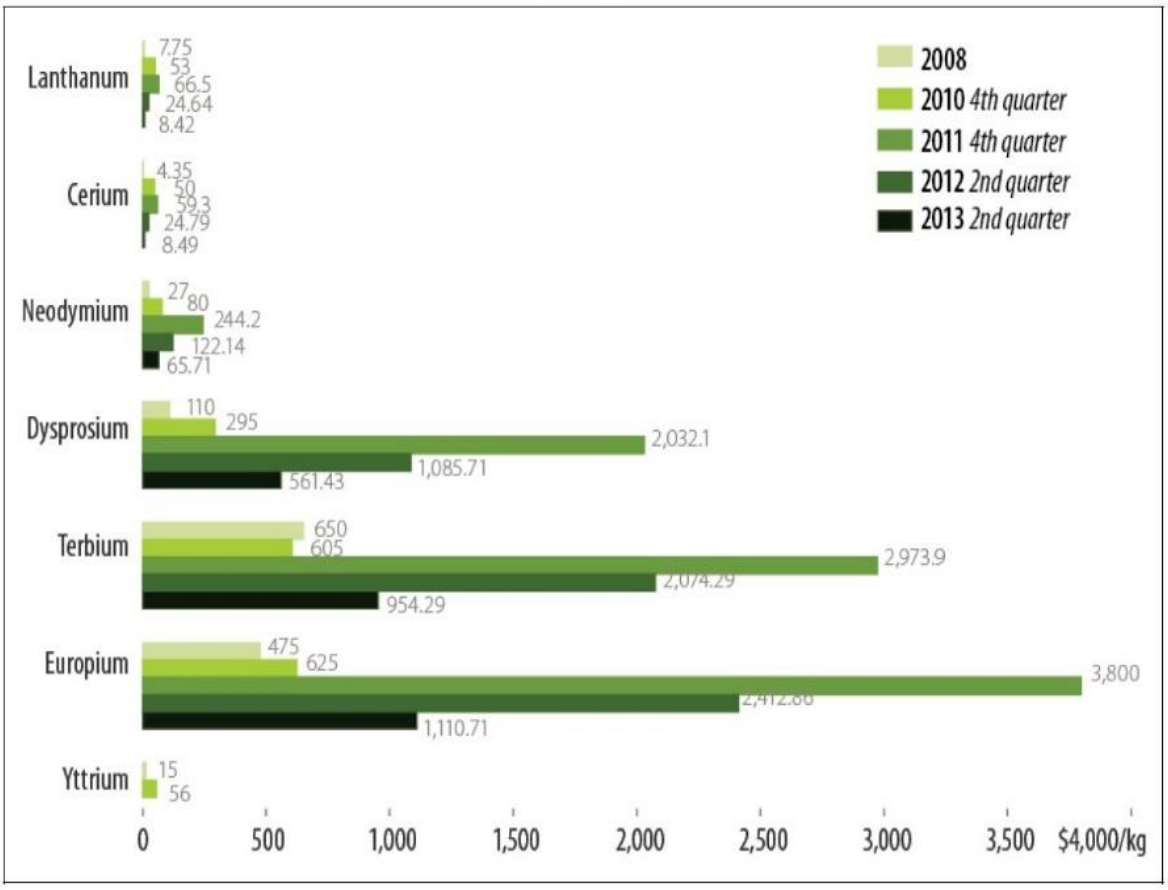

Figure 1.1 According to the Ministry of Economy Trade and Industry (METI) of Japan, prices for dysprosium and neodymium metals rose dramatically. The price for dysprosium metal rose from $250/kg in April 2010 to $2,840/kg by July 2011, while the price for neodymium metal rose from $42/kg in April 2010 to $334/kg in July 2011. [4]

crisis is largely a problem of heavy rare earth supply.[6, 7] There are abundant ores containing the light rare earths (Pr, Nd and Sm) in various parts of the world, but known reserves of the heavy rare earths (Dy and Tb) outside China are very limited in relation to possible demand over the next ten years.[6]

It is clear that availability of Chinese RE elements to other nations depends on continued stability in China's internal politics and economy, and its relation to other countries. Also, RE extraction processes cause serious environmental problems. These issues lead to risks for global markets and geopolitical dynamics with potential to affect the strategic interests of numerous countries. Therefore, technological advances that research on incorporating earth-abundant materials into energy or clean-energy applications become increasingly vital to the economy and energy security of all other nations. In order to overcome this incoming difficulty, several cooperated projected had been issued in the western countries since 2011, such as NANOPYME project in EU and REACT program in USA. All of them focused on developing magnets made from abundant and inexpensive materials.

1.2. Rare-earth-free ferromagnetic compound

During last century, several permanent magnet materials were discovered and commercialized in many diverse applications. Techniques to effectively manufacture these permanent magnets have been established too. The maximum energy product $(BH)_{max}$, which is a key figure of merit of permanent magnets, has been enhanced, starting from ≈ 1 MGOe for steels discovered during the early part of the century, increasing to ≈ 3 MGOe for hexagonal ferrites, and finally peaking at ≈ 56 MGOe for Nd-Fe-B magnets during the past ten years.[2] It is clear that no better magnetic material than $Nd_2Fe_{14}B$ has been discovered since 1984 (see Figure 1.2).[6] The optimization of the material has proceeded already to the point where the best $(BH)_{max}$ value of 59.5 MGOe (470 kJ/m^3) is very close to the theoretical

prediction of 64.8 MGOe (512 kJ/m^3).[8] Because of the remarkable magnetic performance, the production of Nd-Fe-B sintered magnets has steadily increased from about 6,000 tons in 1996 to about 63,000 tons in 2008 and 80,000 tons in 2010 (see Figure 1.3), respectively.[2, 8]

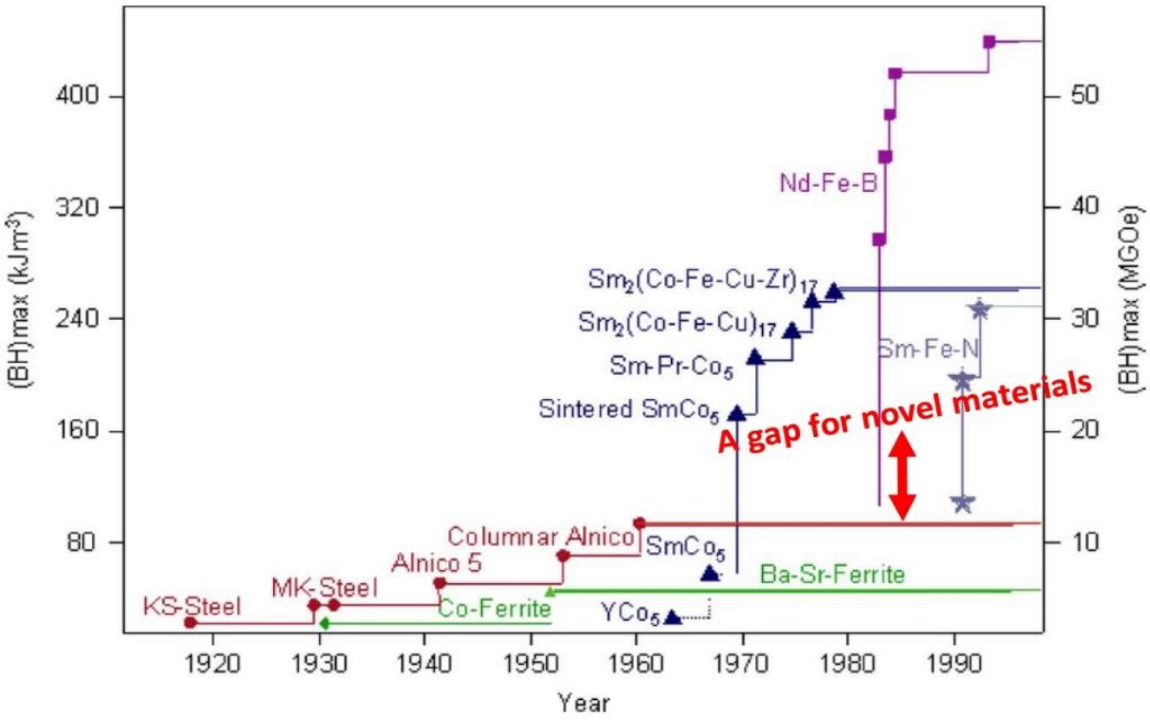

Figure 1.2 Progress of energy product in the course of the 20th century. [5]

Nowadays, the world market for permanent magnets is split roughly between Nd-Fe-B and hexagonal ferrite, with smaller amounts of Sm-Co, alnico, and other materials.[8] Based on the scale data reported in 2010 (see right panel of Figure 1.3), it was found that two-thirds of production comes from high-performance RE magnets (namely Nd-Fe-B and Sm-Co based products). The rest of quota was mainly represented by the ferrite family, which was developed in the Netherlands 60 years ago. The common phases are $BaFe_{12}O_{19}$ and $SrFe_{12}O_{19}$, which have the hexagonal magnetoplumbite structure.[8] Specifically, alnico, developed first in Japan from 1930s, presents about 1 % quota of annual production. It has been in use for many years usually in electric guitar pickups, sensors, loudspeaker, microphones, etc.

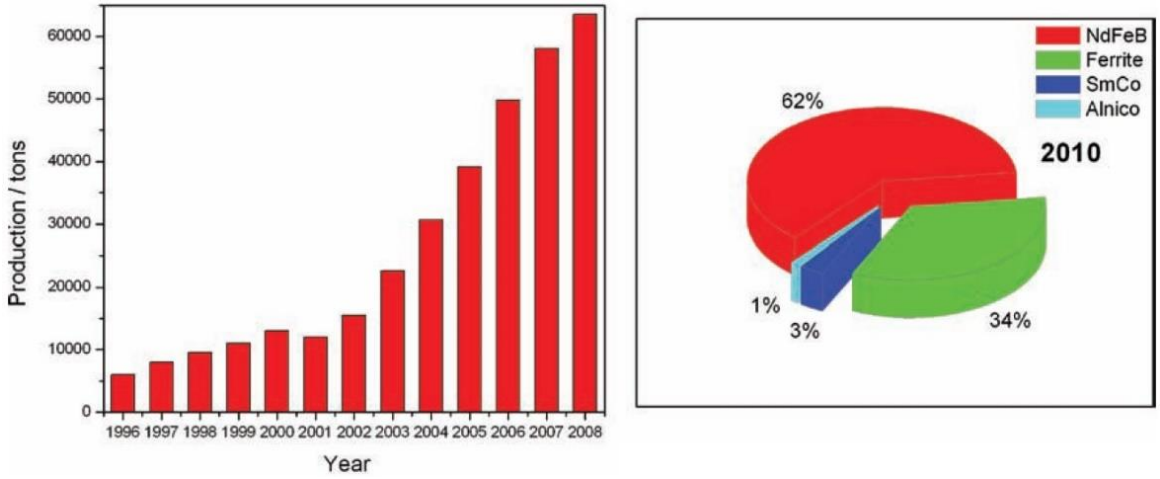

Figure 1.3 Output of NdFeB permanent magnets during the past ten years (left) and predicted percentage sales ($) for 2010 of the major permanent magnets in the world (right). [1]

As discussed above, some RE-free magnets are available in the market at present, namely ferrites and alnico. Therefore, someone may ask questions like "Is it still necessary to find out new magnetic materials?" or "Why not try to improve the magnetic properties of ferrites?". My answer is very simple and straightforward – Yes. It is well-known that both ferrite and alnico families have their own drawbacks, which limit their exploitation for industrial applications. The energy product of these ferrite magnets does not exceed 4.8 MGOe (38 kJ/m^3), although they are cheap and relatively easy to produce (prices < \$5/kg).[8] Alnico has quite high $\mu_0 M_s$ (> 1.1 T) and Curie temperature (> 1200 K), but its demagnetization curves are nonlinear and it is not suitable for motor applications.[2, 6] Moreover, Co is also not cheap material and the supply was unstable previously (ex. so-called Congo crisis).[1] In fact, the erratic supply of Co in the 1970s triggered the search for a Fe-based intermetallic with similar or better properties afterwards. Moreover, if we take a careful look at Figure 1.2, it can be found that there is a big gap in energy products between RE-free and RE magnets. All of these facts reveal that some research efforts should be devoted to developing appropriately priced alternatives with energy products in the range 100~300 kJ/m^3.[9]

As mentioned above, our interdisciplinary project, 'High Performance Permanent Magnets sustainable for Next Generation', was selected by G8 research council and had been funded from Sep of 2012 to Aug of 2015. The consortium of this project is proposed to address the issues of scarce availability and high-cost materials in permanent magnets, and to offer alternative solutions for these potential issues. The materials of choice are mainly Mn-bsed alloy systems such as Mn-Al, Mn-Bi and Mn-Ga. The goal is to achieve an energy product comparable to that NdFeB permanent magnets.

But, why Mn-based compounds? It is because that 'Manganese' is an interesting element with a large unit cell containing four different sites, where Mn atoms bear various magnetic moments ranging from 0.5 to 2.8 μ_B.[9] Extrapolating the Slater–Pauling curve to Mn, with seven valence electrons, suggests that a moment of 3.7 μ_B might be possible.[9] A narrow fully spin-split 3d band could even result in a moment of 5 μ_B on Mn atoms. To achieve magnetic Mn-based permanent magnetic materials, the key point is that Mn–Mn distances need to be adjusted by careful control of the atomic site distribution to maximize the manganese moment per unit volume, and minimize the number of antiferromagnetically coupled Mn sites.[9] Generally, manganese atoms on sites with the shortest Mn–Mn distances, < 240 pm, tend to be nonmagnetic, those in sites with distances in the range 250–280 pm have small itinerant moments, which tend to couple antiferromagnetically, and only manganese atoms in sites with the longest bonds, > 290 nm, tend to have larger moments, that couple ferromagnetically.[4, 9] The intrinsic magnetic properties of several RE and RE-free magnetic compounds are summarized in Table 1.[6, 8] It is clear that LTP-MnBi and τ-MnAl exhibit moderate saturation magnetization and energy products comparable to ferrite and alnico, which make them as potential candidates for magnetic applications in future. This study mainly focuses on sample preparation and micromagnetic orign of Mn-based permanent magnets. Additionally, an interesting study on iron nitride compounds was also completed systematically. All of the detailed information will be discussed in the following chapters.

Table 1.1 Intrinsic magnetic properties of some RE and RE-free permanent materials.[6, 8, 9]

Material	T_c [K]	M_s [MA/m]	K_1 [MJ/m^3]	$(BH)_{max}$ [kJ/m^3]	κ
$Nd_2Fe_{14}B$	588	1.28	4.9	512	1.54
$SmCo_5$	1020	0.86	17.2	231	4.31
Sm_2Co_{17}	838	0.97	4.2	294	1.89
$Sm_2Fe_{17}N_3$	749	1.23	8.6	473	2.13
FePt	750	1.14	6.6	406	2.02
CoPt	840	0.80	4.9	200	2.47
Alnico 5	1210	1.12	0.68	310	0.66
$BaFe_{12}O_{19}$	740	0.38	0.33	45	1.35
LTP-MnBi	628	0.58	0.9	140.8	1.46
τ-MnAl	650	0.6	1.7	100.6	1.95
Mn_2Ga	> 770	0.47	2.35		2.35
Mn_3Ga	> 770	0.18	1.0	29.4	5.0
α''-$Fe_{16}N_2$	810	1.92	1.0		0.43

The criterion, $\kappa = \sqrt{K_1/\mu_0 M_s^2}$, is defined as magnetic hardness parameter of the material, meaning how well a magnet can be fabricated in any shape without demagnetizing itself. An empirical criterion for a permanent magnet is that the K should be greater than unity. Note that the K_1 and $(BH)_{max}$ values of Alnico 5 strongly depend on its shape geometry.

2. Scientific background

2.1. Magnetism

2.1.1. Ferromagnetism

In classical physics, ferromagnetism is the one which shows the most practical magnetic performance among several distinct types of magnetism. Therefore, the most useful magnetic materials, as is known so far, are the so-called ferromagnetic materials. Ferromagnetic materials are principally characterized by a long-range ordering of their atomic magnetic moments even in the absence of external magnetic fields. As found in many real systems, the magnetic moments orient along a direction within the same magnetic domain even though the overall magnetization is zero. Figure 2.1 shows the experimental data on the variation of the saturation magnetization of Fe, Co, and Ni as a function of temperature.[10] This spontaneous interaction between neighboring magnetic moments is observed to vanish above an ordering temperature called Curie temperature.[11]

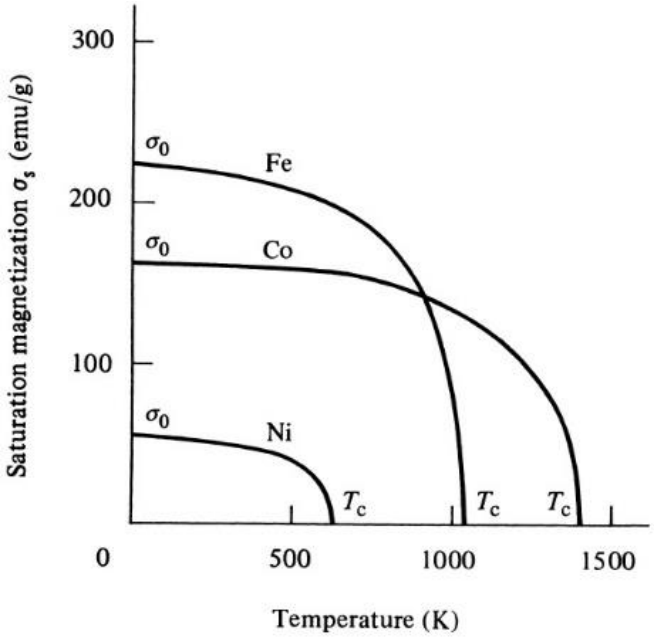

Figure 2.1 Saturation magnetization of iron, cobalt, and nickel as a function of temperature. [10]

It is well known that the magnetism of solids nearly exclusively arises from their own electrons although nuclear moments give rise to significant contribution in some cases (ex. resonance imaging). To evaluate the magnetic moment of an electron, its angular momentum can be visualized classically as a circular motion of electrons around atomic nuclei in terms of circular-current model.[12, 13] The classical angular momentum, however, must be replaced by appropriate quantum mechanical form. The precise expression for the magnetic moments of an electron can be deduced from hydrogen-like 1s electron using Schrödinger equation. Its Hamiltonian is defined by the

$$\widehat{\boldsymbol{\mathcal{H}}} = \boldsymbol{\mathcal{H}}_{\mathrm{Kin},i} + \boldsymbol{\mathcal{H}}_{\mathrm{Nucl},i} = -\frac{\hbar^2}{2m}\nabla^2 - \frac{1}{4\pi\epsilon_0}\frac{e^2}{r} \qquad (\mathbf{2}.1)$$

, where ∇^2 is the operator of the kinetic energy and r is the coordinate of the electron. e^2/r describes the Coulomb interaction between the electron and the nucleus. The orbital moment is eventually obtained as given in Eq. 2.2, and the concept of spin was introduced as Eq. 2.3 later.[10, 12, 13] Therefore, it is concluded that the total magnetic moment (for either an electron or atom) actually is the summation of spin and orbital moments (see Eq. 2.4).

$$\boldsymbol{L}\text{: } m_{orb} = -\frac{\mu_B}{\hbar}\langle L_z\rangle \qquad (\mathbf{2}.2)$$

$$\boldsymbol{S}\text{: } m_{spin} = -\frac{2\mu_B}{\hbar}\langle S_z\rangle \qquad (\mathbf{2}.3)$$

$$m_{total} = m_{spin} + m_{orb} = -\frac{\mu_B}{\hbar}(2\langle S_z\rangle + \langle L_z\rangle) \qquad (\mathbf{2}.4)$$

, where $\mu_B \equiv e\hbar/2m_e = 0.927 \times 10^{-23}$ (J/T or A·m^2) is Bohr magneton, $\langle L_z\rangle$ is electron orbital moment operator, and $\langle S_z\rangle$ is electron spin moment operator.

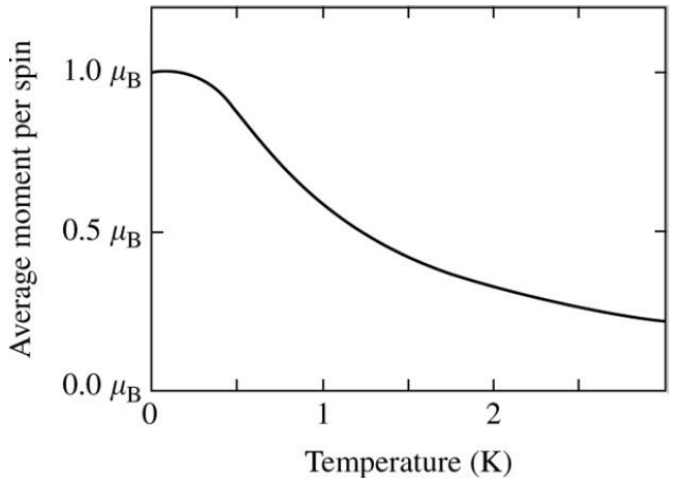

Figure 2.2 Temperature dependent magnetization of an $S = \frac{1}{2}$ ion under a field of 1 T. [12]

In the case of paramagnetism, the phenomena is generally described by a group of non-interacting electrons, which result in the temperature dependent magnetization curve as shown in Figure 2.2.[12] Clearly, the alignment of paramagnetic spins is dramatically reduced, and the applied magnetic field (1 Tesla) is less able to compete against the thermal fluctuation. The magnetic dipole moment interactions are deteriorated as temperature just above 1 K. This evidence suggests that certain strong force is required to keep and stabilize the long-range ordering for ferromagnetism. In 1923, Dirac pointed out that, for the special case of localized electrons in orthogonal orbitals, the effect of the Pauli principle is equivalent to the introduction of additional term in Hamiltonian operator:[11]

$$\mathcal{H}_{\text{Heis}} = -2\sum_{i<j} J_{ij}\boldsymbol{S_i}\cdot\boldsymbol{S_j} \qquad (\mathbf{2}.5)$$

, where i and j can be ascribed to two spins (i and j) in a simple two-electron problem or label all spins in an atomic system. This new term is called exchange interaction, which describes the strong exchange force between two electrons or adjacent atoms. In quantum mechanism, the expression of exchange is generally known as the Heisenberg Hamiltonian although it was first deduced by Dirac and first used extensively by Van Vleck.[11] The

formula indicates that this spin-dependent energy term could be considered as a spin-spin interaction in a vector model. Moreover, the positive(negative) sign of exchange integral, J_{ij} (or J_{ex}), refers to the lowest state leading to parallel(antiparallel) spins ordering. As already discussed above, ferromagnetism originates from the alignment of magnetic moments on neighboring atoms. A positive and negative value of exchange integral is therefore the necessary conditions for ferromagnetism and antiferromagnetism to occur, respectively.[10] Figure 2.3 simply presents these two different types of ordering.[12]

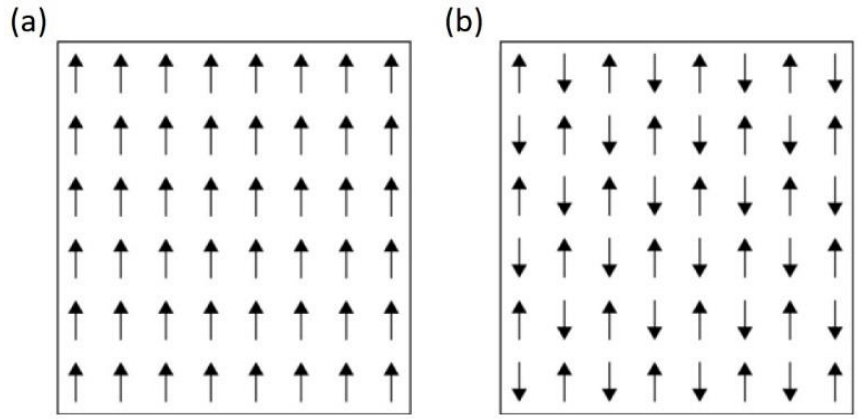

Figure 2.3 Basic types of magnetic ordering: (a) ferromagnetsim and (b) antiferromagnetism. Each arrow represents one atomic spin. [12]

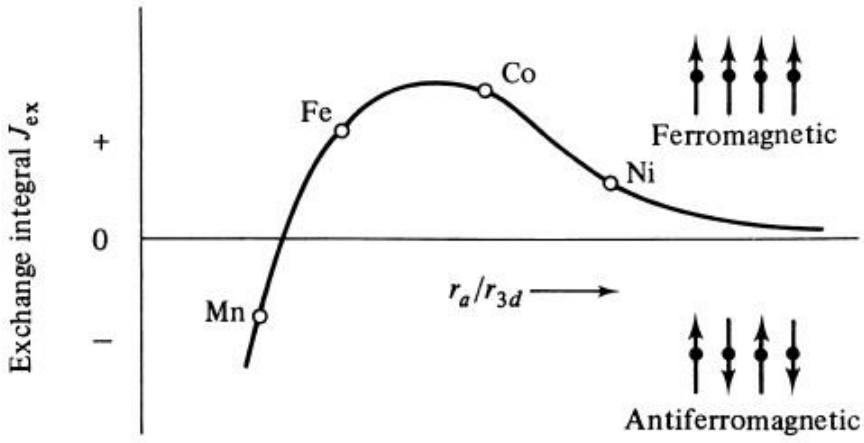

Figure 2.4 Bethe-Slater curve. [12]

With knowledge of quantum mechanics, the exchange interaction allows us to rationalize the appearance of ferromagnetism in some metals and not in

others. The content in Figure 2.4 is usually named the Bethe-Slater curve, that shows the postulated variation of the exchange integral with the ratio r_a/r_{3d}, where r_a is the radius of an atom and r_{3d} the radius of its 3d shell of electrons.[12] The important result here is that J_{ex} changes rapidly with distance. When two atoms of the same kind are brought closer but without any change in the radius r_{3d} of their 3d shells, J_{ex} is positive and becomes stronger, favoring parallel spins. However, a further decrease in the inter-atomic distance brings the 3d electrons so close together that makes the spins antiparallel (negative J_{ex}) leading to antiferromagnetism).

Furthermore, it is known that the magnetization behavior of ferromagnetic materials now can be obtained from Brillouin function, B_s, according to mean-field theory. For any spin moment, the approach to saturation can be described by $M \sim \sqrt{T_c - T}$ as T is close to T_c, correspoding to the mean-field critical exponent β = ½. With knowledge of exchange force, T_c is deduced by linearizing the Brillouin function and is given below

$$\boldsymbol{T}_{\mathrm{c}} = \frac{2S(S+1)}{3k_{\mathrm{B}}} zJ_{\mathrm{ex}} \qquad (\mathbf{2}.6)$$

, where z is the number of nearest neighbors, k_{B} is Boltzmann's constant.[12] Until this step, the cooperative nature of magnetism is much better understood because the physical origin of classical mean-field is found to be related to exchange interaction.

2.1.2. Spin-orbital coupling

Spin-orbital coupling is of extreme importance not just for the interpretation of atomic spectra but also for various magnetic phenomena which are the key to most applications of magnetic materials. For example, spin-orbital coupling is at the root of magnetocrystalline anisotropy, magnetostriction, and magnetic resonance damping, and so on.[11] In the simplest explanation, spin-orbital coupling could be regarded as the effect

of an electron's orbital motion on the orientation of its spin. From the electron rest frame moving about the charged nucleus (see Figure 2.5) it "sees" a positive charge in motion.[11] Hence the electron is situated near the center of a current loop, which generates a magnetic field that causes a preferred direction of orientation for the spin magnetic moment of the electron. It is noted that a more rigorous derivation of spin-orbital coupling must be calculated by magnetic field *B* (using Ampere's law), in a relativistic approach. The spin-orbit Hamiltonian of an electron in a central field of potential V(r) is given finally by the expression in Eq. 2.7:

$$\mathcal{H}_{\mathrm{SO}}(\mathrm{r}) = \frac{1}{2m^2c^2}\frac{1}{r}\frac{\partial V}{\partial r}\boldsymbol{L}\cdot\boldsymbol{S} = \lambda(\mathrm{r})\boldsymbol{L}\cdot\boldsymbol{S} \qquad (2.7)$$

, where λ (or ξ) is spin-orbital energy.[11, 14] In solid-state physics, the Schrödinger equation is nonrelativistic frequently used for electron band-structure calculations. Therefore, the spin-orbit interaction can be included as a relativistic correction to the nonrelativistic Schrödinger equation.

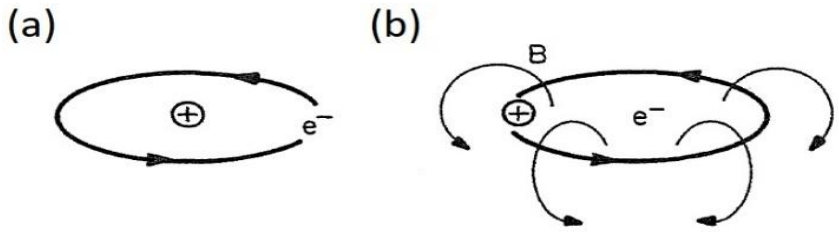

Figure 2.5 (a) An electron orbits about the nucleus. (b) In the electron's rest frame, the nucleus appears to be orbiting around the electron and hence producing a magnetic field in the sense indicated. The interaction of the electron spin with its orbitally induced magnetic field is the spin-orbit interaction. [11]

In theory of magnetism, most of the elements of interest involves two or more d or f electrons, and each electron possesses generally a spin and an orbital momentum (or moment). They may be coupled by spin–orbit interaction to create a total electronic angular momentum $\boldsymbol{J}$, with resultant magnetic moment '$m \propto \boldsymbol{J}$'.[10, 11, 15] In the L-S or Russell-Saunders coupling scheme, the total orbital momentum $\boldsymbol{L} = \sum_i \boldsymbol{L}_i$ and the total spin

momentum $\boldsymbol{S} = \sum_i \boldsymbol{S}_i$ combine to yield the total momentum $\boldsymbol{J} = \boldsymbol{L} + \boldsymbol{S}$. Russell-Saunders levels characterized by the quantum numbers L and S form a term denoted by ${}^{2S+1}L_J$, where 2S+1 is called spin multiplicity and $|L - S| \leq J \leq |L + S|$.[10, 11, 15] Using term symbol (${}^{2S+1}L_J$), each energy level of an atom with a given electron configuration can be obviously described, and the ground-state term symbol is further predicted by Hund's rules.

Hund's rule indicates that there is a preferred sequence of filling the orbitals of a multielectron atom or ion, which leads to three rules as following:[11, 15]

(1) First maximize S for the configuration: This rule forces electrons into different orbital states thereby tending to minimize their Coulomb repulsion.

(2) Then maximize L consistent with S: This also keeps electrons in orbits which circulate in the same sense and have lower probability near the nucleus, again tending to minimize their Coulomb repulsion.

(3) Finally couple L and S to form J: $J = L - S$ if the shell is less than half full, and $J = L + S$ if the shell is more than half full. When the shell is exactly half full, $L = 0$ and $J = S$. This condition tends to minimize the spin-orbit energy, specifically ($\lambda > 0$ for first-half shell and i; < 0 for second-half shell.

It should be clear that Hund's rules (1) are based primarily on Coulomb repulsion (of order 1 eV per atom) and secondarily on spin-orbit interactions (=10^{-2}~10^{-3} eV/atom) and (2) account for the existence of atomic magnetic moments, even in some atoms with an even number of valence electrons.[12] Hence, Hund's rules make up what is sometimes called intra-atomic exchange, which is responsible for atomic moment formation. For practical reasons, magnetic ions are divided into iron-series (3d), palladium-series (4d), platinum-series (5d), and actinide (5f) ions, but other shells (i.e. 2p electrons) may also be involved.[15] Compared to rare-earth 4f electrons, Hund's rules—particularly the second and third rules—are poorly obeyed by 3d shells.[12, 15] This discrepancy basically can be explained by the fact that 4f electrons are more localized compared to 3d

ones. Figure 2.6 shows the difference in the radial electron probability density between 3d and 4f metals.[15] This comparison gives strongly reasonable evidence that Hund's rules are well satisfied for most rare-earths, because the 4f-shell radii of about 0.5 Å are much smaller than the atomic radii of about 1.8 Å. Due to this feature, the localized model is principally suited for 4f electrons in the rare-earth series, R = Pr, . . . , Yb, which have atom-like configuration with an integral number of electrons. A similar picture applies to the heavy actinide (5f) elements, from Am onwards. Unfortunately, these elements become increasingly radioactive; for example, elements such as Bk or Cf are available only in milligram quantities at best.

Nevertheless, it is clear that another theory is necessarily required to understand the origin of ferromagnetism in 3d elements. This issue is discussed in the next subchapter.

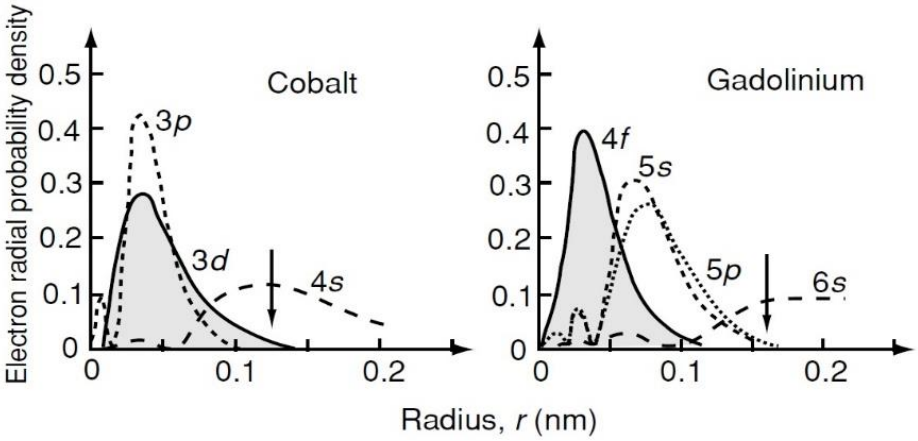

Figure 2.6 Comparison of the radial electron probability density in a 3d metal, Co, and a 4 f metal, Gd. The arrow shows the interatomic spacing in each case. [15]

2.1.3. Itinerant magnetism

In contrast to atoms, molecules, clusters, and oxides mentioned above, the magnetism of the iron-series transition-metal elements is caused by extended, delocalized, or itinerant electrons. The distinct character of

itinerant magnetism is epitomized by the non-integer spin moments per atom, such as the 2.2 μ_B for Fe, 1.7 μ_B for Co, and 0.6 μ_B for Ni.[12] Because each electron spin carries a moment of 1 μ_B, these non-integer values cannot be of ionic origin and suggest the interatomic hopping of the moment-carrying electrons. Before discussing the physical origin of itinerant ferromagnetism, it must be noted that the energy splitting of electron shells looks dramatically different in solids. Figure 2.7 summarizes the density of States $D(E)$ in (a) diatomic model, (b) small clusters, and (c) solids.[12] From the comparison, the electron levels develop on going from the sharply defined energy levels (for atoms) to the bandwidth W (for solids). Because the total number of states $\int D(E)dE \sim D(E_F)W$ is fixed by the number of atoms, $W \sim 1/D(E_F)$.[12]

Because of the delocalized character of the 3d electrons, a better understanding of the magnetism in solids is achieved by considering first the situation for quasi-free atoms. According to band theory, starting point for a discussion of ferromagnetism in metals is the band paramagnetism, which gives so-called exchange-enhanced Pauli susceptibility (χ):[12]

$$\chi = \frac{\chi_p}{1 - UD(E_F)} \qquad (\mathbf{2}.8)$$

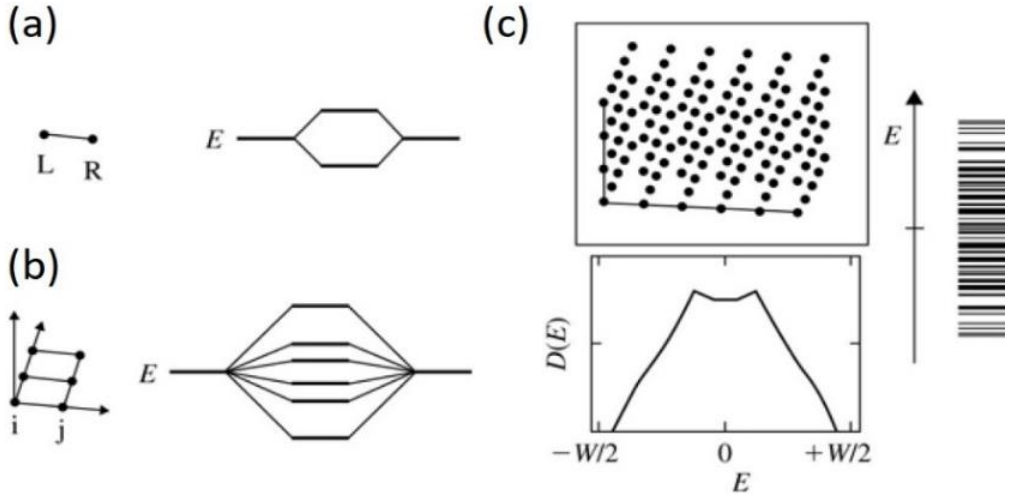

Figure 2.7 Energy levels and density of states (DOS): (a) diatomic model, (b) small cluster and (c) transition to solid. The DOS maxima correspond to regions where the energy levels are particularly dense. [12]

, where χ_p is Pauli susceptibility, U is intra-atomic Coulomb energy, and $D(E_F)$ is DOS at Fermi level. Eq. 2.8 is the key of the explanation for itinerant ferromagnetism because it eventually diverges at very large $D(E_F)$. This unstable state of paramagnetism gives rise to the famous Stoner criterion for itinerant ferromagnetism:

$$UD(E_F) > 1 \qquad (\mathbf{2}.9)$$

, where U is known as the Stoner parameter and frequently denoted by I. Figure 2.8 shows a simplified scheme that ferromagnetism occurs if the coulomb interaction (I or U) is larger than the one-electron level splitting $\Delta E \sim 1/D$.[12] Shortly speaking, the system jumps into a ferromagnetic state with nonzero moment, when the Stoner criterion is satisfied and the paramagnetic state becomes unstable. Besides, the magnitude of the moment depends on the details of the corresponding DOS.[12, 15] Based on the idea of Eq. 2.9, magnetic moments of the elements and alloys can be determined accurately from band structure calculations. The famous Slater–Pauling curve (see Figure 2.9) is then summarized by a plot of the magnetic moment per atom for binary alloys of 3d elements (against Z, the total number of valence electrons per atom).[15]

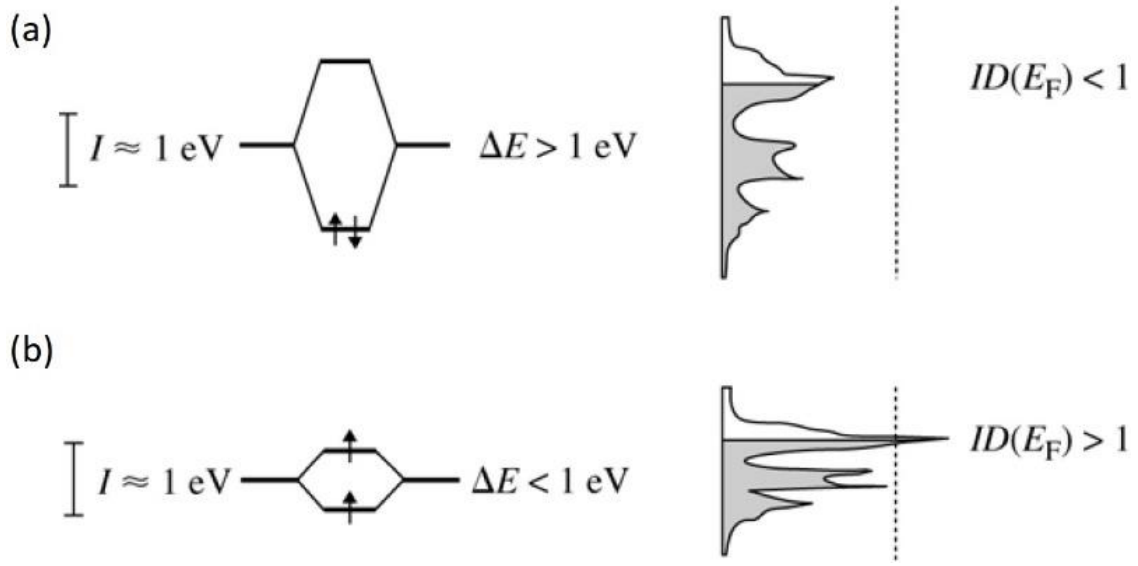

Figure 2.8 Stoner criterion: (a) paramagnetism and (b) ferromagnetism. The dotted line describes the onset of ferromagnetism, *D*(*E*) = 1/*I*. [12]

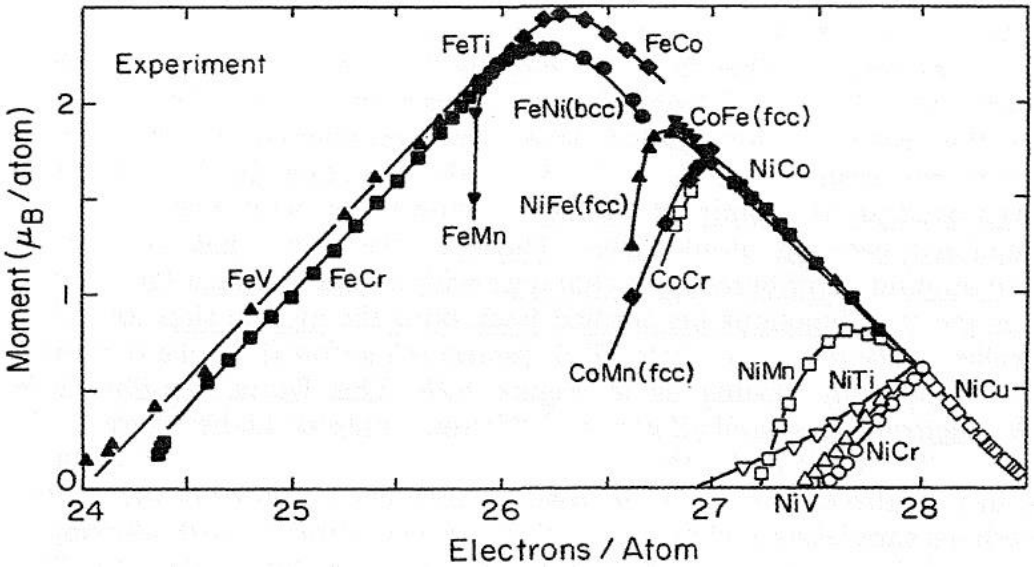

Figure 2.9 The Slater-Pauling curve showing moment per atom (in Bohr magnetons) for metallic alloys as a function of valence electron concentration or alloy composition. [15]

Itinerant magnetism is not restricted to Fe, Co, and Ni but also occurs in many alloys, such as $Fe_{1-x}Ni_x$, PtCo, and the low-T_c intermetallic $ZrZn_2$. Notable exceptions include metallic rare-earth magnetism, where the rare-earth 4f electrons remain localized compared to the outer electrons (5s, 5p, 5d or 6s shells).[11] The more complicated system is rare-earth transition-metal intermetallics (such as $SmCo_5$ and $Nd_2Fe_{14}B$) exhibit both itinerant (3d) and localized (4f) features. At the moment, the popular route to evaluate electronic structure and magnetic properties of an atom is usually carried out with spin-polarized fully relativistic methods using general Hamiltonian of a many-electron configuration given as below: [16]

$$\begin{aligned}\widehat{\mathcal{H}} &= \sum_i \left(\mathcal{H}_{\mathrm{Kin},i} + \mathcal{H}_{\mathrm{Nucl},i} + \mathcal{H}_{\mathrm{SO},i}\right) + \sum_{k\neq i} \mathcal{H}_{\mathrm{Coul},ik} \\ &= \sum_i \frac{\hbar^2}{2m}\nabla_i^2 - \frac{1}{4\pi\epsilon_0}\frac{Ze^2}{r_i} + \lambda_i(r_i)(\vec{l}_i \cdot \vec{s}_i) \\ &\quad + \sum_{k\neq i} \frac{1}{4\pi\epsilon_0}\frac{e^2}{r_i - r_k}\end{aligned} \qquad (\mathbf{2}.10)$$

, where ∇_i^2 is the operator of the kinetic energy and r_i is the coordinate of the electron *i*. Ze^2/r_i describes the Coulomb interaction of the electron *i* with the nucleus. The last term is the interaction of the electron *i* with all other electrons in the atom. $\boldsymbol{\mathcal{H}}_{\mathrm{SO,i}}$ is a single-electron operator and describes only the spin–orbit interaction of the electron *i* by the spin–orbit parameter $\lambda_i(r_i)$. Relativistic two-particle interactions of different electrons *i* and *k* (spin–spin, orbit–orbit, spin–other-orbit) are usually much smaller and could be ignored. For alloys or even more complicated system, the Hamiltonian can be expanded further to include all considerable contribution resulted by neighboring atoms.

2.1.4. Magnetic anisotropy energy

Experimentally, it is found that the magnetization of a magnetic system generally lies in certain preferred directions with respect to crystalline axes and/or the exterior shape. The energy required to rotate the magnetization from a direction of low energy (easy axis) towards a one of high energy (hard axis) is called magnetic anisotropy energy (MAE), typically of the order of 10^{-6} to 10^{-3} eV/atom.[17] In the case of permanent magnets, anisotropy energy densities vary from less than 0.005 MJ/m^3 in very soft magnets to more than 10 MJ/m^3 in some rare-earth permanent magnets.[12] There are several physical origins to generate magnetic anisotropy, such as orbital-moment formation, magnetoelasticity, and magnetoresistance.[10, 12, 17] The details of anisotropic energy can be discussed separately in terms of either by the phenomenological description (at a macroscopic level) or dipole-dipole interactions and spin-orbital coupling (at a microscopic level). Figure 2.10 shows the most obvious experimental manifestations of magnetic anisotropy in single crystals of Fe, Ni, and Co.[11] Take hexagonal Cobalt for example, its easy direction of magnetization is the c-axis; saturating the sample in the basal plane is very difficult.

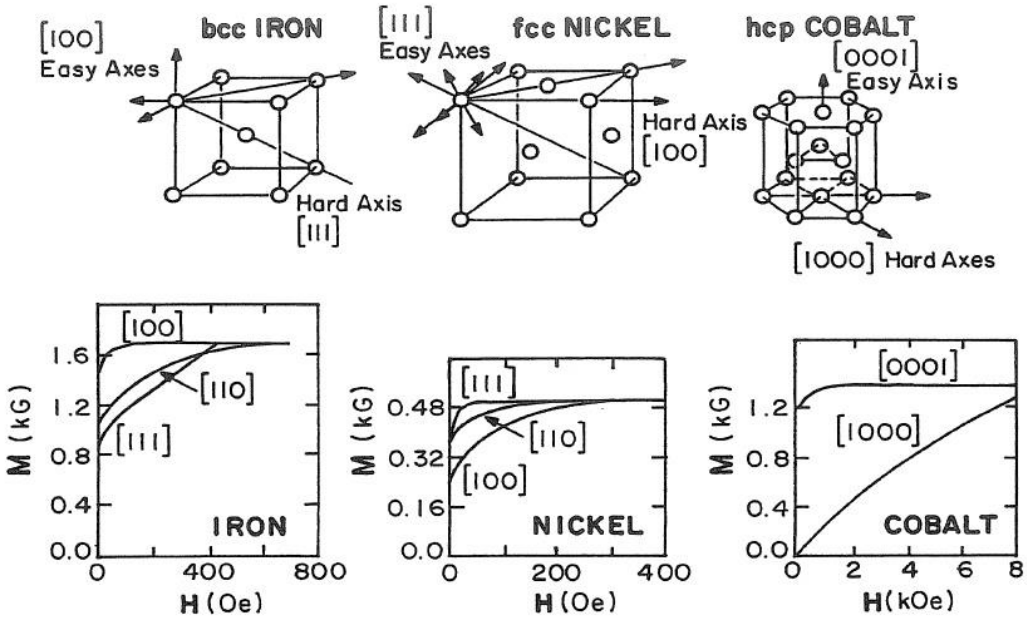

Figure 2.10 Crystal structure showing easy and hard magnetization directions for (a) Fe, (b) Ni, and (c) Co. [11]

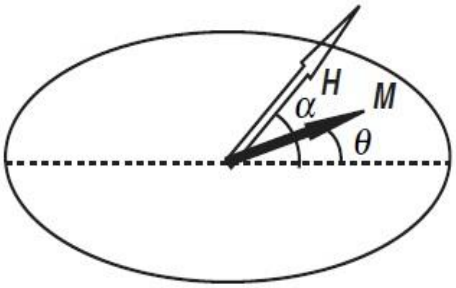

Figure 2.11 A Stoner–Wohlfarth particle. [15]

Under these circumstances the anisotropy energy E depends on only a single angle, the angle θ between the M vector and the c axis (dot lines), and the anisotropy can be described as uniaxial (see Figure 2.11).[15] In phenomenological model, magnetic anisotropy is determined by free energy as a function of the orientations with respect to crystalline axes. The most convenient way to express the anisotropy energy is to expand it in spherical harmonics or in successive powers of the unit vector components, so the usual expression of the anisotropy in hexagonal structure is usually given by

$$E/V = K_0 + K_1 sin^2\theta + K_2 sin^4\theta + \cdots \quad (\mathbf{2}.11)$$

, where V is the volume of the studied system and K_0, K_0, K_0, ... are constants for a particular material at a specific temperature and are expressed in erg/cm^3 (cgs) or J/m^3 (SI).[10, 12, 15]

In addition, macroscopic shape anisotropy has a great contribution in the case of thin films. It originates from dipole interactions due to free poles at surfaces. The analytical expression obtained for an ellipsoid revolution is as following:[12]

$$K_{shape} = \frac{1}{2}\mu_0(1 - 3N_d)M_s^2 \text{ (SI)} \quad \text{or} \quad \frac{1}{2}(1 - 3N_d)M_s^2 \text{ (CGS)} \quad (\mathbf{2}.12)$$

, where N_d is demagnetization factor for the easy axis. For thin films, the demagnetization factors parallel and perpendicular to surface plane can be approximated by 0 and 1, respectively.[15] Therefore, the shape anisotropy is expressed by $1/2\mu_0 M_s^2$ (SI) for thin films. Detailed explanation of demagnetization factor is written in the following subchapter. Although the phenomenological approach shows no mystery to understand its origin, it does not tell much about the real causes of magnetic anisotropy. In addition, it is not valid for some cases; for example, any interaction of dipolar symmetry vanishes when summed over atoms on a cubic lattice.[11] This failure suggests that magnetic anisotropy is not simply due to the anisotropy of the dipole interactions. In other words, a little more subtle mechanism is also required to explain the directional character of magnetic anisotropy. At the microscopic scale, when an ion or atom is embedded in a solid, the Coulomb interaction of its electronic charge distribution with the surrounding charges in the crystal must be considered. This is the so-called crystal-field interaction.[15] Hence, the main source of anisotropy in most magnetic materials is ascribed to magnetocrystalline anisotropy (MCA or MAE$_K$), which involves a combined effect of electrostatic crystal-

field interaction and relativistic spin-orbit coupling.[12, 15] Both of them apply to bulk anisotropy and surface anisotropy, and the same mechanism explains the orbital moment and magnetoelasticity of most magnets, as well as the anisotropic magnetoresistance of metallic ferromagnets.[12] Simplifying somewhat, the spin-orbital coupling affects the real-space motion of the electrons (orbital moment) in a solid, and this motion also adapts to the crystalline environment (crystal-field interaction).[3] Because 3d electrons are more delocalized compared to 4f ones, the magnetocrystalline anisotropy for 3d transition and rare-earth 4f magnets must be treated separately.

For rare-earth 4f magnets, the rare-earth 4f electrons are strongly localized and screened from the crystalline environment. The 4f electrons move faster near the relatively heavy nuclei and experience larger spin-orbital coupling based on relativistic effect. Therefore, the crystal field (~0.01 eV) acting on the rare-earth ions (Re^{3+}) is small perturbation to the leading contribution of spin-orbital coupling (~0.2 eV).[12] According to famous single-ion model, the calculation of this crystal-field perturbation gives frequently the simplified formula as[3, 12]

$$K_1 = -\frac{3}{2}\alpha_J r_{4f}^2 A_2^0 \left(3J_z^2 - J(J+1)\right) \qquad (\mathbf{2}.13)$$

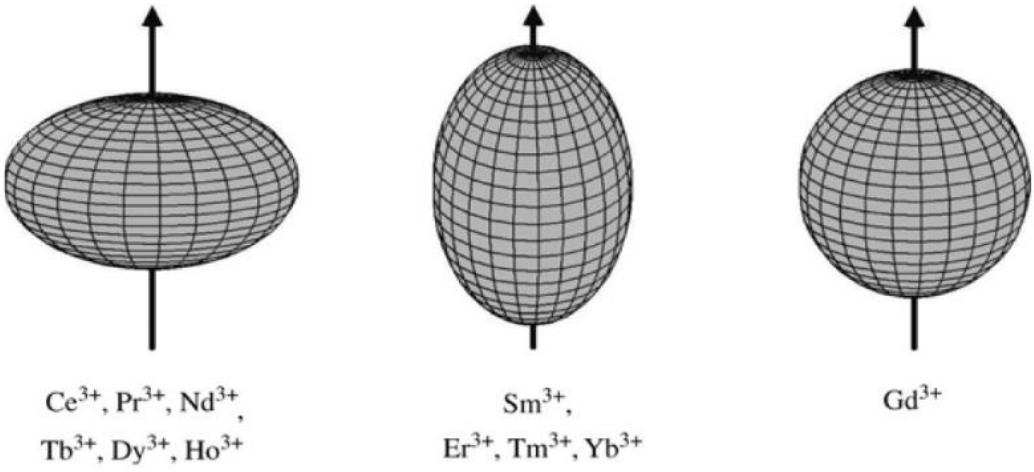

Figure 2.12 Charge distribution of 4f electron cloud based on rare –earth single-ion anisotropy. The shape is mainly determined by Hund's rule. [12]

, where the second order Stevens coefficient α_J describes the shape of the rare-earth 4f shell, r_{4f}^2 is the squared 4f shell radius, J is angular momentum (via Hund's rule), and the crystal-field parameter A_2^0 describes the crystalline environment. The sign of Stevens coefficient represents the real-space shape of the ellipsoidal rare-earth 4f electrons and depends on electron number. Figure 2.12 shows the physical meaning of single-ion model for 4f rare-earth ions, in which positive and negative α_J correspond to prolate and oblate 4f electron cloud.[3, 12]

For 3d transition magnets, the 3d wavefunctions feel a strong crystal field, so they must first minimize their energy by adapting to the crystal field. The crystal energy in this case is typically of the order of 1 eV, i.e. large as compared to its spin-orbital coupling ($\sim 0.05 - 0.1$ eV), which can be neglected in a first approximation.[12] Because of strong crystal field, the energy levels here no longer correspond to a definite quantum number m_L; rather they correspond may be labelled as xy, yz, xz, x^2-y^2, or $3z^2$-r^2, which are hybrids of opposite orbital moment m_L and m_{-L}, so that net orbital moment of these levels is zero.[17] Hence these crystal-field states show so-called quenched orbital moments in 3d ions and metals, namely rather small expectation values of both orbital moment and anisotropy. Nevertheless, the orbital motion itself is directly coupled to the lattice via the electric potential of the ions. Using second order perturbation theory, Bruno proposed that magnetic anisotropy is proportional to the variation of orbital moments only (weak spin-orbital coupling), if the majority spin band is completely filled. His simple physical picture shows that, for example in uniaxial systems, $K_1 \sim \xi^2/W$ where W is the d bandwidth. According to this relation, he found that perturbation theory enables to provide a simple explanation for this order of magnitude of magnetic anisotropy as[15, 17]

$$\Delta E = K_0 + K_1 sin^2\theta \approx -\frac{1}{4}\lambda\Delta\mu_L \quad \text{(uniaxial systems)} \qquad (\mathbf{2}.14)$$

, where $\Delta\mu_L$ represents the variation of orbital moments between different magnetization directions. The virtue of this model is that it is allowed to estimate directly the anisotropy constant K_1 without calculating explicitly

the total energy of the system as a function of magnetization along different directions.

As magnetic anisotropy is the important property as the origin of hysteresis and coercivity. It is always not an easy task to quantitatively measure the strength of the magnetocrystalline (or any other) anisotropy. Experimentally, people usually evaluate the rough values of magnetic anisotropy from the system of interest via two methods as following:[10]

1. By fitting a calculated magnetization curve to the observed angle-dependent torque curve.

2. By measuring a $M(H)$ graph, the area included between two magnetization curves along easy- and hard-axes can be used roughly for determining anisotropy constants. The idea is based directly on the definition of the anisotropy energy E, namely, the energy stored in a crystal when it is magnetized to saturation in a non-easy direction.

Both of these two methods have their own technical limit; nevertheless, the first method (ex. torque curves) is much more accurate and enables to determine not only K_1 but also K_2 values if the contribution of K_2 is not negligible.

2.1.5. Hysteresis and magnetic domain

The wide variety of ferromagnetic materials can be rather easily divided into two groups: the magnetically soft (easy to magnetize and demagnetize) and the magnetically hard (hard to magnetize and demagnetize).[10] The essential practical characteristic of ferromagnetic materials is the irreversible nonlinear response of magnetization M to an external magnetic field H. This magnetic performance can be easily epitomized by their hysteresis loops, in which field is usually presented by to H, rather than B, because the internal field must be distinguished.[15] Figure 2.13 shows some types of hysteresis loops encountered in practice: (a) the major difference between permanent (or hard) magnets and soft magnets is the

magnitude of the coercivity, ranging from less than 10 μT (soft) to more than 1 T (hard); (b,c) two-phase loops are superpositions of single-phase hysteresis loops and relate to macroscopic phase mixtures at the nano- or submicron-scale.[12]

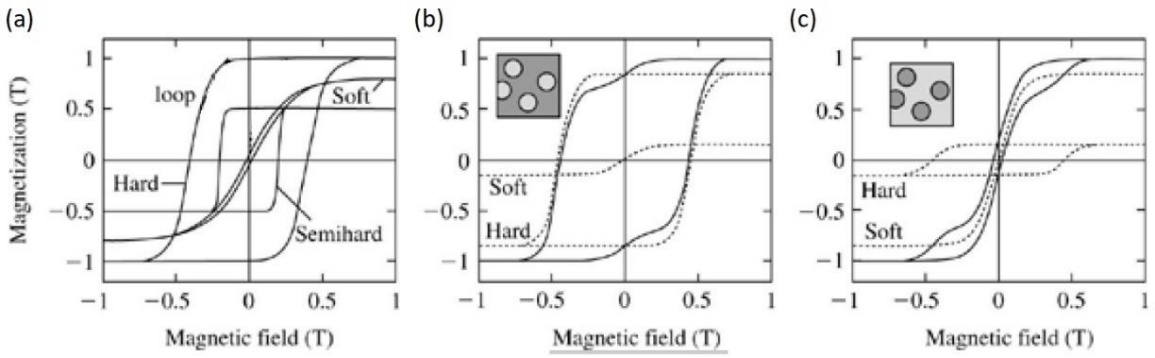

Figure 2.13 Typical hysteresis loops: (a) hard, semihard, and soft magnets, (b) inflected loop (85% hard and 15% soft phases), and (c) wasp-shaped loop (15% hard and 85% soft phases). In (b) and (c), dark and bright regions correspond to hard and soft regions, respectively. [12]

It is obvious that hard magnetic materials have broader and nearly square $M(H)$ loops. They are suitable for permanent magnets because, once magnetized by applying a sufficient field to saturate the magnetization, they remain in a magnetized state. Soft magnetic materials have very narrow loops, and in some cases the open loop is even invisible. Therefore, soft magnets are temporary magnets, which means that their net magnetization nearly disappear as soon as the field is removed. In nanocomposites, exchange interactions between the phases tend to smooth the loops, and the resulting loops are strongly associated with how the magnetic phases mix together. In terms of regular industrial use, people get used to make a simple classification of ferromagnetic materials on the basis of their coercivity (sometimes as well as corresponding remanence magnetization). Generally speaking, hard magnetic materials are those with coercive fields above 1.2 T (12 kOe), while soft magnetic materials are those with coercive fields below 1.2 mT (12.5 Oe).[18]

Studying hysteresis loops is usually based on phenomenological method, so it is important to plot studied loops appropriately. Usually, the hysteresis loops are represented in terms of induction (B) or of magnetization (M) against applied field (H). The relation between magnetization and induction is

$$B = \mu_0(H + M) \qquad (\mathbf{2}.15)$$

, where $\mu_0 = 4\pi \times 10^{-7}$ H/m is the permeability of the vacuum. Sometimes, the relation in Eq. 2.14 is formulated as

$$B = \mu_0 H + J \qquad (\mathbf{2}.16)$$

, where $J = \mu_0 M$ (or I) is called magnetic polarization. This term J is quite frequently used in the circle of hard magnetism.

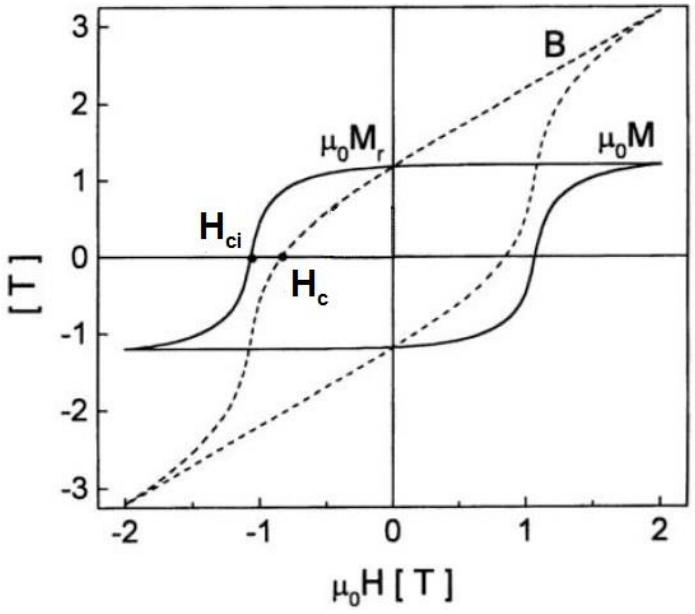

Figure 2.14 Difference between *B*(*H*) and *M*(*H*) hysteresis loops in hard magnets. [19]

In a soft material, it can be fully saturated using a small external field. Hence $B \cong \mu_0 M$ is a reasonable approximation, and plotting $B(H)$ and $M(H)$ makes only a tiny difference. However, B and M have comparable orders of

magnitude in hard magnets, so $B(H)$ curve is significantly different from the $M(H)$ one (see Figure 2.14).[19] Although both $M(H)$ and $B(H)$ exhibit important properties – coercivity ($\mu_0 H_c$) and remanence ($\mu_0 M_r$), there are two possible definitions for the coercivity, depending on whether one considers the point of induction or magnetization reduces to zero. Coercivity of $M(H)$ and $B(H)$ loops is usually denoted as H_{ci} and H_c, respectively. Most frequently considered are ordinary $M(H)$ loops because they are usually recorded directly by conventional magnetometry. In some textbooks, $M(H)$ loops are also known as extrinsic loops. If magnetization is desired to be displayed as intrinsic loops using internal field $H_i = (H - N_d M)$, the demagnetizing field $N_d M$ is necessarily included to describes the geometry shape of the magnet with demagnetizing factor N_d. The physical origin of demagnetizing field can be visualized by the scheme shown in Figure 2.15.[10] It is noted that the name "intrinsic" could be kind of misleading. Intrinsic $M(H_i)$ hysteresis represents actually an extrinsic or real-structure phenomenon, except that the macroscopic sample shape is taken into account.

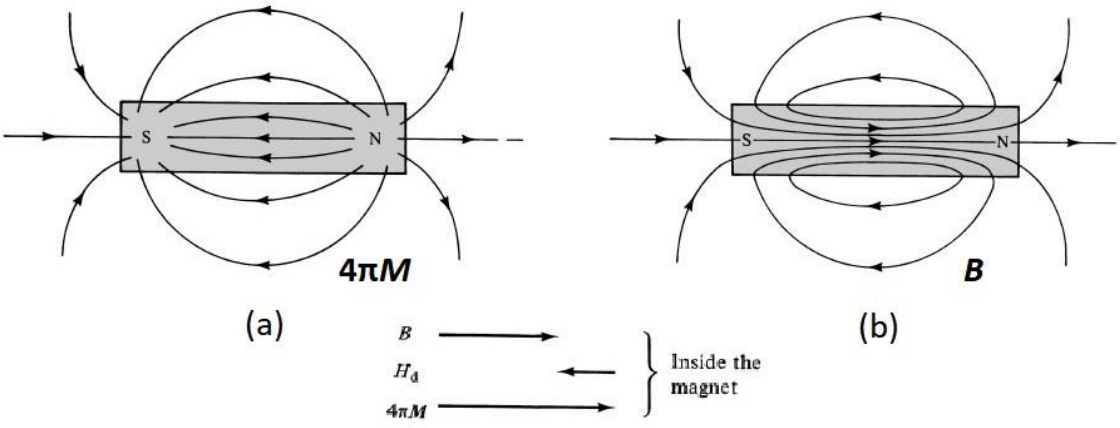

Figure 2.15 Fields of a bar magnet in zero applied field (*H*a): (a) *H* field, and (b) *B* field. The vectors in the center indicate the values and directions of *B*, H_d, and 4πM (cgs units) at the center of the magnet. [10]

Furthermore, the geometry of studied material influences not only magnetization but also the induction. This means that both forms of $M(H)$ and $B(H)$ loops are very sensitive to the specimen shape whether plotted as M-H_a or B-H_a but not when plotted versus internal field, $\mu_0 M$-$\mu_0 H_i$ or $\mu_0 B$-$\mu_0 H_i$ (see

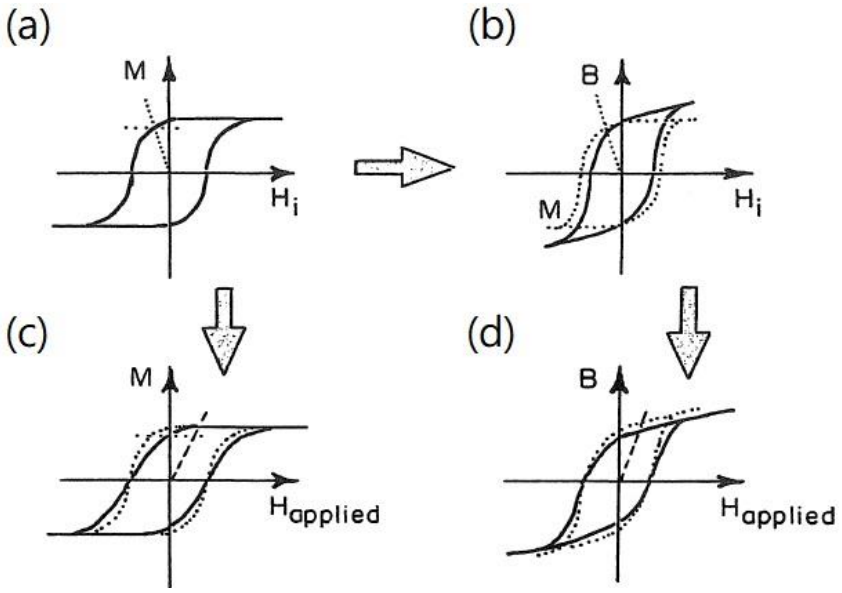

Figure 2.16 (a) The *M*- *H*i loop is an intrinsic characteristic of the material (no shape effects). It appears for reference as the dotted loops in panels (b) and (c). The solid loops in (c) and (d) show the change in loop shape on going from *H*i to *H*a (a→c & b→d) (strong sample shape effects). [11]

Figure. 2.16).[11] When permanent magnets are used in "open circuit" applications (which is nearly always the case), their technical properties are strong functions of the shape of the magnet. Closed-circuit applications could involve the use of a permanent magnet to bias a soft element in a magnetic circuit. Both open circuit and close circuit magnetometers are schemed in Figure 2.17.[11] The more the measurement technique or application design resembles a closed circuit (fewer free surfaces normal to M), the more closely the material performance will reflect the intrinsic properties of the magnet.

With proper correction for demagnetization issue, $M(H)$ curve reflects better the intrinsic properties of the studied system, and $B(H)$ gives a more useful description of the system behavior under working conditions. For modern hard magnets, one of the most improvement is the breaking of the shape barrier in 1950.[15] This means that they could be made in any desired shape, without having to resort to horseshoes and bars to avoid self-demagnetization.

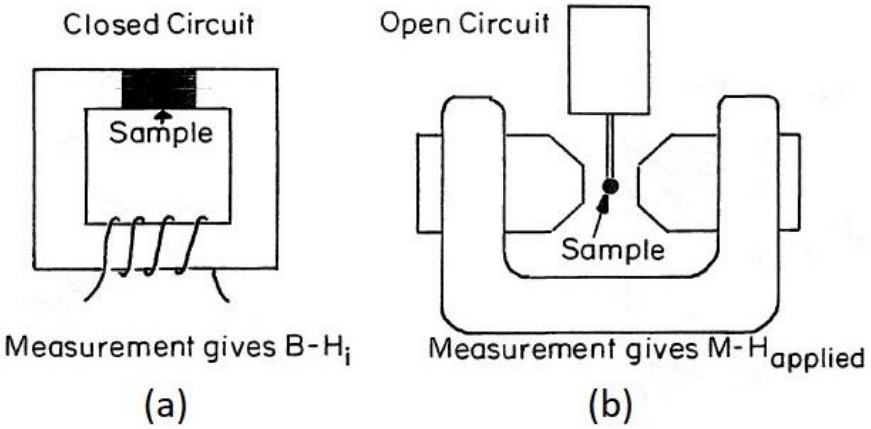

Figure 2.17 Schematic of two ways of measuring properties of permanent magnets. (a) Closed circuit inductive measurements give B-$H_i \approx B$-H_{appl} with negligible demagnetization effects from sample surfaces. (b) Open-circuit magnetometer measurements give M-H_{appl} (not = M-H_i) loops with full sample shape effects. [11]

The description of hysteresis from merely atomic or intrinsic parameters is a major challenge in theory of magnetism. The determination of hysteresis loops from local quantities is the subject of a branch of magnetism known as micromagnetics.[12] The basic premise of micromagnetism is that a magnet is a mesoscopic continuous medium where atomic-scale structure can be ignored: M(r) and H(r) are generally nonuniform, but continuously varying functions of position r. The simplest micromagnetic model is the Stoner-Wohlfarth model, which is an analytic model for coercivity based on the simplification of coherent reversal in single-domain particles.[15] Imagine a Stoner–Wohlfarth particle, a uniformly magnetized ellipsoid with uniaxial anisotropy of shape or magnetocrystalline origin in a field applied at an angle α to the anisotropy axis (see Figure 2.11). The energy density of this ideal system is

$$E_{tot} = K_u sin^2\theta - \mu_0 MHcos(\alpha - \theta) \qquad (\mathbf{2}.17)$$

, where θ and α are the angles between the directions of M and H with respect to easy-axis. Here E_{tot} and K_u, the anistropy constant, are usually

measured in J/m^3. Minimizing E_{tot} with respect to θ gives an important result that the switching field is equal to the coercivity. The hysteresis of a Stoner–Wohlfarth particle is illustrated in Figure 2.18, which presents that switching of magnetization is the irreversible jump and occurs when $d^2E_{tot}/d\theta^2 = 0$.[15] The hysteresis loop is perfectly square when $\alpha = 0$, and in that case the coercivity is equal to the anisotropy field:

$$H_c = 2K_u/\mu_0 M_s \qquad (\mathbf{2}.18)$$

or

$$H_c = \left(\frac{2K_1}{\mu_0 M_s}\right) + [(1-3N)/2]M_s \qquad (\mathbf{2}.19)$$

Here, K_u is the sum of the magnetocrystalline anisotropy (K_1) and the shape anisotropy ($\mu_0 M_s^2(1-3N_d)/4$).[12, 15] These two equations are the core results of Stoner-Wohlfarth model, and the K_u term in former one is usually replaced by K_1 for the cases of bulk permanent magnets. However, this relation is rarely observed due to some facts including the size of particles, morphological inhomogeneities and incoherent magnetic reversal.[12] Although Stoner–Wohlfarth model cannot explain the magnetization curves in sintered magnets, it is a useful starting point for the

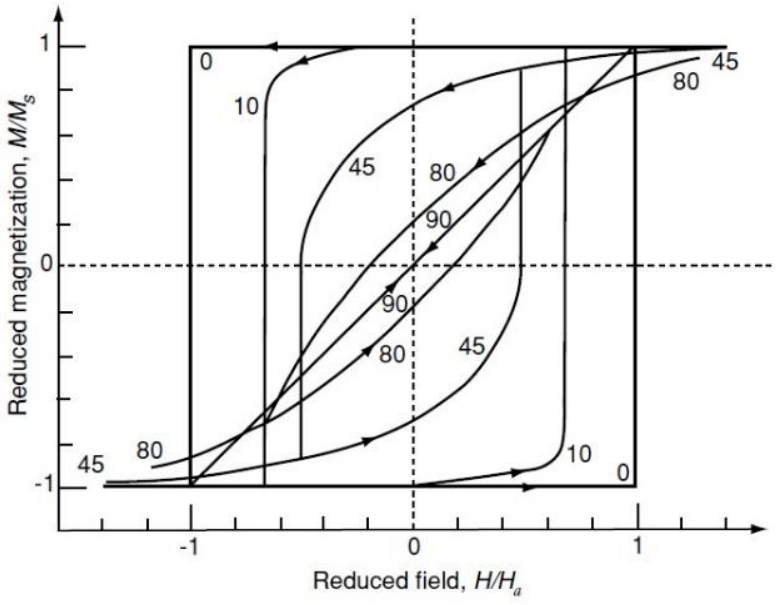

Figure 2.18 A Stoner–Wohlfarth particle. [15]

discussion of the angular dependence of magnetization curves and predicts spin-reorientation transitions.[12, 15]

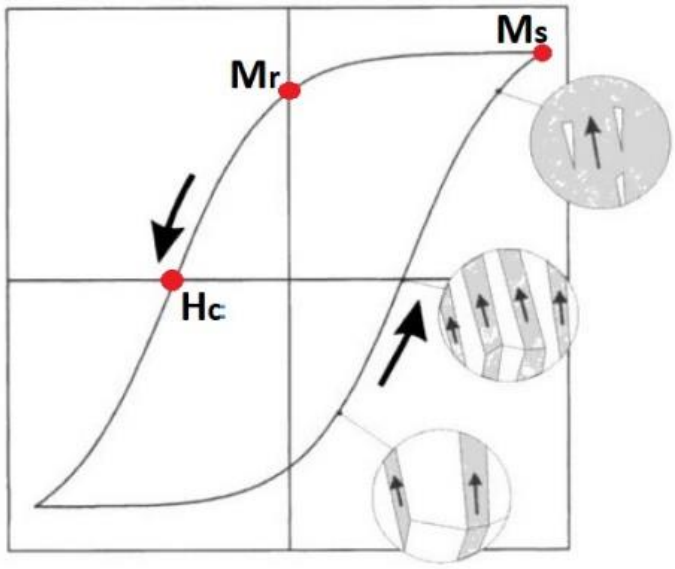

Figure 2.19 Schematic representation of hysteresis loop with corresponding evolution of magnetic domains. [19]

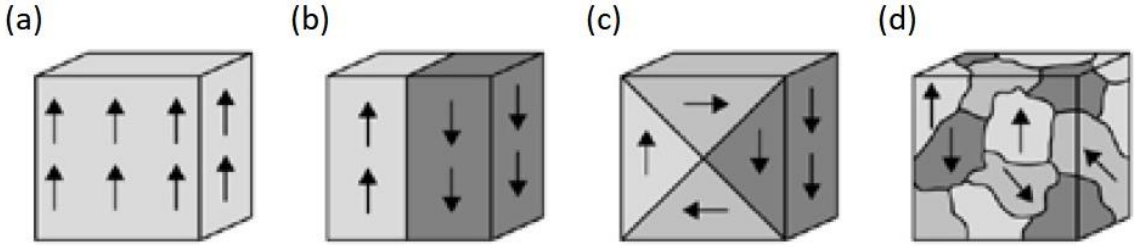

Figure 2.20 Micromagnetic spin configurations: (a) single-domain state, as observed in very small particles, (b) two-domain configuration, as encountered in fairly small particles with uniaxial anisotropy, (c) flux-closure in cubic magnets, (d) complicated domain structure in a polycrystalline magnet. [12]

Moreover, the applied field along hysteresis loop serves to unveil the spontaneous ferromagnetic order that already exists on the scale of microscopic domains. These domain structures are illustrated schematically along the hysteresis loop in Figure 2.19.[19] Historically, the concept of domains was introduced to explain why two pieces of soft iron do not attract each other. In 1907, Weiss postulated the existence of magnetic domains created by

mean-field interactions, accompanied by a loss of net magnetization due to domain formation.[12] Figure 2.20 shows four kinds of possible configurations of magnetic domain: (a) single-doamin, (b) two-domain structure, (c) flux-closure structure, and (d) multi-domain, which are created and stabilized by minimizing the sum of magnetostatic and exchange energy.[10, 12]

In 1932, Bloch introduced the concept of domain walls, and the first quantitative calculations by Landau and Lifshitz are now regarded as the starting point of modern domain theory. As shown in Figure 2.21, two adjacent domains are separated by a thin region called domain wall.[10] The role of domain wall is for continuous spin reorientation between two regions where the magnetization rotates from one easy direction to another. Again, the structure and energy of domain wall is determined in terms of energy minimum. Experimentally, the magnetic domain structure can be

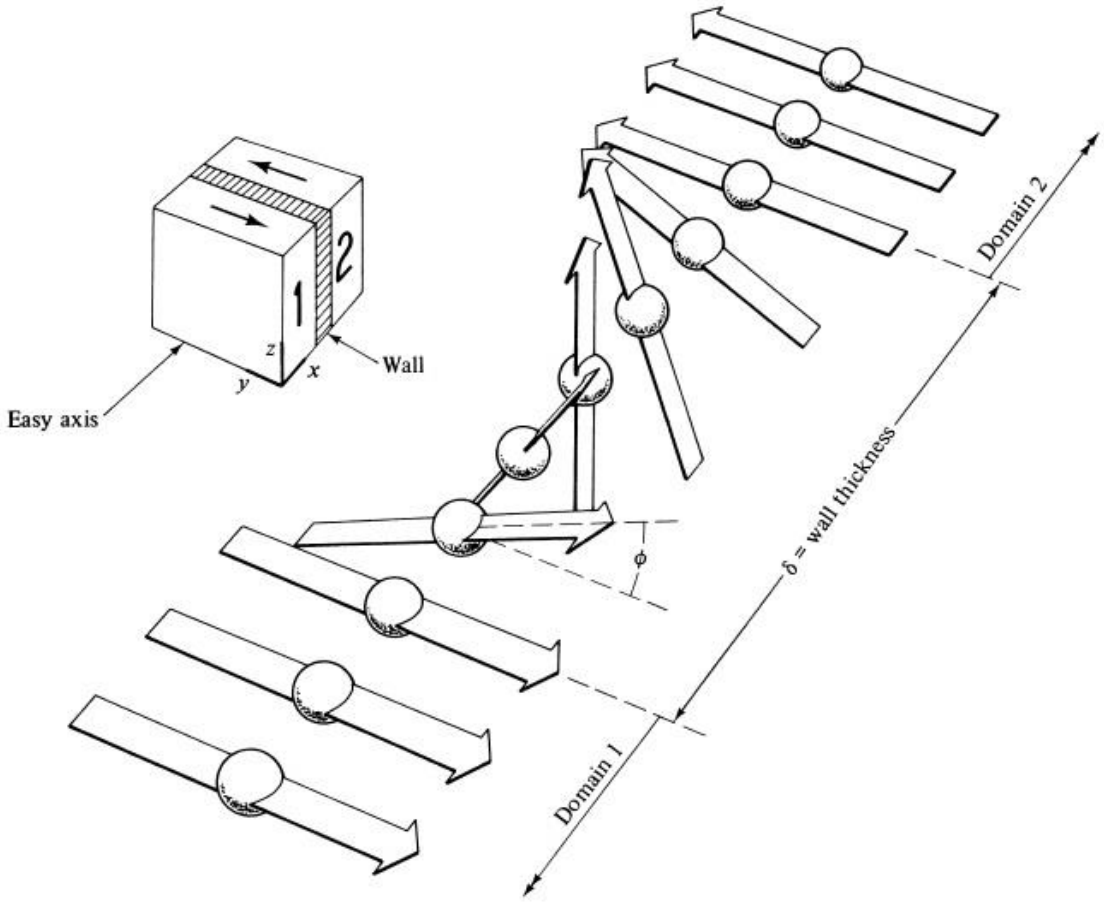

Figure 2.21 Structure of a 180° domain wall. [10]

easily observed by Kerr microscope (optical effect) or magnetic force microscope (tip-sample magnetic interaction). For both of them, it is necessary to polish the specimen properly prior to measurements. The former approach is usually utilized for large-sale probe area (ex. 100 μm × μm), whereas the later one has very high spatial resolution frequently used for nanostructure investigation.

2.1.6. Coercivity mechanism

As discussed above, anisotropy field predicted by Stoner-Wohlfarth model is merely equal to the observed coercivity (see Eq. 2.18). In 1947, Brown further proved rigorously that the coercivity for a homogeneous, uniformly magnetized ellipsoid obeys the inequality:

$$H_c \geq \left(\frac{2K_1}{\mu_0 M_s}\right) - N_d M_s \tag{2.20}$$

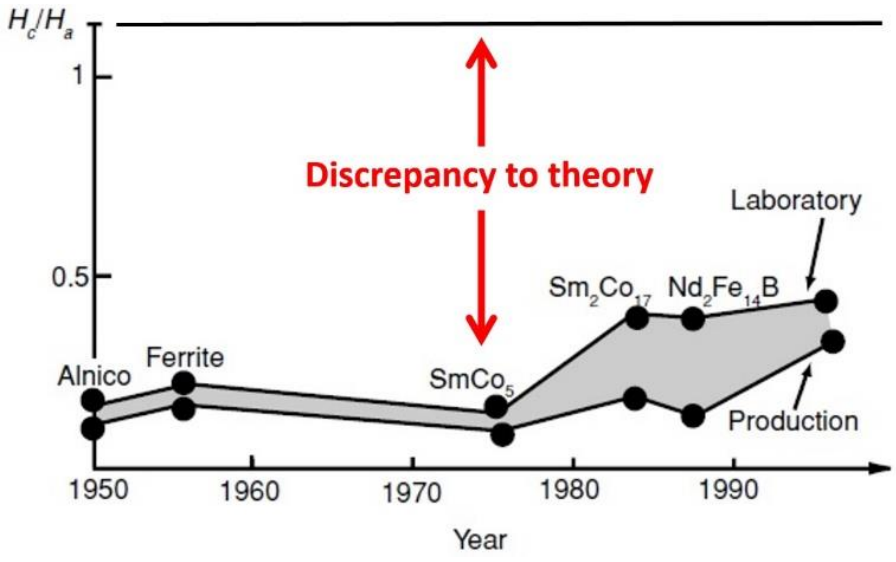

Figure 2.22 Progress towards narrowing the gap between the anisotropy. [15]

, which is a surprising result known in micromagnetics as Brown's theorem.[15, 20] Unfortunately, this equation still gives the theoretical H_c

values which in general are a factor of 10 larger than those actually realized in materials. This discrepancy between theory and experiment is known as Brown's paradox (see Figure 2.22).[15]

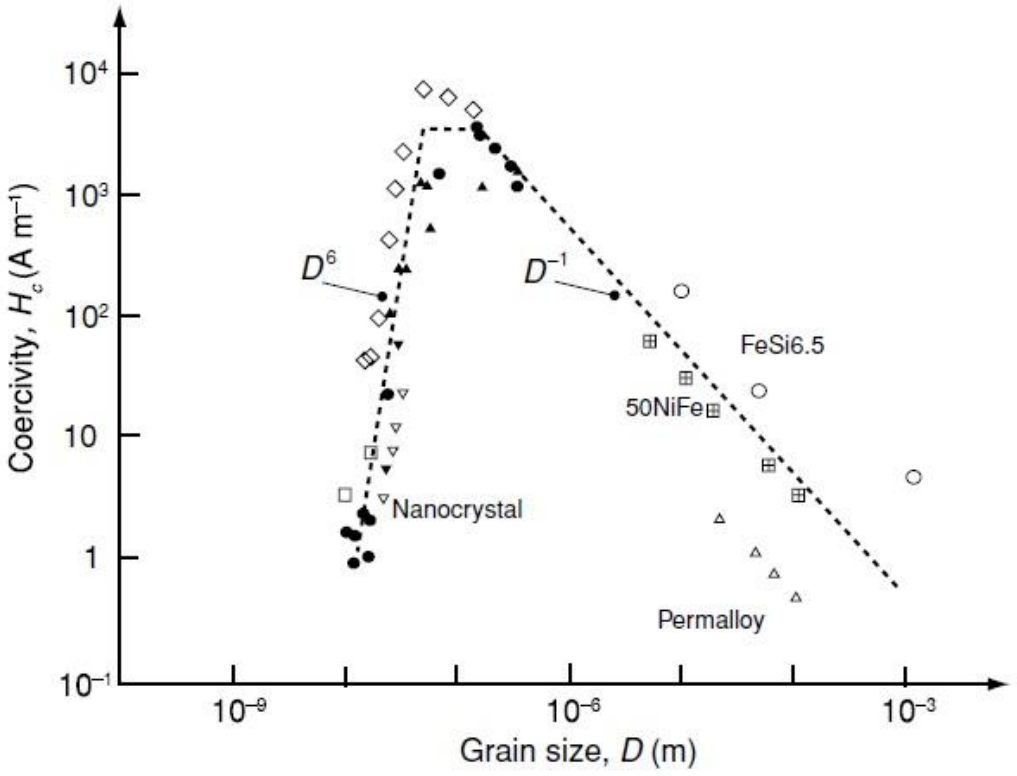

Figure 2.23 Coercivity versus grain size for a range of soft magnetic materials. [15]

The reason for this huge gap is associated with the complicated microstructure in real permanent magnet systems. Firstly, the internal magnetization of all real materials is inhomogeneous, so that the assumption of Brown's theorem is not appropriate any more. Secondly, magnetization reversal is in fact initiated in a small nucleation volume around misaligned regions or a defect. Besides, coercivity is also strongly influenced by the grain-boundary phases and grain size distribution (as shown in Figure 2.23).[15]

In order to explain domain reversal properly, there are two basic mechanisms responsible for producing large coercive fields, i.e., for the so-called magnetic hardening, namely, the reversal of the magnetization by nucleation of reversed domains (nucleation mechanism) and the reversal of the

magnetization by displacement of pinned domain walls (pinning mechanism).[21] In general, nucleation mechanism is connected with the existence of small misaligned or nonmagnetic particles or grains near grain-boundary. The pinning mechanism is associated with structural defects or magnetic inhomogeneities which are present in the grains and act as pinning centers for domain wall motion. The source of inhomogeneities may occur from precipitates, point defects, dislocations, antiphases and so on. In 1987, the coercive field of both nucleation and pinning hardened materials are better described by Kronmüller's universal relation:

$$\mu_0 H_c = \alpha\mu_0 \left(\frac{2K_1}{\mu_0 M_s}\right) - \mu_0 N_{\text{eff}} M_s \qquad (2.21)$$

, where α and N_{eff} correspond to microstructural parameters which include the change of local anisotropy, magnetic homogeneity and effective demagnetization field.[20-22]. In some papers, $\mu_0 M_s$ is replaced by magnetic polarization, J_s. Based on his work, it was found that the reversal of the studied system can be assigned as combination of pinning and nucleation mechanism if α is less than 0.3. If $\alpha > 0.3$, only nucleation mechanism exists for the domain wall movement during reversal process. Furthermore, Eq. 2.21 also provides good description on angle- and temperature-dependent coercivity behavior.

The concepts of domain-wall pinning and nucleation of reverse domains are quite central for the explanation of coercivity in real materials. In ideal permanent magnets, the optimal configuration is the texture consists of single domain grains enclosed by thin decoupled nonmagnetic layer. However, the true magnetic products always contain a relative large amount of defects and broad grain size distribution, so that the true H_c is always far below than theoretical value.

2.1.7. Permanent magnets

The purpose of permanent magnets (or hard magnets) is to provide a magnetic field in a particular volume of space. Magnetic field actually can be produced by either electric current in a conductor or by poles in a magnet. However, a permanent magnet is the better choice for many applications because it provides a constant field without the continuous expenditure of electric power and heat generation. Therefore, permanent magnets can be regarded as an energy-storage device.

The most essential function of a magnet is to provide an external field, so it must have free poles and work on open circuit. In last step of magnet manufacturing process, a strong pulse field is applied to it to reach saturated state and then removed. This working condition forces a permanent magnet to operate at a point somewhere along the second quadrant of the B-H curve (also called demagnetization curve) in absence of external field. Besides, large intrinsic demagnetization field must be taken into account in the case of any permanent magnets, which depends on the shape of the magnets. Based on these requirements, Figure 2.24 shows that the operating point P of the magnet is determined by the intersection of the line OP with the second quadrant of the hysteresis loop.[10] The line 0C is called the load line with slope given by[10]

$$-\frac{1-N_d}{N_d}\ [\text{SI}] \quad \text{or} \quad -\frac{4\pi-N_d}{N_d}\ [\text{cgs}] \qquad (\mathbf{2}.22)$$

It is clear that the operating point is fixed to the demagnetizing factor of the magnet, N_d. From viewpoint of real application, the operation point is rather important because it means how much the actual remanence is really achieved in a given shape having average demagnetization factor.

Another standard figure of merit for permanent magnets is the maximum energy product $(BH)_{max}$, which is measured in MGOe(CGS) or kJ/m^3(SI) The terminology, 'Energy Product', is the measure of the magnetic energy

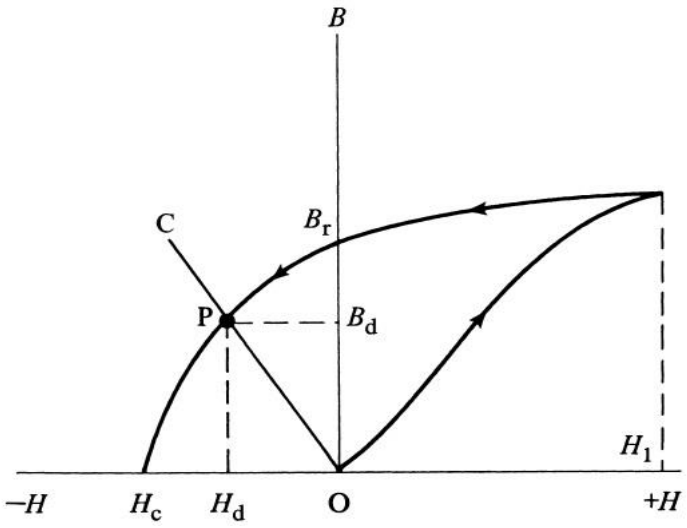

Figure 2.24 Left: demagnetization curve; right: corresponding values of energy product (BH) plotted vs the same B scale. Maximum value of (BH) is indicated on both plots. [11]

which can be stored in a magnetic material (per unit volume). By definition, it is calculated as the maximum product of a material's residual magnetic flux density and its coercivity.[23] In reality, there are several ways to estimate $(BH)_{max}$ from the second quadrant of the B-H loop. Figure 2.25 gives an example of two usual methods:[11]

(a) The value is determined by the point on the second-quadrant branch that gives the largest area for an enclosed rectangle. It may be found at the point on the loop that extends furthest into the hyperbolic contours of constant BH product (shown by dashed lines).

(b) Another common way is to calculate the BH products by point from left panel and plot its value on the right side as seen in the figure. The location of $(BH)_{max}$ is the point at which the material characteristics of a permanent magnet are most efficiently used. Therefore, the design of products is usually based on the O point to achieve the highest magnetic performance. However, the actual $(BH)_{max}$ for each commercial product must be precisely determined according to its own shape, taking load line into account. This means that the O point here is replaced by operation point P (see Figure 2.24).

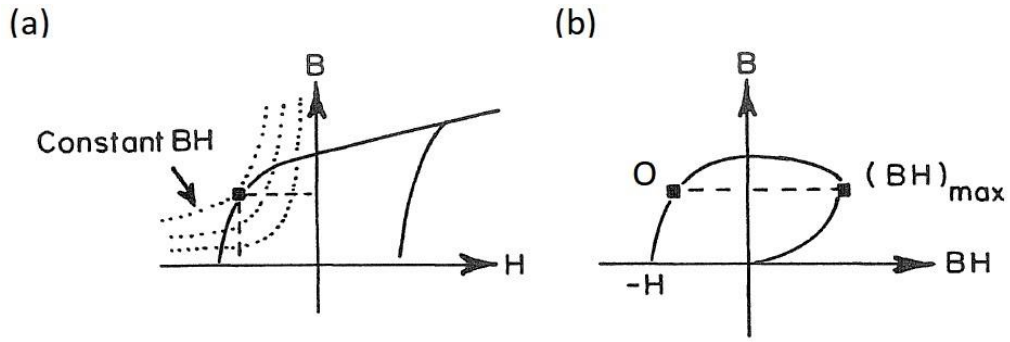

Figure 2.25 (a) Partial B-H loop showing contours of constant B-H in second quadrant and (B-H)max rectangle enclosed; (b) a common way of calculating and displaying (BH)max from second-quadrant data. [10]

In summary, the criterion of modern permanent-magnet alloys in performances is: (1) magnetization, (2) anisotropy, and (3) Curie temperature. Furthermore, the actual magnetic performance of single magnet includes both intrinsic magnetic properties, such as M_s and K_1, and two extrinsic properties, like M_r and H_c.[15] The hysteresis loop is a central approach which enables us to quickly examine H_c, B_r and the shape of magnetization curve. Hence physicists endeavor to explain it, materials scientists aim to improve it and engineers work to exploit it.

2.2. Rare-earth free ferromagnetic materials

In this thesis, the experimental work focuses on three rare-earth-free magnetic compounds: LTP-MnBi, τ-MnAl and α'-Fe_8N. The former two materials are the main research targets of our G8 project. Fe-N magnetic system is another interesting topic because it was reported that the ordered phase, α''-$Fe_{16}N_2$, could shows giant saturation magnetization. The physical properties of these three compounds are described in detail as following.

2.2.1. LTP-MnBi

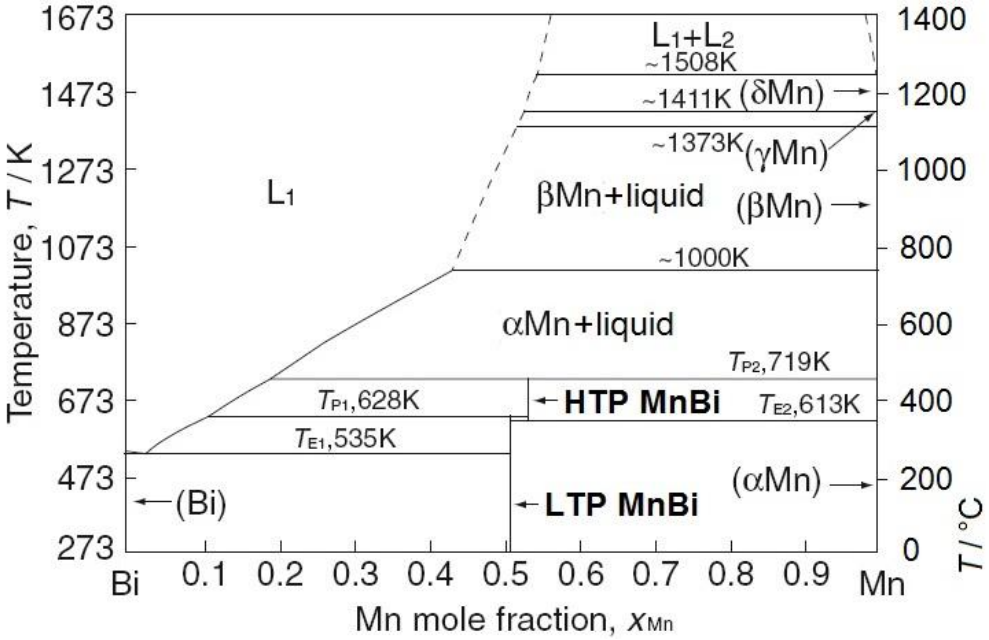

Figure 2.26 Phase diagram of MnBi system. (reproduced from [24])

The binary MnBi compound crystallizes into two phases: the low temperature phase (LTP) and the high temperature phase (HTP), as shown in the phase diagram (see Figure 2.26).[24] At around 630 K, the ferromagnetic LTP with NiAs-type structure (MnBi, $P6_3/mmc$) transforms to a paramagnetic HTP with a Ni_2In-type structure ($Mn_{2.23}Bi_{1.88}$, *Pmma*) through peritectic decomposition temperature (T_{P2}).[25, 26] Additionally, there is a eutectic reaction at 535 K (262 °C), L ⇋ Bi + MnBi. This nature limits the maximum temperature to which the material can be exposed. While this eutectic temperature is about 62 K higher than the desired operating temperature of 473 K (200 °C), it is rather low for a typical bulk magnet fabrication method such as sintering and hot pressing.[26]

HTP-MnBi itself cannot be used as a data storage material, because it is thermally unstable.[27] Conversely, LTP-MnBi exhibits several remarkable magnetic properties: high (uniaxial) first-order magnetocrystalline anisotropy (K_1) and a coercivity higher than that of Nd-Fe-B magnet at high temperatures. The positive temperature coefficient (β) of coercivity for

LTP-MnBi magnets above room temperature is a great advantage compared to the current hard magnetic materials, like Nd-Fe-B and Sm-Co compounds with negative coefficients, for high temperature applications. Theoretically, LTP-MnBi exhibits magnetic moment of 3.63 μ_B/f.u. (714 emu/cm^3), density of 8900 kg/m^3, $\mu_0 M_s$ of 8.2 kG (0.82 T), intrinsic coercivity of greater than 17 kOe, magnetocrystalline anisotropy constants (K) of -0.275×10^6 J/m^3, and an energy product of 17.7 MGOe (140.8 kJ/m^3) at 0 K.[25-28] Furthermore, T_c was calculated to be 711 K by the mean field theory.[28]

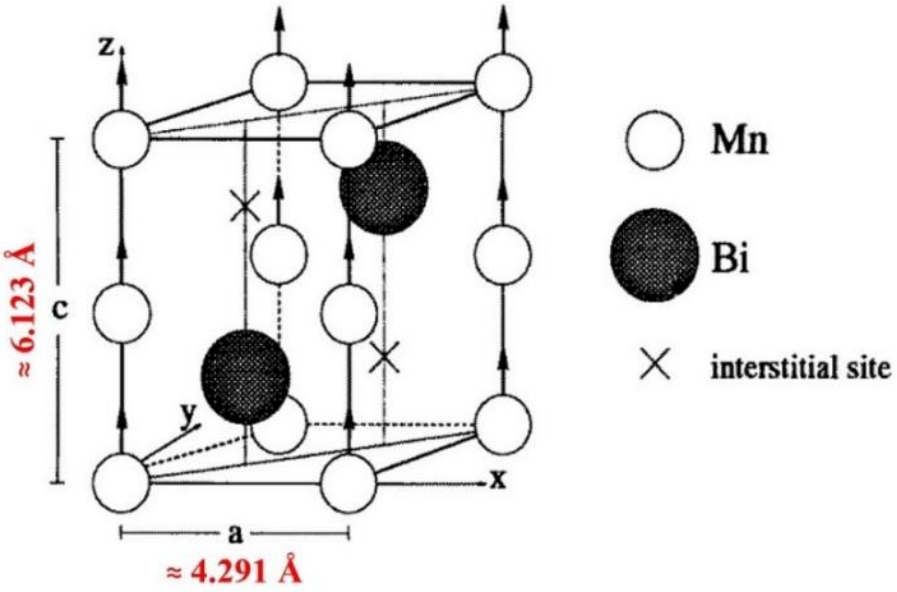

Figure 2.27 Crystal structure of LTP-MnBi. [27]

Figure 2.27 shows the crystal structure of LTP-MnBi, which is a stacking of alternate planes of Mn and a nonmagnetic atom.[27] The Mn–Mn distance is 305 pm, and the moment per Mn, measured by neutron diffraction, is 3.5 μ_B at room temperature and 4.0 μ_B at 10 K.[9] However, the magnetization is not high due to the space occupied by bismuth and a small negative induced moment on it. Moreover, hybridization of the Mn and Bi orbitals may contribute to its interesting temperature dependent magnetocrystalline anisotropy. According to several neutron diffraction reports, the magnetization of Mn is along the c-axis from 240 to 650 K. It begins to deviate gradually from the c-axis at about 200 K, and continues to approach the ab-plane down to 10 K, where the magnetization does not totally lie in the *ab*

plane.[29, 30] This finding is supported by the reported ac susceptibility measurement, which shows a spin reorientation around 90 K.[29]

Although Bi is inexpensive in the market ($18/kg in 2014), this is somewhat deceptive; the price reflected the current demand for the metal, which is obtained in quantities less than 10000 tons/year as a byproduct of lead production. In fact, the amount of Bi is also quite rare, so the price could skyrocket if further quantities were required for permanent magnet manufacture.[9]

2.2.2. τ-MnAl

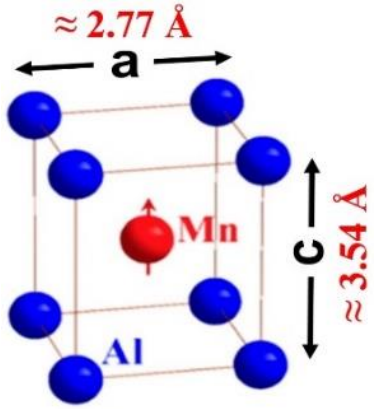

Figure 2.28 Crystal structure of τ-MnAl. (reproduceded from [33])

τ-MnAl alloy is another attractive Mn-based permanent magnetic compound due to its good magnetic properties (superior to conventional ferrites), high technological properties (mechanical strength and corrosion resistance) and low cost (~$4/kg).[9, 31] This metastable phase in the MnAl system, first reported by Kono and Koch et al., forms with the CuAu type-I structure and is highly anisotropic with the easy axis of magnetization in the [001] direction (see Figure 2.28).[4, 32, 33] The calculated magnetic moment and MAE_K for τ-MnAl are 2.37 μ_B/f.u. (830 emu/cm^3) and 1.525 × 10^6 J/m^3, respectively, which result in the maximum energy product of 12.64 MGOe (100.6 kJ/m^3) and the anisotropy field of 38 kOe.[34, 35] Due to low density of 5200 kg/m^3, τ-MnAl has a high-energy

product per unit weight compared to classical ceramic and Alnico magnets (see Table 2.1);[36] therefore, intensive research studies have been conducted on the fabrication and improvement of MnAl-based magnets over several decades.

Table 2.1 Comparison of the estimated $(BH)_{max}$, density and $(BH)_{max}$ per unit weight for several commercial permanent magnets.[36]

Material	$(BH)_{max}$ [MGOe]	Density [kg/m^3]	$(BH)_{max}$/Density [$kGOem^3/kg$]
$Nd_2Fe_{14}B$	45	7600	5.92
Sm-Co	30	8300	3.61
τ-MnAl	12	5200	2.31
AlNiCo	6	7000	0.86
Ferrites	4.5	5000	0.90

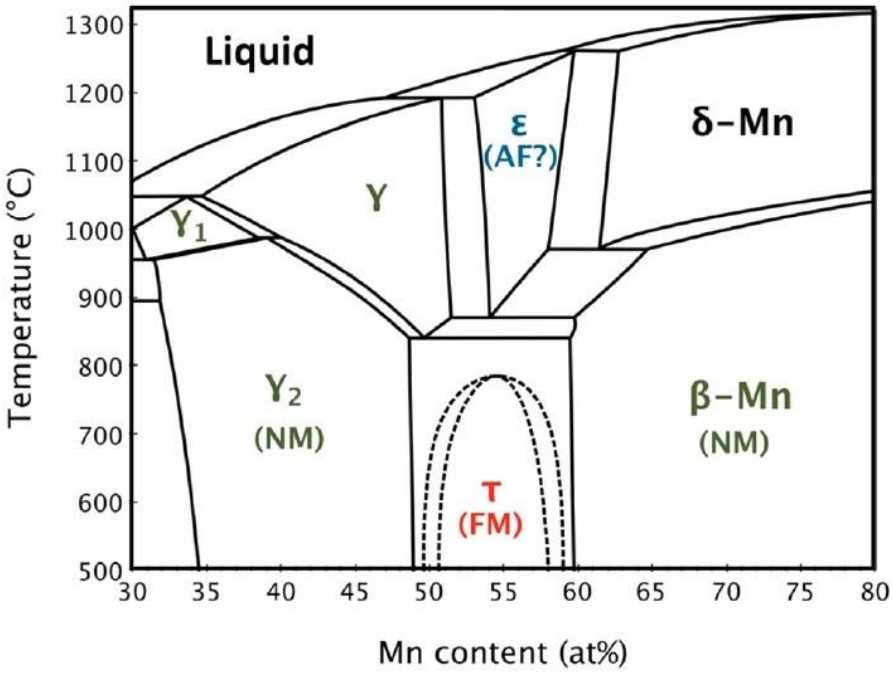

Figure 2.29 Phase and magnetic diagram at the near-equiatomic region of Al-Mn alloys. [37]

As shown in Figure 2.29, the phase diagram indicates that the atomic ratios of the ferromagnetic tetragonal τ-phase are in the vicinity of the equiatomic composition.[37] Other crystalline phases exhibit distinct magnetic response depending on the crystallographic structure and the Mn content. The equilibrium γ_2-phase (with 31-47 at.% Mn) and the β-MnAl structure (with > 60 at.% Mn) were reported to be nonmagnetic (NM).[37] The τ-phase (P_4/mmm) is usually obtained with excess Mn by a rapid quench of the hexagonal ε-phase with A3-type structure ($P6_3/mmc$) followed by isothermal annealing from 400 to 700 °C.[31, 37, 38] Both τ- and ε-phases are metastable due to volume expansion at room temperature, and mechanically milling, for example, results in the formation of equilibrium rhombohedral γ_2-phase with Al_8Cr_5-type structure ($R3m$) and cubic β-phase with Al_8Cr_5-type structure ($P4_132$).[4, 37] Although post-annealing transforms part of the ε-phase into the τ-phase; the γ_2- and β-phases are still present in essentially the same amounts as before annealing.[36]

It was found that addition of interstitial carbon can stabilize τ-phase and retard decomposition into the non-magnetic equilibrium phases.[4, 31, 39] However, the magnetic properties of MnAl-C alloys are sensitive to the microstructure and presence of defects developed during τ-phase formation, comprising martensitic or massive transformation mechanisms, and is therefore strongly influenced by the production routes.[40] Saturation magnetization can be enhanced by carbon, but with clear drop in both the Curie temperature and the anisotropy field.[4] Nevertheless, excess C is also problematic, which reduced the M_s due to the formation of the other non-ferromagnetic phases.[41]

Commercial products with magnetic properties of B_r = 5.75 kG, H_C = 3.0 kOe and $(BH)_{max}$ = 7 MGOe have been made by hot extrusion of annealed gas-atomized Mn–Al–C powders.[4] However, the performance improvement as compared to the ferrite magnets was not sufficient to justify the cost of the manufacturing. A clear shortage is that warm extrusion is a difficult process requiring heavy machines. Furthermore, MnAl–C magnets have a very low T_c, ~290–300 °C, compared to ~700–800 °C for Alnico and ~450

°C for ferrites. Finally, the invention of RE-based magnets ($RECo_5$) in the 1960's shifted the research interests off from MnAl-based materials.[42]

2.2.3. α'-Fe_8N

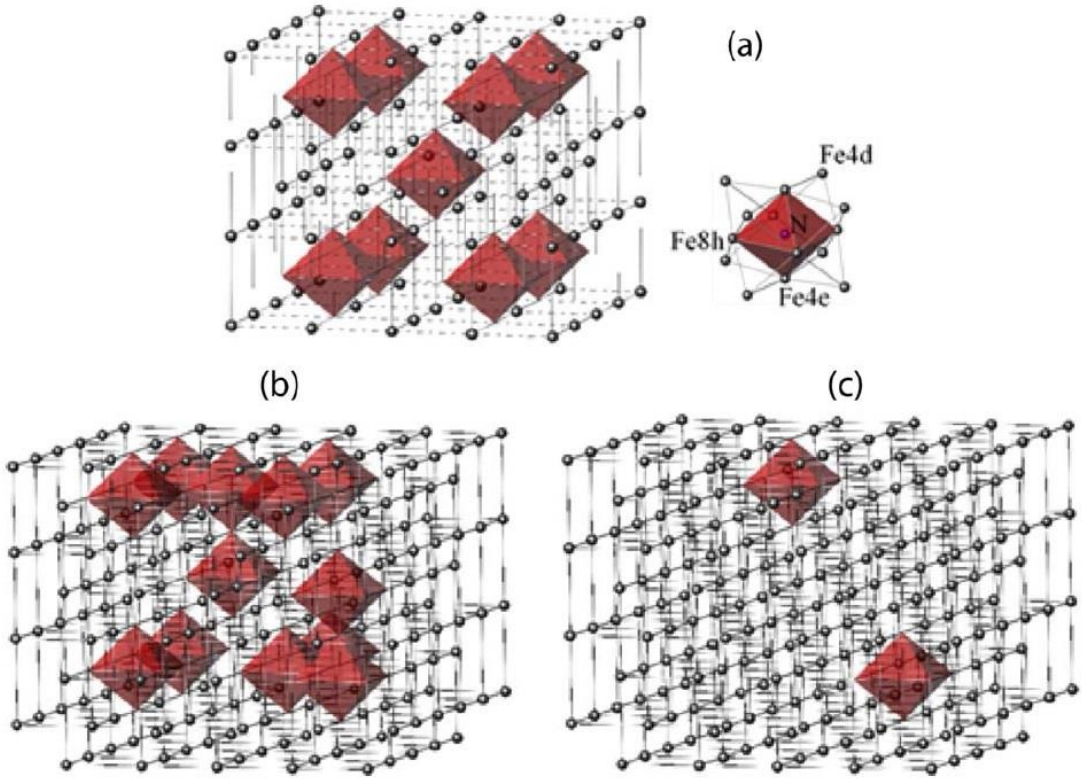

Figure 2.30 F-N crystal structures: (a) $Fe_{16}N_2$, (b) N-rich in Fe_8N, and (c) N-poor Fe_8N. [43]

Besides Mn-based compounds, several magnetic materials, like Permendur (FeCo alloys) and amorphous FeCoB, have been obtained with saturation magnetizations of ~2 T.[11] Among them, the well-known $Fe_{65}Co_{35}$ alloy shows the highest theoretical $\mu_0 M_s$ (~2.45 T at room temperature), which was predicted in the famous Slater-Pauling curve based the classical itinerant magnetism theory.[11, 43] The Fe-N binary system was thoroughly investigated since early century due to the importance of nitrogen steels in metallurgy.[44] In 1972, Kim and Takahashi first reported a material, α"-$Fe_{16}N_2$ thin film, with a giant saturation magnetization of ~2.6 T, that exceeds the known limit form $Fe_{65}Co_{35}$ alloy.[43, 45] About 20 years later,

Sugita's group at Hitachi published a convincing evidence that α"-$Fe_{16}N_2$ compound actually exhibits $\mu_0 M_s$ as high as ~2.9 T (at room temperature), particularly a large magnetic moment per Fe atom.[43, 46] Because of its giant value (~3.2 μ_B per Fe atom),[46] this iron-nitride phase immediately has attracted a great deal of attentions in the world. However, the existence of the "giant" Fe magnetic moment remains controversial as many researchers were not able to reproduce these findings.[43, 45, 47] The reason of highly scattered data in the reported $\mu_0 M_s$ values, ranging from 240 to 315 Am^2/kg, is mainly due to the ambiguities in the phase identification and the error in estimated volume fraction of α"-$Fe_{16}N_2$.[45] In addition to α"-$Fe_{16}N_2$, there is the secondary phase, α'-Fe_8N, which frequently found in the reported thin films. Figure 2.30 shows the crystal structure of both (a) α"-$Fe_{16}N_2$ and (b,c) α'-Fe_8N, which all have body-centered-tetragonal (bct) structures.[43] The difference between these two phases is that α'-Fe_8N is a chemically disordered phase with randomly located nitrogen atoms, while α"-$Fe_{16}N_2$ phase is an ordered one. Based on the previous reports, it is clear that the phase and unit structure of Fe-N system is tunable in a wide range by varying the N partial pressure during deposition, as shown in the

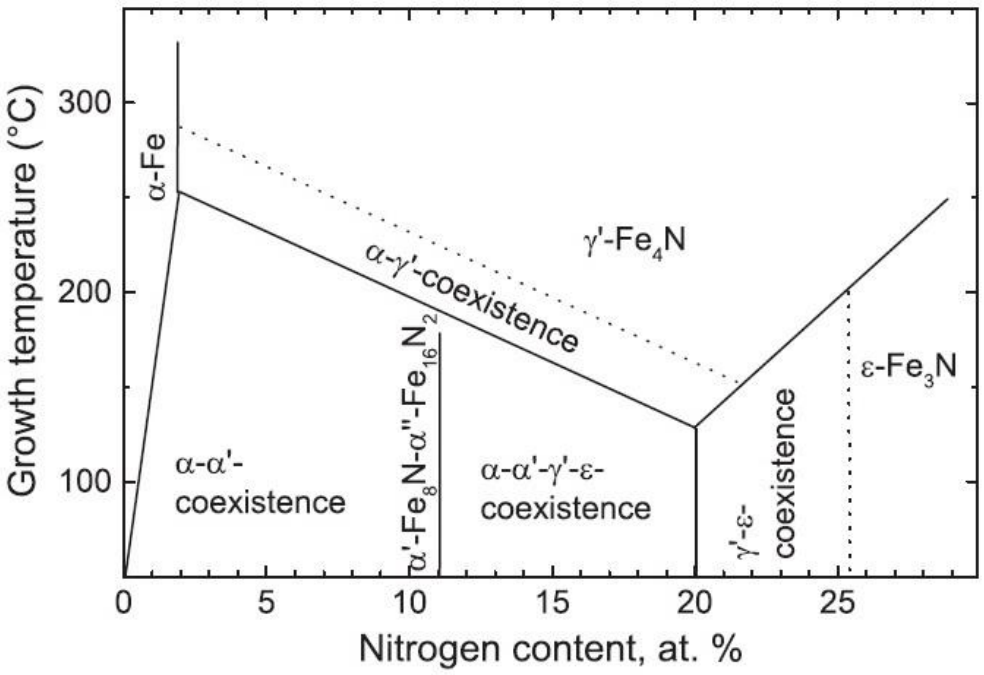

Figure 2.31 Fe-N phase diagram of thin films fabricated on MgO substrate. α, α', γ' and ε refer to α-Fe, α'-Fe_8N_x, γ'-Fe_4N and ε-Fe_3N, respectively. [48]

phase diagram (see Figure 2.31).[48] Therefore, great care must be taken to achieve single-phase products.

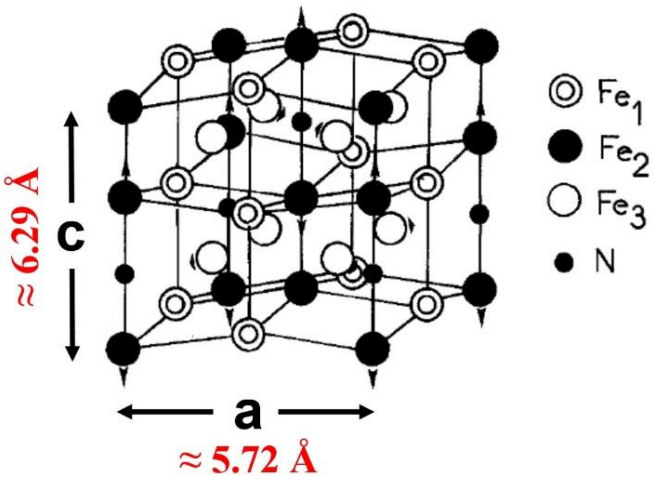

Figure 2.32 The crystal structure of Fe_8N. The arrows show the main displacements of Fe atoms induced by nitrogen. [44]

Furthermore, it has been discussed in the literature based on a local-spin-density approximation that transition metals undergo a phase transition from a non-magnetic to a magnetic state as a function of their density.[49] For example, α-Fe undergoes a second-order transition to a non-magnetic state with decrease of its unit cell volume. By contrast, increasing unit cell volume may lead to an increase of the magnetic moment per iron, even well beyond the famous value of 2.2 μ_B per Fe atom. This assumption is exactly the potential explanation for the giant Fe atomic moment and the increased magnetocrystalline anisotropy energy in α"-$Fe_{16}N_2$ and α'-Fe_8N materials.[47, 50] To realize this theoretical prediction, our G8 partner, Prof. Gutfleisch's group, has successfully fabricated a series of α'-Fe_8N thin films. They observed that the measured magnetic moments of the studied specimens change systematically with the amount of added nitrogen. The volume expansion caused by nitrogen incorporation induces increasing MAE_K via departing from the equilibrium atomic positions (see Figure 2.32).[44, 49]

2.3. X-ray Absorption

2.3.1. Synchrotron radiation

Since the initial discovery of x-rays by Wilhelm Röntgen on the evening of 8 November 1895, there have been many novel developments in instrumentation for x-ray optics.[51] Among them, synchrotron facilities provide a broad range of applications for multidisciplinary research in the last two decades. Today, there are more than 70 facilities worldwide in operation or under construction, providing services for approximately 100,000 users from virtually every discipline of the natural sciences.[51]

For applications using synchrotron light, storage rings are designed and dedicated to generate tunable beams of electromagnetic radiation from the far infrared to the hard x-ray regime with optimization of the photon flux (or brilliance). Figure 2.33 shows that there has been a tremendous increase in the brilliance available to researchers by a factor of 10^{14} in the last four decades.[51] Furthermore, up to another nine orders of magnitude of peak brilliance are promised with the development of x-ray free-electron lasers (XFELs) required for modern experimentation.[51]

In general, synchrotrons consist of an evacuated storage ring in which high-energy electrons circulate at highly relativistic velocities. The users can collect their measuring data in the so-called beamlines using synchrotron light emitted by the electrons tangentially to their orbital path at positions defined by components known as bending magnets and/or insertion devices (shown in Figure 2.34).[51] Nowadays, third-generation synchrotrons principally contain five main components: 1. a source of electrons; 2. a booster ring; 3. a storage ring; 4. radio frequency (RF) supply,

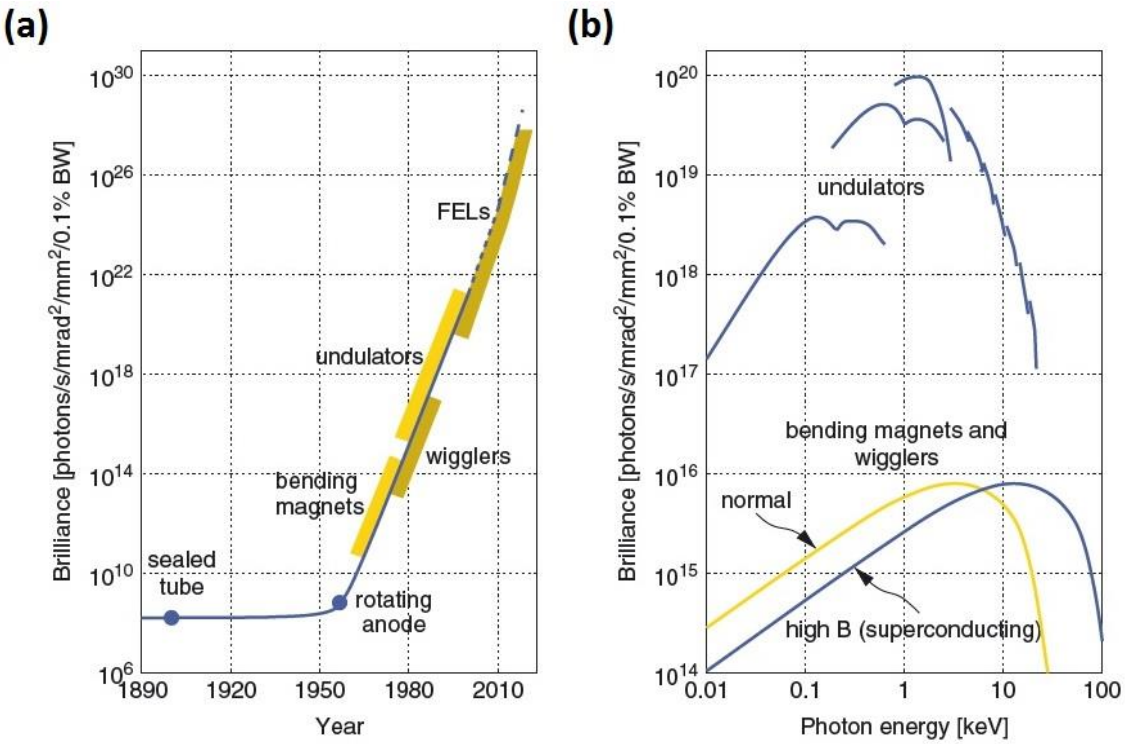

Figure 2.33 The brilliance of x-ray sources. (a) A historical graph showing the enormous increase in brilliance. (b) Typical spectral brilliance curves of devices commonly used in third-generation synchrotrons. [51]

and 5. beamlines. In order to generate synchrotron radiation, a numbers of electrons from a source (e.g. a heated filament in an electron gun) are accelerated in a linear accelerator (linac) into an evacuated booster ring, where they undergo further acceleration either up to the energy of the electrons in the main storage ring, or (less commonly, especially for modern facilities) to a somewhat lower energy. Under normal operation, electrons are then periodically injected into the storage ring, so that the specified storage ring current is maintained. This procedure is traditionally performed when the storage ring current drops to about $1 - 1/e \approx 70\%$ of the initial current. Inside the storage ring, the electrons are circulating in a closed path using bending magnets at arc sections. The beamlines use the radiation emitted either from bending magnets or insertion devices (wigglers or undulators), and therefore are positioned downstream, on the axis of emission. In the case of bending magnets, it is necessary to keep the electrons on a circular orbit in the storage ring, whereas undulators/wigglers

are installed on the straight sections in between. The energy lost by radiation of synchrotron light by the electrons is replenished by a radio frequency (RF) supply.[51]

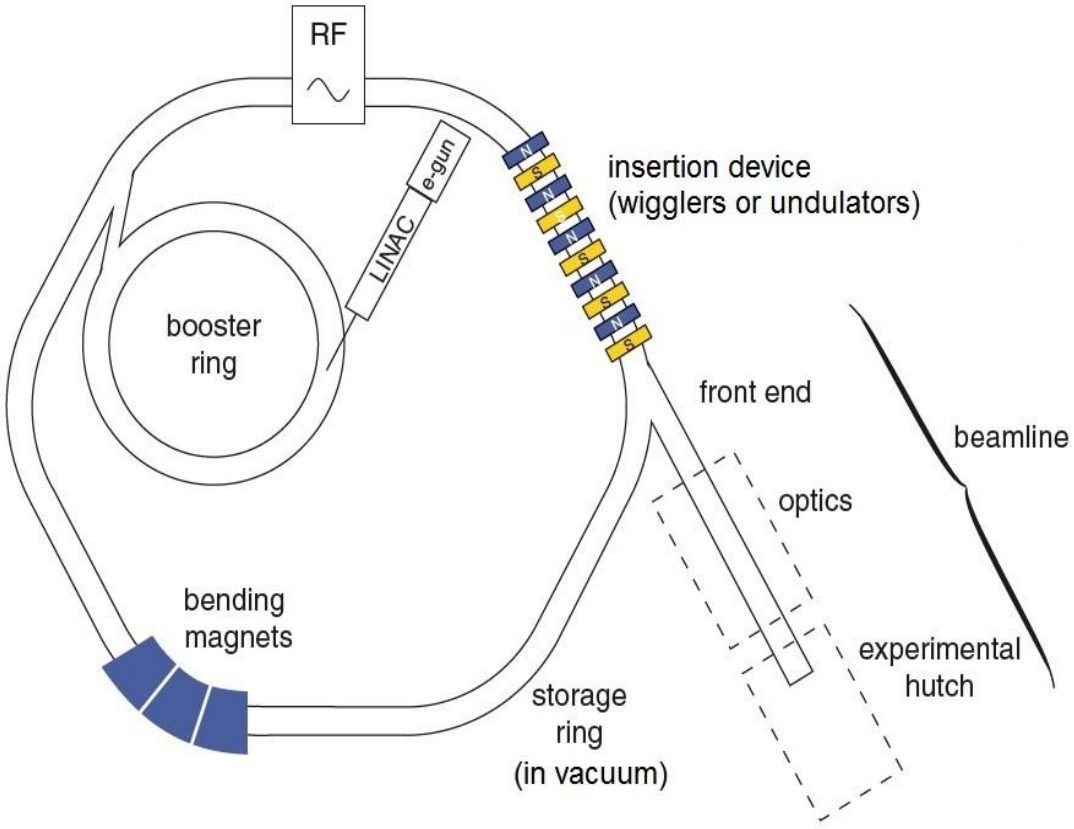

Figure 2.34 Simple schematic of a third-generation synchrotron. [51]

Table 2.2 Important information of selected third-generation synchrotrons.[52, 53]

Facility, Country	Beamline	Storage ring energy [GeV]	Current [mA]	Energy range [keV]	Insertion device	Top -up
ANKA, Germany	WERA	2.5	200	0.1~1.5	Bending magnet	N
ALBA, Spain	BOREAS	3	400	0.08~4.5	Undulator	Y

In this study, the traditional 3d transition elements were mostly studied in WERA beamline at ANKA synchrotron source, where our self-built XMCD instrument is located. In order to clarify the role of Bi in LTP-MnBi, the X-ray absorption (XAS) spectra at Bi $M_{4,5}$ and $N_{4,5}$ edges were especially recorded in BOREAS beamline at ALBA synchrotron center, where the state-of-the art beamline optics and elliptical undulator source offer high flux of soft x-rays having outstanding energy range (see Table 2.2).

2.3.2. X-ray Magnetic Circular Dichroism (XMCD)

Theoretical understanding of XMCD can be traced to work by Erskine and Stem who predicted that the XMCD intensity ratio between $L_{2,3}$ edges is equal to −1 for a simple atomic-like model.[54] The observation of hard x-ray magnetic circular dichroism (MCD) was pioneered by Schütz et al. in 1987, followed by Chen et al.'s similar experiment on Ni using soft x-ray beam in 1990.[55, 56] With theoretical support by Thole et al. and Carra et al., their sum rules relate the ground state expectation values of $\langle L_z \rangle$ and $\langle S_z \rangle$ to the dichroism spectra of corresponding atoms respectively.[57, 58]

In conventional XAS, the transition intensity measured as the white line intensity $I_{L3} + I_{L2}$ is proportional to the number of 3d holes, N_h.[59, 60] To obtain so-called XMCD signal, the XAS spectra (μ_+ and μ_-) must be recorded by use of both left (σ^+) and right (σ^-) circularly polarized X-rays. The spin moment and orbital moment of a specific element can be further determined from the dichroic difference intensities A and B separately in terms of optic sum rule, as shown in Figure 2.35.[60]

From a simple picture above, XMCD effect can be described as a two-step process. Take Co metals for example, its 2p core states are split in a $j = 3/2$ (L_3 edge) and $j = 1/2$ levels (L_2 edge), where spin and orbit are coupled parallel and antiparallel, respectively. In the first step, the x-ray incoming

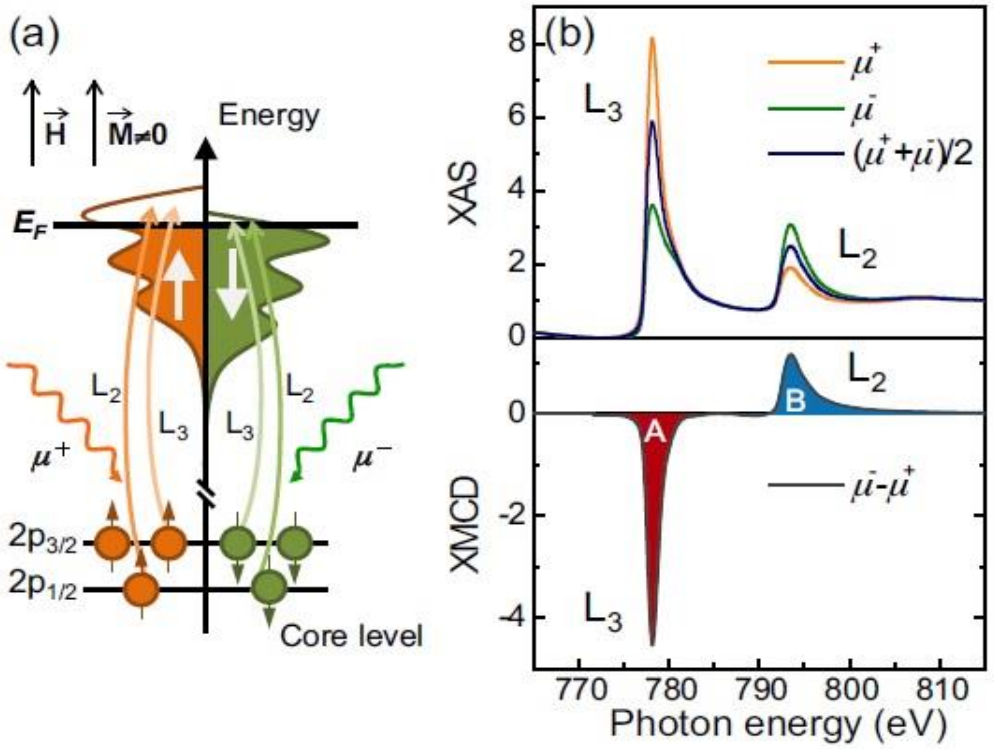

Figure 2.35 (a) Diagram of the two-step picture of XMCD for a single-electron in the resonant excitation process for a magnetic material. In the first step, a circularly polarized photon excites a spin polarized electron from the spin–orbit split 2p level (Fano-effect). From the $2p_{3/2}$ level (L_3 edge) X-rays with positive helicity (q = +1) excite 62.5% spin up electrons and those with negative helicity (q = −1) excite 37.5% spin-up electrons, while the $2p_{1/2}$ level (L_2 edge) q = +1 gives 25% spin-up and q = −1 gives 75% spin-up. Note that the minority spin direction (= majority hole spin direction) is the same as that of the sample direction. In the second step the spin polarized electrons have to find a place in the unoccupied 3d band, resulting in a difference if the 3d electron are spin polarized. (b) XAS at the Co $L_{2,3}$ for left (σ^+) and right (σ^-) circular polarization together with the difference spectrum: the XMCD. [60]

beam with the light helicity vector parallel (antiparallel) to the 2p orbital moment results in excited electrons of preferred spin up (down) direction. In the second step the excited photoelectrons have to find their places in the unoccupied 3d valence band. If there are less available spin-up than spin-down holes, the XMCD spectrum has a net negative and positive intensity at L_3 and L_2 peaks, respectively. In fact, the polarization dependent selection rules give rise to a multiplet structure in a more sophisticated picture, which can serve as a fingerprint for the ground state electronic and magnetic structure.[60, 61]

When electromagnetic radiation with photon energy E strikes on matters of interest, its intensity I_0 decays with penetration depth d due to the interaction between the photons and the materials. The attenuation of the initial intensity I_0 follows the Beer-Lambert law:[62, 63]

$$I(E) = I_0(E)e^{-\mu_a d} \tag{2.23}$$

, where μ_a is the atomic attenuation coefficient. If the absorption is the dominant process compared to other processes like Compton scattering and inelastic scattering, the absorption coefficient μ(E) will be, in a good approximation, equal to the attenuation coefficient μ_a.[63] At the atomic scale, XAS is to measures the x-ray absorption coefficient of each element depending on the photon energy $E = \hbar\omega$. Because μ is proportional to the photo-absorption cross section σ_{abs} of a single atom, the XAS intensities refer to the absorption cross section of corresponding elements. According to Fermi's Golden Rule, σ_{abs} of an N-electron atom for x-rays polarized in the $\boldsymbol{\epsilon}$ direction and with the wavenumber $\boldsymbol{k}$ is given by[64]

$$\sigma_{abs} = \sum_f \frac{4\pi^2\hbar^2\alpha}{m^2E} \left|\left\langle \Phi_f \middle| \sum_{j=1}^{N} e^{i\boldsymbol{k}\cdot\boldsymbol{r}_j}(\boldsymbol{\epsilon}\cdot\boldsymbol{P}_j) \middle| \Phi_i \right\rangle\right|^2 \times \delta(E_f - E_i - \hbar\omega) \tag{2.24}$$

Here $\boldsymbol{r}$, $\boldsymbol{P}$, Φ_f and Φ_i are the electron position vector, electron momentum vector, the final state wavefunction, and initial state wavefunctions, respectively. E_i and E_f are many-electron energies of the corresponding states. $\alpha = e^2/\hbar \approx 1/137$ is the fine structure constant. In x-ray absorption spectroscopy, the wavelength of incident x-rays is much larger than the radius of the core wavefunction, i.e. $\boldsymbol{k}\cdot\boldsymbol{r} \ll 1$ and $e^{i\boldsymbol{k}\cdot\boldsymbol{r}_j} \approx 1$. Thus σ_{abs} can be evaluated to a good approximation as[64]

$$\sigma_{abs} \approx \sum_f 4\pi^2\alpha\,(E_f - E_i)\left|\left\langle \Phi_f \middle| \sum_{j=1}^{N}(\boldsymbol{\epsilon}\cdot\boldsymbol{r}_j) \middle| \Phi_i \right\rangle\right|^2 \times \delta(E_f - E_i - \hbar\omega) \tag{2.25}$$

, which corresponds to an electric dipole transition. In the usual cases of 3d elements, the quadrupole transitions or the higher-order transitions are usually some hundred times weaker than the dipole transitions and could be neglected. From Eq. 2.24, the absorption coefficient is basically characterized by the transition matrix between initial and final electron states. According to the optic selection rules, the allowed transitions must obey the following conditions:[63]

(1) electric dipole transitions: $\Delta s = 0;\ \Delta l = \pm 1;\ \Delta m = 0, \pm 1$
(2) electric quadrupole transitions: $\Delta s = 0;\ \Delta l = 0, \pm 2;\ \Delta m = 0, \pm 1, \pm 2$

In other words, the profile of the experimentally observed XAS spectra can be understood and theoretically computed with non-zero dipole matrix element $\left|\langle \Phi_f | \sum_{j=1}^{N} (\boldsymbol{\epsilon} \cdot \boldsymbol{r}_j) | \Phi_i \rangle\right|$, while the orbital quantum number of the final state differs by 1 from the initial state ($\Delta l = \pm 1$, i.e. s → p, p → s or d, etc.) and the spin is conserved ($\Delta s = 0$).[61]

2.3.3. XMCD measurement & Data analysis

An experimental scheme is shown in Figure 2.36,[65] in which the XMCD signal is proportional to a change in the scalar product between the magnetization vector $\vec{M}$ of the specimen and the unit vector of the circular polarization $\vec{P}$.

In order to achieve the maximal change in the scalar product, XMCD measurements are usually performed by switching between parallel and antiparallel orientations of these two vectors (μ^+ and μ^-).[65, 66] In practice, reversing either magnetization direction or light helicity shows no difference if all magnetization components are rotatable by an external field.

Besides, there are three different methods utilized for recording XAS data in synchrotron facilities: (1) transmission mode, (2) total electron yield mode (TEY) (3) total fluorescence mode (TFY). Because XMCD sum rule is

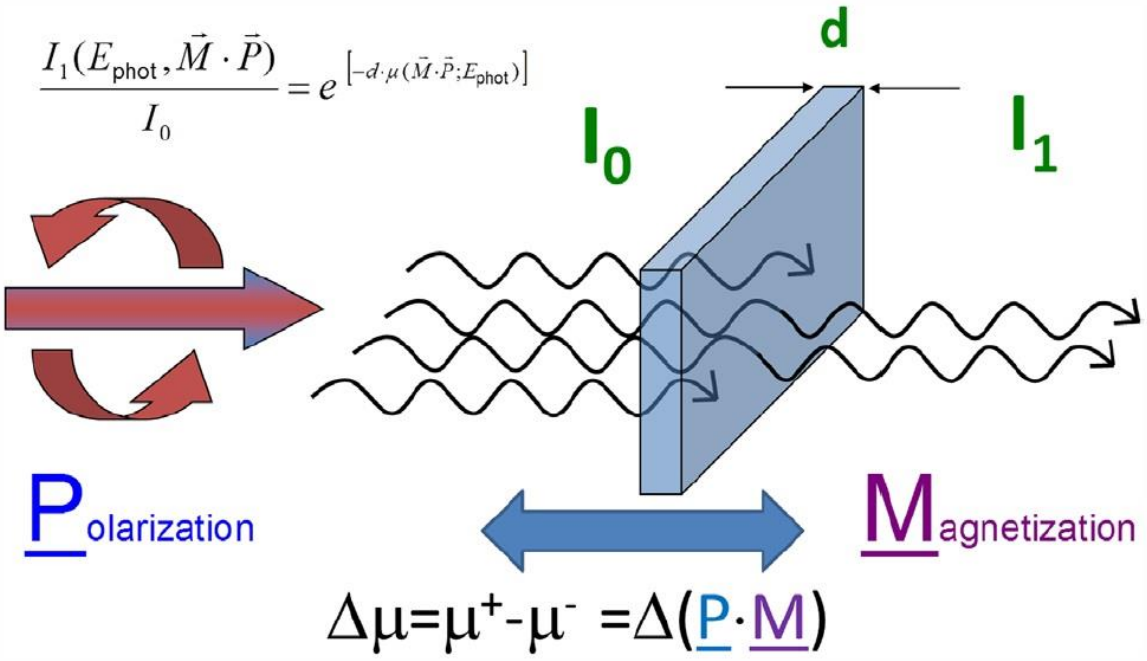

Figure 2.36 The XMCD effect depends on the change in the scalar product between the magnetization and the axial unit vector of the circular light polarization. [65]

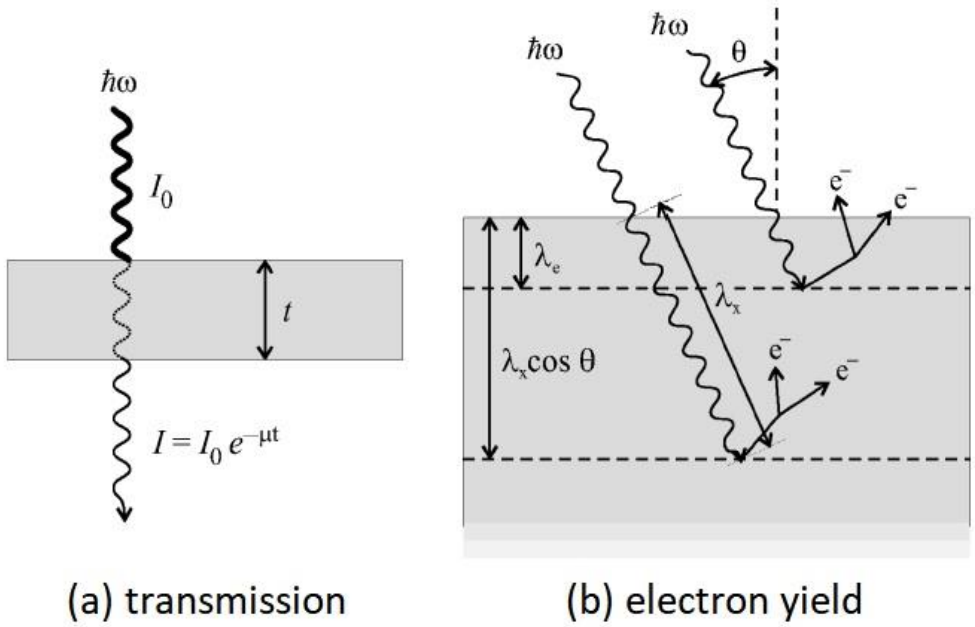

Figure 2.37 Qualitative description of (a) transmission and (b) electron yield methods for x-ray absorption measurements. [68]

only valid for the transmission and TEY measurements, TFY mode is not discussed here.[67] Among all, only transmission mode provides direct

measurement of the absorption cross section because it detects exactly the photon flux before and after the sample (see Figure 2.37 (a)).[68] Combined with the XAS theory, transmission mode is probably the most reliable method and has been widely applied in hard x-ray beamlines. Unfortunately, this is not the case for the users who studies 3d transition metals or compounds because the required beam range is within soft x-ray region. Due to short attenuation length of 3d transition elements (~20 nm), only very thin film (thickness less than 100nm) could be successfully investigated in transmission mode.[66]

To overcome this issue, TEY offers another possibility to relate sample drain current the amount of excited core holes in a surface near region if

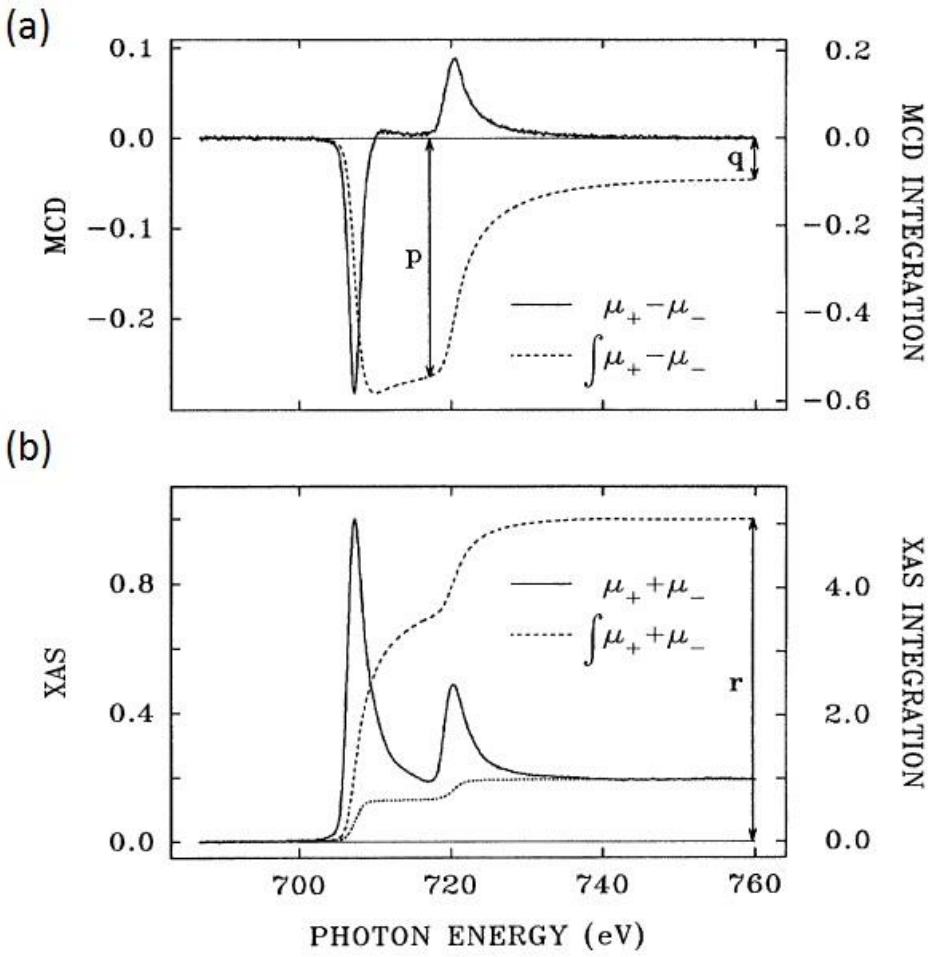

Figure 2.38 The simple method to gain three important paraters from (a) XMCD signal and (b) nonmagnetic XAS white line. These data were recorded from pure iron. [72]

saturation effect is negligible.[69] It is generally assumed that the TEY signal consists of two contributions: (i) the excited photoelectrons and Auger electrons from the decay of the core hole (elastic electrons) and (ii) the cascade of low-energy electrons produced in the inelastic scattering events.[70] In Figure 2.37(b), it can be seen that the escaping electrons originated from Auger decay experience multi-scattering process at difference depth before leaving the sample surface.[68] Numerous studies have been completed to demonstrate TEY measurements could give reasonable XMCD signal if some issue including saturation effect, magnetic bias, and reentering electrons are taken in account.[68-71] It is noted that the Auger electrons can escape from the solid if they are created in about the top 10 nm of the sample.[67] That means TEY signal is extremely surface sensitive, thus bulk-like information can only obtained by transmission or TFY measurements.

As mentioned in preceding section, the magnetic moments could be determined by XMCD sum rules for $L_{2,3}$ edges of 3d transition metal compounds and $M_{4,5}$ edges of rare-earth compounds. Following Thole and Carra's work, Chen et al. showed a simplified process to apply sum rule on conventional 3d ferromagnetic elements. In Figure 2.38, three parameters (p, q, r) are required for sum rum calculation; that is, (1) integration of XMCD signal at L_3 edge, (2) integration of whole XMCD signal, and (3) integration of whole nonmagnetic XAS spectra (μ_0).[72]

Based on the Eq. 2.26 and 2.27 obtained in Ref. [72], the orbital and effective spin moments of each element can be determined separately as:

$$m_{\mathrm{orb}} = -\frac{\int_{L_3+L_2}(\mu_+ - \mu_-)dE}{\int_{L_3+L_2}(\mu_+ + \mu_0 + \mu_-)dE} = \frac{-4q}{3r}N_h \qquad (\mathbf{2}.26)$$

$$m_{\mathrm{spin}} = \frac{\int_{L_3}(\mu_+ - \mu_-)dE - 2\int_{L_2}(\mu_+ - \mu_-)dE}{\int_{L_3+L_2}(\mu_+ + \mu_0 + \mu_-)dE} = \frac{-(6p-4q)}{r}N_h \qquad (\mathbf{2}.27)$$

, where N_h is the hole numbers of 3d states and $\mu_0 = (\mu_+ + \mu_-)/2$. For different core-to-final transitions, these formulas must be recalculated by the original sum rules.

Moreover, it is possible to obtain high quality elemental specific hysteresis loops using total electron yield as a probe for the magnetization dependent XMCD effect.[71] Because the magnitude of XMCD effect is proportional to the atomic magnetization, the macroscopic magnetization curve resembles the ratio of drain current intensities between pre-edge and resonance peak ($I_{\text{peak}}(E)/I_{\text{pre-edge}}(E)$) at varied field. Figure 2.39 shows a simple proof that this concept could be realized if x-ray beam quality is reasonable and magnetic bias is eliminated.[71] For the low signal measurements, the shape of elemental specific hysteresis loops can be further achieved by the difference of the integrated XMCD peaks as a function of external field. Because XAS provides elemental information, XMCD hysteresis loop is a unique method to revolve overall magnetization curve of a composite system into separate magnetic contribution of each element.

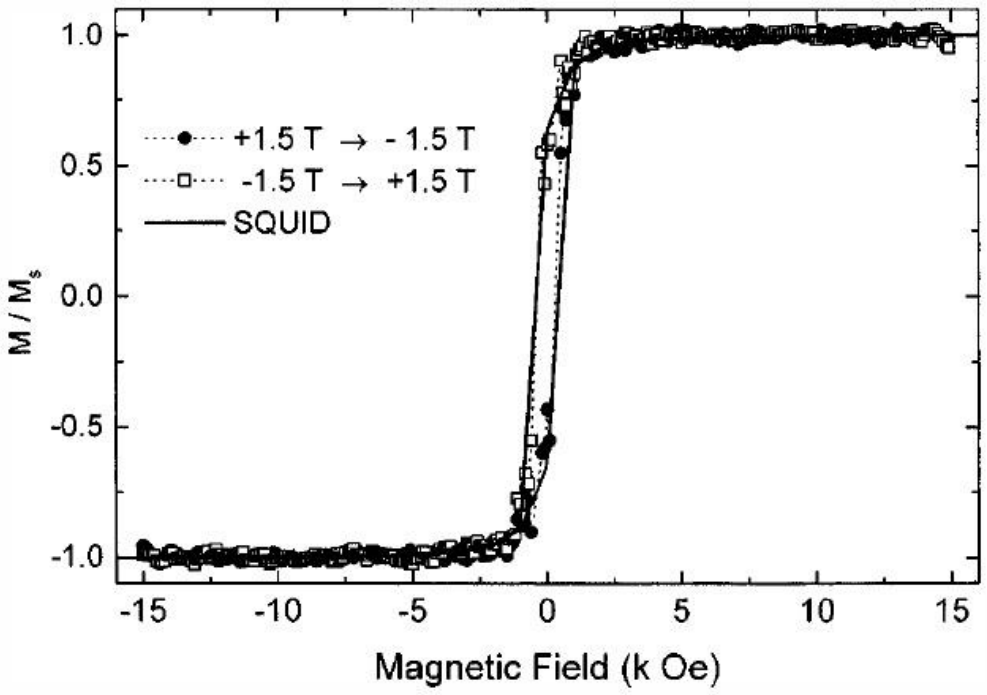

Figure 2.39 Comparison of the normalized elemental specific hysteresis loop (dots) and corresponding SQUID curve (straight line). [71]

2.3.4. **Saturation effect**

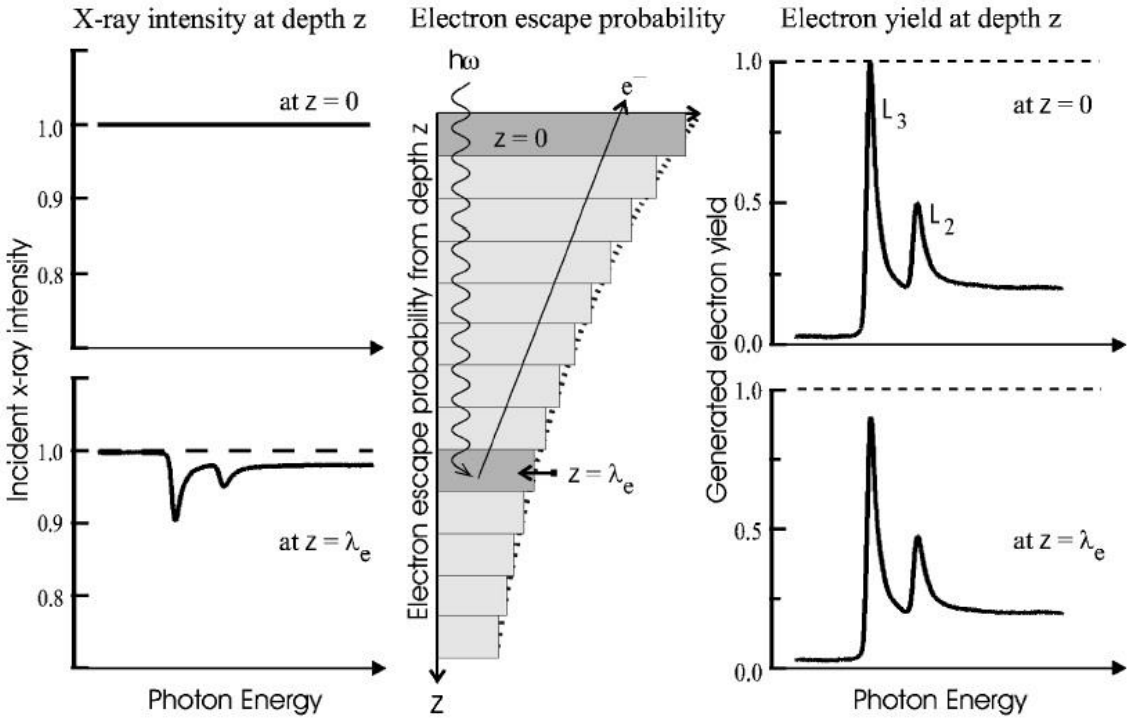

Figure 2.40 Illustration of saturation effect for Fe. Left: The difference in the x-ray intensity arriving at depth $z=\lambda_e=17$ Å is shown, compared to the incident x-ray intensity at z=0 (I_0=1). Center: Probability of electron escape, plotted in a horizontal bar graph as a function of depth z. The probability of escape is unity at the sample surface (z=0) and drops to 1/e at $z=\lambda_e$. Right: Hypothetical electronyield spectra generated from the absorbed photons in layers at a depth z=0 and $z=\lambda_e$. The measured total electron yield spectrum outside the surface consists of contributions from the various layers weighted by the probability of escape from the surface (shown in center). [68]

Although TEY mode enables us to probe magnetic information from various types of samples, it easily give rise to wrong answers if some complications occur. Just for the sample having thickness (d) of ~100 Å, it is difficult to obtain and do not guarantee the homogeneity of the sample over the illuminated area (~1 mm^2).[73] Hence, the so-called saturation effect is undoubtedly an important problem, especially for the ultrathin films.[74] The mechanism of saturation effect is represented in Figure 2.40.[68] It is clear that this effect unambiguously originates from exponential decay probability for escaped electrons within surface region. Without proper correction, saturation effects result in a recorded signal

which is not proportional to the absorption cross section, thus the orbital and spin moments could be deviated from true values by 100 % and 20%, respectively. To reduce this unwanted issue, the angle-dependent TEY signal must be re-evaluated by pre-normalized XAS data after edge jump treatment using Henkel table, the formula is given as following:[70, 75]

$$\mu_{corr}(E) = \frac{\mu_{mess}}{1 - \mu_{mess} \times \frac{\xi_{e^-}}{\cos\alpha}} \qquad (\mathbf{2}.28)$$

, where μ_{corr} is the corrected absorption coefficient, μ_{mess} is the measured absorption coefficient, ξ_{e^-} is effective electron escape length, and α is the angle of incidence of the x rays with respect to surface normal. Using corrected XAS spectra, the re-evaluated magnetic moments usually show much more consistent tendency for angle-dependent data, particularly the value measured at grazing angle.

2.3.5. **WERA beamline**

WERA ("Weichröntgen-Analytik-Anlage") is a specific beamline for soft x-ray spectroscopy, microscopy, and spectromicroscopy.[76] It is owned and operated by the Institute for Solid-State Physics (IFP), Karlsruhe Institute of Technology (KIT). WERA provides important electron spectroscopies in the photon energy range of 100 – 1500 eV and combines them in situ with photoemission microscopy, particularly for magnetic materials. The schematic layout of the WERA beamline is illustrated in Figure 2.41, from which it is clear that WERA station is a unusually long beamline compared to other ones.[76] There are three main experimental instruments available in WERA beamline, which are PEEM, PES/NEXAFS, and XMCD chambers respectively. In order to focus desired x-ray beam at the end of the long light path, complicated optics are equipped for this purpose, including a spherical grating monochromator and bendable focusing mirrors. The polarization of x-ray beam can be quickly selected by the aperture (ANKA dipole) for spectroscopic measurements.

In this thesis, most of XMCD measurements were performed using our MPI XMCD machine at the WERA beamline. The setup consists of four different components and a state of art "Fast Ramping 7 Tesla Cryogen-Free Magnet System" developed from Cryogenic Ltd (London, UK), that was installed and first commissioned with this framework. The sketch and true picture of MPI setup are shown in Figure 2.42.

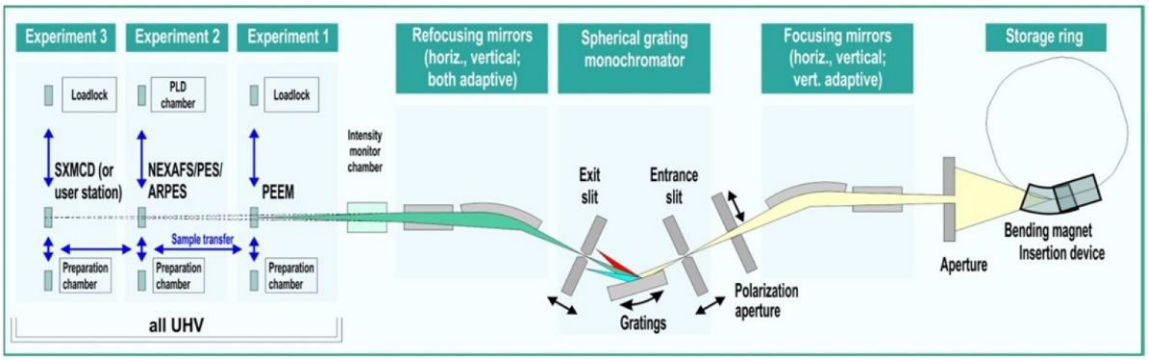

Figure 2.41 Schematic layout of the WERA beamline. [76]

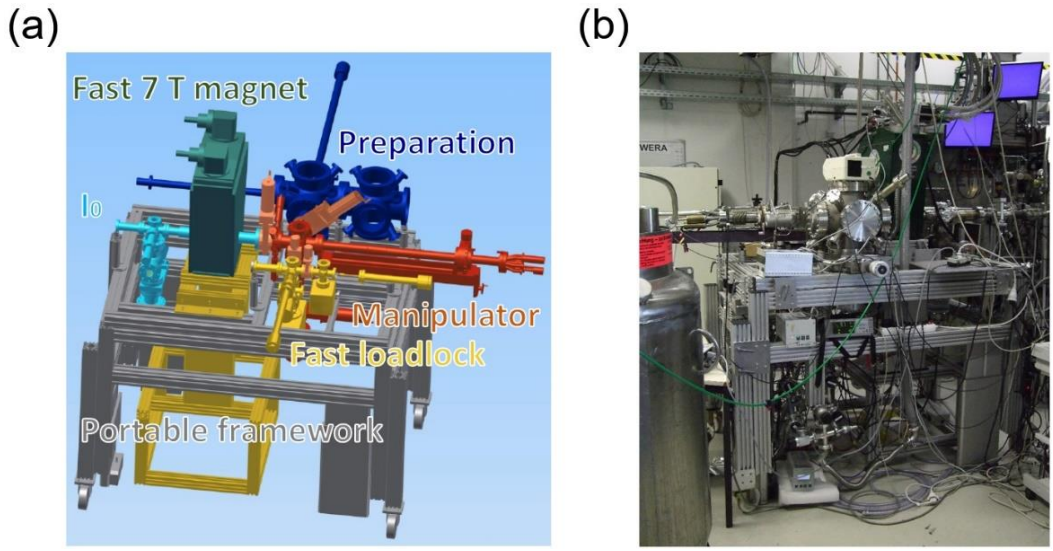

Figure 2.42 (a) 3D CAD drawing of MPI XMCD instruments. (b) Real picture of the machine taken during beamtime in 2015.

For beamtime users, five samples can be loaded into the carriage of the fast loadlock and transfer system (yellow colored) at once under high vacuum condition (~10^{-7} mbar). To measure easily oxidized bulk materials (ex.

MnBi magnets), clean sample surface could be obtained by either in-situ polishing or cleavage in the loadlock section prior to measurement. While the specimen is placed into the sample stage of XMCD manipulator (orange colored), angle- and/or temperature-dependent measurements can be performed in light of research requirements under UHV environment (a base pressure of ≤ 10^{-10} mbar), namely 0°~70° and 7 K~380 K respectively. The most notable advantage of our measuring system is, of course, the fast ramp magnet system that enables to switch applied magnetic field between ±7 Tesla at a maximum rate of 1.5 Tesla/sec. Using this remarkable superconducting magnet system, it is possible to investigate hard magnetic systems within a reasonable measuring time (typically a couple of days). If users want to conduct argon sputtering and/or in-situ preparation of thin films, related work could be completed in the preparation chamber (dark blue colored). Furthermore, another important feature is that whole setup is portable, meaning that self-integrated I_0 section (cyan colored) is necessary in order to probe the incoming beam intensity from other synchrotrons for normalization of the measured absorption spectra.

2.3.6. **BOREAS beamline**

The BOREAS beamline is fully operational and has been open to outside users since May of 2012. The special characteristic of BOREAS is that an X-ray absorption spectra in a broad range of energy (80 to 4500 eV) can be acquired routinely in 2~3 minutes (if using the "on-the-fly" mode) with high accuracy and repeatability, allowing circular or linear dichroism studies.[52] The beamline optics is optimized to provide the highest photon flux and energy resolution in the range between 150 eV and 2000 eV. Besides, the APPLE II undulator enables users to measure specimens with ~100 % degree of circularly polarization at soft x-ray energy range between 80 and 1100 eV. However, the monochromator and undulator are capable of reaching a lower energy level down to 80 eV in circular polarization. Above 2000 eV, the optics of the beamline have a reduced performance in comparison with typical hard X-ray beamlines. Nevertheless, the flux and energy resolution has been demonstrated to be high enough to be able to

perform X-ray absorption experiments at important edges (L edges of all 4d metals, etc.). BOREAS beamline is specially designed for two novel end-stations: one for XMCD/XMLD and the other for X-ray scattering spectroscopy as shown in Figure 2.43.[52]

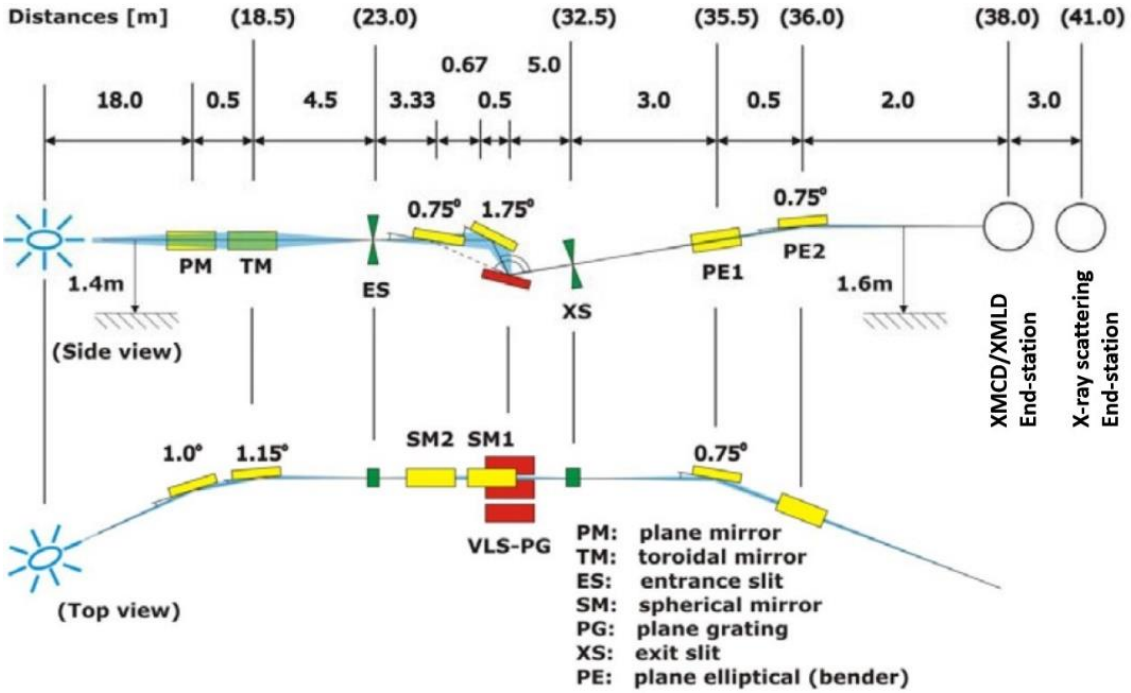

Figure 2.43 Schematic layout of the BOREAS beamline. [52]

Similarly, all measurements are performed in a UHV environment (a base pressure of ~10^{-10} mbar), and the specimen is mounted on a specific sample holder attached to the cold finger of a cryostat depending on measuring mode, with temperatures variable between approximately 2 K and 370 K. The core part of BOREAS dichroism end-station is a UHV-compatible cryomagnet (manufactured by Scientific Magnetics) containing three orthogonal superconducting coils allowing maximum fields up to 6 Tesla (in the horizontal plane along the beam direction, with a sweep rate of ~2 Tesla/min) and 2 T (in the horizontal plane perpendicular to the X-ray beam and in the vertical plane, with a sweep rate of ~0.6 Tesla/min).

For WERA and BOREAS beamline, they are both good choices for investigation of hard magnets. Undoubtedly, the merit of BOREAS is the high and

stable beam flux with unusual broad energy range compared to other presently operating beamlines. However, applying bias voltage is not available at the moment for TEY measurements (still in progress), therefore it is inevitable to record artificial signals caused by returning electrons due to stray magnetic field near sample surface.

2.4. Fabrication techniques

2.4.1. Arc melting

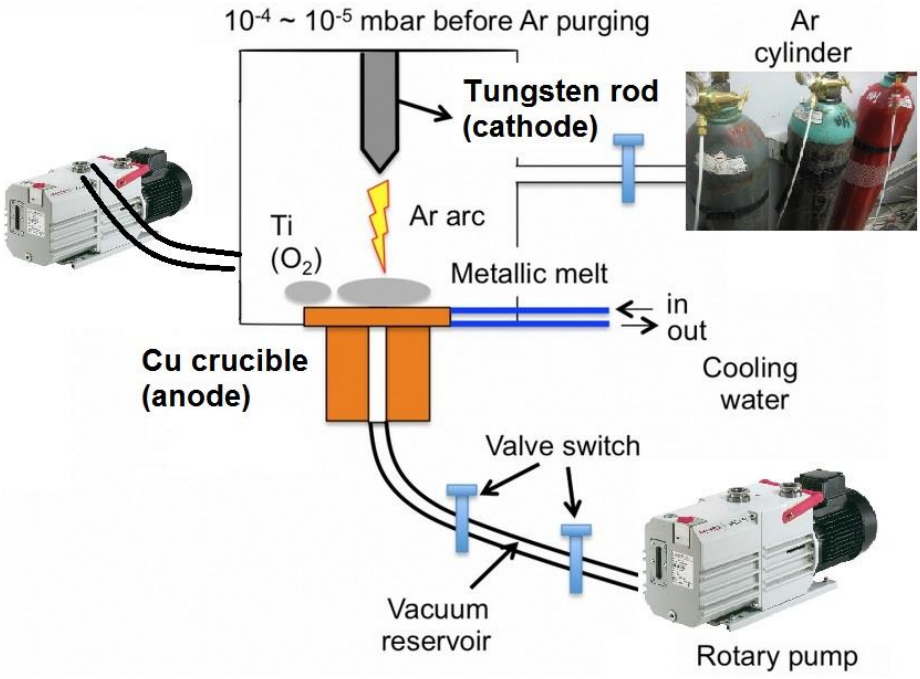

Figure 2.44 A simplified sketch of a arc melting machine. [78]

Arc melting (or plasma melting) provides an excellent technique for fabricating the alloys which constituents possess greatly different melting temperatures and vaporization pressures. On the industrial scale, large arc-melting furnaces work with carbon electrodes, and temperatures up to 4000 K are achievable.[77] The operation of arc melting is similar to that of arc-welding, where an electrical arc is generated between two electrodes (ex. Tungsten rod and Cu crucible), as shown in Figure 2.44.[78]

An electric arc originates from a stream of inert gas (argon or helium) supplied by the torch to produce an intense plasma. The cathode shaped in a sharp rod is made of W with 2 wt% Th, which can bear high temperatures without melting. Conversely, the anode is usually a Cu crucible designed to hold the pure elements and cooled by a circulating water to avoid overheating. In order to melt materials effectively, the cathode is approached to the pure elements that are placed on the Cu crucible by turning a millimetric screw. When the cathode is close enough, an arc that melts the elements is discharged by ionizing the gas. It is necessary to weigh the melted ingots after each melting reaction to control possible weight losses, which must be negligible to maintain the desired stoichiometric ratio. Even refractory alloys are easy to obtain with this method, but it presents an inevitable drawback: cooling rate is much different over all ingots when the arc is broken off. This problem arises from the faster cooling at the bottom of the sample, where there is contact with the water-cooled Cu crucible. Therefore, the flip-and-melt process was required to improve the homogeneity of the alloys.

2.4.2. Powder preparation

Particle size reduction achieved by milling is a crucial step in many technological applications, which is defined as mechanical breakdown of solids into smaller particles. For the preparation of modern permanent magnets, size reduction is particularly important process prior to the post-sintering, because it is desired to have anisotropic grains which size is close to single domain in the texture. Nowadays, several types of size reduction equipment are available, for example, cage mills, hammer mills, pulverizers and grinding. The right tool must be selected for the task to add energy most efficiently for the application. The product of milling is powder, typically a few micrometers in diameter, with corresponding internal nanocrystalline structure.

On lab scale, ball mills are widely used and considered as a very efficient tool for grinding various materials into fine powders (approximately 1 μm and below). Ball mills basically can be divided into two types: centrifugal and planetary mills. For a simple centrifugal ball mill, a single bowl fastener is horizontally and driven while not rotating itself, whereas planetary ball mills have two or four bowl fasteners, each of which accommodates one grinding bowl, fixed to a supporting disc. In general, planetary action gives up to 20 g acceleration and reduces the grinding time to about 2/3 of a simple centrifugal mill.[79] No matter which method is applied, it is necessary to decrease particle size of the desired materials to less than 10 mm, for example, using a mortar and pestle in advance. In this work, the ball milled MnBi and MnAl powders were prepared by planetary mills at room temperature (RT). The principle of planetary mills is simply sketched in Figure 2.45.[80] It can be seen that planetary mills also exploit the principle of centrifugal acceleration instead of gravitational acceleration. During milling operations, the grinding bowls and supporting disc rotate in opposite directions, so that two different centrifugal forces act on the bowl contents leading to attrition and impact.[79] Also, each grinding medium influences the grinding process via the specific weight of milled balls.

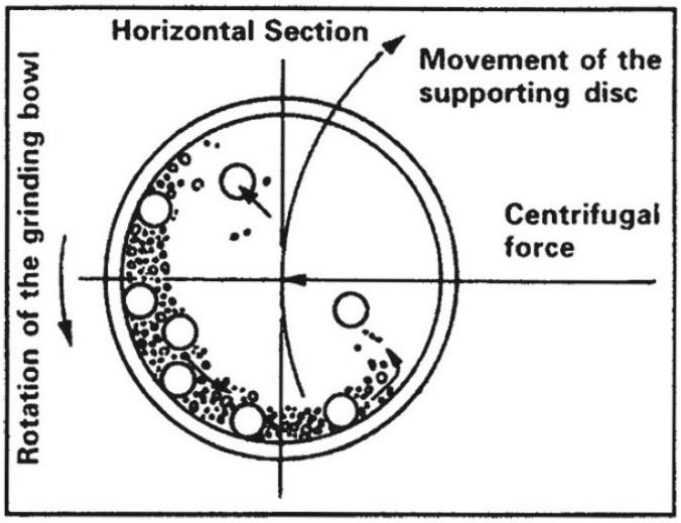

Figure 2.45 Relative movements of working parts and balls in a vial of a planetary ball mill (Top view). [80]

2.4.3. Hot compaction (HC)

Hot compaction (or hot pressing) is a suitable and classical method for densifying materials with poor sintering behavior. This technique, which combines powder pressing and sintering into one single operation, offers many advantages over conventional powder consolidation. By simultaneous application of temperature and pressure, it is feasible to achieve near theoretical density in a wide range of hard to process materials.[79] As the resistance of metal particles to plastic deformation decreases rapidly with increase in temperature, much lower pressures are required for consolidation by hot pressing. In addition, densification by hot pressing is relatively less sensitive to powder characteristics – shape, size and size distribution which are important in cold pressing and sintering.[81]

Sintering temperatures of 650~2400 °C are normally used. For hot pressing technology, two different types of heating can be found in use: (a) Inductive heating (b) Indirect resistance heating.[82] For the case of inductive heating (see Figure 2.46(a)),[82] heat is produced within the mold when it is subjected to a high-frequency electromagnetic field, generated by using an induction coil coupled to an electronic generator. The mold is usually made of graphite or steel, and pressure can be applied by one or two punches onto the powders. The advantage for this method is that the pressure and the inductive power are completely independent. But, its disadvantages include the expense of a high frequency generator and the need for proper alignment. If the mold, for example, is placed off-center, the heat distribution is uneven. Therefore, uniform heating is usually the issue because of the dependence of the process on good inductive coupling and heat conductivity of the mold. Another potential problem is the heating rate. Too high heat rate could lead to high temperature difference between the surface and core, which can destroy the mold.

With indirect resistance heating technique (see Figure 2.46(b)), the mold is placed in a heating chamber. The chamber is heated by halogen lights or resistance heating elements, from which heat is generated by electric current. Because the thermal flow is transferred from heating units to the mold in a secondary step, the process is called indirect resistance heating.

Advantages are high achievable temperatures, independent of the conductivity of the mold and independent of pressure. However, the inevitable disadvantage is that it takes a relatively long time for heat transfer from the furnace atmosphere to the mold surface and subsequently throughout the cross-section of the mold. Nevertheless, hot compaction as a fabrication process, has been increasingly used in the preparation of materials having improved properties through the control of composition, microstructure and density. At present, it has also been employed in the fabrication of various high temperature components, multiphase ceramics, ceramic–metal systems.[79]

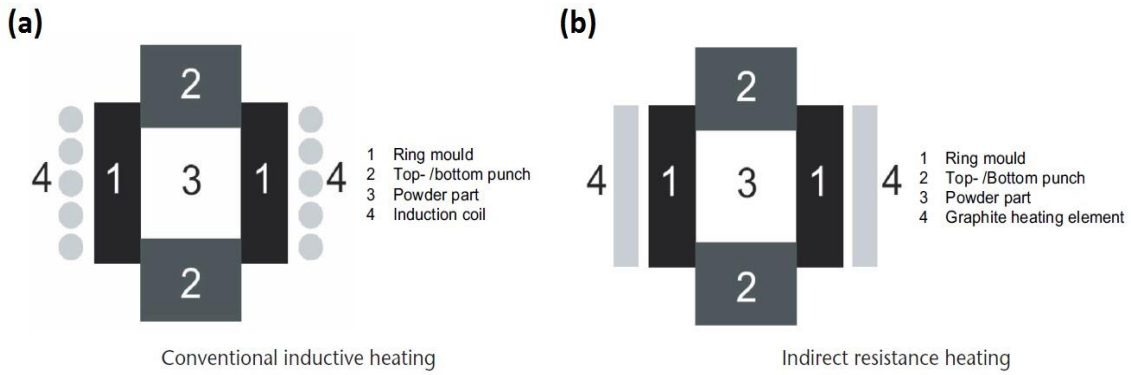

Figure 2.46 Schematic representation of conventional sintering systems. [82]

2.4.4. Spark plasma sintering (SPS)

Besides conventional hot-pressing, the most novel and increasingly used method is spark plasma sintering (SPS), which provides possibility to consolidate nanometric powders to near full densification with little grain growth.[83] Other advantages include that achieving sintered bulks with homogeneous microstructure, controlled stoichiometry and small grain size, which are the attractive characteristics for industry nowadays. So far, many reports have been published on SPS-compacted electronic devices,

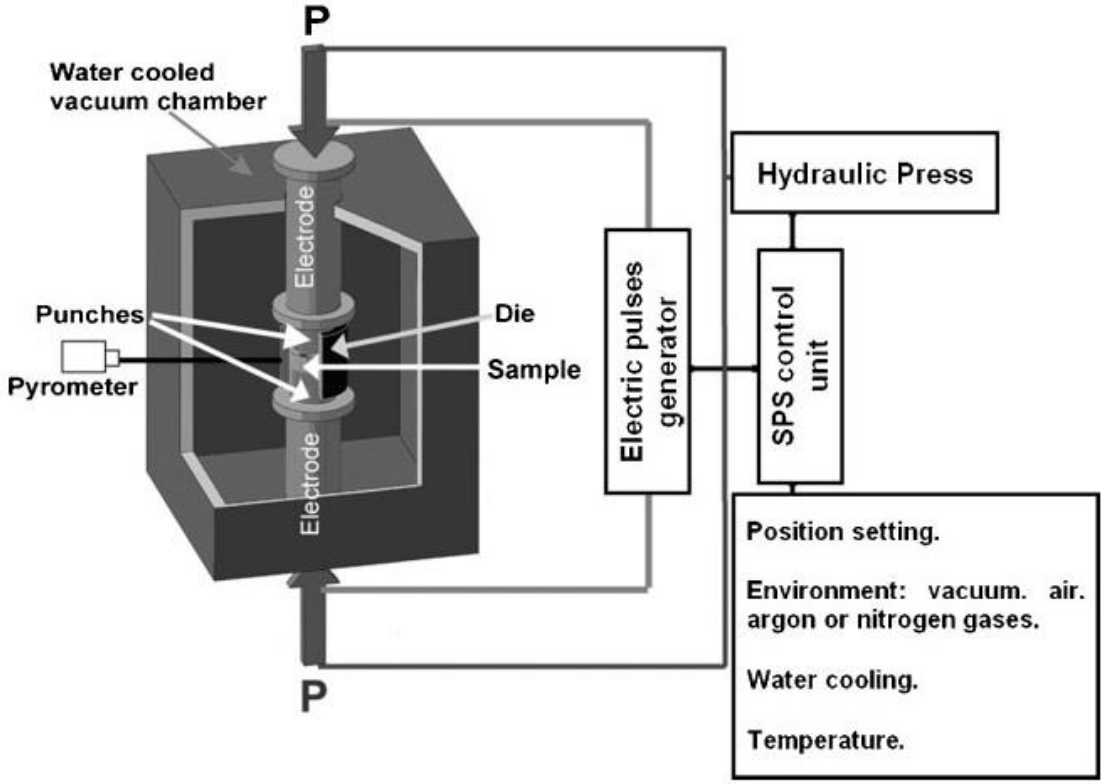

Figure 2.47 Schematic drawing of an SPS machine. [83]

especially about the size effects of the properties in the sub-micrometer range and approaching the nanometer scale (~100 nm).[83]

The operation of a SPS unit is presented schematically in Figure 2.47.[83] It consists of a uniaxial pressure device, in which the water-cooled punches also serve as electrodes, a reaction chamber that can be evacuated, a pulsed direct current (dc) generator and pressure-, position- and temperature regulating systems. In an SPS experiment, a weighed amount of desired powder is placed in a die and fixed with two punches from top and bottom sides. The die can be made of various materials, such as high-strength graphite or refractory alloys. For electrically conductive materials, energy is dissipated directly within the sample and the electrically conductive parts of the pressing tool. In the case of electrically non-conductive powder, electrically conductive tools must be used, where the heat produced by Joule heating is quickly and efficiently transferred by conduction to the sample.[84] Depending on the used hardware it is possible to define pulse and pause durations or more specialized pulse patterns. The role of the

current and the sintering mechanism is still subject of many debates between plasma formation and electro-migration supporters;[83], however, this is the main difference between SPS and other sintering methods. Due to Joule effect of the dc current, both die and powder are directly heated. Therefore, it is possible to raise the temperature to 2000 °C at heating rate of up to 1000 °C/min or even higher. Combined with the application of pressure, SPS has been demonstrated to enable the consolidation of some materials like ceramics and intermetallics within minutes and the ability to obtain fully dense structure at comparatively low sintering temperatures (typically a few hundred degrees lower than in normal hot pressing).[83] Based on the advantages mentioned above, part of bulk samples were prepared by SPS technique to study the influence of microstructure on the corresponding magnetic properties.

2.5. Sample characterization

2.5.1. X-ray diffraction (XRD)

X-ray powder diffraction is most widely technique used for the phase identification and structure determination of unknown crystalline materials (e.g. minerals, inorganic compounds). There are three basic components in X-ray diffractometers: an X-ray tube, a sample holder, and an X-ray detector (illustrated in Figure 2.48).[85] In common commercial instruments, X-rays are generated in a cathode tube by heating a filament to produce thermal electrons, which are accelerated toward a target (usually Cu or Mo) by applying a voltage, and bombarding the target material.[85] The interaction of the incident x-ray beam with the sample causes x-ray diffraction peaks on a CCD or PSD detector by constructive interference when conditions of diffracted rays satisfy Bragg's Law.

Practically, there are two principal types of instrument geometry for laboratory powder diffractometers: reflection (Bragg-Brentano geometry) and transmission (Debye-Scherrer geometry).[85] In this work, quick check

was performed at room temperature in reflection geometry using Panalytical X'Pert diffractometer with Co $K\alpha_1$ radiation, while the temperature-dependent measurements were completed in transmission geometry using Bruker D8-Advance diffractometer with Mo $K\alpha_1$ radiation. Due to the polycrystalline nature of the sintered compacts, all of the studied samples were grinded into small particles prior to measurement. For the quick check, the specimens were placed in a flat plate and measured in air. In order to record convincing XRD results at elevated temperatures, the particles were fixed inside quartz-glass capillaries and sealed under argon atmosphere.

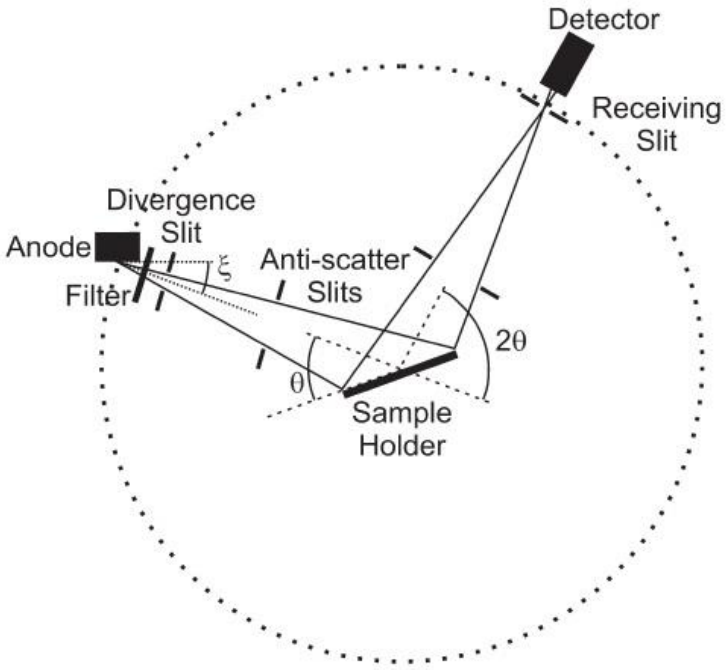

Figure 2.48 A sketch of usual XRD geometry. [85]

Crystal structures and phase contents of the studied samples were determined by whole patterns, using Rietveld-based technique, which is the only diffraction technique suited to multi-phase samples where the emphasis is to derive phase identification and quantification.[85] The data analysis was solely assisted by Prof. Dr. Leineweber. For the MnBi specimens, it is unfortunate that the evaluated phase fractions are different from those estimated by the corresponding SQUID analysis. This problem

could mainly arise from large difference in absorption cross sections between Mn and Bi elements. Nevertheless, the crystalline phases and temperature-dependent lattice constants were precisely determined for each sample of interest.

2.5.2. Superconducting quantum interference device (SQUID)

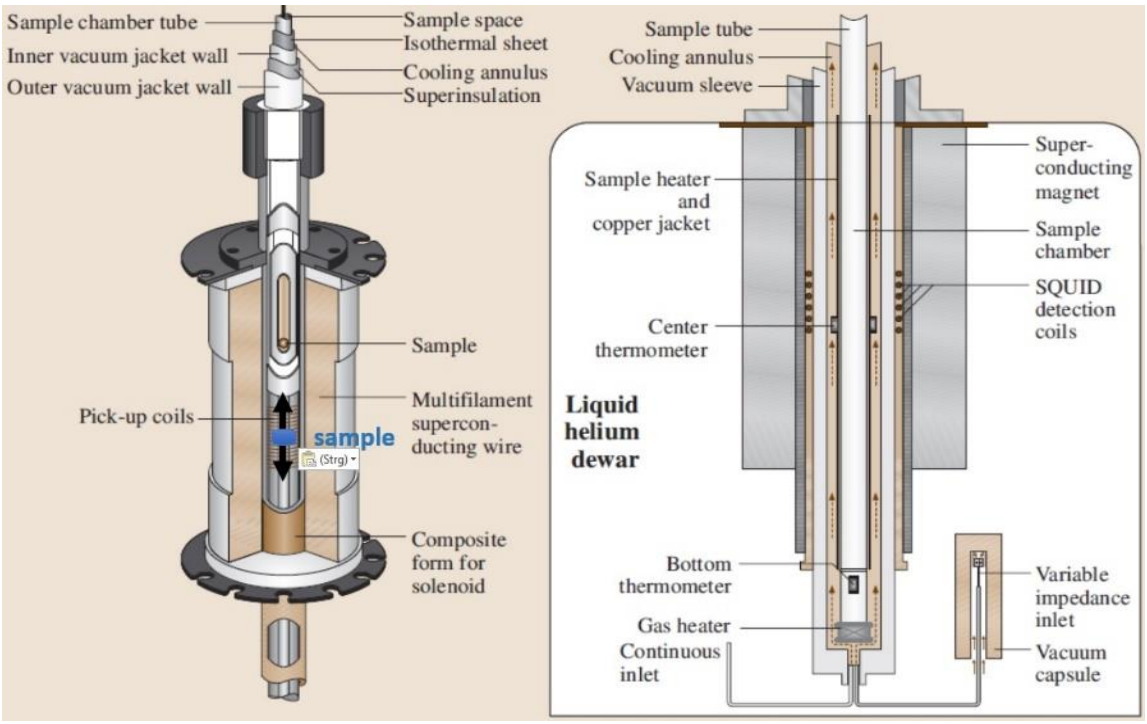

Figure 2.49 Schematic view of a commercial SQUID magnetometer consisting of a liquid–He cryostat, a superconducting magnet, the variable-temperature sample chamber with thermometers and the detection coils close to the sample position. [86]

The Superconducting Quantum Interference Device combines the physical phenomena of flux quantization and Josephson tunneling to determinate the magnetic moments of the studied specimens. A commercial SQUID instrument mainly consists of five important components: (a) superconducting magnet; (b) a multifilament superconducting wire; (c) SQUID detection coils; (d) liquid–He cryostat as well as a controller system (see Figure 2.49).[86] SQUID is highly sensitive to magnetization signals

because it responds to a fraction of the flux quantum. The SQUID sensor is usually a thin film that functions as an extremely sensitive current-to-voltage-converter.

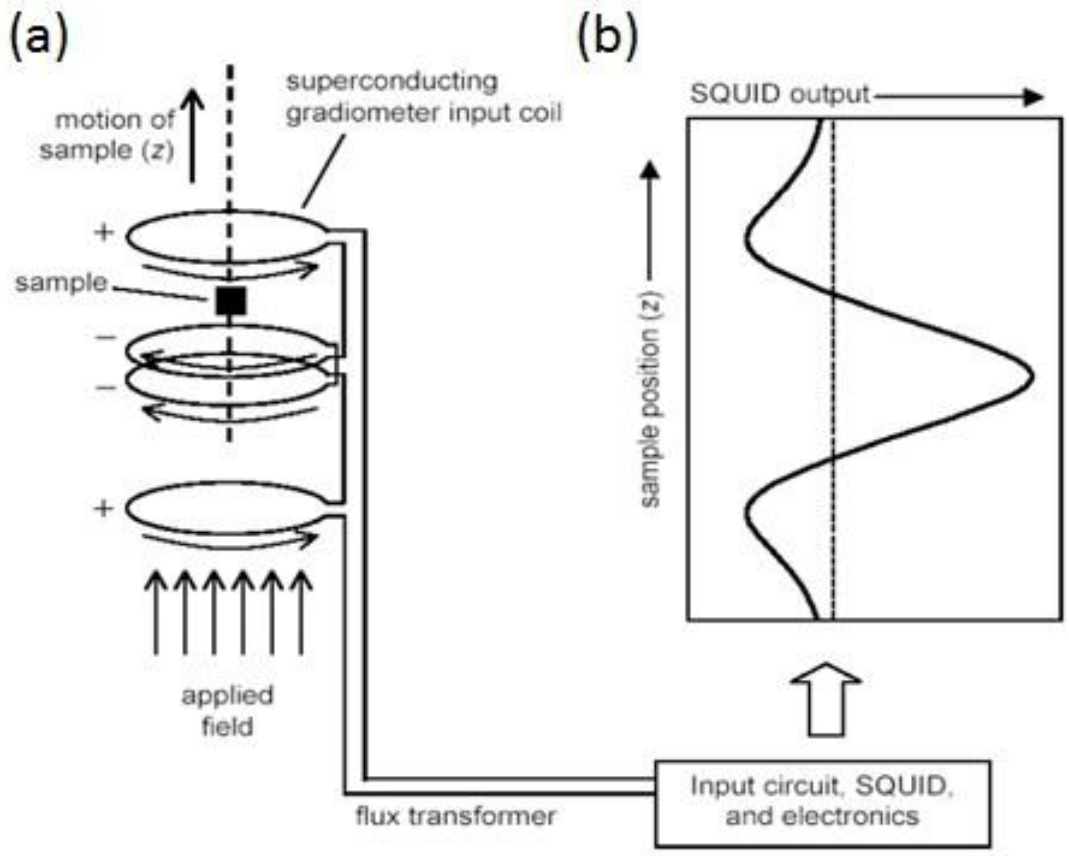

Figure 2.50 A scheme of SQUID measuring method. [86]

To make a measurement, a sample, typically less than a few millimeters in size, is first attached to a sample rod. The sample is then scanned through the center of a first- or second-order superconducting gradiometer (see Figure 2.50(a)). The gradiometer forms a closed flux transformer that is coupled to a SQUID and the signal from the SQUID is typically recorded as a function of sample position (illustrated in Figure 2.50(b)).[86] Due to this up and down movement, the magnetic moment of the sample induces an electric current in the pick-up coil system. A change of the magnetic flux in these coils alerts the persistent current in the detection circuit, and it in turn generates variation in the SQUID output voltage which is related to the magnetic moment of test sample.

To identify the magnetic properties of our specimens, all bulk samples were cut into small pieces with dimensions of 1×1×2 mm (width×length×hight). Angle- and temperature-dependent measurements $M(H)$ were intensively performed using our new state-of-the-art MPMS3 magnetometer (Quantum Design). Precise moment determination was calibrated by MPMS XL 7 magnetometer (Quantum Design). The $B(H)$ loops were evaluated using corresponding measured density values and effective demagnetization factors N. The demagnetization factor of each bulk specimen was calculated by its three-dimensional lengths using the analytic equation given in Ref. [87]. Nominal $(BH)_{max}$ values were determined by the value on the second quadrant of B-H curves intersected with the corresponding load lines. For powder samples, they were first fixed with resin under alignment field onto thin quartz plate, and then carefully clamped with clean scotch tapes and a small fragment of drinking straw before loading into sample chambers of Quantum Design SQUID systems.

2.5.3. **Kerr microscopy**

Although conventional magnetometers (SQUID or VSM) can precisely determine the magnetic moments of studies specimens, no direct information regarding magnetic microstructure can be obtained by this method. To observe micromagnetic feature (ex. magnetic domains and domain walls), Kerr microscopy is a handy tool to examine the surface domain structure of magnetic materials at mesoscopic scale.[88] The working principle of Kerr microscopy is based on the so-called magneto-optical Kerr effect, which is one of the magneto-optic phenomena. This interesting effect was discovered by John Kerr in 1877, who noticed that the plane of polarization of light reflected from the polished iron pole face of an electromagnet was rotated by less than 1°.[15] Kerr effect is very similar to Faraday effect; however, Kerr effect describes the changes to linearly polarized light reflected from a magnetic surface rather than the changes to light transmitted through a magnetic material. Upon reflection from a magnetic surface, a beam of linearly polarized light in general will change its state of

polarization depending on the relative orientation of the magnetization of the sample and the polarization axis.[89]

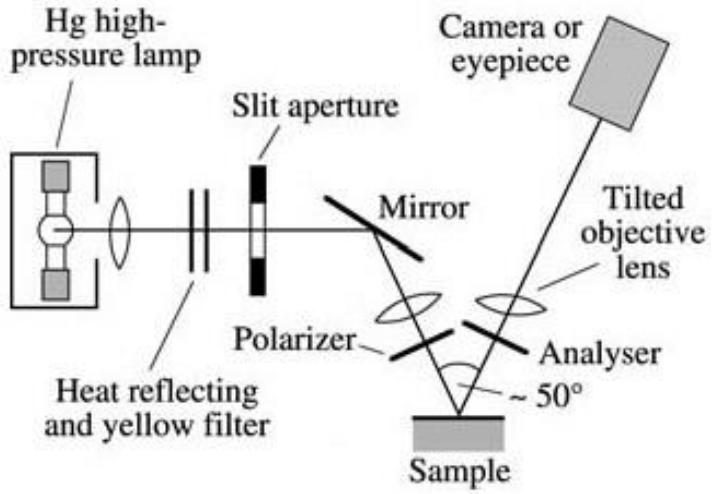

Figure 2.51 Simple schematic picture of Kerr microscope. [87]

The simple scheme of a typical Kerr microscope is sketched in Figure 2.51, which is recommended for low resolution applications in the longitudinal or transverse effects to obtain an overview of the domain pattern of larger samples.[88] The advantage of this arrangement is that no optical elements other than the sample exist between polarizer and analyzer, so that contrast conditions are optimal. A high pressure mercury lamp with suitable spectral filters to select the green and yellow mercury lines is recommended as the light source in general cases.[88] The amount of Kerr rotation usually is quite small (much less than 1°), and depends the material and on the direction and magnitude of the magnetization relative to the plane of incidence of the light beam. To observe the domain contrast, both the white light of a source and reflected light from the sample must be selected by polarizers, which only transmits specific plane polarized light. Resolution in this arrangement is practically limited by the achievable numerical aperture and aberrations. With appropriate digital image processing, Kerr microscopy can extract domain contrast from the surface of virtually any ferro- or ferrimagnetic sample. It is noted that all of magneto-optic techniques only probe the first 10~50 nm below the

surface of a metallic sample because of the limited penetration depth of light.

In this work, Kerr images were taken from the finely polished samples using a Zeiss Axio Imager.D2m microscope equipped with a polarized light function in Prof. Oliver Gutfleisch's laboratory (TU Darmstadt). Measurements were carried out using the polar component of the reflected light, and a subtraction method was used to reduce the topological effects.

2.5.4. Differential scanning calorimetry (DSC)

Calorimetry is a primary technique for measuring the thermal properties of materials to find out a connection between temperature and specific physical properties of substances. So far, it is the only method for direct determination of the enthalpy associated with the process of interest.[90] Among various kinds of calorimeters, differential scanning calorimeter (DSC) is a popular method measuring heat flow rates (power) and characteristic temperatures of reactions or phase transition as well.[91]

The characteristic feature of all DSC measuring systems is the twin-type design and the direct in-difference connection of the two measuring systems which are of the same kind.[90] Based on the operation principle, DSC can be classified into two types: heat-flux DSC and power-compensated DSC. For a heat flux DSC, both the specimen, enclosed in a flat pan, and an empty reference pan are placed on a thermoelectric disk surrounded by a furnace. The furnace is heated at a linear heating rate, and the heat is transferred to the sample and reference pan through the thermoelectric disk. However, owing to the heat capacity (C_p) of the sample, there would be a temperature difference (ΔT) between the sample and reference pans, which can be measured by area thermocouples.[91] Conversely, the sample and reference pans are placed in separate furnaces heated by separate heaters in the case of a power-compensated DSC. The sample and reference are maintained at the same temperature, and the difference in thermal

power required to maintain them at the same temperature is measured and plotted as a function of temperature or time.

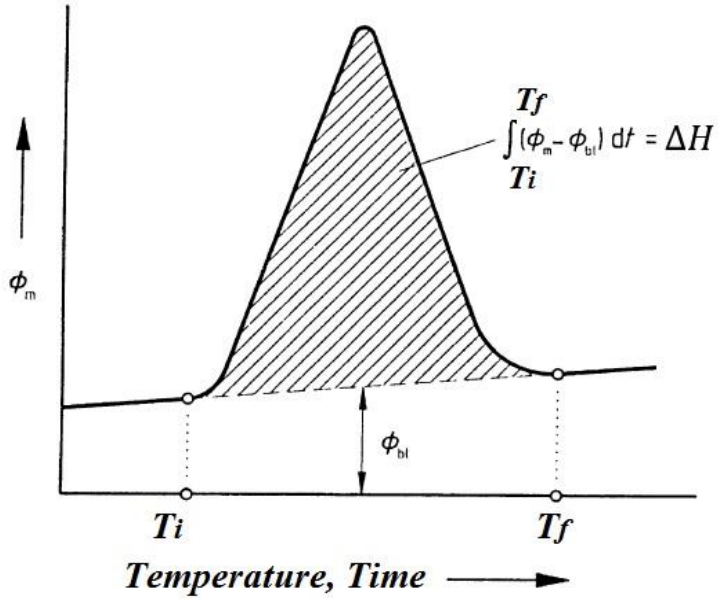

Figure 2.52 The analysis of typically measured DSC peak. [90]

In this study, the thermal properties of the bulk MnBi samples were investigated with a power-compensation DSC. In each measurement, the specimen was subjected to a linear temperature program, and the measured heat-flow rate, $\phi(t)$ either released or absorbed by a sample, into the sample is proportional to its instantaneous specific heat. Several temperature sensors enable to compute numerically the heating/cooling rate, dT/dt, thus $\phi = C_p \cdot (dT/dt)$ is obtained. Figure 2.52 presents that the T-integration of the peak in $d\phi/dT$, which appears only at the first-order transition, yields the value of the enthalpy (ΔH) and the entropy change (ΔS):[90]

$$\Delta H = \int_{T_i}^{T_f} C_p(T)dT \; ; \; \Delta S = \int_{T_i}^{T_f} \frac{C_p(T)}{T} dT \qquad (\mathbf{2}.29)$$

, where T_f and T_i are the temperatures which are the finishing and starting transition temperatures respectively. Furthermore, the temperature of the

first-order phase transition, T_t, could be evaluated as the temperature at the maximum of the $d\phi/dT$ peak.

The DSC device (Perkin Elmer Pyris 1 in Prof. Eric Mittemeijer's department (MPI-IS)) used in this study was calibrated using the temperature and enthalpy of melting of three elements (In, Zn and Al) prior to real measurements. All measurements were completed with the help of Dr. Bastian Rheingans. Sample and reference (empty) pans were made of Y_2O_3, and a new specimen disc was always used for each measurement. Isochronal annealing was performed starting from room temperature at heating rates in the range from 5~20 K/min. Several consecutive heating runs were performed for each sample in order to determine the baseline and the extent of phase transformation. The results indicate that no further reaction was observed in the second run.

2.5.5. Density measurement (Archimedes method & Gas pycnometry)

Bulk density is an important parameter for evaluating the energy products of bulk magnets. The definition of density is rather straightforward, that is, the mass of an object divided by its volume. Determining mass is not a difficult task; however, it is not easy to obtain actual volume when a solid material is in irregular shape and contains porous texture. Due to this issue, a traditional method to measure the actual density of bulk objects is based on the famous Archimedes' principle using water as a medium. Before starting measurements, all the samples should be cleaned and gently polished. Three weights are required for final evaluation: dry-weight in air ($W_{dry,air}$), wet-weight in air ($W_{sat,air}$), and finally wet–weight in water (W_{sat,H_2O}). To get Wet-weight in air, the sample is immersed in water for a while till all of opening space is filled by water before measurement. With those three weights, the bulk density can be calculated by following equation:

$$\rho_{\text{bulk}} = \frac{\rho_{H_2O} \times W_{dry,air}}{W_{sat,air} - W_{sat,H_2O}} \quad (\mathbf{2}.30)$$

, where ρ_{H_2O} is the actual density of the water at measuring temperature.

In addition to Archimedes method, the bulk density of the studied samples was further determined by gas pycnometry. Automatic gas pycnometers have been identified as the instruments of choice to accurately measure the true density of solid materials for a long time. This technique ensures quick density measurement with the highest accuracy. An inert gas, rather than a liquid, is used because gas molecules can penetrate even the finest pores and eliminate the influence of surface chemistry. In general, He is recommended as the displacement gas due to its size and inert behavior. The simplified scheme of a gas pycnometer is shown in Figure 2.53, in which there are two gas chambers—a sample chamber (calibrated volume of V_{cell}) and a calibrated reference chamber (calibrated volume of V_{ref}).[92]

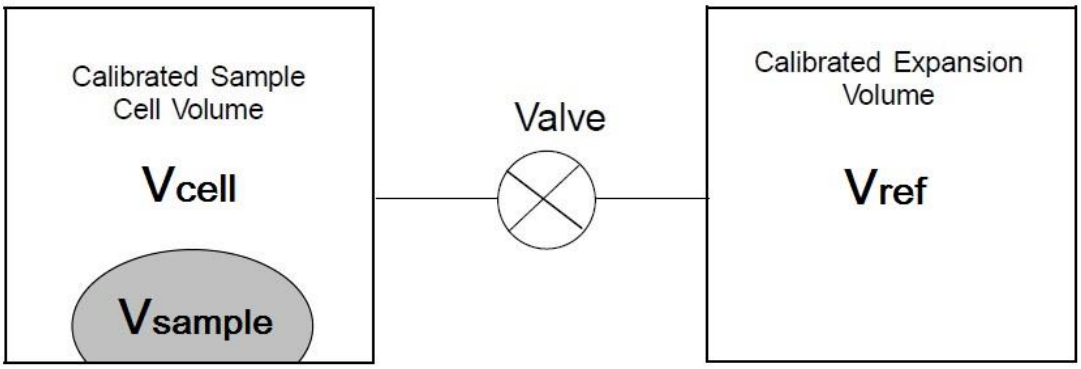

Figure 2.53 Scheme of a simplified gas pycnometer. [92]

Gas operates by employing Archimedes' principle of fluid displacement and Boyle's Law of gas expansion.[93] After loading the studied specimen into the sample chamber, the ambient pressure (P_a) in both chambers is measured. A sealed sample chamber of known volume (V_{cell}) is then pressurized to a target pressure with the displacement gas. Once stabilized, the new pressure (P_1) is recorded. A valve is subsequently opened allowing the gas to expand into the reference chamber whose volume (V_{ref}) is also

known. Till reaching equilibrium, this second pressure (P_2) is measured. Because the measurement depends only upon the pressure drop ratios, there is no need for calibration of the pressure transducers. Finally, the sample volume can be evaluated by using the following equation:[92]

$$V_{sample} = V_{cell} - \frac{V_{ref}}{\frac{P_1 - P_a}{P_2 - P_a} - 1} \qquad (\mathbf{2}.31)$$

To obtain accurate data from a gas pycnometer, there exists a proper ratio between the volume of the reference chamber and that of the sample chamber. If this ratio is too large or too small, the subsequent pressure-drops created during the analysis can lead to inaccuracies. This is why most of commercial gas pycnometers possess multiple reference volumes.

In this work, the true density values of all bulk samples were carefully determined by both Archimedes method (the setup in Prof. Oliver Gutfleisch's laboratory (TU Darmstadt)) and gas pycnometry (Micromertics, AccuPyc 1330 in Prof. Joachim Maier's department (MPI-FKF)). Each specimen was weighted five times to get an average value. No clear difference was found between the results estimated by these two techniques.

2.5.6. Inductively coupled plasma-optical emission spectroscopy (ICP-OES)

ICP-OES is a technique used for bulk elemental chemical analysis or quantitative determination of metals and certain non-metals in solution. It is a type of emission spectroscopy and so-called wet sampling method whereby samples are introduced in liquid form for analysis.[94]

The schematic diagram of a ICP system is simply sketched in Figure 2.54, which contains five major constituent parts: (i) the sample introduction system (nebulizer), (ii) the ICP torch, (iii) the high frequency generator, (iv) the transfer optics and spectrometer, (v) the interface and computer.[94] Following the standard procedure, a solution of the studied element, whose

concentration is to be determined, is nebulized into the core of inductively coupled argon plasma, that is generated by inductive heating (temperature up to 10,000 K), to excite and dissociate unknown specimen. The light emitted by the atoms or ions in the ICP is converted to an electrical signal by a photomultiplier in the spectrometer and subsequently resolved into a spectrum of its constituent wavelengths. The intensity of this electrical signal is compared to a previous measured intensity of a known concentration of the element, and then a concentration of the specimen is computed.

ICP is an effective source of atomic emission which can, in principle, be used for the determination of all elements other than argon.[95] Using a commercial spectrometer (ex. Spectro Ciros ICP-OES in this work), each of diffracted light is consequently collected and used for quantitative purposes by comparison with calibration standards. The ability of ICP to complete simultaneous analysis of 20-40 elements at the same time as a

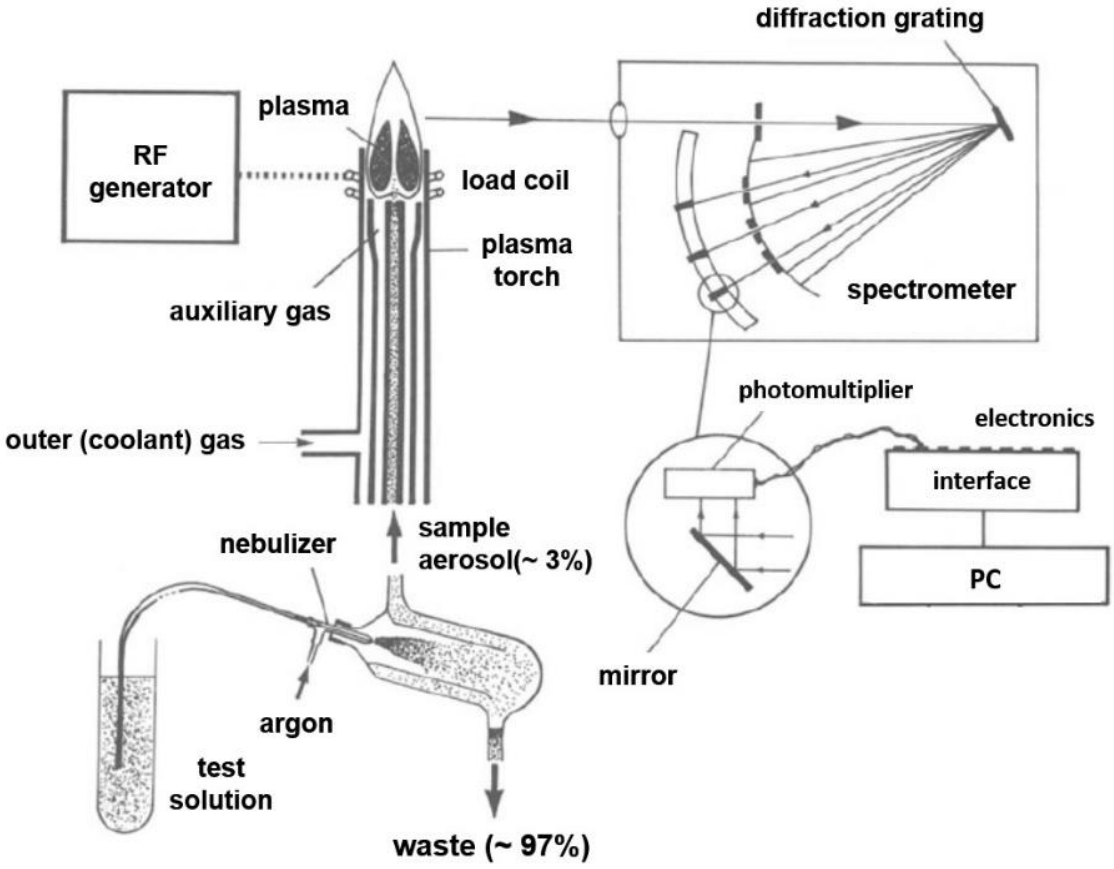

Figure 2.54 Schematic diagram of a conventional simultaneous ICP system. [94]

single-element analysis is clearly one of the most fundamental advantages of the method.

2.5.7. XMCD spectroscopy

The XMCD measurements in this study were completed in WERA and BOREAS beamlines, where data recording is basically operated in the same method. For each XAS spectrum, the total drain current (I_1) and the reference current (I_0) were recorded simultaneously from sample and I_0 gold mesh by two Keithley 6517A electrometers. All spectra were measured by continuous scan mode instead of step-by-step scan mode.

With MPI XMCD system, additional Keithley 6517A electrometer can be connected to collect total fluorescence yield signals, which provide bulk-like XMCD information compared to TEY signals. To prevent leaving electrons from returning into the studied samples, negative bias voltage was always applied via Keithley electrometers throughout whole WERA beamtime (-60 V for TEY and -200 V for TFY modes).[69] The extra sample bias (negative voltage) is particularly important for the XMCD research on hard magnets. Low-temperature measurements were carried out by newly integrated Lakeshore temperature sensors (Cernox™ 1050) and monitored by model 336 cryogenic temperature controller with cooling sources (either liquid N_2 or He). Room- and low-temperature measurements were operated under a pressure of $\leq 2 \times 10^{-9}$ mbar. For high-temperature measurements, the heating power was generated directly by tungsten wire regulated by Lakeshore 336 controller. Due to severe degassing above 350 K, the high-temperature measurements were completed under a pressure of $\sim 10^{-8}$ mbar.

For BOREAS beamtime in ALBA synchrotron, the sample transfer and beam alignment were operated with the help of the assigned beamline scientist, Dr. Hari Babu Vasili.

In order to study a series of specimens quantitatively, the XAS data for each specimen measured at TEY mode were treated with careful offset modification followed by nonmagnetic XAS (μ_0) fitting normalization. The fitting parameters extracted from μ_0 spectra were in turn used for background subtraction of μ_+ and μ_- spectra in order to make sure the shape of the dichroism curve ($\mu_+ - \mu_-$) is not affected. For angle-dependent measurements, saturation effect was further considered and eliminated to reach minimum error in estimation of magnetic moments. Moreover, all values evaluated from ANKA measurement were divided by the finite circular polarization of 0.8.

3. Fabrication and characterization of LTP-MnBi

3.1. Powder

In order to mix different metals together, the MnBi ingots were prepared from Mn pieces (Alfa Aesar, 99.95 %) and Bi granules (Aldrich, ≥ 99.99 %) with designed Mn:Bi atomic ratios of 55:45 and 45:55, via arc-melting in argon atmosphere after high pre-vacuum (around 10^{-8} mbar). The flip-and-melt process was always repeated three times to improve the homogeneity of the alloys. The ingots were subsequently annealed at 573 K in vacuum for 1~3 days, and finally the annealed ones were crushed manually and immediately ground into finer powder in a planetary ball mill (Fritsch PULVERISETTE 6, see Figure 3.1) at 150 rpm.[96] The ball milling (BM) process was completed in hexane under argon atmosphere with hardened steel balls for 2~12 hours at room temperature. The as-milled powders were cleaned by ethanol to remove hexane residue, and then purified by magnetic separation to collect strongly ferromagnetic particles. The preparation process of LTP-MnBi powder and bulk samples is simply sketched in Figure 3.2.

Figure 3.1 Planetary Mono Mill PULVERISETTE 6. [96]

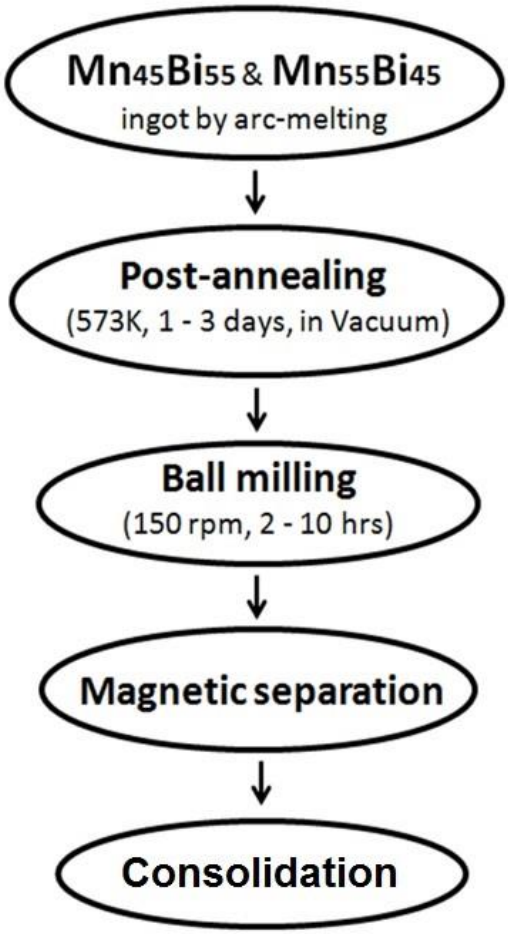

Figure 3.2 The flow chart of MnBi sample fabrication.

In order to identify the starting atomic ratios for all LTP-MnBi powder and bulk magnets, $Mn_{55}Bi_{45}$ and $Mn_{45}Bi_{55}$ specimens are marked with black and red in the following contents respectively.

3.2. Hot-compacted bulk magnets

Because the purified 2h-BM Mn_xBi_{100-x} (x = 45, 55) powders exhibit the highest mass saturation magnetization (M_s) and remanence (M_r), only they were used for consolidation. To fabricate bulk magnets, the powders were first placed into a cylinder die made of Ni-based alloy and aligned under a perpendicular magnetic field of 1.8 T at room temperature. After pre-alignment, the powders were cold-pressed under a uniaxial pressure of 200

MPa, which was applied parallel to the axis of cylinder die. The aligned Mn_xBi_{100-x} (x = 45, 55) compacts were then consolidated by hot-compaction in vacuum at 473, 523, and 573 K for 5 minutes, respectively. Throughout hot-compaction process, a uniaxial pressure of 200 MPa was applied parallel to the initial cold compaction direction. In the following, the hot-compacted samples are denoted as $Mn_{55}Bi_{45}$($Mn_{45}Bi_{55}$)-473, -523 and -573 respectively.

The hot-compacted samples were prepared using the self-built hot-pressing system in Prof. Oliver Gutfleisch's laboratory (TU Darmstadt). The experiments were assisted by Dr. Simon Sawatzki, Dr. Semih Ener.

3.3. SPS-compacted bulk magnets

The purpose of this work is to study the influence of spark plasma sintering on the magnetic performance because there are only a few published work regarding isotropic bulk magnets prepared by SPS technique.[97-99] In the beginning, the starting material was purified 7h-BM Mn_xBi_{100-x} (x = 45, 55) powder because they showed narrower particle size distribution (0.5∼5 μm). The powder was first placed into graphite foils inside a high-strength graphite die, and then fast consolidated by the SPS method. All samples were treated in low vacuum under a uniaxial pressure of 90 MPa with heating rate of 200 °C/min. The sintering temperature (T_s) was set to 593 K, and dwell time was 5 minutes holding at sintering temperatures. Following this procedure, the bulk products are magnetically isotropic because no magnetic alignment was included in the preparation procedure.

To obtain high-performance anisotropic SPS-compacted magnets, purified 2h-BM $Mn_{55}Bi_{45}$ powder was mainly used as the starting material because it shows the highest record magnetic properties for ball-milled LTP-MnBi powder so far. In this work, the purified powder was aligned via two different routes before consolidation. For the route #1, the powder was in-situ aligned by two commercial Sm_2Co_{17} bulk magnets ($\mu_0 B_r$ ∼1.1 T) from top and bottom sides. Therefore, the specimens were sintered under the stray field of the Sm_2Co_{17} magnets parallel to the compaction direction. For

the route #2, the powder was firstly mixed with the binder (Empower materials, QPAC® 40) inside a hardened steel cylinder die, and then shaped into green compacts under 200 MPa with a perpendicular magnetic field of 1.8 T. Also, the green compacts or powder were consolidated in vacuum under a uniaxial pressure of 80 MPa with heating rate of 200 °C/min. The sintering temperatures (T_s) varied from 533 to 573 K with different dwell time (30 seconds, 2 minutes and 5 minutes) holding at T_s. The anisotropic SPS-compacted samples are hereinafter denoted by the aberrations in the following order: SP1 (or SP2), T_s and dwell time. For example, the bulk sample denoted as SP2-533-30s means that the starting powder was aligned by the route #2 and then sintered at 533 K for 30 seconds.

The SPS-compacted samples were prepared using a commercial SPS instrument (FCT Systeme GmbH, HP D 5/2 press) in Prof. Joachim Maier's department (MPI-FKF). The experiments were assisted with help from Dr. Giuliano Gregori.

3.4. XMCD measurements

Most of the measurements on LTP-MnBi were completed in WERA beamline using MPI XMCD instrument, and only the Bi $M_{4,5}$ edges were exclusively measured in BOREAS beamline. Prior to the assigned beamtime, all anisotropic bulk specimens were carefully cut and fixed onto the stainless steel holders exactly parallel or perpendicular to the magnetic alignment directions. This preparation method enables us really to measure the samples along two principle axes (easy- and hard-axis) at normal incidence condition, namely negligible self-absorption effect. All samples were gently polished by sand papers under high vacuum condition ($\leq 10^{-7}$ mbar). The scratched particles were removed as much as possible by a NdFeB magnet fixed in the loadlock chamber before transferring into the main chamber.

Prior to detailed XAS scans, survey spectra were repeated to check the level of surface oxidation and chemical composition, as shown in Figure 3.3. It is proved that the specimens have negligible extrinsic contamination except the Ni absorption peaks most likely coming from the particles on the beam path.

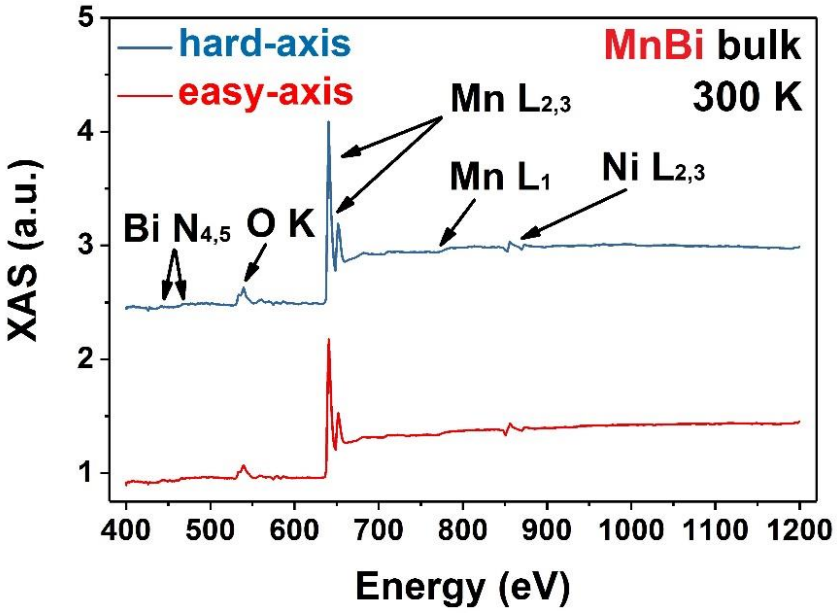

Figure 3.3 Overview XAS scan of $Mn_{45}Bi_{55}$-573 along easy- and hard-axes. The hard-axis spectra was shifted upward for clarity.

3.5. Results and discussions

3.5.1. Powder

A systematic work indicates that the ingots with 55 at.% Mn always exhibit better magnetic performance, hence the discussion here focuses on the ball-milled $Mn_{55}Bi_{45}$ powders. Figure 3.4(a) shows the XRD patterns of the as-milled $Mn_{55}Bi_{45}$ powder as a function of ball milling time. Three phases can be identified from the diffraction patterns, which are LTP-MnBi [$P6_3/mmc$, a = 4.291 Å, c = 6.123 Å], α-Mn [$I\bar{4}3m$, a = 8.921 Å], and Bi [$R\bar{3}m$, a = 4.547 Å, c = 11.872 Å], respectively. It is noted that no high temperature

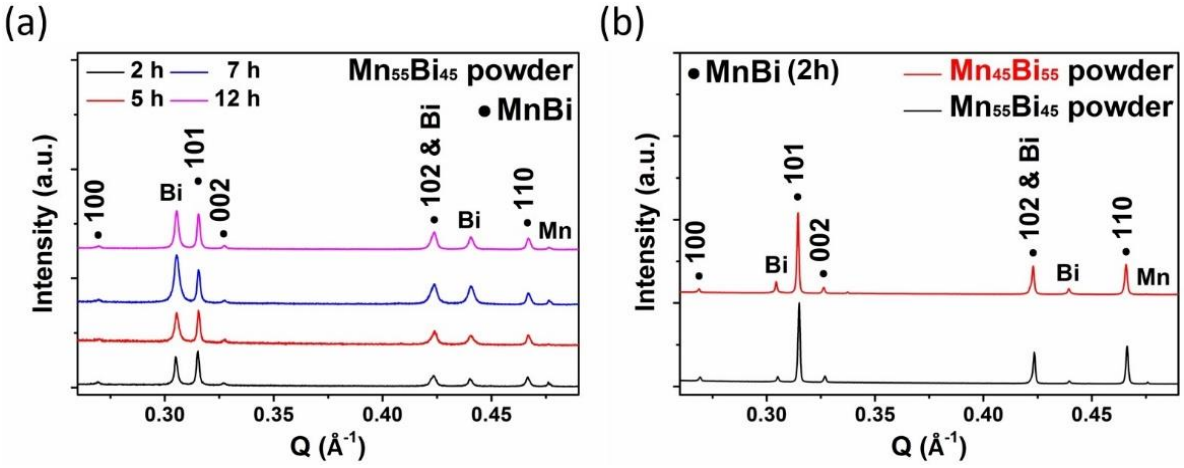

Figure 3.4 Room-temperature XRD patterns: (a) as-milled $Mn_{55}Bi_{45}$ powder for different ball-milling times. (b) purified $Mn_{55}Bi_{45}$ and $Mn_{45}Bi_{55}$ powder (2h-BM).

phase (HTP) of MnBi could be found in all powder samples within the detection limit of our XRD measurements. For the $Mn_{55}Bi_{45}$ powders, the intensities of characteristic Bi peaks increase significantly with increasing ball milling time, which indicate the decomposition of the LTP-MnBi during ball milling procedure. Rietveld analysis shows that the LTP content of as-milled $Mn_{55}Bi_{45}$ powders goes down from 49 wt.% (for 2h-BM) to 29 wt.% (for 7h-BM), while the Bi content increases from 38 wt.% (for 2h-BM) to 70 wt.% (for 7h-BM). The increase in Bi residue is also observed by the chemical analysis (ICP-OES) from which, for example, the purified 2h- and 7h-BM $Mn_{55}Bi_{45}$ powder contain 45.6 and 54.7 at.% Bi, respectively. In contrast, the $Mn_{45}Bi_{55}$ powders always have high level of Bi (> 52 at.%) without obvious systematic variation in atomic ratios (not shown here). Figure 3.4(b) proves that the fraction of LTP in the 2h-BM powders can be further enriched through magnetic separation. The Rietveld analysis reveals that the LTP content increases dramatically, for example, from 49 wt.% for as-milled $Mn_{55}Bi_{45}$ powders to 90 wt.% for corresponding purified ones. Conversely, a significant decrease is observed in the peak intensities of the non-ferromagnetic Bi and Mn peaks. However, we found that long-term milled powders are not easily purified, therefore only purified 2h-BM powders were selected for consolidation. Furthermore, a relatively high fraction of secondary phase Bi (~6 wt.%) is always present, even for the finely purified powders as can be seen in Figure 3.4(b). It is quite usual to

have decomposed phases at the surface of ball milled particles, therefore we suggest that part of the powders should be covered by a thin Bi-rich layer. In order to maximize the magnetic properties (i.e. wt% of LTP-MnBi), powders were always purified by magnetic separation before consolidation. It is noted that the actual Mn:Bi atomic ratios of the purified 2h-BM $Mn_{55}Bi_{45}$and $Mn_{45}Bi_{55}$ powder are 53:47 and 46:54, which are slightly different from the designed values. Additionally, we emphasize that the SQUID values are more reliable than the phase contents given by Rietveld refinement due to the large difference in X-ray scattering factors of Mn and Bi elements.

The room-temperature $M(H)$ curves of the purified $Mn_{55}Bi_{45}$ powders milled for different time are shown in Figure 3.5. All powders were aligned with resin under 2 T magnetic field prior to the SQUID measurements. It is obvious that the M_s and M_r ratios of purified $Mn_{55}Bi_{45}$ powders drop rapidly with increasing milling time. Although long-term BM can slightly enhance the coercivity, it reduces magnetization drastically and even leads to a kink in the low field range for 12h-BM powders. The drop in magnetization indicates decomposition of LTP-MnBi after low-energy ball-milling.

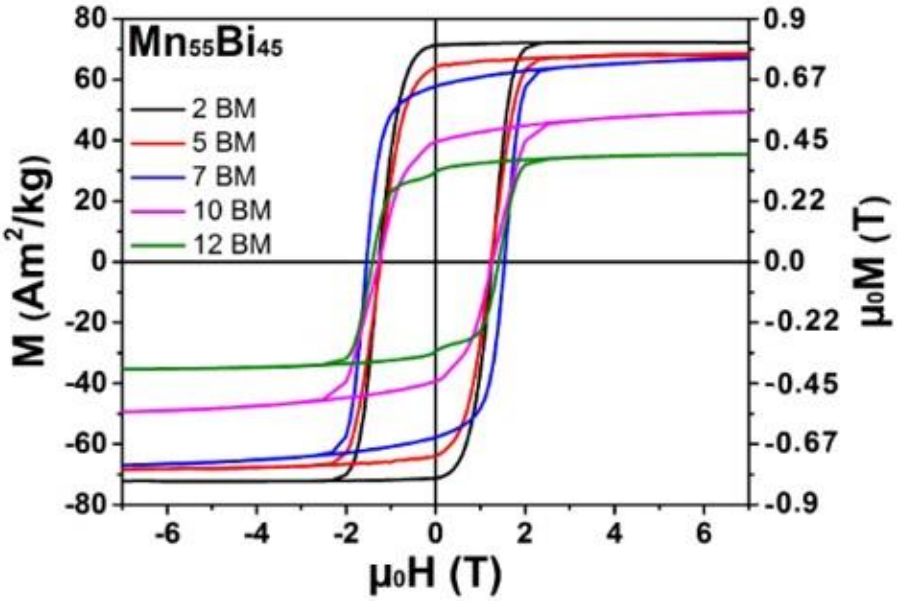

Figure 3.5 $M(H)$ curves of purified $Mn_{55}Bi_{45}$ powder milled for different time at 300 K.

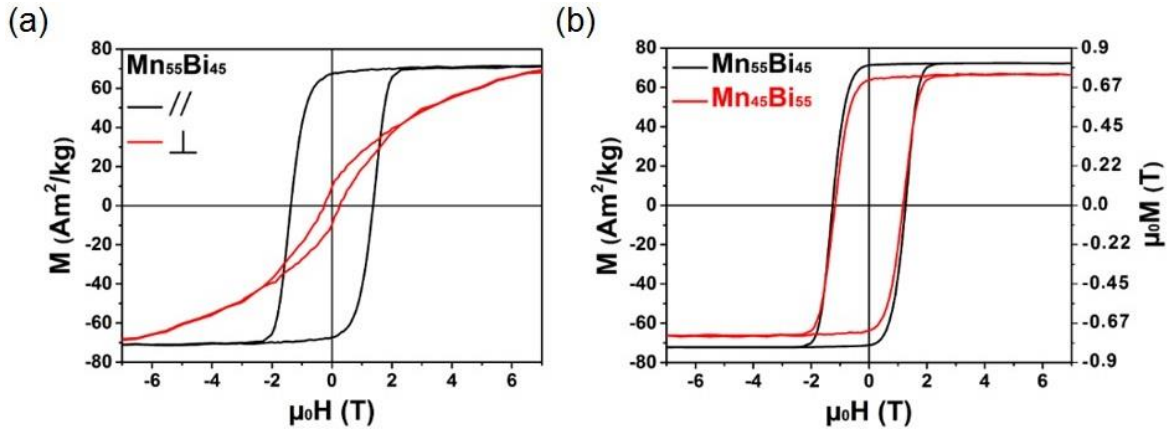

Figure 3.6 *M*(*H*) curves of purified powder at 300 K: (a) 2h-BM $Mn_{55}Bi_{45}$ measured parallel (⊥) and perpendicular (//) to the alignment directions. (b) purified 2h-BM $Mn_{55}Bi_{45}$ and $Mn_{45}Bi_{55}$ powder.

Figure 3.6(a) shows the $M(H)$ curves of purified 2h-BM $Mn_{55}Bi_{45}$ powders measured parallel and perpendicular to the alignment direction at 300 K, which demonstrates that the aligned powder samples are highly anisotropic. Similar trends were found for the $Mn_{45}Bi_{55}$ series (not shown here). In agreement with Refs. [25] and [100], the SQUID measurements reveal that $Mn_{55}Bi_{45}$ series always exhibits larger M_r and M_s than those of $Mn_{45}Bi_{55}$ samples after identical preparation procedure (see Figure 3.6(b)). The highest magnetic properties obtained from the finely purified 2h-BM $Mn_{55}Bi_{45}$($Mn_{45}Bi_{55}$) powder are M_r of ~71(65) Am²/kg, M_s(7T) of ~72.5(68) Am²/kg and $\mu_0 H_c$ of ~1.23(1.18) T at 300 K. The LTP content of the purified 2h-BM $Mn_{55}Bi_{45}$ powder is estimated to be over 90 wt% compared to the theoretical prediction of $M_{s,LTP}$ (80 Am²/kg).[101] To our knowledge, the M_r of ~71 Am²/kg is the highest reported value for ball-milled MnBi powder so far.[26, 102, 103] The volume magnetization of the purified 2h-BM $Mn_{55}Bi_{45}$ powder was further evaluated by theoretical density of LTP-MnBi (8.9 g/cm³),[26] giving $\mu_0 M_r$ = 0.79 T and $\mu_0 M_s$ = 0.81 T. Combined with the observed coercivity of 1.23 T, the nominal $(BH)_{max}$ of this purified $Mn_{55}Bi_{45}$ powder reaches 120 kJ/m³, which is close to the theoretical prediction of 140.8 kJ/m³.[26, 28] Although the $\mu_0 M_r$ of our powder is slightly lower than that of reported value (74 Am²/kg) in Ref. [26], it is noted that our powder was pre-aligned under 2 T and then measured with

a field of 7 T. Nevertheless, we have to emphasize that the purified 2h-BM $Mn_{55}Bi_{45}$($Mn_{45}Bi_{55}$) powder usually shows M_s(7T) of 70(66) ±2 Am^2/kg. It is our experience that the ingot quality has a profound influence on the magnetic performance of the powder, including M_s and $(BH)_{max}$. Therefore, it is crucial to mix metallic Mn and Bi homogeneously during arc-melting process in order to obtain high performance powders.

3.5.2. Hot-compacted bulk magnets (anisotropic)

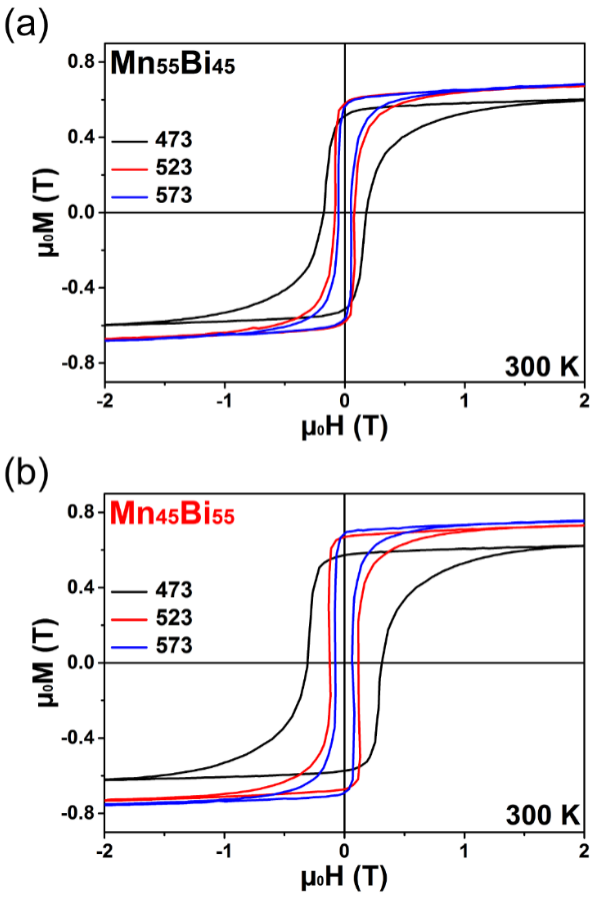

Figure 3.7 *M*(*H*) curves of (a) $Mn_{55}Bi_{45}$ and (b) $Mn_{45}Bi_{55}$ hot-compacted magnets at 300 K.

Figure 3.7 compares the *M*(*H*) curves of the $Mn_{55}Bi_{45}$ and $Mn_{45}Bi_{55}$ magnets hot-compacted at 473, 523, 573 K, which were measured along the pre-alignment direction at 300 K. The highest volume magnetization is observed in $Mn_{55}Bi_{45}$-523 and $Mn_{45}Bi_{55}$-573, respectively. In contrast to the

starting purified powders, the $Mn_{45}Bi_{55}$ bulk series exhibits higher magnetic performance compared to the $Mn_{55}Bi_{45}$ bulk one, namely higher area fraction of LTP-MnBi (see Table 3.1 for detailed information).

Table 3.1 Chemical compositions (ICP-OES) and room-temperature magnetic properties of hot-compacted bulk magnets.

Sample	Mn [at.%]	Bi [at.%]	$\mu_0 H_c$ [T]	$\mu_0 M_r$ [T]	$\mu_0 M_s$(7T) [T]
$Mn_{45}Bi_{55}$-473	45.0	55.0	0.31	0.57	0.65
$Mn_{45}Bi_{55}$-523	51.5	48.5	0.14	0.67	0.77
$Mn_{45}Bi_{55}$-573	52.6	47.4	0.08	0.68	0.79
$Mn_{55}Bi_{45}$-473	54.4	45.6	0.18	0.51	0.64
$Mn_{55}Bi_{45}$-523	57.8	42.2	0.08	0.57	0.71
$Mn_{55}Bi_{45}$-573	59.7	40.3	0.05	0.56	0.73

This difference is actually caused by removal of excess Bi from bulk samples because we observed that the compacts and the inner shell of the steel die were covered by many tiny Bi-rich fragments (> 98 at.% Bi by ICP-OES analysis) after hot-compaction process. Due to the low Bi melting point of 545 K close to the sintering temperatures, the liquid Bi from residue or decomposition of LTP was extruded out during consolidation.[26] Conversely, the melting point of Mn is rather high (1518 K), so most of the excess Mn is left inside the microstructure.[30] As a result, the actual Mn:Bi atomic ratios of bulk samples differ a lot from the designed values and those of starting powders (see Table 3.1). It is noted that both $Mn_{45}Bi_{55}$-523 and $Mn_{45}Bi_{55}$-573 contain excess of Mn even though they were prepared by Bi-rich powders. Among these specimens, $Mn_{45}Bi_{55}$-573 shows $\mu_0 M_r$ = 0.68 T and $\mu_0 M_s$(7T) = 0.79 T at 300 K, which are the highest magnetization values reported for MnBi sintered magnets so far.[26, 102] Compared to the starting powders, the $\mu_0 M_r$ and $\mu_0 M_s$ values of the $Mn_{45}Bi_{55}$-573 bulk samples decrease slightly by 6% and 4% respectively. However, all hot-compacted samples show relatively low coercivity (≤ 0.31 T) at 300 K in comparison

with the previously published work.[26, 102] To clarify this issue, the microstructure of the bulk samples was examined by SEM characterization. Because the SQUID results show that $Mn_{45}Bi_{55}$ magnets exhibit better magnetic performance at different temperatures, the following discussions will mainly focus on them.

The backscattered electron (BSE) images of $Mn_{45}Bi_{55}$ powder and three bulk magnets are shown in Figure 3.8. Figure 3.8(a) reveals that the particle size of 2h-BM powder ranges from 0.5 to 8 μm with average size less than 3 μm. As shown in Figures 3.8(b)-(d), three phases [α-Mn (black), Bi (white) and LTP-MnBi (gray)] can be distinguished in the bulk samples, which are confirmed by EDS mapping (not shown here). BSE images suggest that some grains are elongated along alignment direction with length

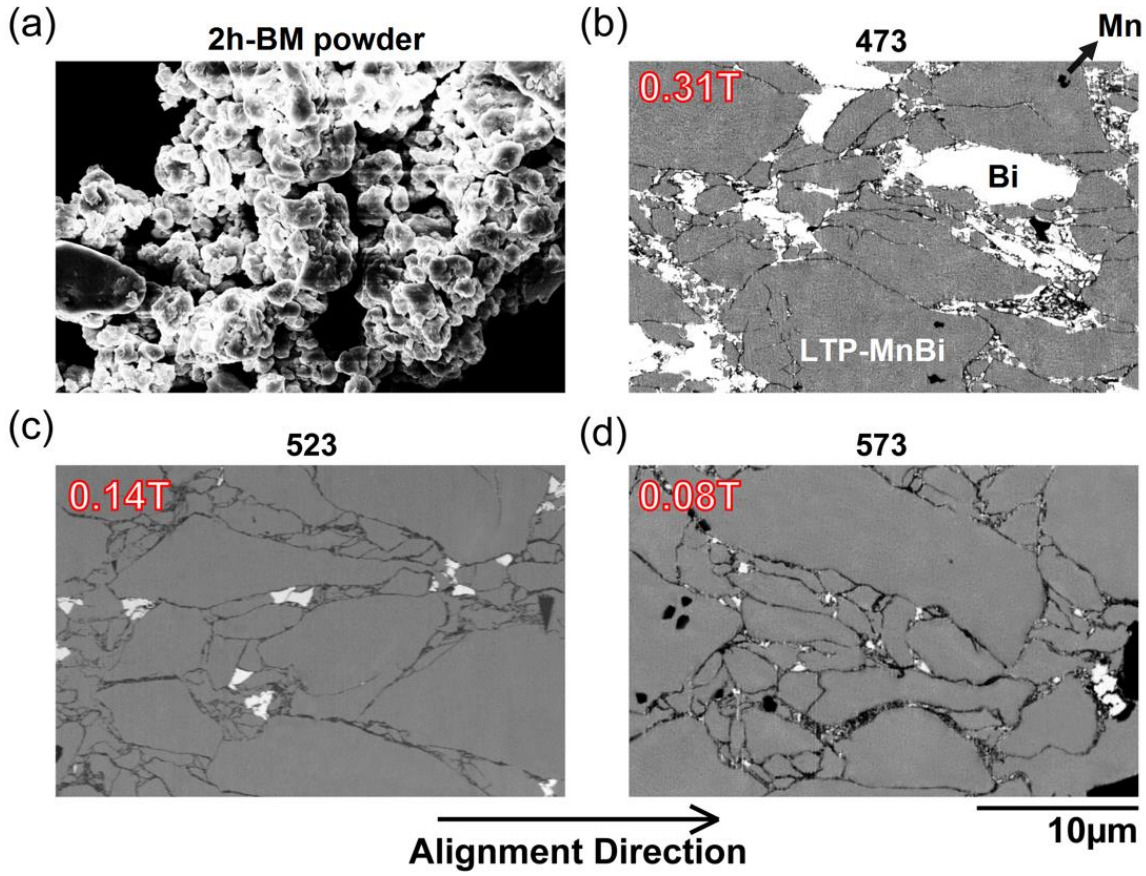

Figure 3.8 BSE images of $Mn_{45}Bi_{55}$ (a) 2h-BM powders and (b, c, d) bulk magnets. The value on the top-left corner in each micrograph of the bulk samples refers to the observed coercive fields ($\mu_0 Hc$). The grains were particularly elongated along the alignment direction (roughly horizontal).

longer than 15 μm, therefore significant grain growth indeed occurred during the consolidation. We also analyzed the grain size distribution in these bulk samples, and it was found that their grain size distribution looks very similar. But, the number of very large grains (length > 18 μm) slightly increases as the consolidation temperature goes up. Because single domain size of LTP-MnBi is ~0.5 μm at 300 K,[28, 104] the small measured coercive field of our bulk samples can be partially understood due to the existence of the larger grains observed here. This assumption is consistent with the reported relation between grain (or particle) size and $\mu_0 H_c$ values in nanocrystalline thin films[105] and powders[106]. Specifically, the experimental data in Ref. [106] show that MnBi powders with diameter of 20 μm exhibit $\mu_0 H_c$ of ~0.5 T, which is slightly larger than that of $Mn_{45}Bi_{55}$-473. Therefore, we suggest that the observed low coercive field should be related to the domain wall movement in the large grains.

Table 3.2 Area fraction of three phases in the microstructure of $Mn_{45}Bi_{55}$ hot-compacted samples.

Sample	MnBi [area %]	α-Mn [area %]		Bi [area %]	$\mu_0 H_c$ [T]	$\mu_0 M_s$ [T]
		Residue	Grain-boundary			
$Mn_{45}Bi_{55}$-473	78.6	2.6	1.8	17	0.31	0.65
$Mn_{45}Bi_{55}$-523	83.5	3.3	7.8	5.4	0.14	0.77
$Mn_{45}Bi_{55}$-573	89.4	1.9	7.8	0.9	0.08	0.73

The area fractions of three phases (MnBi, α-Mn, and Bi) of the compacted samples were further determined from randomly selected surface area (80 μm × 80 μm). The data in Table 3.2 suggest that bulk magnets with more Bi residue have higher coercive field. This tendency can be explained by

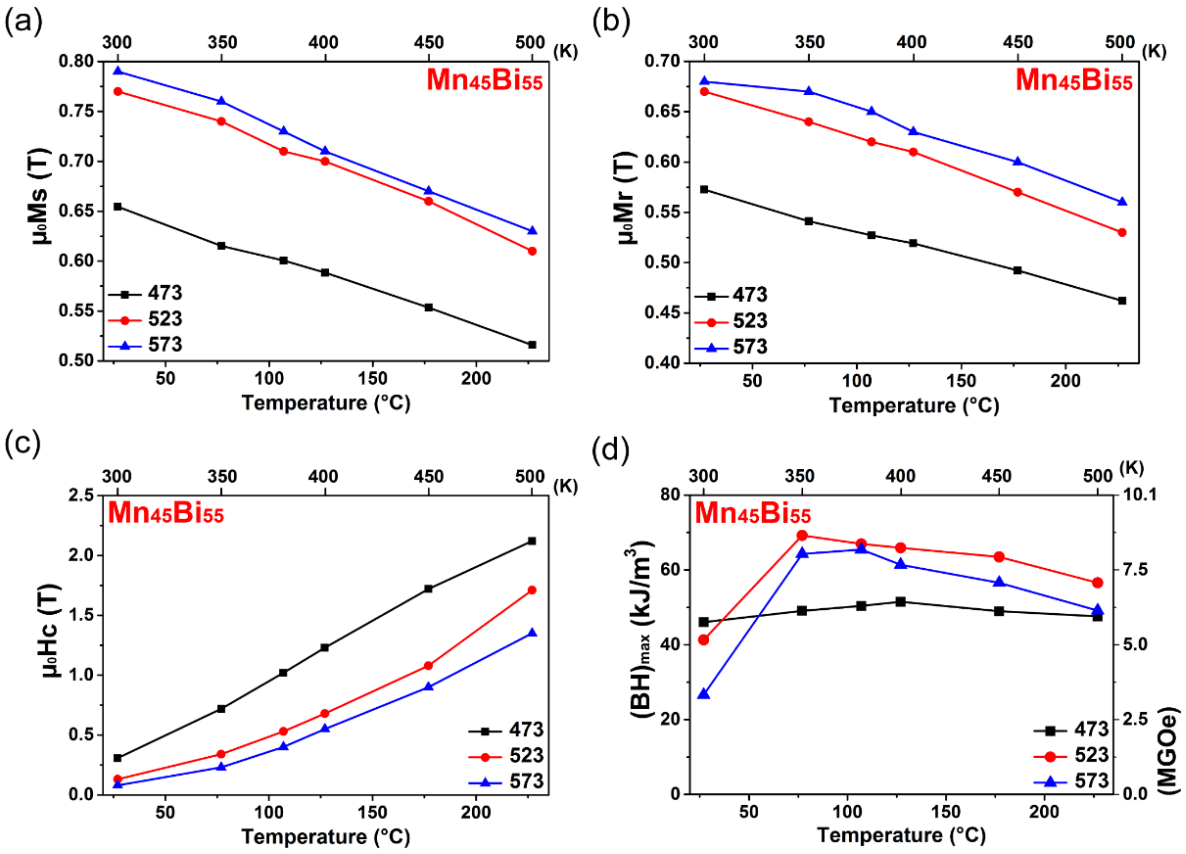

Figure 3.9 Temperature-dependent magnetic properties of $Mn_{45}Bi_{55}$ bulk magnets: (a) volume saturation magnetization, (b) volume remanent magnetization, (c) coercive field and (d) (BH)max values at different temperatures (measured along alignment direction).

considering Bi as decoupling layer between LTP grains. Because metallic Bi is diamagnetic material, the LTP-MnBi grains surrounded by thicker Bi area have better magnetic decoupling from others (i.e. $Mn_{45}Bi_{55}$-473 shows the largest $\mu_0 H_c$). Furthermore, the $Mn_{55}Bi_{45}$ bulk series exhibits even lower coercivity because less Bi and a relatively high amount of antiferromagnetic α-Mn is embedded inside the microstructure (not shown here). Theoretically, the exchange coupling between two magnetic phases is considered as a short-range interaction. It is clear that better magnetic decoupling should be achieved between either LTP-MnBi grains or LTP-MnBi/α-Mn phases as the amount of Bi residue increases.

The change of magnetic properties of $Mn_{45}Bi_{55}$ hot-compacted magnets is summarized in Figure 3.9 as a function of measuring temperature. Among these three samples, $Mn_{45}Bi_{55}$-573 exhibits the highest magnetization

(both $\mu_0 M_r$ and $\mu_0 M_s$) within measuring temperatures, which decreases from 0.68 T and 0.79 T at 300 K to 0.56 T and 0.63 T at 500 K, respectively. Grain misalignment usually causes a drop in the remnant magnetization of bulk magnets. SQUID curves indicate that all $Mn_{45}Bi_{55}$ magnets are highly textured because the M_r/M_s ratios are all above 0.86 within the measuring temperature range (300~500 K). However, the largest temperature-dependent coercive fields are found in $Mn_{45}Bi_{55}$-473, which increases from 0.31 T at 300 K to 2.1 T at 500 K. Therefore, the highest nominal $(BH)_{max}$ value of $Mn_{45}Bi_{55}$ series at 300 K is 46.1 kJ/m^3 found in $Mn_{45}Bi_{55}$-473. Although the highest $(BH)_{max}$ value in this study is lower than the reported value of 61.6 kJ/m^3 in Ref. [26], it is higher compared to that of commercial ferrite or alnico 5 magnets. We also note that the nominal $(BH)_{max}$ of all $Mn_{45}Bi_{55}$ samples is above 40 kJ/m^3 at 500 K, which is higher than experimental $(BH)_{max}$ of $Nd_2Fe_{14}B$ (15.8 kJ/m^3).[28, 104] Furthermore, it was found that all $Mn_{45}Bi_{55}$ and $Mn_{55}Bi_{45}$ bulk samples retain the same magnetic properties after one-day heating at 500 K under inert atmosphere. This evidence strongly suggests that LTP-MnBi can be a good candidate for high temperature applications, while the proper surface coating is carried out to prevent oxidation problem.

3.5.3. SPS-compacted bulk magnets (isotropic)

Based on the great experience in hot-compacted samples, a systematic work was repeated by using SPS-technique because it is always desired to achieve homogeneous microstructure. Magnetization curves, $M(H)$, of all isotropic SPS-compacted samples were measured up to an applied filed of 6 Tesla (60 kOe). It is noted that again the purified 7h-BM $Mn_{45}Bi_{55}$ powder has larger M_s(6T) of 49 Am^2/kg at 300 K compacted to $Mn_{45}Bi_{55}$ one, in contrast to the purified 2h-BM $Mn_{45}Bi_{55}$ powder discussed above. Temperature-dependent $M(H)$ curves of the isotropic $Mn_{45}Bi_{55}$ and $Mn_{55}Bi_{45}$ bulk magnets are plotted in Figure 3.10(a) and (b). The as-prepared $Mn_{45}Bi_{55}$ bulk samples also possess higher M_s(6T) of ~64 Am^2/kg and remanence of ~34 Am^2/kg at 300 K, regardless of the slightly lower $\mu_0 H_c$ values. To our knowledge, these values are the highest reported for

MnBi isotropic magnets so far.[107] The LTP- MnBi content in this $Mn_{45}Bi_{55}$ bulk sample is ~80 wt.% since intrinsic LTP- MnBi powder would show M_s of 80 Am^2/kg.[107] The SQUID results clearly show that the coercivity of the isotropic SPS-compacted magnets increases at elevated temperatures and reaches a maximum at T ~600 K. This behavior obviously differs from all previous reports, in which the maximum $\mu_0 H_c$ values occur at T ≤ 550 K.[30, 99, 102]Even if the sintered magnets were heated up to 650 K, which is well beyond the phase transition temperature of ~630 K, the samples still surprisingly retain hard magnetic behavior. It is noted that both powder and sintered magnets were not saturated yet under this external field due to the high magnetocrystalline anisotropy of LTP- MnBi.

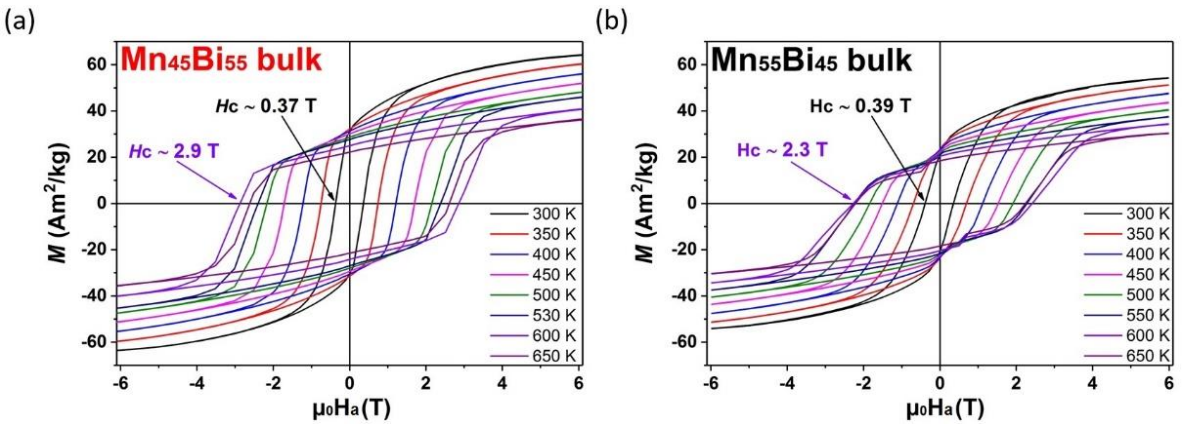

Figure 3.10 Temperature-dependent *M*(*H*) curves of (a) $Mn_{45}Bi_{55}$ and (b) $Mn_{55}Bi_{45}$ SPS-compacted bulk magnets show that the coercivity gradually increases in both cases and peaks at around 600 K. Noted that the starting powders were purifited 7h-BM powders here.

The temperature-dependent M_s and $\mu_0 H_c$ results are summarized in Figure 3.11(a), in which both values are still large at high temperatures (T ≥ 500 K). According to Refs. [108, 109], the phase transition temperature of LTP-MnBi in MnBi-Bi composites is shifted to higher temperatures with increasing external magnetic fields. Therefore, the reason for the unusual thermal stability here could arise from similar mechanism, namely the fine-grained microstructure surrounded by small amount of Bi. Figure 3.11(b) shows the thermomagnetic curve of the $Mn_{45}Bi_{55}$ sample measured with external

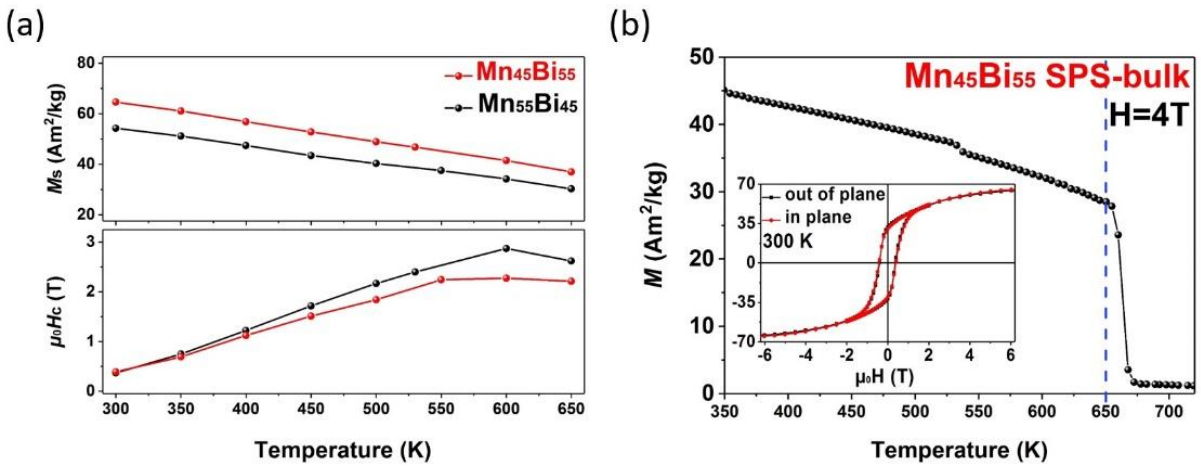

Figure 3.11 (a) Summary of M_S and $\mu_0 H_c$ as a function of temperature. (b) Thermal magnetic curve of the $Mn_{45}Bi_{55}$ magnet under an applied field of 4 T (cooling). The inset shows the sintered sample is magnetically isotropic. Noted that the starting powders were purifited 7h-BM powders here.

field of 4 T, indicating the magnetization clearly drops abruptly while temperature exceeds 650 K. The discontinuous jump located at around 535 K is due to the reformation of LTP-MnBi. The insets demonstrate that the bulk samples are magnetically isotropic, which can be understood since no external field was applied during compaction procedure (also for $Mn_{55}Bi_{45}$ samples). The theoretical $(BH)_{max}$ value of the isotropic $Mn_{45}Bi_{55}$ magnets is 29.5 kJ/m^3 (3.7 MGOe) at 300 K. So far, the highest reported $(BH)_{max}$ value is 62.1 kJ/m^3 (7.8 MGOe), published recently from the 'anisotropic' magnets [26]; however, it is less than 50 % of the theoretical value, 143.3 kJ/m^3 (18 MGOe).

Figure 3.12(a) and (b) present the secondary electron SEM images of the as-prepared $Mn_{45}Bi_{55}$ and $Mn_{55}Bi_{45}$ bulk magnets. Compared to other published SEM results in Refs. [26, 102] and our hot-compacted samples, the grains of the isotropic SPS-compacted magnets are much smaller and the grain boundary is less visible. To observe clear microstructure, etching was performed after mechanically polishing. The images of the etched surface are shown in Figure 3.12(c) and (d), where we found that the isotropic SPS-compacted magnets consist of fine and uniform grains with average size

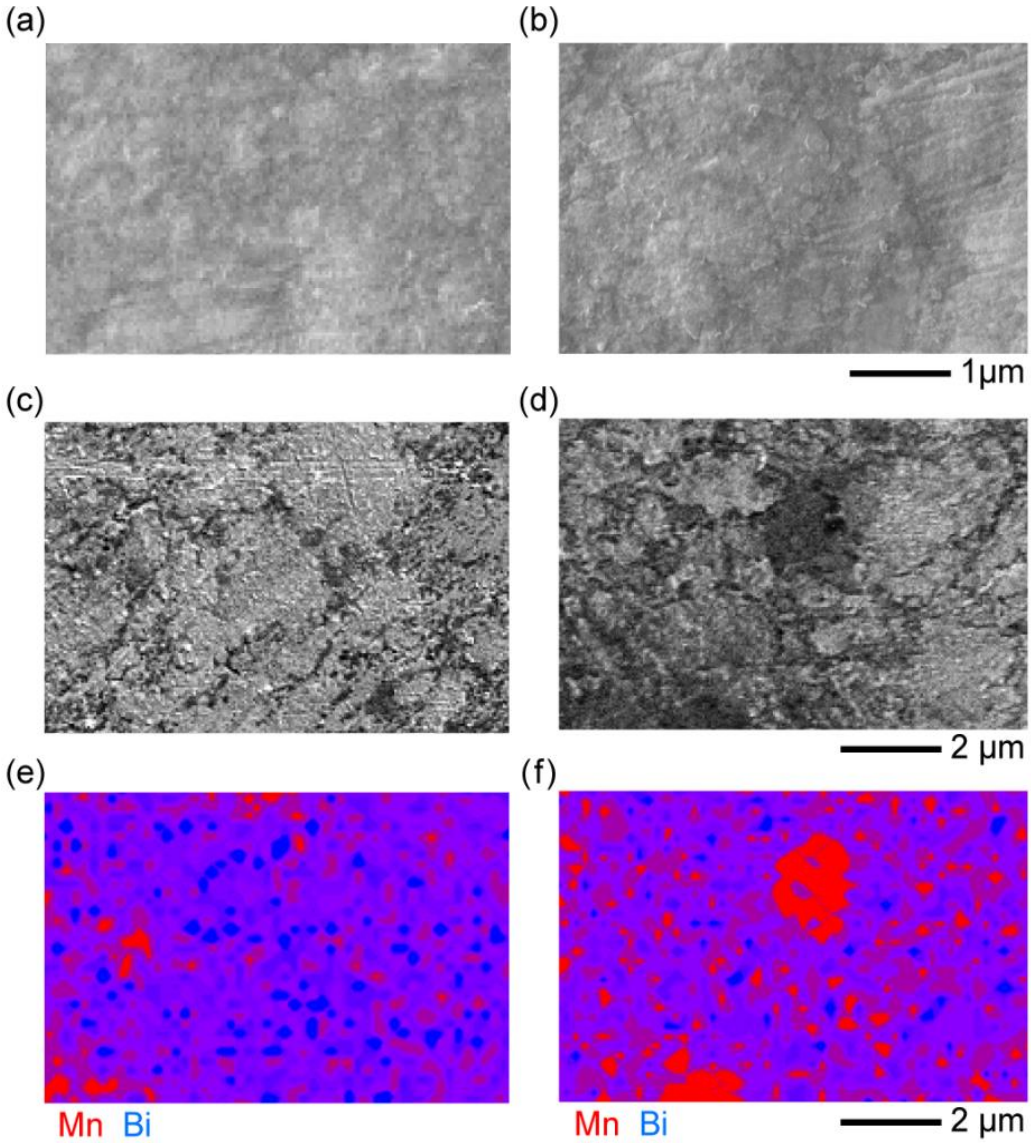

Figure 3.12 SEM images of the as-prepared (a) $Mn_{45}Bi_{55}$ and (b) $Mn_{55}Bi_{45}$ isotropic bulk magnets. There is no clear grain boundary in both bulk samples. The etched surface of both samples and corresponding EDX elemental (Bi and Mn) maps of $Mn_{45}Bi_{55}$ and $Mn_{55}Bi_{45}$ bulk magnets are shown in (c,e) and (d,f) respectively.

less than 5 μm. The shape of the grains in the sintered magnet is irregular similar to that of the original powder, meaning that no obvious grain growth happened during SPS process. Corresponding EDX elemental maps confirm more unreacted Mn metal embedded in the $Mn_{55}Bi_{45}$ matrix (see Figure 3.12(e) and (f)) within the technical limit of the SEM instrument. In addition, the surface structure of the as-prepared magnets was also studied by the focused ion beam scanning electron microscope (Nova NanoLab 600

DualBeam), which gives similar results (not shown here). Combined with the XRD patterns in Ref. [107], we suggest that the outer shell of LTP-MnBi grains is Bi-rich because we did not observe significantly large metallic Bi area in all SEM images, as suggested in the Figure 14 of Ref. [26].

Although the bulk samples show unusual coercivity behavior at T > 550 K, there is still a strong positive correlation between temperature and the measured $\mu_0 H_c$ values in the temperature range from 300 to 600 K. It is suggested that coercivity behavior of LTP-MnBi is related to its temperature-dependent magnetocrystalline anisotropy, K(T).[104] For example, the reported experimental K(T) data (blue curve in Figure 3.13(a)) measured from a non-perfect MnBi single crystal can explain the variation of the corresponding observed $\mu_0 H_c$ in previous work, which has maximum coercivity at 500 K and then rapidly drops at higher temperatures [110]. However, this experimental K(T) curve does not fit well with the theoretically calculated one (black curve in Figure 3.13(a)) given in Ref. [111]. In this study, the variation of the $\mu_0 H_c$(T) values (red curve) is in good agreement with the change in theoretically calculated K(T). We suppose that this finding could be related to the mentioned fine-grained microstructure. To clarify this assumption, some sintered samples were fabricated following the same procedure but for much longer dwell times (30 and 45 minutes). For these specimens, the grains have clear and smooth boundary with larger average grain sizes similar to the reported hot-compacted magnets.[107] With this distinct texture, it was found that the magnets can only exhibit hard magnetic behavior below 630 K with maximum coercivity occurring at T < 550 K. Therefore, we strongly suggest that the microstructure can have a great effect on the observed temperature-dependent coercivity behavior and high thermal stability.

A further aspect that has been addressed is the stability of magnetic properties of MnBi samples after thermal cycling. Basically, permanent magnets cannot keep their hard phase behavior once the ambient temperature rises beyond their phase transition temperature. Therefore, manufacturers usually provide information about the maximum working temperatures of their permanent magnets. In order to evaluate the thermal stability of the

isotropic SPS-compacted magnets, several samples were heated in vacuum up to 650 K repeatedly, which is well beyond the phase transition point. Most remarkably, all specimens still retain hard magnetic properties after cooling back to room temperature as displayed in Figure 3.13(b). There is no visible reduction in the saturation magnetization and coercivity, showing that the loss of LTP MnBi from eutectic and peritectic reactions is fully reversible after cooling. Compared to previous studies on LTP-MnBi magnets,[107] this unprecedented result is very promising for future high temperature applications.

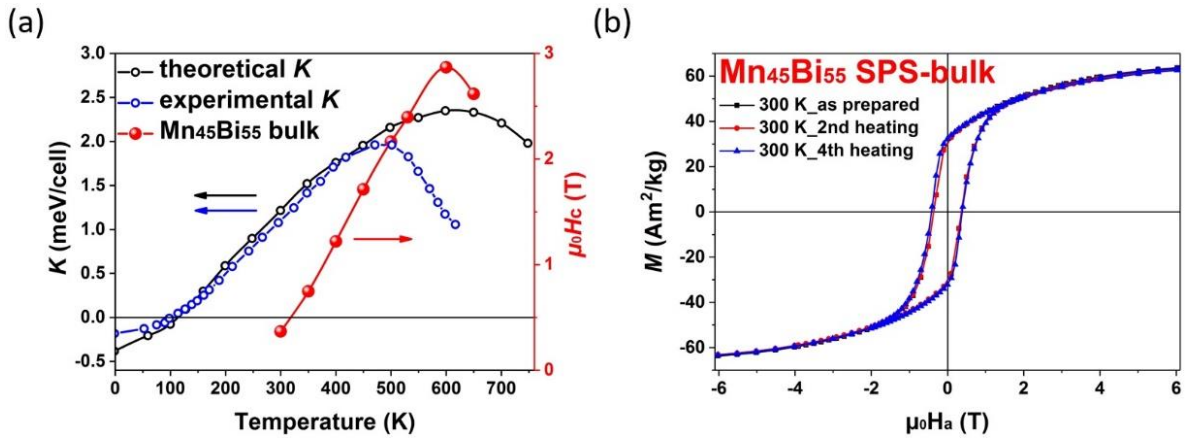

Figure 3.13 (a) Summary of the temperature-dependent $\mu_0 H_c$ values of the isotropic $Mn_{45}Bi_{55}$ magnet with the calculated and experimental *K* values both reported in Ref. [111]. (b) Bulk magnets show unique thermal stability of hard magnetic phase after thermal cycles to 650 K.

The performance of our SPS-compacted magnets could be further enhanced by (i) using powder with higher M_s and $\mu_0 H_c$ and (ii) producing anisotropic samples under magnetic field during compaction procedure. The preliminary attempt in these directions has indeed demonstrated that anisotropic SPS-compacted MnBi samples could be achieved and will be discussed in the next subchapter.

3.5.4. SPS-compacted bulk magnets (anisotropic)

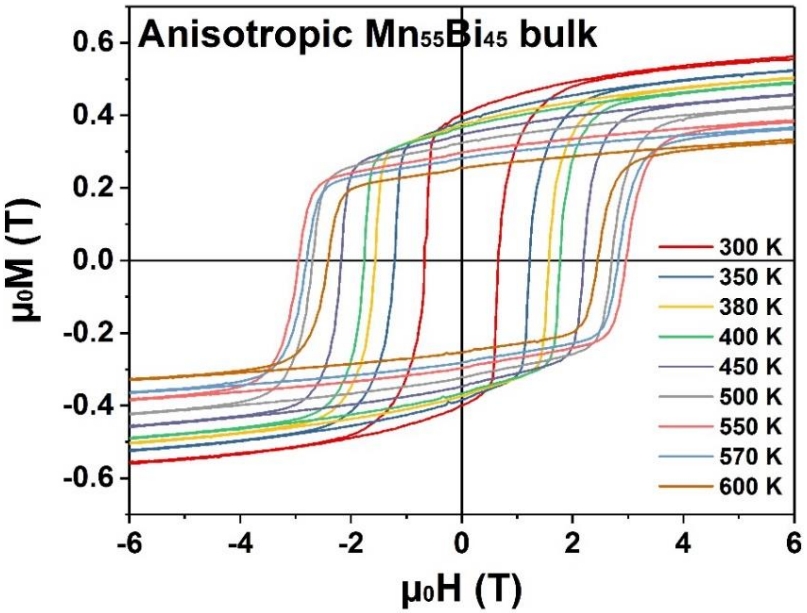

Figure 3.14 Temperature-dependent *M*(*H*) curves of the anisotropic $Mn_{55}Bi_{45}$ magnet measured along alignment direction (easy-axis). Noted that the starting material used here is the purified 7h-BM $Mn_{55}Bi_{45}$ powder.

As discussed above, in-situ magnetic alignment is necessarily required to achieve magnetically anisotropic SPS-compacted magnet, so numerous samples were at first prepared by route #1 to examine the influence of magnetic alignment during SPS-compaction. The preliminary test was performed using purified 7h-BM $Mn_{55}Bi_{45}$ powder, which was consolidated at 533 K for 2 minutes. The magnetization curves of this specimen are plotted as a function of temperature in Figure 3.14. It is clear that the shape of its hysteresis loops looks more square compared to those of isotropic ones. Table 3.3 summarized the comparison of detailed magnetic properties between isotropic and anisotropic magnets. The most remarkable improvement caused by in-situ alignment is the increased values of coercivity and M_r/M_s ratio, which are enhanced by 0.25 kOe and 32%, respectively.

Table 3.3 Influence of in-situ magnetic alignment via route #1. The starting material was purified 7h-BM $Mn_{55}Bi_{45}$ powder. Noted that the isotropic specimen was compacted at 533 K for 5 minutes, while the dwell time for anisotropic one was 2 minutes.

Sample	H_c [kOe]	M_r [Am^2/kg]	M_s(6T) [Am^2/kg]	M_r/M_s
Isotropic	3.9	21	54	38%
Anisotropic	6.4	36	51	70%

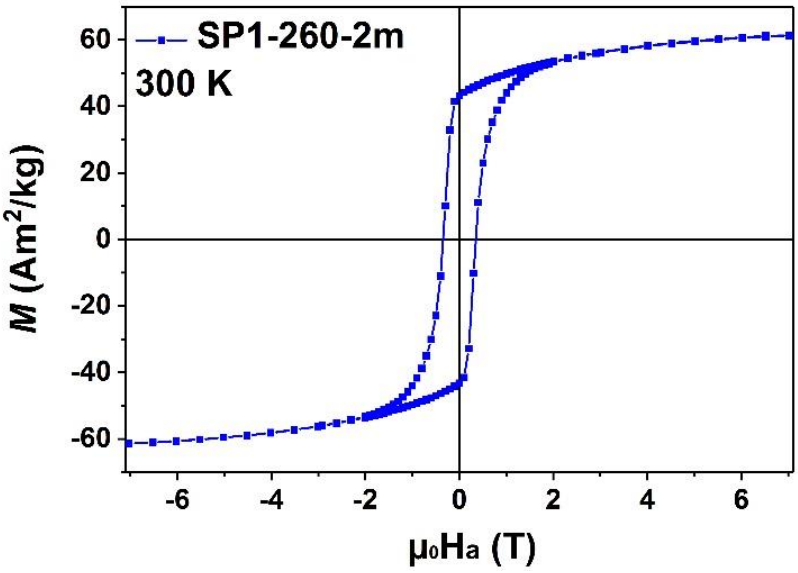

Figure 3.15 Room-temperature *M*(*H*) curve of SP1-260-2m along alignment direction (easy-axis). Noted that the starting material used here is purified 2h-BM $Mn_{55}Bi_{45}$ powder.

Although the magnetic performance is indeed advanced with aid of magnetic alignment, the observed remanence is still not good enough in comparison with hot-compacted samples. The same test was carried out for purified 7h-BM $Mn_{45}Bi_{55}$ powder, but no surprising results were found except slightly increased coercive field. In order to further increase M_r and M_s, the starting material was changed to the purified 2h-BM $Mn_{55}Bi_{45}$ powder. So far the sample, SP1-260-2m, shows the highest magnetic performance considering all the factors like $\mu_0 M_s$, $\mu_0 M_r$, etc. The magnetization curves of SP1-260-2m are plotted in Figure 3.15, which give M_s(7T) of

~61 Am²/kg and M_r of ~42 Am²/kg at 300 K. The magnetization of SP1-260-2m is actually larger compared to all SPS-compacted magnet mentioned above. Using the measured bulk density of 8.7 g/cm³, the evaluated $\mu_0 M_r$ and $\mu_0 M_s$(7T) are 0.48 T and 0.67 T with $\mu_0 H_c$ of 0.38 T at 300 K. It is noted that both the isotropic samples and anisotropic ones(prepared via route #1) can not be saturated under a field of 7 T at room temperature, suggesting that the LTP-grains inside these samples still have some degree of misalignment. Due to the large anisotropy field (≥ 3 T),[105, 112] the stray filed of SmCo magnets is definitely not sufficient to align powder during sintering.

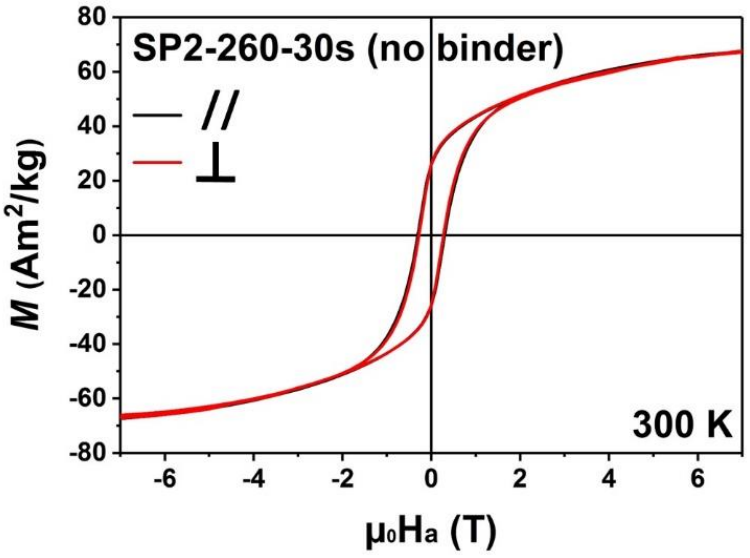

Figure 3.16 *M*(*H*) curves of the SP2-533-30s magnet(no binder) measured parallel (⊥) and perpendicular (//) to the compaction direction at 300 K.

In order to boost the magnetic texture of SPS-compacted magnets, the rest of samples were fabricated via route #2 because a field of 1.8 T is the highest available value under our experimental condition. At the beginning, the powder was shaped into bulk cylinders under magnetic field but without any addition. Subsequently, green bodies were directly consolidated in the SPS instrument. Interestingly, it was found that all SPS-compacted samples only show isotropic magnetization. Figure 3.16 shows that SP2-533-30s(no binder), prepared from the pre-aligned compact without binder,

has high $\mu_0 M_s$(7T) of 0.71 T but small $\mu_0 M_r$ of 0.27 T and $\mu_0 H_c$ of 0.3 T. The low M_r/M_s ratio (~0.38) and magnetically isotropic behavior strongly suggest that the interaction between pulse DC current and the intrinsic magnetic properties of starting materials could lead to severe misalignment during SPS-compaction (no in-situ alignment field).

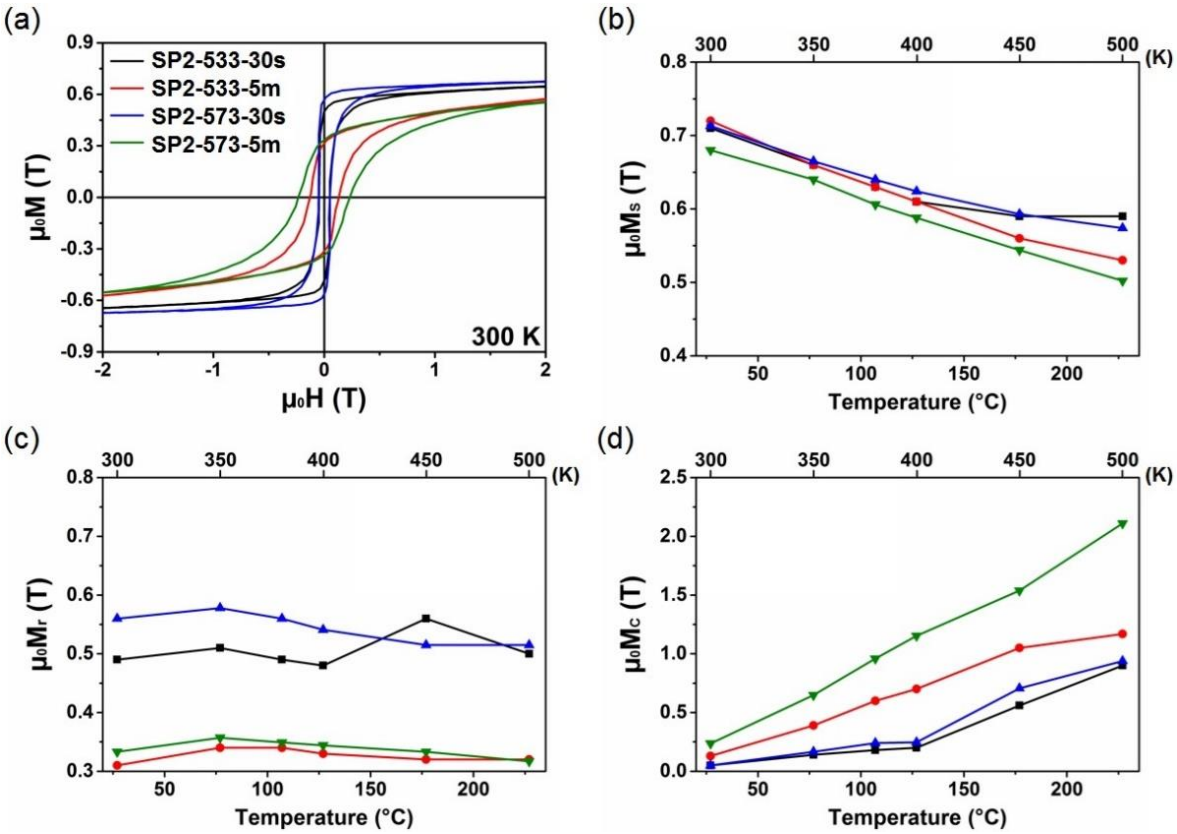

Figure 3.17 Magnetic properties of SPS-compacted samples using pre-alignment route #2: (a) *M*(*H*) curves 300 K with the corresponding temperature-dependent (b) volume saturation magnetization, (c) volume remanent magnetization and (d) coercive field. The results presented here were measured along the alignment direction. Note that $\mu_0 Ms$ refers to the $\mu_0 Ms$(7T).

Because commercial SPS machines generally are equipped without external magnetic field coils, binder was employed to assist alignment of MnBi grains during consolidation process. Taking four specimens for example (shown in Figure 3.17(a)), it is obvious that the M_r/M_s ratio of SP2-533-30s and SP2-573-30s is significantly improved ($M_r/M_s \geq 0.7$) compared to that of SP2-533-30s(no binder).

According to the thermogravimetric analysis provided by the company, the binder used in this study decomposes instantly above 513 K (240 °C) and can be easily removed in vacuum. Therefore, thermal decomposition of binder should be the main reason for the significant drop in the M_r/M_s ratios of SP2-533-5m and SP2-573-5m, while the dwell time increases from 30 seconds to 5 minutes. The effect of dwell time not only leads to distinct M_r/M_s ratio but also change in the compaction density and coercive field. With longer dwell time at sintering temperature, the compaction density increases from ~8.4 g/cm^3 for SP2-533-30s(SP2-573-30s) to ~8.7 g/cm^3 for SP2-533-5m(SP2-573-5m). Similarly, the coercive field at 300 K increases from 0.05 T(0.05 T) for SP2-533-30s(SP2-573-30s) to 0.14 T(0.24 T) for SP2-533-5m(SP2-573-5m). Furthermore, it is more difficult to saturate the samples as the dwell time increases. Among these samples, SP2-573-30s has the highest $\mu_0 M_r$ of 0.56 T and $\mu_0 M_s$ of 0.71 T at 300 K, which is are higher than those of the reported values in Refs. [107] and [99] by over 30 %. However, its $\mu_0 H_c$ is only 0.05 T so that the $(BH)_{max}$ value at 300 K is 13 kJ/m^3 (1.6 MGOe). The temperature-dependent $\mu_0 M_s$, $\mu_0 M_r$ and $\mu_0 H_c$ values are summarized in Figure. 3.17(b)-(d). As what can be seen, all of the specimens show typical magnetic behavior of LTP-MnBi, namely increased coercive field at elevated temperatures. However, it is noted that the hard magnetic properties disappear above phase transition temperature (~630 K). For anisotropic SPS magnets, the temperature-dependent variation in magnetic properties is consistent with that of hot-compacted specimens, but in contrast to isotropic SPS results. Again, this discrepancy could be ascribed to the high level of Bi residue in isotropic SPS-compacted samples as discussed in previous subchapter. Furthermore, the magnetization and magnetic anisotropy of the SPS-compacted specimens in this study is lower compared to that of hot-compacted ones. According to the $M(H)$ measurements, it is concluded that preparing MnBi bulk magnets with SPS method must be carried out under sufficiently large external magnetic field in order to achieve both high M_r and $(BH)_{max}$.

Since SPS technique enables easily varying preparation parameters in a large range, the magnetization and coercivity of SPS-compacted samples show diverse magnetic response. In this thesis, the samples consolidated

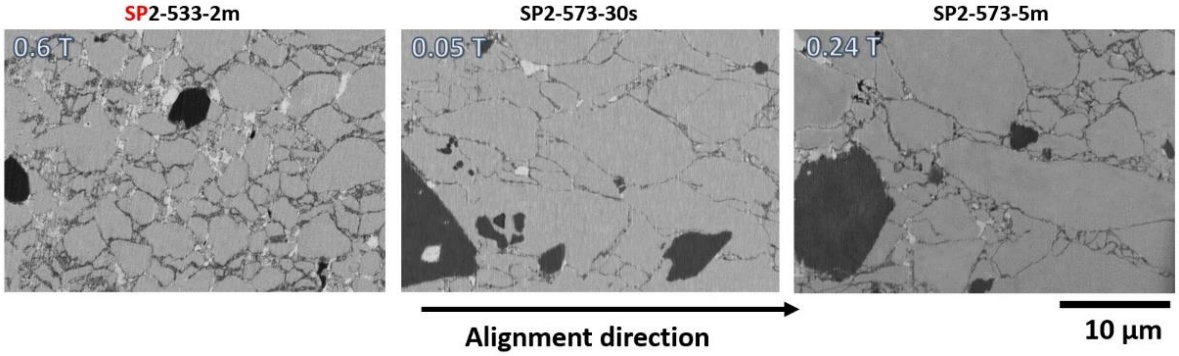

Figure 3.18 BSE images of three SPS-compacted magnets. The value on the top-left corner in each micrograph refers to the corresponding observed coercive field. The grains were particularly elongated along the alignment direction (roughly horizontal). Noted that SP2-533-2m was prepared by purifited 7h-BM $Mn_{45}Bi_{55}$ powder.

by the route #2 still have low coercivity although they show relatively high magnetization. The effect of microstructure on the observed coercive field was again investigated in detail by SEM measurements. Figure 3.18 presents the BSE images of three representative specimens. Similarly, the MnBi grains are elongated along the alignment direction as what was observed in the hot-compacted specimens (Figure 3.8). Since the particle size of the 2h-BM powder ranges from 0.5 μm to 8 μm with mean size of ~3 μm, significant grain growth also occurs for SP2-573-30s and SP2-573-5m. Conversely, the grain growth is somewhat limited for SP2-533-2m while T_s decreases from 573 to 533 K. It is noted that SP2-533-2m is an important specimen in this thesis, because it has the largest coercivity among all SPS-compacted samples. Moreover, the grain length along alignment direction apparently increases with longer dwell time. Therefore, the SEM study indicates that the majority of aligned LTP-MnBi grains undergo a shape transformation from originally spherical into prolate feature as T_s or dwell time goes up.

Additionally, the area fractions of three phases (MnBi, α-Mn, and Bi) are also analyzed and listed in Table 3.4. Combined with the observed coercive field values, the phenomenal analysis suggests that increased area fraction of Bi residue leads to higher coercive field. This tendency reconfirms the

validity of the previous assumption that Bi residue plays a role as decoupling layer between LTP grains. Based on a systematic work on SPS-compacted samples, it is suggested that the optimal fabrication condition for LTP-MnBi magnets is sintering aligned powder at 573 K for around two minutes. Unlike hot-compaction method, the Bi-rich liquid formed throughout SPS-compaction process remains in the texture because the specimens were enclosed in graphite foils. Consequently, dwell time of 2 minutes at sintering temperature can result in a sufficient extent of Bi residue in grain-boundary with limitation of unwanted grain growth. Unfortunately our SPS system had been damaged for a long time, hence some experimental plans could not be completed. More research work is for sure required to correlate the grain growth mechanism and alignment with corresponding SPS consolidation.

Table 3.4 Area fraction of the three phases in the microstructure of the SPS-compacted samples following route #2. Noted that SP2-533-2m was prepared by purified 7h-BM $Mn_{45}Bi_{55}$ powder.

Sample	MnBi [area %]	α-Mn [area %]		Bi [area %]	$\mu_0 H_c$ [T]	$\mu_0 M_s$ [T] at 7T
		Residue	Grain-boundary			
SP2-533-2m	80.6	1.5	11.4	6.5	0.6	0.62
SP2-573-30s	86.5	6.6	6.1	0.8	0.05	0.71
SP2-573-5m	87.7	6.2	2.6	3.5	0.24	0.68

3.5.5. Coercivity mechanism and thermal properties

It is well-known that the coercivity mechanism in real systems can be rather complicated, particularly hard magnets as introduced in section 2.1.6. As mentioned above, it was found that the experimental values of coercive field are strongly connected to the area fraction of Bi residue regardless of sintering methods. In order to clarify the origin of coercivity in more detail,

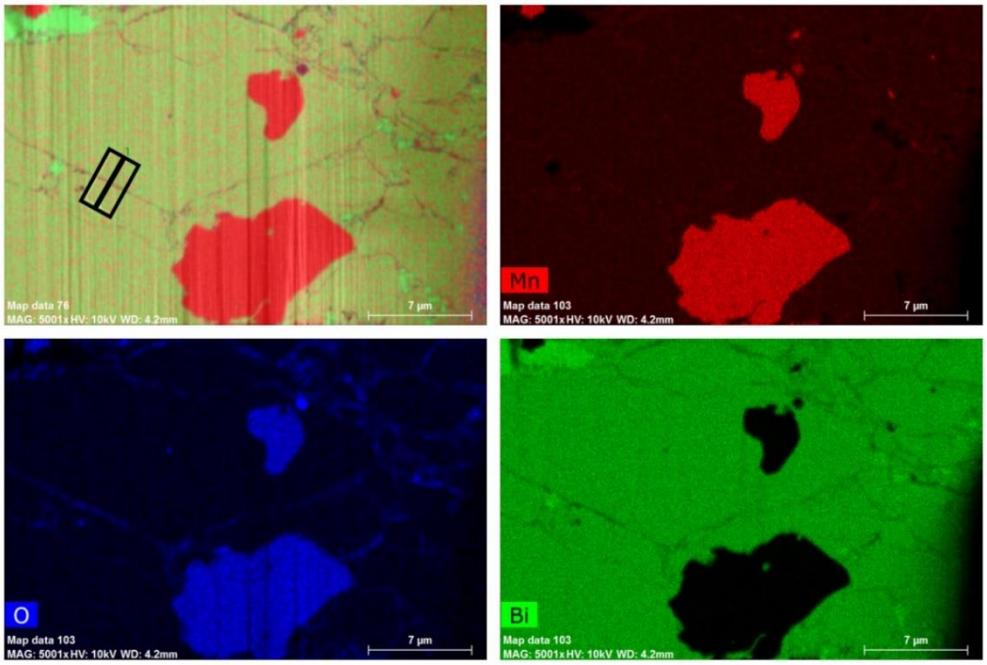

Figure 3.19 EDS mapping imaging. The result shown here was obtained from $Mn_{45}Bi_{55}$-473. As can be seen here, the LTP-MnBi grains were marked with black manually.

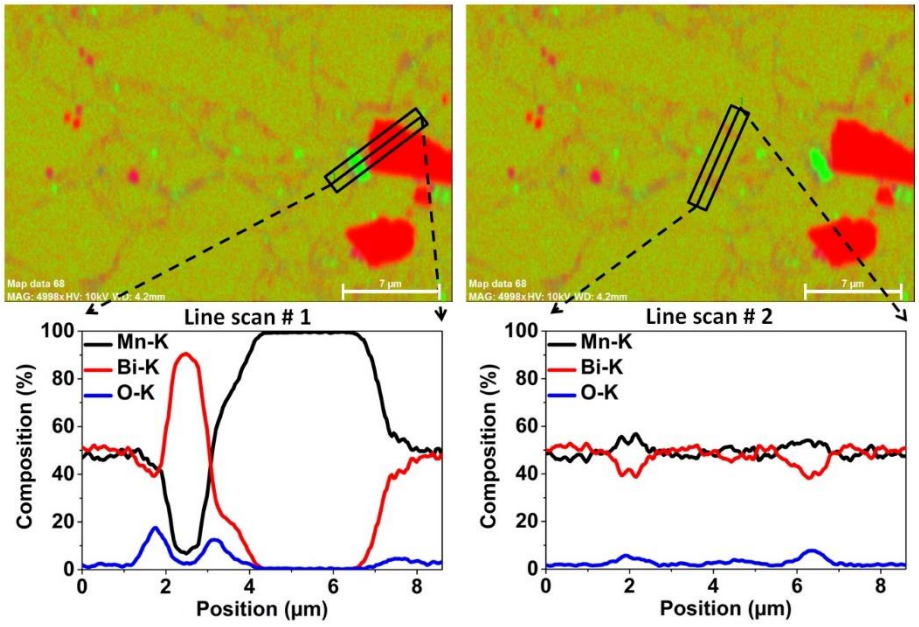

Figure 3.20 EDS line-scans used for determination of grain-boundary composition. The result shown here was obtained from $Mn_{45}Bi_{55}$-573.

the grain boundary phases of six representative samples were analyzed be-

cause all grain-boundary regions in Figure 3.8 and 3.18 clearly show a different phase contrast. The EDS mapping analysis was performed as displayed in Figure 3.19, taking $Mn_{45}Bi_{55}$-573 as an example. The black box in the composite diagram (top-left) is the selected area for single EDS line-scan analysis. The results of EDS line-scans show that the grain boundary of $Mn_{45}Bi_{55}$-573 is enriched with Mn (~53 at.%) with a tiny amount of oxygen (see Figure 3.20). Besides, the peak width of Mn K-edge profile indicates that the grain-boundary between neighboring LTP grains has a length of ~1 μm or even longer. It is worth noting that the Mn residue sometimes is embedded inside LTP-MnBi grains, while the Bi residue is generally located between them.

Table 3.5 Chemical compositions of grain-boundary phases determined by EDS analysis in unit of atomic percentage [%]. Noted that SP2-533-2m was prepared by purified 7h-BM $Mn_{45}Bi_{55}$ powder.

Sample	Mn		Bi		O		$\mu_0 H_c$
	Ave	Std	Ave	Std	Ave	Std	[T]
$Mn_{45}Bi_{55}$-473	53.30	3.62	41.31	3.45	5.38	0.56	0.31
$Mn_{45}Bi_{55}$-523	74.97	5.18	25.03	5.18			0.14
$Mn_{45}Bi_{55}$-573	53.29	0.47	40.63	2.58	6.08	2.11	0.08
SP2-533-2m	54.71	1.85	38.73	5.67	6.56	4.57	0.6
SP2-573-30s	53.69	2.22	36.31	4.08	10	3.09	0.05
SP2-573-5m	57.14	2.11	34.92	4.78	7.94	5.06	0.24

The detailed EDS results of the six representative are presented in Table 3.5, and it is obvious that all specimens have Mn-rich boundary between LTP-MnBi grains consistent with Ref. [107]. It can be concluded that the bulk samples exhibit similar grain-boundary compositions within the error limit, except $Mn_{45}Bi_{55}$-523. The extremely high Mn/Bi ratio for $Mn_{45}Bi_{55}$-523 could be because its T_s is close to the eutectic temperature (535 K). Nevertheless, no clear connection can be found between the coercive field and the grain-boundary compositions in the bulk samples.

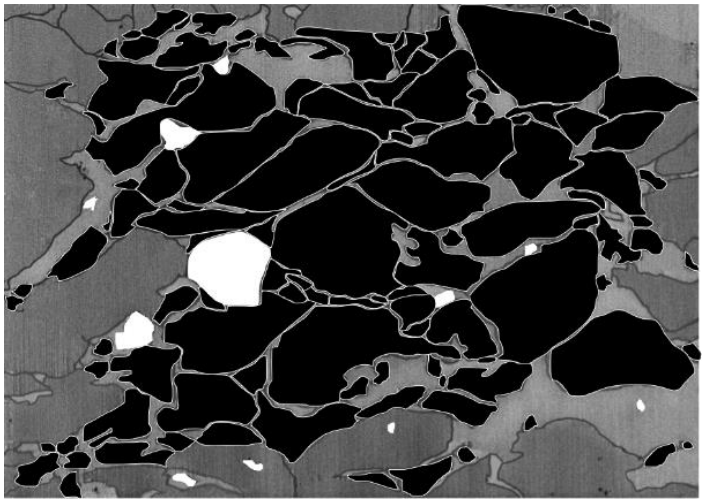

Figure 3.21 Grain size analysis by using BSE imaging. The result shown here was obtained from $Mn_{45}Bi_{55}$-473. As seen here, the LTP-MnBi grains were marked with black manually.

After examining the phase contents and grain-boundary phases, another critical factor is the dimensions of LTP-MnBi grains distributed in the bulk magnets. The mean grain size and grain size distributions were determined by large SEM images (~80 μm × 80 μm) on each specimen. Since each sample consists of four different phases, the most efficient method for this issue is to mark each single LTP-grain manually (see Figure 3.21). The evaluated results are summarized in Figure 3.22, which was assisted by our previous master student, Mr. Shreyas Muralidhar.[112] The histogram in each micrograph presents that the LTP-MnBi grains of the four representative samples all have a log-normal distribution. Taking a careful look at each size distribution, we suggest that both mean size value and its standard deviation increase with increased sintering temperature or longer dwell time. From SP2-533-30s and $Mn_{45}Bi_{55}$-473, the structure analysis shows that these two bulk samples have a similar particle size distribution (mean diameter value of ~3 μm) and coercive field regardless of sintering methods. The relatively larger $\mu_0 H_c$ for $Mn_{45}Bi_{55}$-473 could come from better magnetic decoupling, namely larger area fraction of Bi residue. SP2-533-2m has the smallest mean particle size (~2 μm) among these four samples, while $Mn_{45}Bi_{55}$-573 shows the largest value of 4 μm. Combined with the measured coercive field (on the top-left corner of each SEM image), there is a

reverse correlation between the mean grain diameter and coercivity for the bulk samples (see Figure 3.22). This tendency is in good consistent with the D^{-1} slope coefficient, where D refers to mean grain diameter, reported in Figure 2.23. In addition to the influence of grain size, the presence of a decoupling layer between the grains further increases the observed coercivity. Based on a comprehensive analysis on the microstructure of bulk magnets, it was found that the observed variation in coercivity has a close relation with corresponding mean grain diameter, along alignment direction, and the area fraction of Bi. In contrast, grain-boundary phases may not play a role on this issue in our studied systems.

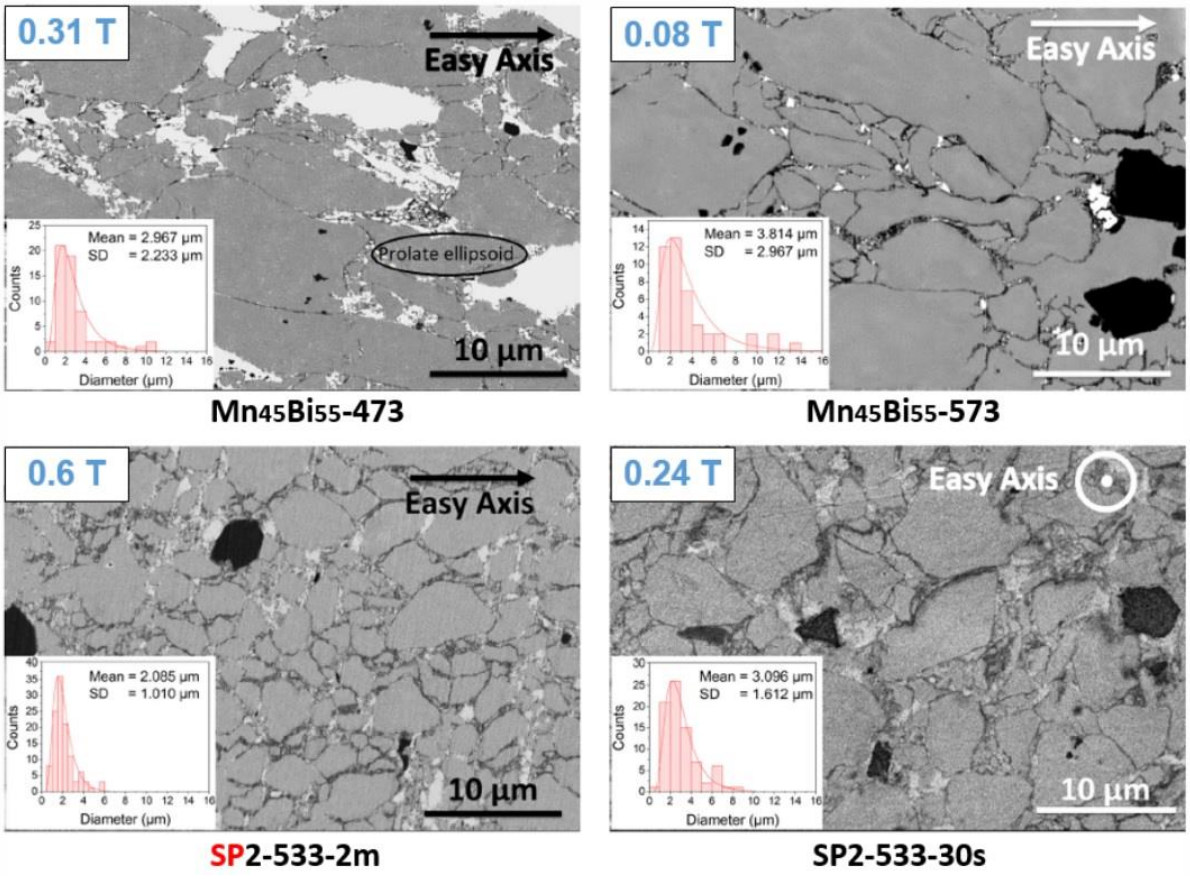

Figure 3.22 Grain size distribution of four representative samples: two from hot-compacted and two from SPS-compacted samples. (reproduced from [112]) The value on the top-left corner in each micrograph of the bulk samples refers to the observed coercive field ($\mu_0 Hc$).

Table 3.6 Experimental values of K(T) and M_s(T) as a function of temperature determined by SPD measurements on a polycrystalline magnet.

Temperature [K]	K [MJ/m^3]	M_s [kA/m]
200	0.91	695
250	1.40	670
300	1.80	645
350	2.10	615
400	2.25	585
450	2.30	550
500	2.18	510
550	2.00	460
600	1.76	410

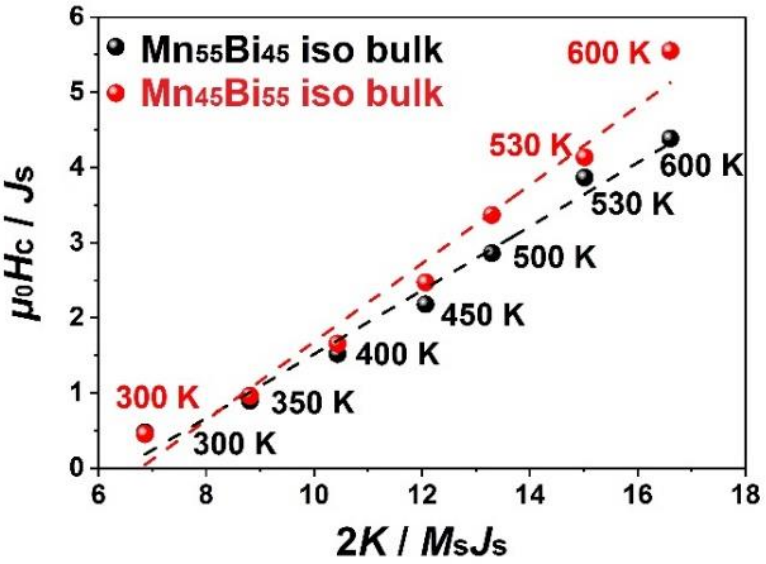

Figure 3.23 Analysis of the temperature-dependent $\mu_0 H_c$ of the isotropic SPS-compacted magnets in terms of nucleation field model.

Apart from the room-temperature coercivity behavior, the most attractive characteristic of LTP-MnBi is the unusual temperature-dependent coercivity mechanism within high temperature range (300~600 K). As mentioned in section 2.1.6, this phenomena could be quantitatively investigated by Eq.

2.21 in terms of Kronmüller's nucleation field model.[20] Nucleation model consists of two important microstructural parameters: α describes the influence of the non-perfect surface of the grains on the crystal anisotropy,

Table 3.7 Fitted values of α and N_{eff} for iso- and anisotropic bulk samples in comparison with previous work. Noted that the isotropic SPS-compacted and anisotropic samples were prepared using purified 7h-BM and 2h-BM powder, respectively.

Group	Sample	anisotropy	α	N_{eff}	$Mn_{residue}$ [area %]	Bi [area %]	$\mu_0 H_c$ [T]
Iso-SPS	SPS $Mn_{55}Bi_{45}$	iso	0.42	2.73		High	0.39
	SPS $Mn_{45}Bi_{55}$	iso	0.52	3.54		High	0.37
Aniso-SPS	SP2-573-30s	aniso	0.16	1.18	6.6	0.8	0.05
	SP2-573-5m	aniso	0.34	1.97	6.2	3.5	0.24
Aniso-HC	$Mn_{45}Bi_{55}$-473	aniso	0.34	1.83	2.6	17.0	0.31
	$Mn_{45}Bi_{55}$-523	aniso	0.29	1.92	3.3	5.4	0.14
	$Mn_{45}Bi_{55}$-573	aniso	0.23	1.58	1.9	0.9	0.08
Ref	Rao et al	aniso	0.25	1.62			
	Yang et al	aniso	0.30	0.75			

and effective demagnetization factor (N_{eff}) is due to enhanced stray field at the edges and corners of the grains.[30, 104, 113] To do so, the values of the required parameters, including effective K(T) and M_s(T), were quoted from in Ref. [114] and listed in Table 3.6. The values of α and N_{eff} were then estimated by plotting dimensionless quantities $-\mu_0 H_c/J_s$ vs $2K/M_s J_s$ as a function of the measuring temperature. As shown in Figure 3.23, for example, the fitting can give a linear-like relation between $\mu_0 H_c/J_s$ and $2K/M_s J_s$ for isotropic SPS bulk samples. This linear slope implies that the micromagnetism of isotropic SPS bulk samples follows the nucleation field model. The same analysis work was performed on anistropic MnBi samples as presented in Table 3.7. The evaluated values from our bulk samples cover a

broad range of microstructural evolution in comparison with the reported ones in Rao et al.'s [102] and Kronmüller et al.'s work [104]. Firstly, the isotropic SPS-compacted ones show quite large α and N_{eff}, which could refer to better exchange decoupling and irregular grain texture, respectively. As seen in the EDS mapping (Figure 3.12), the large α should be associated with high level of Bi residue because the starting material, purified 7h-BM powders, contain large volume fraction of Bi.[107, 113] Major origins of N_{eff} are usually ascribed to grain size, grain shape and the existence of non-ferromagnetic phases since these factors have a great impact on effective stray field.[30, 115] Also, the SEM images indicate that large N_{eff} values here could originate from the smaller and more irregular grains in comparison with anisotropic cases. It is noted that the huge microstructural parameters, for isotropic samples, could also originate from the unusual high-temperature stability, because only they present increased coercivity up to 600 K.

For anisotropic samples, SPS- and hot-compacted magnets must be discussed separately, as the starting material and sintering methods are different for anisotropic samples. However, it is obvious that α values of anisotropic specimens are enhanced systematically with increased area fraction of Bi and coercive fields. This tendency is understood because α is proportional to the extent of exchange decoupling, provided that the degree of grain alignment of the samples in each group has less deviation.[104, 113] For anisotropic SPS specimens, it is found that the change of N_{eff} values is accompanied by α parameter. This feature is strongly connected with the collective behavior of the exchange coupled grains.[113] In light of the SEM images, the larger N_{eff} for SP2-573-5m is most likely due to the irregular grain shape and higher level of Bi residue caused by longer SPS dwell time. For anisotropic hot-compacted samples, the variation observed in N_{eff} could be explained by the difference in area fraction of Mn residue, which is expected to generate stray field locally.[20, 115] Moreover, the reduced N_{eff} can be strongly caused by the obvious elongation in grain shape for $Mn_{45}Bi_{55}$-573, as suggested by the research on hot-compacted NdFeB magnets in Ref. [115]. Finally, it is emphasized that the pinning mechanism may be important for the samples with $\alpha <$

0.3, which is connected to surface imperfection. This suggests that the deteriorated grain-boundary region, which has less Bi residue, give rise to locally reduced anisotropy constant.[104] Because there is a certain amount of large grains inside all bulk samples, it is clear that the displacement of the boundary wall between multi-domains should be expressed by nucleation mechanism instead of Stoner-Wohlfarth model. In summary, a comprehensive analysis unambiguously demonstrates that the change of coercivty observed in our MnBi systems is closely connected to the intrinsic magnetic properties and corresponding microstructure.

The related investigation was afterwards further extended by Muralidhar et al. using first order reversal curve (FORC) measurement. In light of his temperature-dependent FORC analysis, the coercive field distribution of LTP-MnBi was clarified microscopically at various temperatures. In Ref. [112], Muralidhar et al. purposed a potential explanation on the experimentally observed temperature-dependent variation in coercive field distribution, using a modified nucleation model for ellipsoidal particles (see Figure 3.24). Noted that the log-normal distribution of the particle diameter (gray area) is roughly estimated assuming that the geometric shape

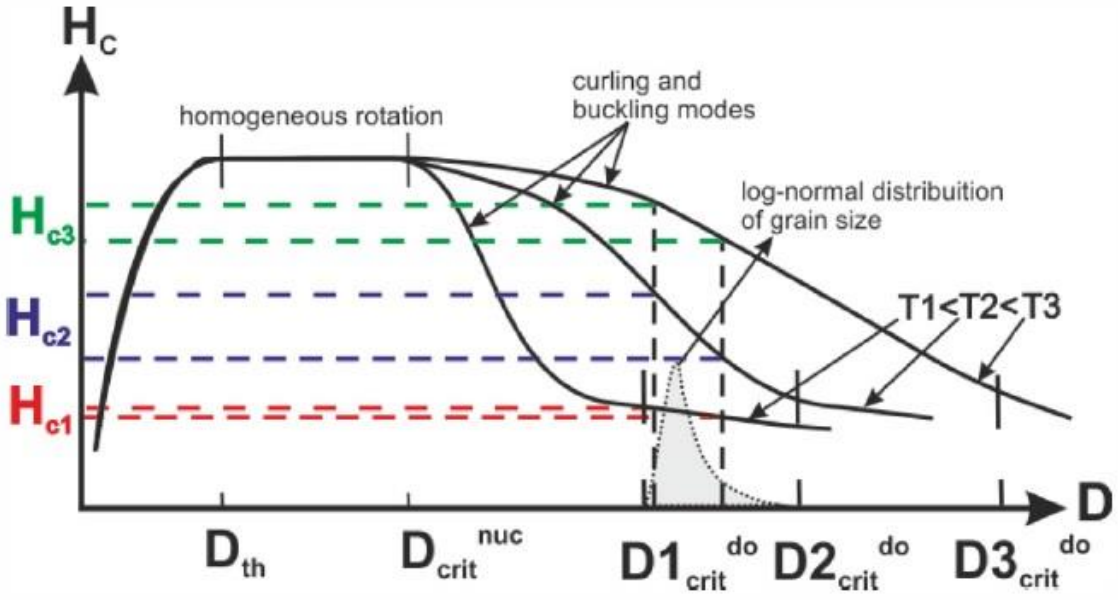

Figure 3.24 Schematic representation of the variation of the nucleation field dependence on the particle diameter with increasing temperature for LTP-MnBi. [112]

of the majority of grains is prolate ellipsoid with an easy axis along the major axis.

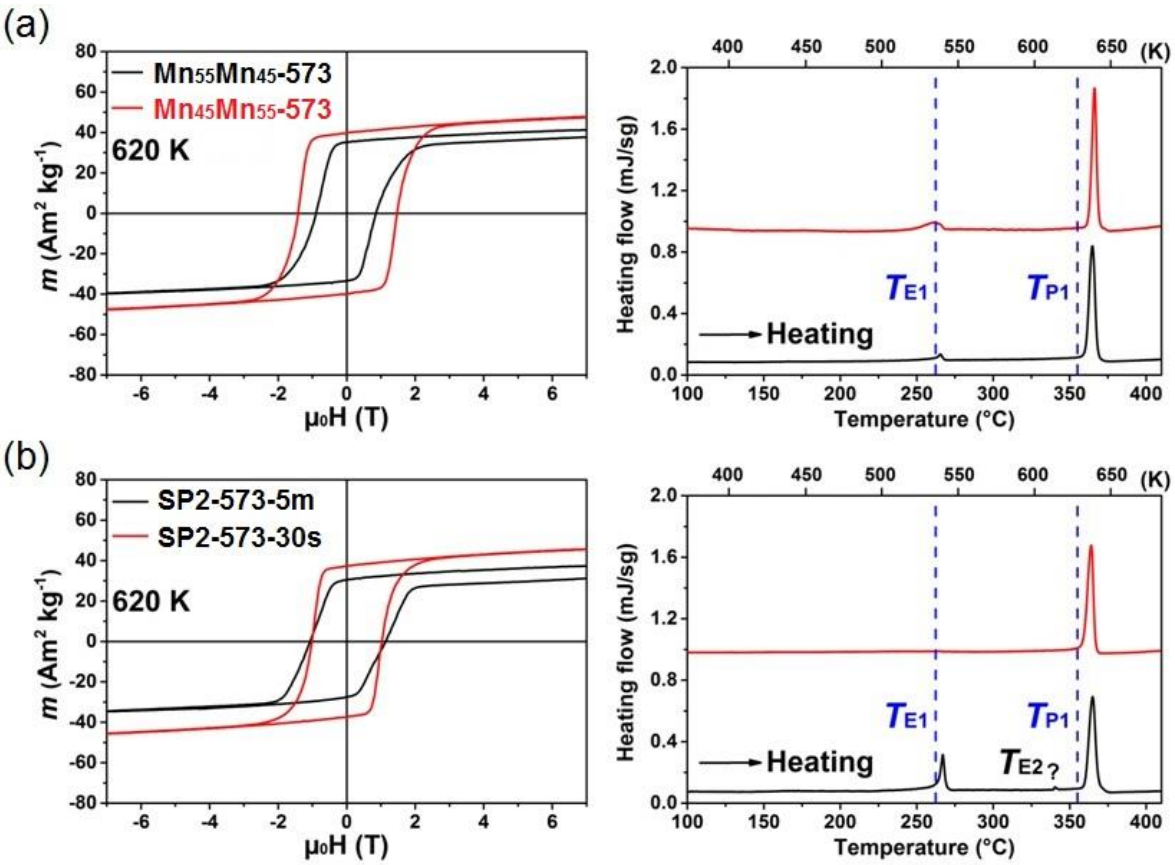

Figure 3.25 *M*(*H*) curves measured at 620 K and DSC results for (a) $Mn_{55}Bi_{45}$/ $Mn_{45}Bi_{55}$-573 and (b) SP2-573-5m/30s magnets.

After identifying the possible origins of the coercivity mechanism in LTP-MnBi magnets, the last critical issue is thermal stability of our bulk samples because LTP-MnBi compound is considered as a promising material for high-temperature applications. To study the effect of high-temperature exposure on the magnetic properties, the *M*(*H*) curves of bulk samples were repeatedly measured in the temperature range of 550~650 K. It was found that, for the anisotropic hot-compacted samples, the hard magnetic phase of $Mn_{45}Bi_{55}$ specimens mostly persists up to 620 K, but not for the $Mn_{55}Bi_{45}$ ones. Figure 3.25(a) shows the difference in 620 K hysteresis loops between $Mn_{55}Bi_{45}$-573 and $Mn_{45}Bi_{55}$-573 as examples for the hot-compacted magnets consolidated with two atomic ratios. This observation can be

firstly well explained by the MnBi LTP→HTP phase transitions reported in the phase diagram (see Fig. 2.26). For Bi-rich MnBi-alloys, the LTP→HTP transition occurs at the peritectic temperature T_{P1} = 628 K, whereas for Mn-rich MnBi-alloys, the LTP→HTP transition already occurs at eutectoid temperature T_{E2} = 613 K. The thermal stability was further investigated by DSC analysis (see right panel of 3.25(a)), and detailed results are listed in Table 3.8. The corresponding DSC analysis shows that the integrated area of the endothermic peak near T_{E1} is larger in $Mn_{45}Bi_{55}$-573, which implies that more Bi actually exists in the texture as supported by our SEM study. Furthermore, $Mn_{45}Bi_{55}$-573 also shows larger integrated area at the second endothermic peak near T_{P1}, which confirms the existence of higher fraction of LTP-MnBi (namely higher M_s).

Table 3.8 Detailed information provided by DSC analysis. Note that these data were collected in absence of magnetic field. The reference values are quoted from [24, 26, 30, 109].

Sintering method	Sample	T_{E1} Peak Area [J/g]	T_{E2} Peak	T_{p1} Peak onset [K]	T_{P1} Peak Area [J/g]
HC	$Mn_{45}Bi_{55}$-573	2.5	No	635.8	11.1
	$Mn_{55}Bi_{45}$-573	1.2	No	633.8	10.6
SPS	SP2-573-30s	0.03	No	633.1	10.1
	SP2-573-5m	4.02	Yes	632.1	11.1
Ref	Cui et al	≤ 4.3	Yes	≤ 615	≤ 3.4
	Yang et al		Yes	633	
	Oikawa et al			632	4.08
	Toshiyuki et al			628	

For the SPS case, we observed that it is possible to enhance thermal stability by reducing dwell time (see Figure 3.25(b)). Although both samples

were consolidated using purified 2h-BM $Mn_{55}Bi_{45}$ powder, SP2-573-30s also shows typical hysteresis loop at 620 K like $Mn_{45}Bi_{55}$-573.

This interesting result implies that less LTP decomposition could be helpful for thermal stability because dwell time of SP2-573-30s is extremely short. Therefore, only one sharp peak near T_{P1} can be easily observed in its DSC measurement. The DSC curve of SP2-573-30s indicates that the phase transition process basically follows the vertical line at Mn mole fraction of 0.5 in the phase diagram. Conversely, long-time sintering caused significant decomposition as well as locally inhomogeneous microstructure (partially Bi- or Mn-rich area). It turns out that there is one additional small peak near T_{E2} in the DSC curve of SP2-573-5m, which is the eutectoid temperature of HTP MnBi into LTP MnBi and α−Mn. Besides, the higher onset of T_{P1} peak and T_{P1} peak area provide another evidence that our bulk samples actually have higher thermal stability and volume content of LTP-MnBi with respect to the reported values in Refs. [24, 26, 30, 109]. The relative difference in T_{P1} peak area is consistent with corresponding saturation magnetization data. It is noted that all DSC measurements were completed in the absence of magnetic field, so the phase transition temperature could be slightly lower than that of SQUID measurement. Due to this reason, it is not possible to confirm the unique thermal stability of the isotropic SPS-compacted samples using our DSC machine.

Furthermore, the effect of thermal cycles on magnetic properties was examined by repeated RT-SQUID measurements after in-situ heating bulk samples up to 500 K and cooling back to 300 K. The RT-$M(H)$ curves imply that no clear change in magnetic properties for all bulk samples However, they exhibit lower magnetization and slightly larger coercivity once heating temperature increases to 530 K. This means that the decomposition of LTP MnBi through eutectic reaction (at 535 K) cannot be completely recovered.

According to the SEM and SQUID measurements, it is relevant to claim that we achieved highly anisotropic MnBi bulk samples having multi-domain configuration. Nevertheless, it is better to directly see the real domain

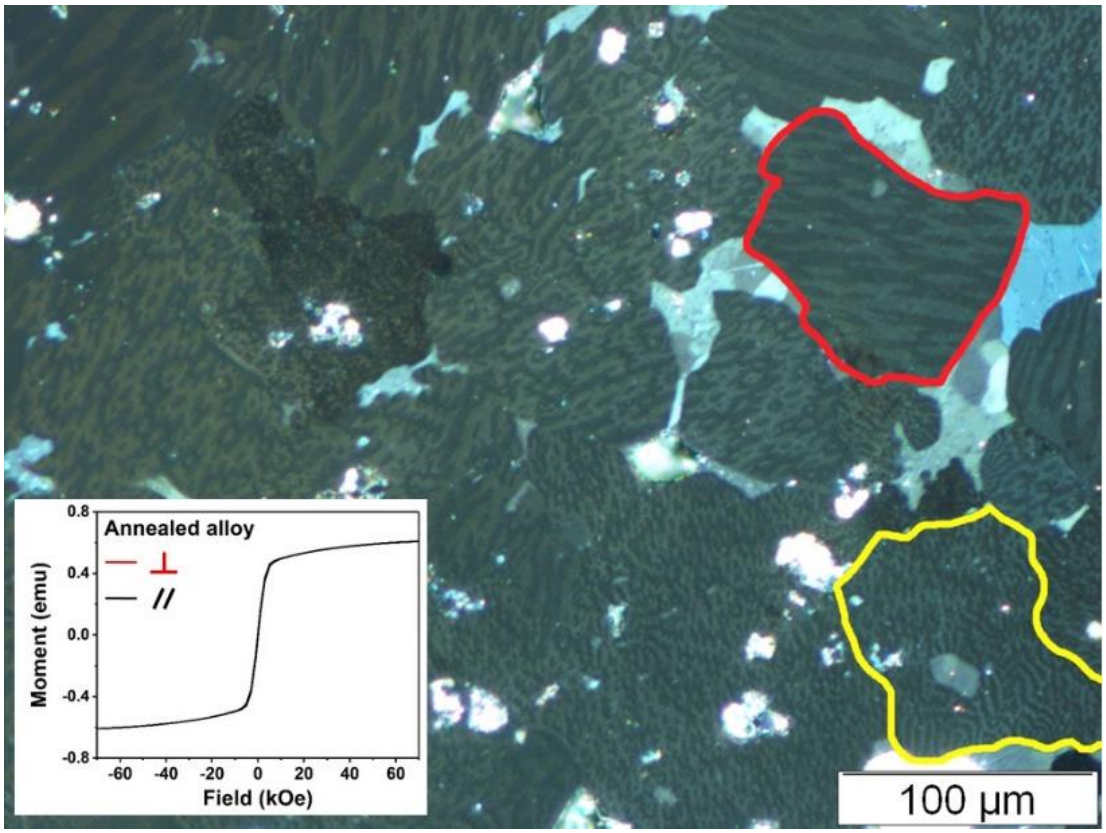

Figure 3.26 Kerr image of annealed $Mn_{55}Bi_{45}$ alloys at 300 K.

structure in order to confirm our assumption used in the above discussion. The observation of magnetic domain is usually acquired by conventional Kerr microscopy with an analyzer polarizing filter. Because LTP-MnBi is easily oxidized and mechanically soft, flat surface compulsory for Kerr imaging was gently polished with ethanol as a lubricant. Figure 3.26 shows the clear magnetic domains taken from an annealed $Mn_{55}Bi_{45}$ alloys. As can be seen, a great number of large LTP-MnBi grains are formed after post-annealing. Since single domain size of LTP-MnBi is ≤ 0.5 μm, all large grains nearly exhibit multi-domain configuration. In addition, it is noted that some of grains show so-called bitter pattern (ex: the red-circled area), which refers to the grains with c-axis roughly parallel to sample surface. Otherwise, orange-circled area exhibit spiral-shaped domain pattern, meaning that the grains have out-of-plane easy axis.[116] Due to the broad distribution of crystal orientations observed here, the magnetic response

of the annealed alloys is isotropic as supported by correspond hysteresis loops.

For practical applications, the grains inside the permanent magnets should be aligned as much as possible. In Figure 3.27, only bitter pattern could be observed from two hot- and SPS-compacted samples within resolution limit, regardless of the grain size. This suggests that most of the grains are actually oriented along in-plane direction, namely the direction of magnetic alignment. The light regions that do not display any domain structure are nonmagnetic phases (ie. Mn or Bi residue), while the invisible domain structures in some grains should be derived from non-flat surfaces. Theses Kerr images clearly confirms that the bulk samples in this work are highly anisotropic. Moreover, it seems that the magnetic domains are continuous at the grain boundary. Unfortunately, field-dependent measurement has not been performed yet to monitor the domain wall movement.

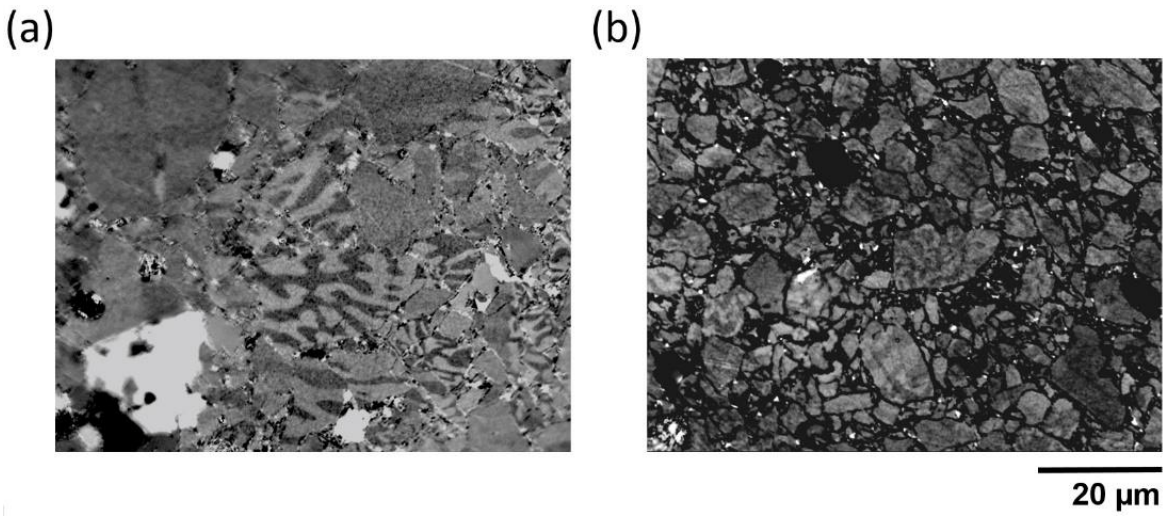

Figure 3.27 Kerr images measured roughly perpendicular to alignment direction at room temperature from (a) $Mn_{45}Bi_{55}$-573 and (b) SP2-533-2m.

3.5.6. XMCD investigation on Mn $L_{2,3}$ edges (at RT)

In the preceding subchapter, the considerable deviation of experimental coercivity ($\mu_0 H_c$) from corresponding anisotropy field ($2K_1/\mu_0 M_s$) was explained in terms of microstructural constituents. In order to study the the

unique coercivity mechanism (or MAE_K) of LTP-MnBi at atomic scale, $Mn_{45}Bi_{55}$-573 was intensively investigated using XMCD technique as it contains the highest level of LTP content for sintered magnets reported so far. At first, the angular XAS measurements were performed at Mn $L_{2,3}$ edges along four difference angles: 0°(easy-axis), 20°, 50° and 90°(hard-axis). In order to avoid self-absorption issue, two specimens were fixed exactly along either easy- or hard-axis on the sample holders. Therefore, the spectra obtained along easy- and hard-axes were recorded at normal incidence. The 20° and 50° measurements were performed by rotating the sample with respect to the easy-axis.

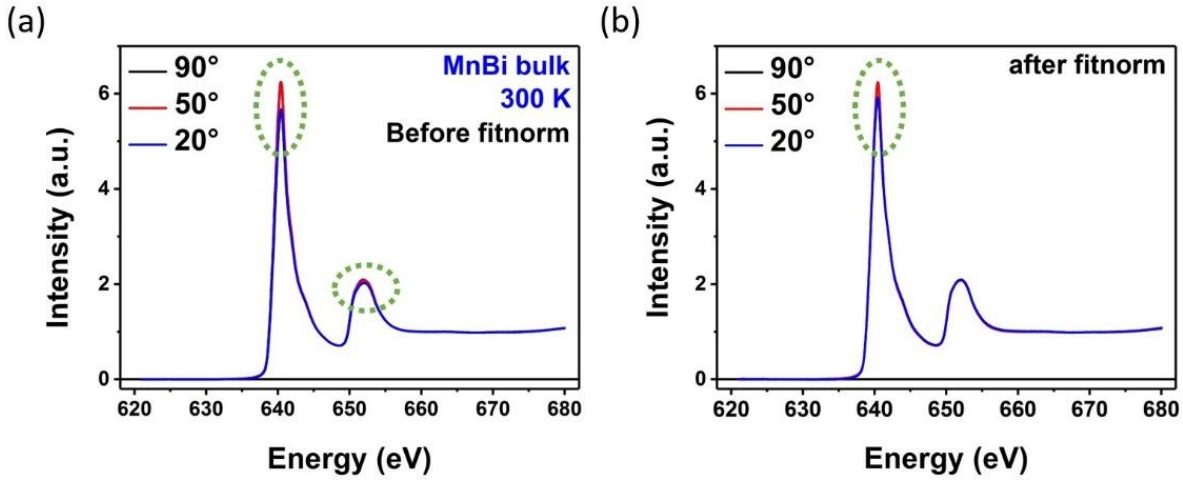

Figure 3.28 Angle-dependent normalized μ_0 curves of $Mn_{45}Bi_{55}$-573 magnet at Mn $L_{2,3}$ edges: (a) before and (b) after fit-normalization at 300 K.

The left side of Figure 3.28(a) shows the raw data of RT-normalized XAS (μ_0) spectra on Mn $L_{2,3}$ edges measured at various angles, in which the peak intensity has a significant difference between 20° spectrum and others. The angular XAS spectra should in principle have the same intensities in the non-resonant region, hence the data were treated further by profile fitting normalization to adjust background signal to the same level. The corrected XAS spectra were plotted in the right side in 3.28(a), and it is clear that they have nearly the same peak height at L_2 edge although little gap in peak intensities at L_3 edge is still present. The same background correction was

also applied to all μ_+ and μ_- spectra; for example, the spectra acquired along easy- and hard-axis in Figure 3.29.

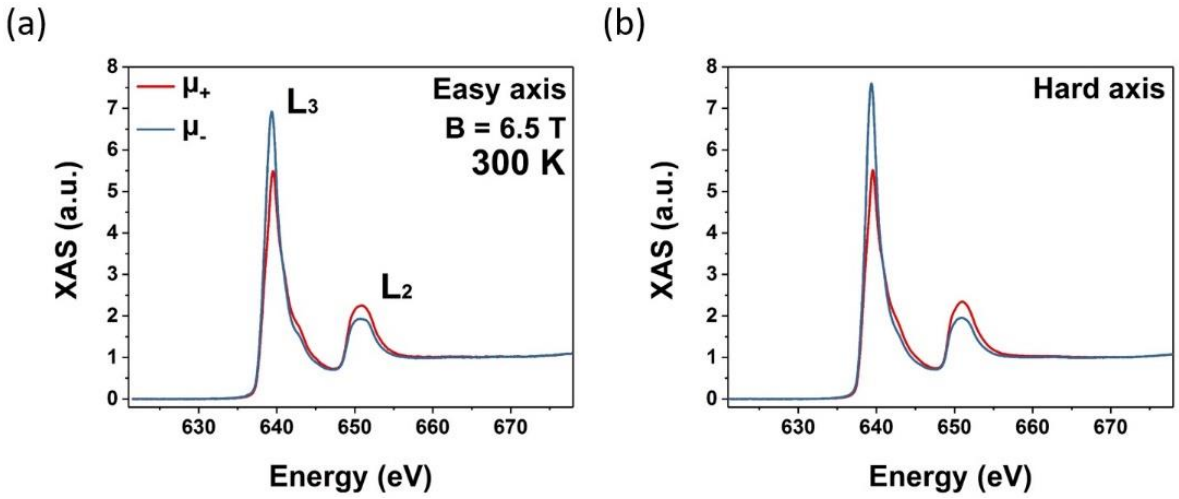

Figure 3.29 Corrected normalized μ_+ and μ_- curves of $Mn_{45}Bi_{55}$-573 magnet at Mn $L_{2,3}$ edges: (a) easy and (b) hard-axes at 300 K.

Table 3.9 Angular $m_{\text{eff-spin}}$ and m_{orb} at Mn 3d shell in LTP-MnBi at 300 K.

Sample	angle	m_{orb} [μ_B]	$m_{\text{eff-spin}}$ [μ_B]	m_{total} [μ_B]	$\frac{m_{\text{orb}}}{m_{\text{eff-spin}}}$
$Mn_{45}Bi_{55}$	0° (easy)	0.0492	1.3006	1.3499	0.0378
	20°	0.0484	1.6531	1.7015	0.0293
	50°	0.0726	1.6538	1.7264	0.0439
	90° (hard)	0.0768	1.5634	1.6402	0.0491

After background correction, a systematic variation was observed in the angular XMCD spectra. Figure 3.30 indicates that the XMCD signals of LTP-MnBi increase seemingly from easy- to hard-axis. Therefore, it is worthy to note that background correction, including offset adjustment, is crucial for normalizing μ_+ and μ_- spectra prior to XMCD analysis. The angle-dependent magnetic moments at 300 K were evaluated by XMCD sum rules according to as Eq. 2.26 and 2.27. Noted that the value of 4.5, for N_h at Mn

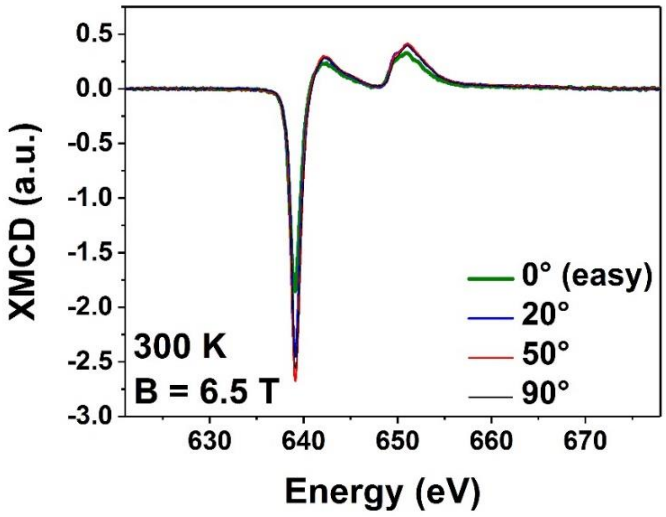

Figure 3.30 Angle-dependent Mn $L_{2,3}$ XMCD curves of $Mn_{45}Bi_{55}$-573 magnet at 300 K.

3d shell, was quoted from Ref. [117] in order to complete evaluation. The raw data in Table 3.9 suggests that both orbital (m_{orb}) and spin ($m_{\mathrm{eff-spin}}$) moments are enhanced from easy- to hard-axis within certain experimental uncertainty. Because the spin moment (m_{spin}) is expected to be larger along easy-axis, it implies that we must take the magnetic dipole term, T_z, into account for LTP-MnBi compound as mentioned in Ref. [58, 59, 118]. It is noted that LTP-MnBi has a hexagonal crystal structure, so that the contribution of T_z term (m_T) can not be neglected as the case of cubic systems.[56, 119] The assumption, $m_T^{Easy} + 2m_T^{Hard-plane} = 0$, given in Refs. [118-120] was utilized to deal with this issue for 3d metals in uniaxial systems, provided that no in-plane anisotropies is present in the basal plane of the crystal. Moreover, it was reported that the spin-orbit constant (~0.041 eV) is much smaller than the exchange interaction (~3.5 eV) for Mn 3d states.[14, 111] Therefore, it is valid that a nearly isotropic spin moment $\langle m_{\mathrm{spin}}^{\mathrm{x,y,z}} \rangle = m_{\mathrm{spin}}$ can be extracted when the sample is magnetically saturated along all Cartesian axes by a strong magnetic fields.[118] Following these requirements, the contribution of T_z term was calculated by the relation, $m_{\mathrm{spin}} = (m_{\mathrm{spin}}^{0^\circ} + 2 \times m_{\mathrm{spin}}^{90^\circ})/3$, and listed in Table 3.10.

Table 3.10. The magnetic moments at Mn 3d shell in LTP-MnBi at 300 K derived first from sum rules and then scaled by the corresponding SQUID data. The m_{spin} term is defined as $m_{spin} = (m_{spin}^{0^\circ} + 2 \times m_{spin}^{90^\circ})/3$, and $7m_T^{x,y\ or\ z} = m_{eff-spin} - m_{spin}$.

Direction	m_{orb}	$m_T^{x,y\ or\ z}$	m_{spin}	m_{total}^{XMCD}	m_{total}^{SQUID}	m_{orb}^{c}	m_{spin}^{c}
	[μ_B]	[μ_B]	[μ_B]	[μ_B]	[μ_B]	[μ_B]	[μ_B]
Easy (0°)	0.0492	−0.025	1.4758	1.525	3.35	0.11	3.24
Hard (90°)	0.0768	0.0125	1.4758	1.553	3.30	0.16	3.14

After considering the T_z term contribution of Mn 3d states, the values of angular total magnetic moments (m_{total}^{XMCD}) are still far smaller than corresponding SQUID values (m_{total}^{SQUID}). To clarify the origin of this discrepancy, the Mn $L_{2,3}$ XAS spectra was preliminarily fitted by a data analysis technique called moment analysis, which could be performed by a summation of Gaussian lines as reported in Ref. [121]. Although the presence of little overlap between Mn L_3 and L_2 edges is found due to small orbital moments, the possible spin correction factor (maximum ~50%, caused by all mixng and hybridization effects in Ref. [122-124]) still can not account for the low XMCD sum rules values. At this point, it is important to recall that the width of grain-boundary region is ~1 μm at least as shown in the SEM measurements (see Figure 3.20). This fact means that the surface-sensitive TEY signals should be dominated or partially originated by the covered Mn-related nonferromagnetic layers rather than LTP-MnBi grains. Therefore, the true sum rule values must be further scaled by the angle-dependent SQUID data to compensate the loss of ferromagnetic signal. As shown in Table 3.10, the final values of spin moments are 3.24 and 3.14 μ_B along easy- and hard-axis, respectively. For the orbital moments, the values along easy- and hard-axes are 0.11 and 0.16 μ_B at 300 K. Since it was reported that orbital sum rule can provide more precise result,[125, 126] the experimental value of orbital moment obtained along easy-axis (0.11 μ_B) in this work is in good agreement with the theoretical prediction of 0.125 μ_B in Ref. [111].

Besides, the difference in orbital moments along easy- and hard-axis is 0.05 μ_B also consistent with the theoretical value of ~0.06 μ_B in Ref. [111]. Although this result is larger than another theoretical value of 0.02 μ_B in Ref. [28], the tendency still remains and suggests that the orbital moment should be larger along hard-axis at 300 K.

In common magnetic compound, the orbital moment is larger along easy-axis as mentioned in Bruno's model, which gives a particularly simple and beautiful picture for the origin of the MCA based on the anisotropy of the orbital moment.[17, 127] However, Bruno's model is only valid for the magnetic systems with a filled majority spin band. To explain the opposite tendency here, the orbital anisotropy and MCA should be discussed using van der Laan's extended model, which includes the case of minority as well as majority spin contributions.[128] In the framework of the van der Laan's model, the MCA energy is related to spin-subband orbital moment and to the magnetic dipole operator using second-order perturbation treatment takes as following:

$$\delta E \approx -\frac{1}{4}\xi\widehat{\boldsymbol{S}}\cdot\left[\langle\boldsymbol{L}^{\downarrow}\rangle-\langle\boldsymbol{L}^{\uparrow}\rangle\right]+\frac{\xi^2}{\Delta E_{\mathrm{ex}}}\left[\frac{21}{2}\widehat{\boldsymbol{S}}\cdot\langle\boldsymbol{T}\rangle+2\langle(L_\zeta S_\zeta)^{\mathbf{2}}\rangle\right] \tag{3.1}$$

, where ξ is the radial part of spin-orbital coupling constant, $\boldsymbol{L}^{\downarrow(\uparrow)}$ is the orbital moment vector of the spin down (up) band, and ΔE_{ex} is exchange interaction. To simplify the whole picture, the squared diagonal spin–orbit interaction $\langle(L_\zeta S_\zeta)^{\mathbf{2}}\rangle$ could be ignored because the spin–orbit-induced part of the spin anisotropy is small in 3d transition metals.[128] According to Eq. 3.1, the MAE_K between two principle axes (α, α') can be formulated as

$$\Delta E \approx -\frac{1}{4}\xi\widehat{\boldsymbol{S}}\cdot\left(\langle L\rangle_{\alpha'}-\langle L\rangle_{\alpha}\right)+\frac{\xi^2}{\Delta E_{\mathrm{ex}}}\left[\frac{21}{2}\widehat{\boldsymbol{S}}\cdot\left(\langle T\rangle_{\alpha'}-\langle T\rangle_{\alpha}\right)\right] \tag{3.2}$$

, in which $\langle L\rangle_\alpha=\langle\boldsymbol{L}^{\downarrow}\rangle_\alpha-\langle\boldsymbol{L}^{\uparrow}\rangle_\alpha$ and the magnetization direction $\widehat{\boldsymbol{S}}$ is set to 1 if the specimens are measured in a saturation state. Because the majority

spin band of Mn in LTP-MnBi could be full-filled, the MAE_K induced by Mn 3d shell is evaluated by assuming that the orbital magnetic anisotropy, $\Delta L = L^{\downarrow}_{0^\circ} - L^{\downarrow}_{90^\circ}$ with DFT calculated ΔE_{ex} of 3.5 eV and ξ of 0.041 given in Ref. [111]. All data are listed in Table 3.11, and it is obvious that our MAE_K^{exp} value has not only wrong magnitude but also opposite sign compared to the theoretical value in Refs. [111] and [129]. The dramatic difference between MAE_K^{exp} and MAE_K^{Cal} implies that the previous assumption, Mn has a full-filled majority spin band, is wrong so that the orbital magnetic anisotropy could originate from both majority and minority bands. To check the role of majority band in MAE_K, the MAE_K^{exp} value was recalculated by assuming that the orbital magnetic anisotropy is merely due to the existence of electron holes in Mn 3d majority band, namely $\Delta L = L^{\uparrow}_{0^\circ} - L^{\uparrow}_{90^\circ}$ From the MAE_K^{exp} evaluated from either pure majority or minority band, it was found that the MAE_K^{Cal} value lies between those two extreme values. Therefore, we suggest that the smaller Mn 3d orbital moment along easy-axis should be caused mainly by the holes in the majority band. It was reported that Mn 3d states are strongly hybridized with Bi 6p ones between -4 to 3 eV with respective Fermi level.[111, 117, 129] It is not surprised that there is charge transfer from Mn 3d to Bi 6p, so some electron holes remain leading to nearly-full filled majority band. In Ref. [117], the authors claimed that the electron numbers at Mn 3d majority band are 4.505 consistent with our assumption of nearly-full filled states (see Table 3.12). However, the authors in Ref. [129] proposed that Mn 3d majority band is fully filled to reach high spin moments at Mn site. The filling of Mn 3d states in LTP-MnBi is left as an open question, but we believe that our XMCD results provide a strong evidence for the assumption of nearly-full filled Mn majority band.

Table 3.11 Understanding of magnetic anisotropy energy of LTP-MnBi at atomic scale. Noted that $\widehat{\boldsymbol{S}}$ is set to 1 due to the saturated condition.

Source	ξ [meV]	ΔE_{ex} [eV]	$\widehat{\boldsymbol{S}}$	ΔL	ΔT_Z	MAE_K^{exp} [meV/atom]	MAE_K^{Cal} [meV/atom]
Pure $S^{\downarrow}$	41	3.5	1	−0.05	−0.0823	−0.097	0.6
Pure $S^{\uparrow}$	41	3.5	1	0.01	−0.0823	0.517	0.6

Table 3.12 Numbers of s, p, d and f electrons per LTP-MnBi unit cell obtained by fully relativistic calculation in Ref. [117]. There are two formula units MnBi per unit cell.

Element		Number of electrons		Under $\vec{B}$
		↑	↓	
Mn	4s	0.63	0.52	↑
	4p	0.69	0.63	↑
	3d	9.01	1.96	↑
	4f	0.06	0.06	-
Bi	6s	1.83	1.80	↑
	6p	2.76	3.20	↓
	6d	0.37	0.25	↑

3.5.7. XMCD investigation on Bi $M_{4,5}$ edges (at RT)

Besides Mn 3d shell, some theoretical reports claimed that the original of MAE_K is also strongly connected to the electron configuration of Bi element.[111, 129] Using available x-ray energy range in WERA and BOREAS

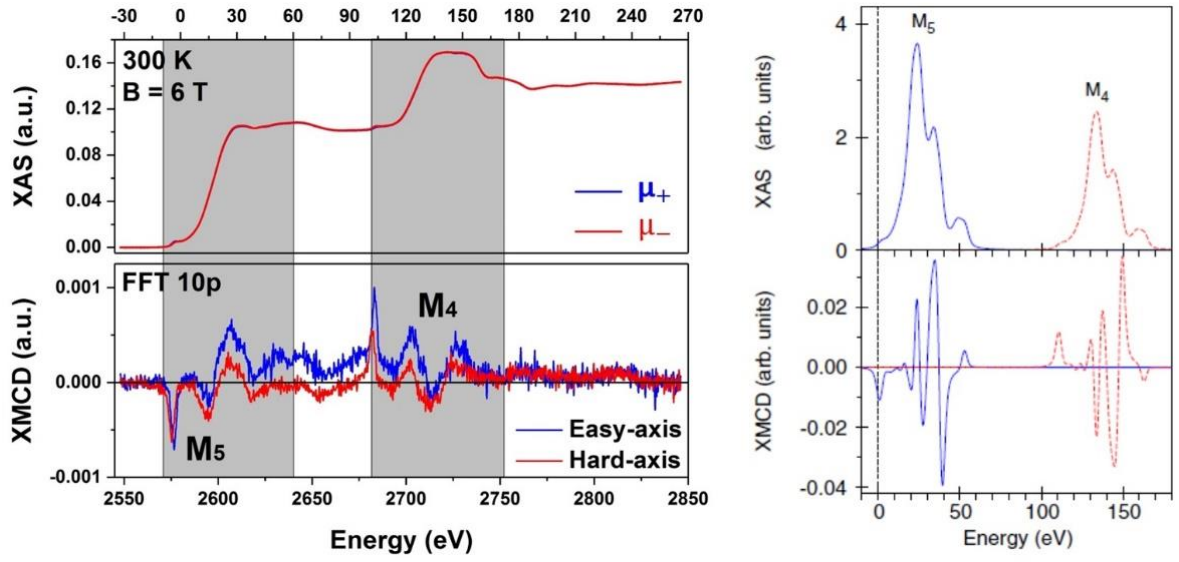

Figure 3.31 Left side: Bi $M_{4,5}$ XAS and XMCD curves of $Mn_{45}Bi_{55}$-573 magnet at 300 K. Right side: simulated Bi $M_{4,5}$ XAS and XMCD curves quoted from [111].

beamlines, both $M_{4,5}$ and $N_{4,5}$ edges of Bi element were studied at 300 and 350 K.

On the left side of Figure 3.31, the XAS and corresponding XMCD spectra at 300 K are presented in the top and bottom panels respectively. It is clear that the XMCD effect at Bi $N_{4,5}$ edges is extremely weak. Nevertheless, the feature of XMCD effect is still notable and, to some extent, matches those in the simulated spectra on the right side of Figure 3.31.[111] In order to extract the magnetic moments of Bi 6p electrons, the related XMCD sum rules were deduced for d→P electronic transition using the original formulas in Ref. [58] as following:

$$m_{\text{orb}} = \frac{\int_{L_3+L_2}(\mu_+ - \mu_-)dE}{\int_{L_3+L_2}(\mu_+ + \mu_0 + \mu_-)dE} = \frac{4q}{3r}N_h \tag{3.3}$$

$$\begin{aligned} m_{\text{spin}} &= \frac{\int_{L_3}(\mu_+ - \mu_-)dE - \frac{2+1}{2}\int_{L_2}(\mu_+ - \mu_-)dE}{\int_{L_3+L_2}(\mu_+ + \mu_0 + \mu_-)dE} \\ &= \frac{2(5p-3q)}{3r}N_h \end{aligned} \tag{3.4}$$

, where three parameters (p, q, r) refer to the integration of XMCD signal at M_5 edge, integration of whole XMCD signal, and integration of whole non-magnetic XAS spectra. Table 3.13 presents the detailed information of the magnetic moments of Bi 6p electrons evaluated from XMCD spectra at Bi $M_{4,5}$ edges. Because it is not possible to acquire reasonable value of integrated μ_0 spectra, the constant C is used to stand for this important parameter. For the values measured along hard-axis, the spin and orbital moments are antiparallel to the external field, namely anti-coupling to the magnetic moments of Mn 3d electrons. This resulting tendency is in good agreement in all reported theoretical calculations as shown in Table 3.13. [111, 117, 129] The easy-axis measurements can not provide reasonable results since there is a significant offset problem for its XMCD spectrum in the energy range from 2625 to 2725 eV (see Figure 3.31). This offset could

not be reduced at BORES beamline, because no negative voltages could be applied to the sample to reduce such TEX phenomena. This offset issue leads to wrong integrated XMCD signal as shown in Figure 3.32.

Table 3.13. The magnetic moments at Bi 6p shell in LTP-MnBi at 300 K analyzed using XMCD spectra at Bi $M_{4,5}$ edges. Noted that the constant C corresponds to the values of integrated XAS area and electron holes.

angle	m_{orb}	m_{spin}	$\frac{m_{\mathrm{orb}}}{m_{\mathrm{eff-spin}}}$
	$[\mu_B]$	$[\mu_B]$	
0° (easy)	0.126×C	−0.070×C	1.785
90° (hard)	−0.019×C	−0.041×C	0.475

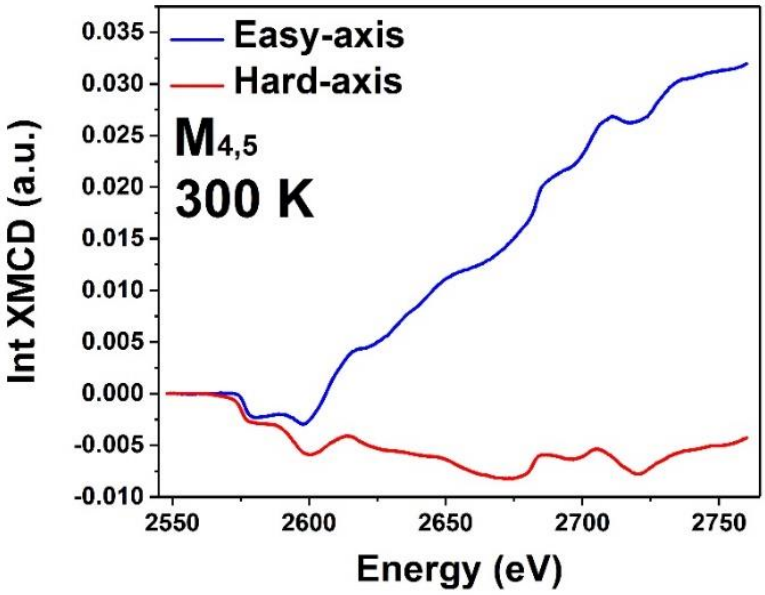

Figure 3.32 Integrated XMCD signals at Bi $M_{4,5}$ edges measured along easy- and hard-axis (at 300 K).

3.5.8. XMCD investigation on Bi $N_{4,5}$ edges (at RT)

The magnetic response of Bi 6P electrons can be also studied by Bi $N_{4,5}$ edges, which correspond to 4d→6P transition. Although the TEY signal is very small for Bi $N_{4,5}$ edges as seen in Figure 3.3, a systematic work was still completed using temperature- and angular-dependent measurements. For Bi $N_{4,5}$ edges, they were unambiguously observed in the XMCD spectra measured along hard-axis while we decided to have a quick check in BOREAS beamline. Because of this unexpected finding, the rest of measurements were subsequently carried out in WERA beamline. Unfortunately, the operation condition of ANKA synchrotron has been problematic since three years ago. Hence only the XAS and corresponding XMCD spectra measured along easy- and hard-axes are discussed here (see Figure 3.33).

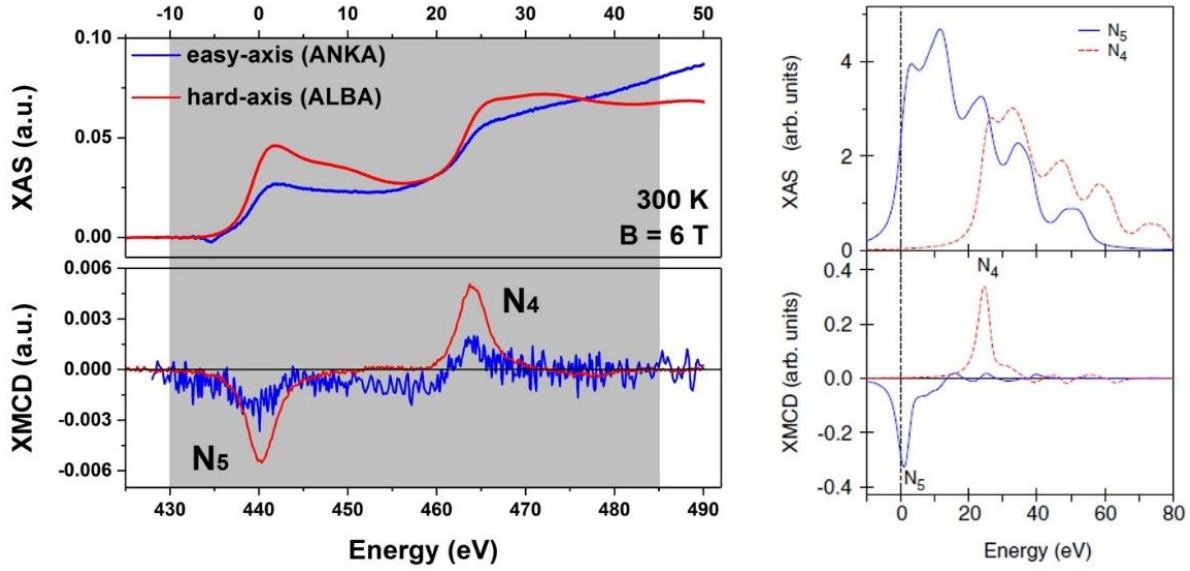

Figure 3.33 Left side: Bi $N_{4,5}$ XAS and XMCD curves of $Mn_{45}Bi_{55}$-573 magnet at 300 K. Right side: simulated Bi $N_{4,5}$ XAS and XMCD curves quoted from [111].

It is noted that the measurements of hard- and easy-axis spectra were acquired in BOREAS (ALBA) and WERA (ANKA) beamlines respectively. Furthermore, it is not clear why the nonmagnetic XAS spectra look so different for the easy- and hard-axes. This fact makes the comparison very inappropriate. Nevertheless, the feature of XMCD effect here resembles

that of simulated spectra. Again, the magnetic moments of Bi 6P electrons were evaluated using Eq. 3.3 and 3.4 and summarized in Table 3.14. Here, the directions of spin and orbital moments are consistent with the DFT results even though they were performed in different beamlines. Based on the results of Bi $M_{4,5}$ and $N_{4,5}$ spectra, it can be concluded that the magnetic moments of Bi 6p electrons should be anti-coupling to those of Mn 3d electrons as suggested in the theoretical reports. Although it is difficult to do further evaluation, it seems that the Bi 6p electrons should have large orbital moment anisotropy at room temperature owing to the large difference in the ratio of m_{orb} to $m_{\mathrm{eff-spin}}$. However, the contribution of T_z term (m_T) of Bi 6p electrons should not be ignored in $m_{\mathrm{eff-spin}}$ term due to strong hybridization with Mn 3d shells, so that it is not appropriate to say that the orbital moment is higher along easy-axis.

Table 3.14. The magnetic moments at Bi 6p shell in LTP-MnBi at 300 K analyzed using XMCD spectra at Bi $N_{4,5}$ edges. Noted that the constant B corresponds to the values of integrated XAS area and electron holes.

angle	m_{orb} [μ_B]	m_{spin} [μ_B]	$\frac{m_{\mathrm{orb}}}{m_{\mathrm{eff-spin}}}$
0° (easy)	$-0.323\times B_1$	$-1.094\times B_1$	0.295
90° (hard)	$-0.250\times B_2$	$-3.405\times B_2$	0.073

The anisotropy of Bi 6P states at 300 K was further studied by the angular measurements. Although we do see certain systematic variation at at Bi $N_{4,5}$ edges, the data can not give reliable physical picture because of high noise level. Further measurements are required to be done in future in order to provide convincing evident for the anisotropy of Bi 6p states.

3.5.9. XMCD investigation on Mn $L_{2,3}$ edges (temperature-dependnet)

In addition to room-temperature measurements, two sets of temperature-dependent XMCD spectra were completed in WERA and BOREAS beamlines in order to clarify the origin of the varied coercivity at elevated temperatures. In some published reports, it is claimed that the unusual positive temperature coefficient of coercive field for LTP-MnBi (from 100 up to 540 K) is strongly linked to its thermal expansion and corresponding

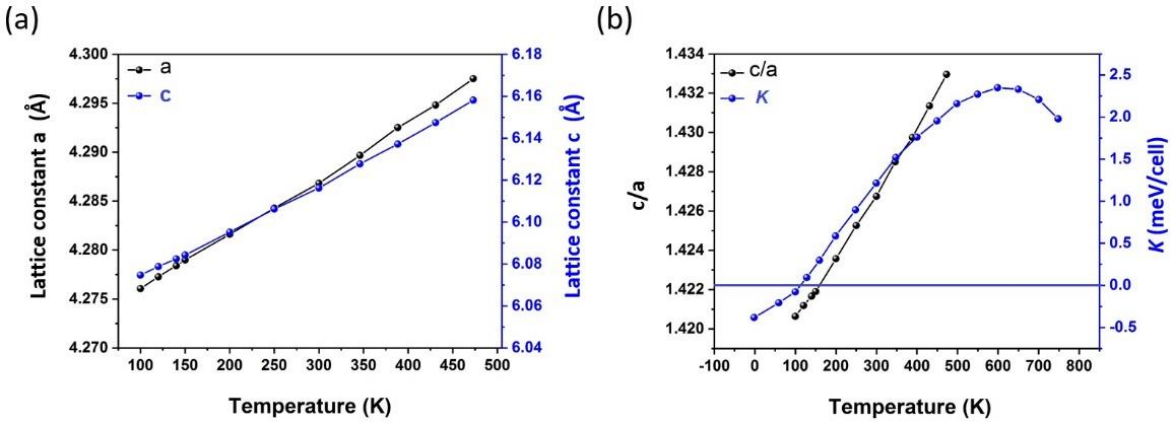

Figure 3.34 Temperature-dependent (a) lattice constants and (b) c/a ratio of $Mn_{45}Bi_{55}$-573 magnet. The theoretical *K* values at different temperatures are quoted from [111].

increased MAE_K.[101, 129, 130] Although the neutron diffraction studies demonstrated that the magnetic moments on Mn atoms change with anisotropic lattice expansion at elevated temperatures, no direct proof has been found to explain the origin of the increased coercivity, namely MAE_K.

Prior to detailed XMCD studies, the temperature-dependent crystalline structure of the specimen, $Mn_{45}Bi_{55}$-573, was determined using XRD method combined with Rietveld refinement. The XRD analysis indicates that both lattice constants c and a of LTP are raised steadily from 100 to 450 K as presented in Figure 3.34(a). Moreover, Figure 3.34(b) presents the more important feature of LTP-MnBi: the c/a ratios go up, like the theoretical MAE_K values given in Ref. [111], as a function of temperature. The values of c/a ratios are well consistent with the experimental data in some

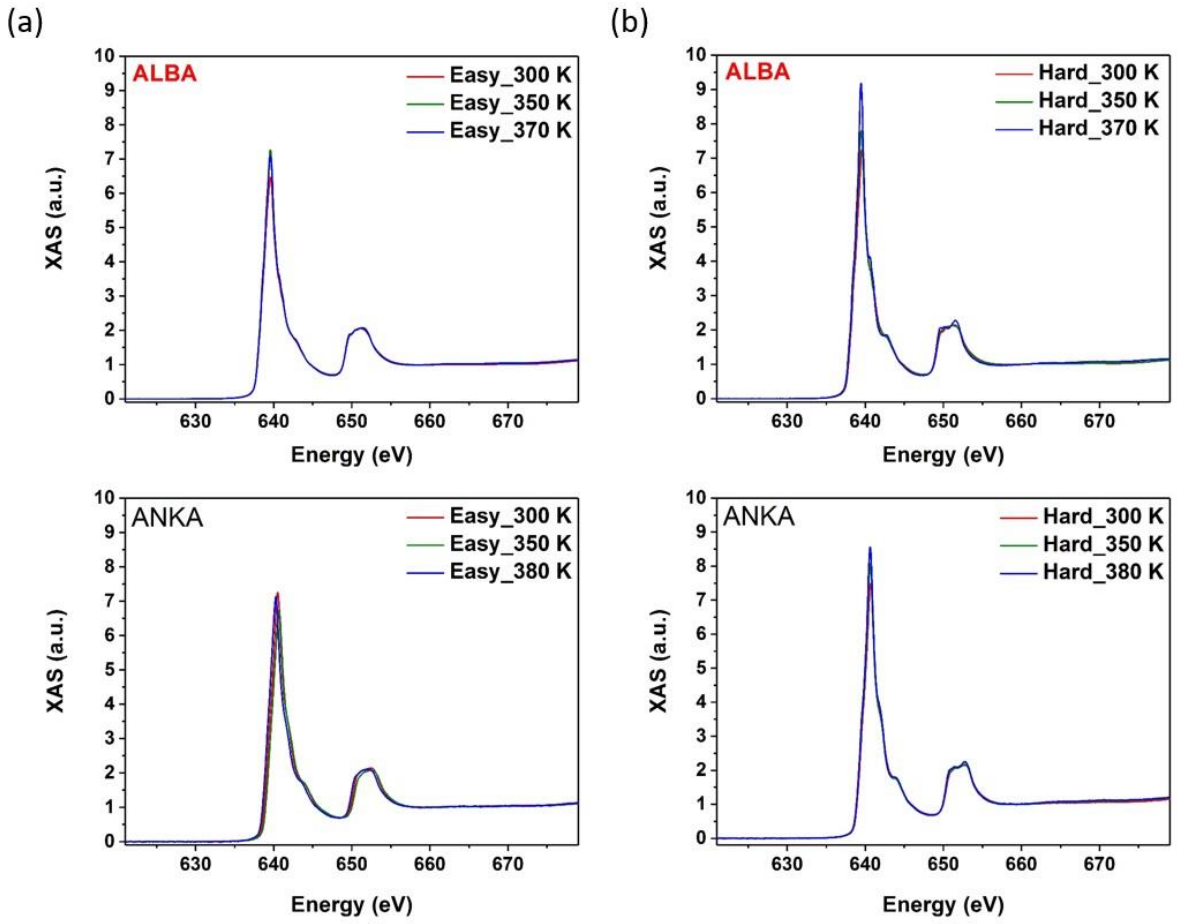

Figure 3.35 Temperature dependent XAS spectra (μ_0) measured along (a) easy- and (b) hard-axes recorded in ALBA and ANKA synchrotron centers.

previous work.[101, 112] After making sure the specimen has normal thermal expansion, the XAS spectra were measured up to 380 K and 370 K along exactly easy and hard-axes in WERA and BOREAS beamlines respectively. In Figure 3.35, two sets of temperature-dependent XAS spectra (μ_0) are summarized for easy- and hard-axes directions. The results indicate that the L_3 peak intensities are apparently larger along hard-axis at a fixed temperature regardless of the type of synchrotron beamline optics, whereas there is no obvious change at L_2 edge. In contrast, the XMCD signals at L_3 edge along easy-axis are much stronger in comparison with those along hard-axis (see Figure 3.36).

Because the XAS spectra (μ_0) are the average results of μ_+ and μ_- measurements, this means that the x-ray absorption was generated by two

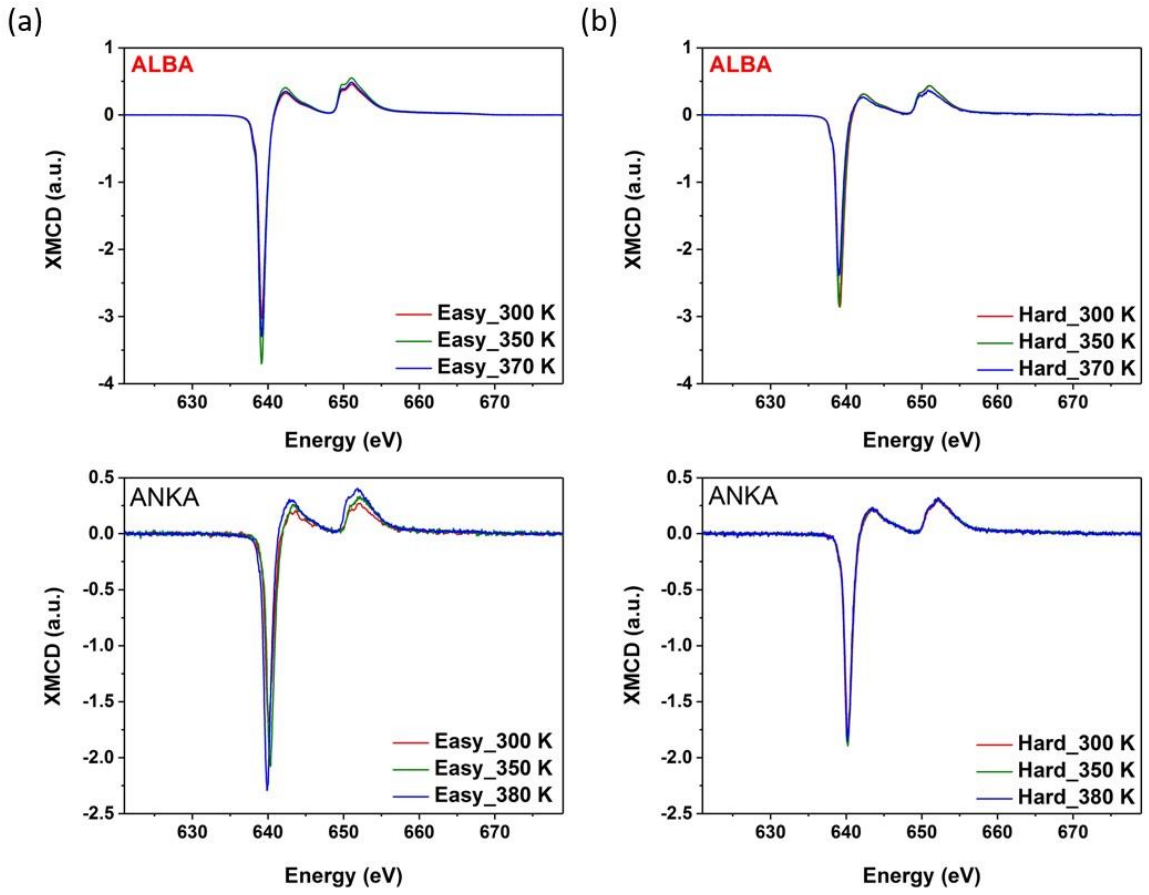

Figure 3.36 Temperature dependent XMCD spectra measured along (a) easy- and (b) hard-axes obtained in ALBA and ANKA synchrotron centers.

circularly polarized lights (either left or right). When the measurements were carried out along easy-axis, the electric filed vectors ($\vec{E}$) of incoming x-ray beam are oriented in hard-plane of LTP-MnBi crystal. In this configuration, the transition intensity depends on the electronic states along a-axis. In contrast, $\vec{E}$ components of x-ray beam can be partially parallel to either a- or c-axis while the spectra were obtained along hard-axis. Therefore, we suggest that more unoccupied states are created at Mn 3d spin-up band along c-axis at elevated temperatures, because the L_3 peak intensity is unambiguously larger in hard-axis measurements. This assumption is supported by the stronger temperature-dependent XMCD signals at L_3 edge while the μ_+ and μ_- spectra were recorded along c-axis (easy-axis).

The sum rule values of temperature-dependent XMCD studies on Mn 3d states are summarized in Table 3.15 and 3.16. If we ignore the data measured at 370 (380) K due to unexpected experimental error, two sets of data show similar tendency in the change of spin and orbital moments between 300 K and 350 K measurements. It is noted that we still used the same value of N_h (4.5) here for evaluations of magnetic moments, since no DFT calculation is available. In order to study the temperature-dependent behavior of LTP-MnBi quantitatively, it is necessary to get a hint provided by DFT calculation. Otherwise, the tiny but crucial change in magnetic moments could be smeared out by large experimental uncertainties.

Table 3.15 Temperature-dependent magnetic moments of Mn 3d electrons derived using sum rules along easy- and hard-axes. The values presented here were evaluated from the data recorded in WERA beamline.

Direction	T_m	m_{orb}	$m_{\mathrm{eff-spin}}$	$\frac{m_{\mathrm{orb}}}{m_{\mathrm{eff-spin}}}$	m_{total}
	[K]	[μ_B]	[μ_B]		[μ_B]
Easy-axis	300	0.0451	1.3050	0.0346	1.3501
	350	0.0522	1.4416	0.0362	1.4938
	380	0.0096	1.4039	0.0068	1.4135
Hard-axis	300	0.0646	1.0306	1.0952	1.0952
	350	0.0183	1.1341	1.1523	1.1523
	380	0.0199	1.0298	1.0497	1.0497

Table 3.16 Temperature-dependent magnetic moments of Mn 3d electrons derived using sum rules along easy- and hard-axes. The values presented here were evaluated from the data recorded in BOREAS beamline.

Direction	T_m [K]	m_{orb} [μ_B]	$m_{\mathrm{eff-spin}}$ [μ_B]	$\frac{m_{\mathrm{orb}}}{m_{\mathrm{eff-spin}}}$	m_{total} [μ_B]
Easy-axis	300	0.0635	1.4668	0.0433	1.5302
	350	0.0763	1.6238	0.0470	1.7000
	370	0.0846	1.4493	0.0584	1.5338
Hard-axis	300	0.0736	1.2722	0.0579	1.3458
	370	0.0642	1.2263	0.0523	1.2904
	370	0.0423	0.9876	0.0428	1.0299

Based on the temperature-dependent measurements, it is important to determine the exact partial density states of the $3d_{5/2}$ shell in order to understand the origin of the difference in magnetic moments between easy- and hard-axes. Unfortunately, all of the published DFT calculations only present the band structure at ~0 K.[14, 111, 117] It is not possible to have a deeper insight into this issue at the moment. Related calculation work has been partially done by Dr. V. P. Antropov, who is the theoretical physicist in Ames laboratory (USA). With his support, we believe that the detailed mechanism regarding the relation between orbital anisotropy and corresponding variation in electronic structure will be identified in the near future.

4. Fabrication and characterization of τ-MnAl

4.1. Powder

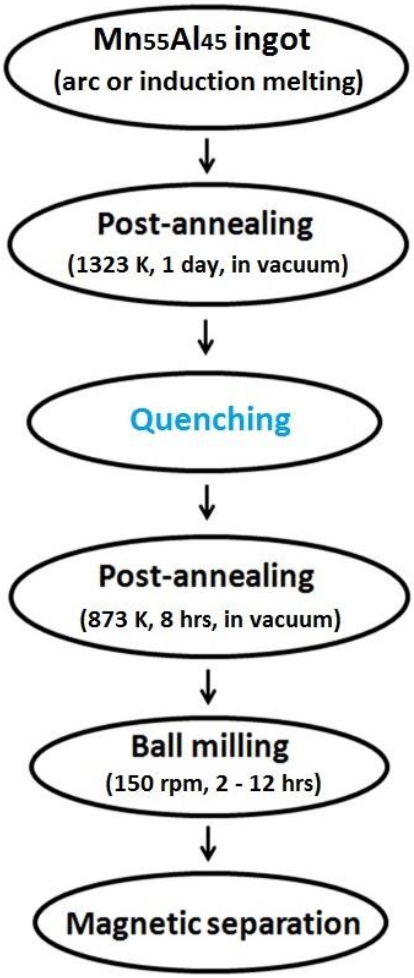

Figure 4.1 The flow chart of MnAl τ-powder fabrication.

Various production techniques have been employed for preparation of homogeneous MnAl alloys: melt-spinning, levitation melting with splat quenching, spark erosion, ball milling, mechanical grinding.[31, 35] In this study, the MnAl powders were prepared in the similar way as how the MnBi samples were fabricated. It was found that the amount of τ-MnAl in the final product strongly depends on the starting ratio of Mn in the melting process.[131] Therefore, an atomic ratio of 55-45 for Mn-Al (Alfa Aesar, 99.95 %) was chosen as a starting composition in order to produce high purity ferromagnetic τ-phase. The crucial point is that quenching (in ice

water) is included here to obtain the high temperature ε-phase first after 1 day post annealing at 1323 K. (see Figure 2.29). τ-phase is subsequently transformed from ε-phase via second post-annealing at 873 K. The annealed ingots were manually crushed in air, and then immediately grinded in hexane under argon atmosphere using the planetary mill. Ball milling time varies from 2 to 12 hours to reduce the averaged particle size. At the end, all milled powders were purified by magnetic separation. The whole procedure is briefly sketched in Figure 4.1.

As mentioned in the section 2.2.2., carbon is usually added to stabilize τ-phase crystal structure as demonstrated in many published reports.[4, 31, 35, 41, 132] In our G8 project, MnAl-C specimens were mainly studied by Dr. Hong Jian, who was working in Prof. Oliver Gutfleisch's laboratory in TU Darmstadt. In contrast to my work, Jian et al. added carbon during arc-melting procedure to obtain $Mn_{53.3}Al_{45}C_{1.7}$ alloys. 3 wt.% of Mn in excess was mixed to compensate the evaporation during the melting process. The procedure of post-annealing and following ball milling is the same as mentioned above. Another difference is that as-milled MnAl-C powders were annealed again at 773 K for half hour in the final step to optimize the magnetic properties instead of magnetic separation.[35]

4.2. XMCD measurements

The measurements were completed in WERA beamline of ANKA synchrotron center. Prior to the assigned beamtime, the anisotropic MnAl-C bulk samples (provided by Dr. Jian) were also carefully cut and fixed in the same as what was done for MnBi bulk specimens. Similarly, all samples were gently polished by sand papers and cleaned by a NdFeB magnet in the load-lock chamber ($\sim 10^{-7}$ mbar) before transferring into the main chamber ($\sim 10^{-10}$ mbar).

Survey spectra were also repeated to check the level of surface oxidation and chemical composition before detailed XAS scans, as shown in Figure 4.2. It is proved that the specimens have negligible extrinsic contamination.

Only Mn element is measured for MnAl-C samples because the binding energy of Al K-edge (~1560 eV) is far beyond the soft x-ray energy range. The strong absorption signal

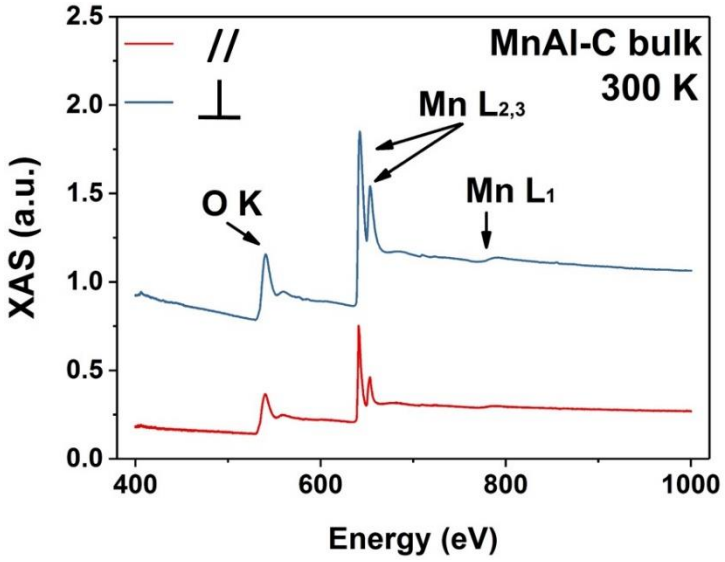

Figure 4.2 Overview XAS scans of MnAl-C bulk sample at 300 K. The spectrum taken along the direction perpendicular (⊥) to magnetic alignment was shifted upward for clarity.

4.3. Results and discussions

4.3.1. τ-MnAl Powder

The as-milled $Mn_{55}Al_{45}$ powders always consist largely of spherical powders with some large flakes. After magnetic separation, large flakes were motely removed. Room temperature magnetic properties of purified $Mn_{55}Al_{55}$ powders were measured along two different directions (⊥ and // to alignment direction). Among them, the powders milled for two hours show the highest saturation magnetization of 125 Am^2/kg at 7 T, which is not far away from the theoretical value of 161 Am^2/kg (see Figure 4.3).[34] Using theoretical density of 5.2 g/cm^3, the volume magnetization, M_s(7T), of the purified 2h-BM $Mn_{55}Al_{45}$ powders is 650 kA/m. This value is the same as the highest reported value for ball-milled MnAl powders (in Ref.

[131]), and also higher than those of MnAl-C reports ([35, 42, 133, 134]). However, other magnetic properties, including M_r of 41 Am²/kg, $\mu_0 H_c$ of 0.26 T and magnetic anisotropy, are all rather low, most likely due to the insufficient alignment and large mean particle size (tens of μm).[135] As ball milling time goes up, it was found that the mean particle size declines (similar to LTP-MnBi) but the saturation magnetization drops dramatically to 64 and 16 Am²/kg for the 4h-BM and 10h-BM powders, respectively. Such noticeable deterioration is usually ascribed to the increased defects and microstructural changes through the prolonged milling.[42] Because τ-MnAl is a metastable, it was found that input mechanical energy via low-energy mechanical milling leads to build up a high density of defects and a high level of internal strain, even without decomposing the metastable τ-MnAl alloys.[136] The prerequisite for fabricating highly anisotropic bulk magnets is to obtain starting powders with dimension close to single domain, which is ~780 nm for τ-MnAl.[135] If no carbon is doped in the interstitial position to stabilize the structure, it seems clear that it is not possible to obtain small τ-MnAl particles (≤ 1 μm) without a big loss in magnetic performance. Therefore, the research work regarding $Mn_{55}Al_{45}$ particles has ceased, and our experimental target shifted to MnAl-C powder and anisotropic bulk magnets.

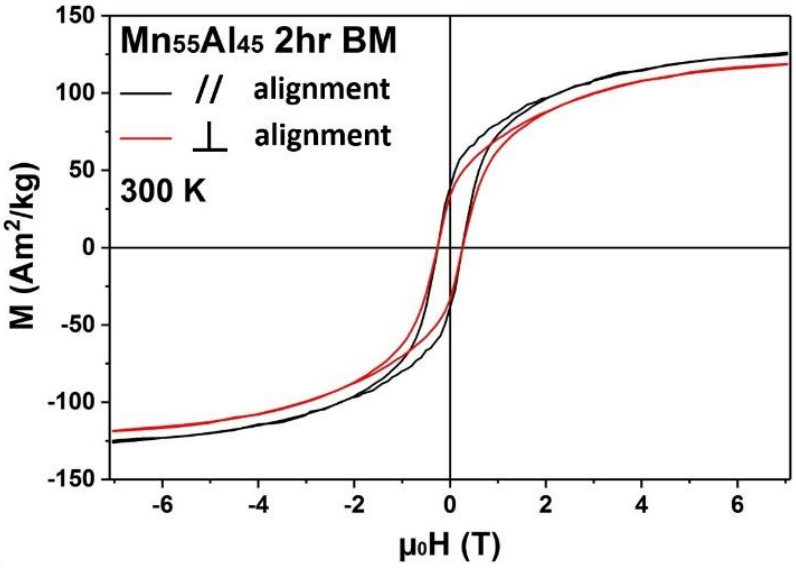

Figure 4.3 Magnetization curves of 2h-BM $Mn_{55}Al_{45}$ powders parallel and perpendicular to alignment directions.

4.3.2. τ-MnAl-C Powder

Figure 4.4 summarizes the evolution in phase structure of the as-milled $Mn_{53.3}Al_{45}C_{1.7}$ flakes with increasing milling time.[35] All the diffraction peaks could be attributed to τ-phase. The diffraction peaks became broader as milling time increased, indicating reduced grain size and crystallinity as some of the diffraction peaks disappeared after long time milling. Nevertheless, no obvious sign of decomposition was observed at this stage.

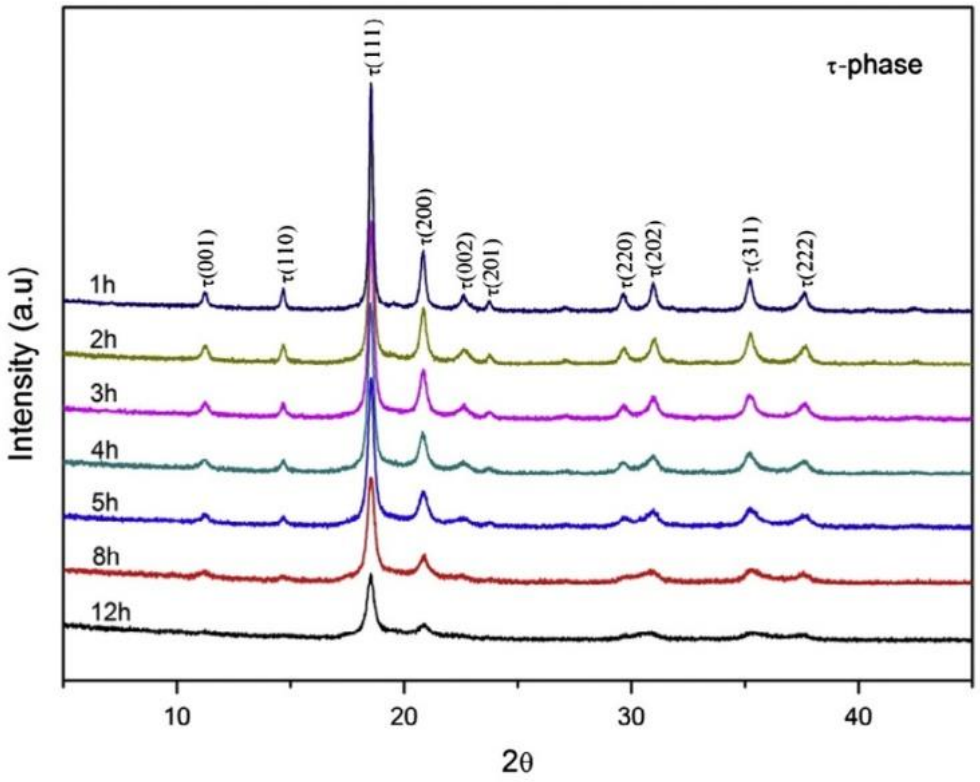

Figure 4.4 XRD patterns of as-milled $Mn_{53.3}Al_{45}C_{1.7}$ powders mechanically milled for 1–12 hours. (quoted from Ref. [35]) It is noted that no magnetic seperation was perform for MnAl-C powders.

Since M(2T) decreases drastically from 86.5 to 23.0 Am^2/kg as the milling time increases from 1 to 12 hours (not shown here), the as-milled powders were annealed at 773 K for 30 minutes to recover the weight fraction of τ-phase. The XRD patterns of the annealed powders are plotted in Figure 4.5, where the equilibrium γ_2 and β phases appear after post-annealing. It is expected that the larger density of defects in as-milled powders would

make the atoms have higher mobility and favor the τ-phase decomposition. Hence the amount of equilibrium phases increased with longer milling time because of the accumulated defects.[35, 136] Nevertheless, the crystal structure of τ-MnAl was greatly recovered, as can be seen both from the well-defined diffraction peaks and the magnetization measurement. This tendency is further supported by the SQUID measurements of the annealed powders, which show clear dependence of magnetic properties on the milling time (shown in Figure 4.6).[35] Comparing with the as-milled powders, both M(2T) and M_r of annealed ones exhibit significant improvement after post-annealing.

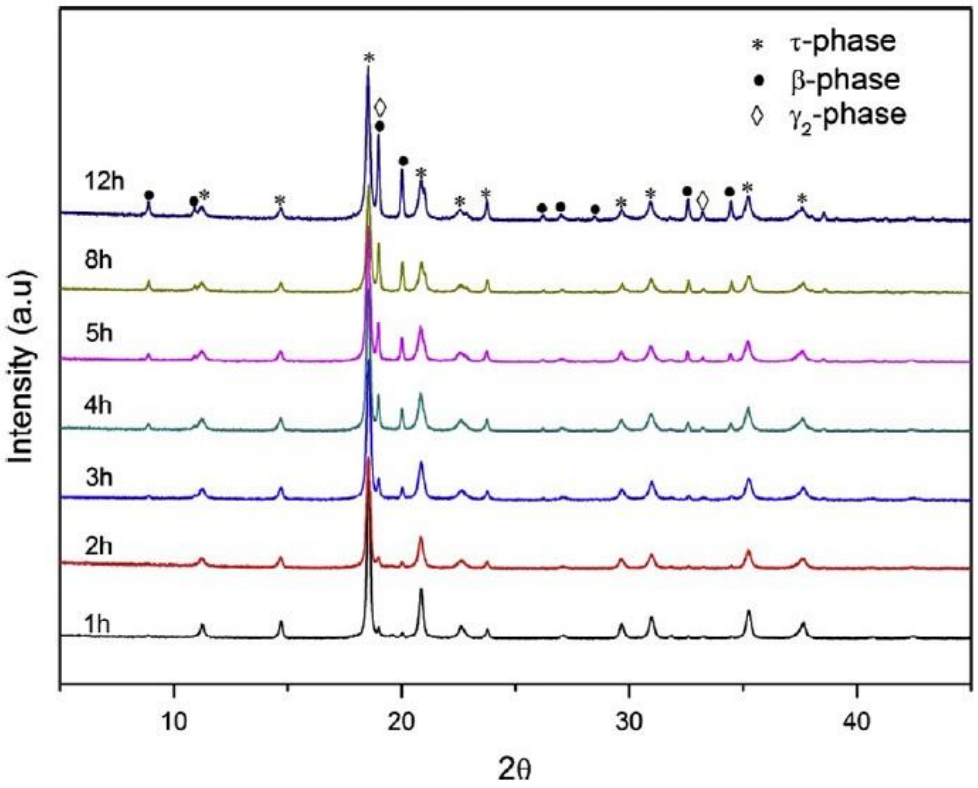

Figure 4.5 XRD patterns of annealed $Mn_{53.3}Al_{45}C_{1.7}$ powders mechanically milled for 1–12 hours. [35] It is noted that no magnetic seperation was perform for MnAl-C powders.

In Jian et al.'s work, the optimized magnetic properties, M_r of 54.8 Am²/kg, $\mu_0 H_c$ = 0.28 T, $(BH)_{max}$ = 2.05 MGOe, were obtained from the powders milled for 5 h and further annealed at 773 K for 30 minutes.

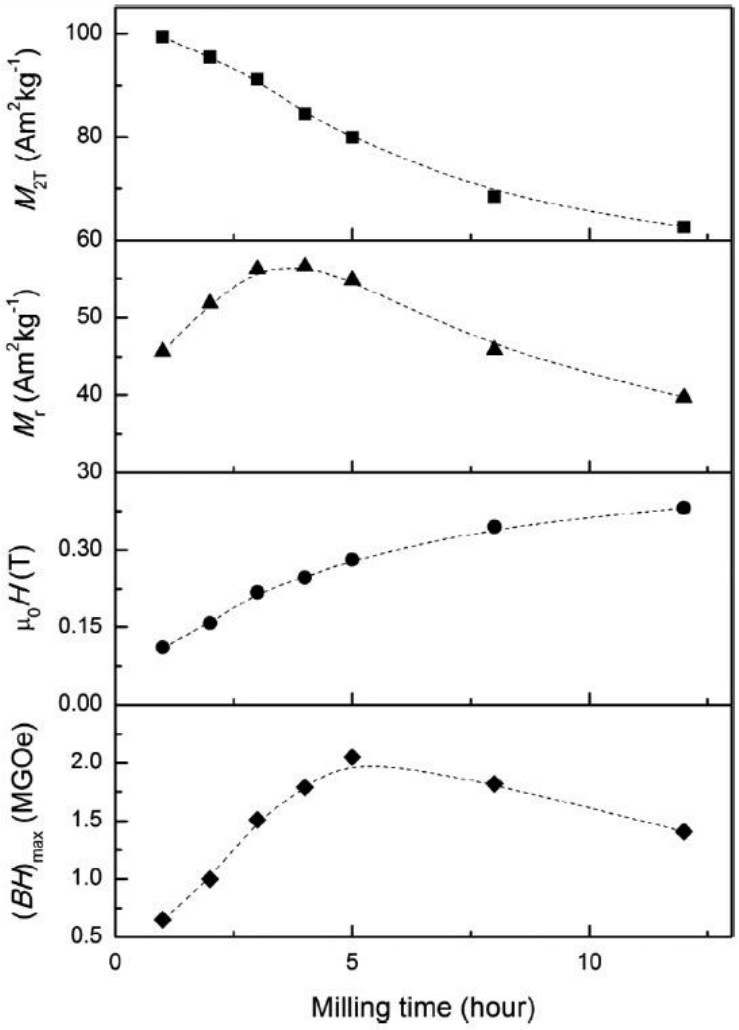

Figure 4.6 Dependence of magnetic properties on the milling time of $Mn_{53.3}Al_{45}C_{1.7}$ powders mechanically milled and annealed at 773 K for 30 minutes. It is noted that the magnetic properties here were recorded under a maximum field of 2 Tesla. [35]

4.3.3. **Hot-compacted bulk magnets**

The annealed 5h-BM powders were further hot-compacted at 500 °C under 200 MPa for 5 minutes. Before fast consolidation, magnetic field of 1.8 T was applied to align powders which were placed in the tungsten carbide die. The field lie perpendicular to the pressing direction. Figure 4.7 shows the SEM images of the hot-compacted samples parallel and perpendicular to alignment directions (//), namely perpendicular and parallel to pressing

directions (⊥). It is clear that the grains or flakes tend to lie parallel to alignment direction (i.e. perpendicular to the pressing direction).

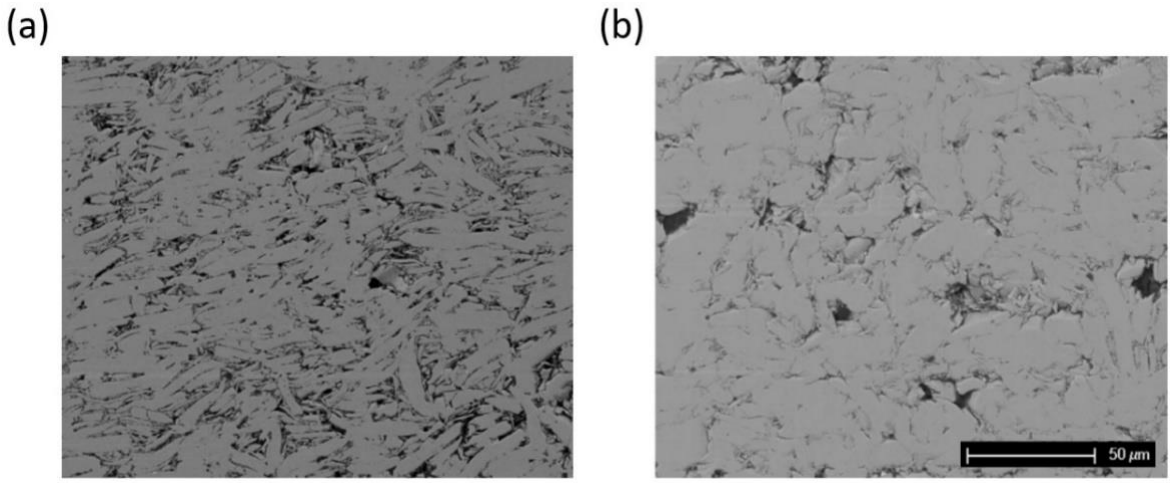

Figure 4.7 SEM images of anisotropic MnAl-C bulk magnets: surface plane (a) parallel (//) and (b) perpendicular (⊥) to magnetic direction. (provided by Dr. Hong Jian)

Comparing the XRD patterns measured parallel to and perpendicular to alignment directions, it can be seen that the relative intensity of (001) and (002) peaks is stronger in the longitudinal direction, indicating that crystallography texture actually exist in the bulk sample (shown in Figure 4.8). Furthermore, the hysteresis loops indicate that the easy axis of the hot compacted sample lies in the longitudinal direction, as shown in Figure 4.9. It is noted that these bulk samples were prepared just for XMCD investigation. Although the magnetic properties of the bulk samples are not optimized yet, they still exhibit obvious magnetic anisotropy.

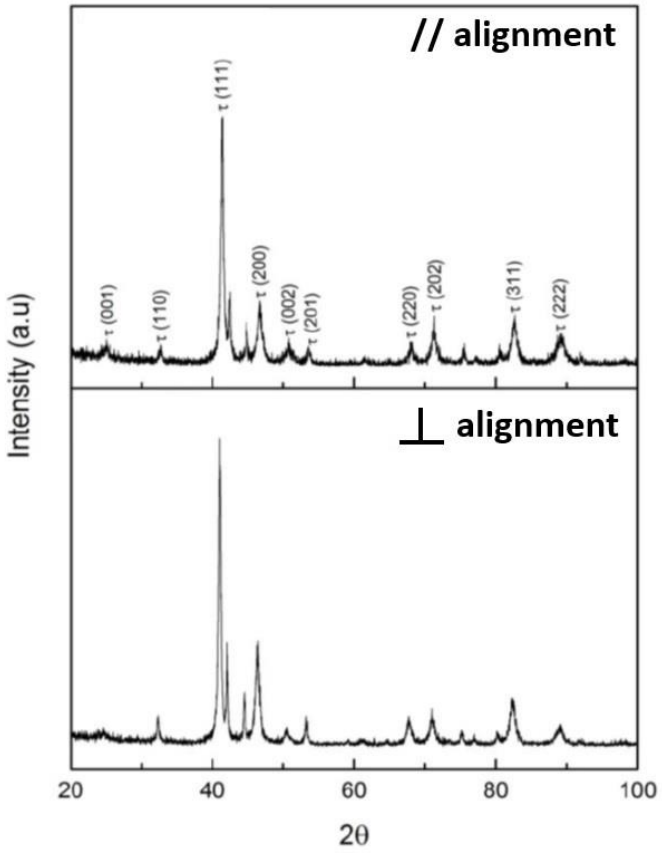

Figure 4.8 XRD patterns of anisotropic MnAl-C bulk magnet along and perpendicular to magnetic alignment. The peaks without phase identification mainly originate from γ_2 and β phases. (provided by Dr. Hong Jian) Note that the data were collected using Mo Kα radiation.

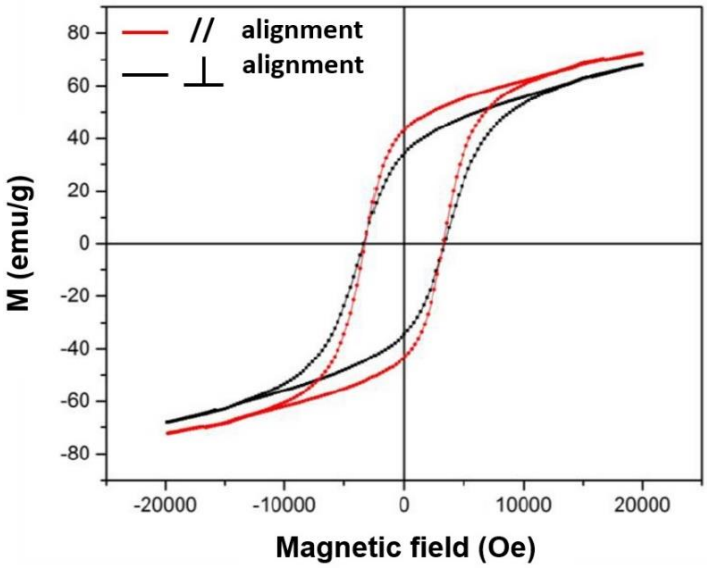

Figure 4.9 Magnetization loops of anisotropic MnAl-C bulk magnets: (a) parallel to and (b) perpendicular to magnetic alignement. (provided by Dr. Hong Jian)

4.3.4. XMCD investigation

The preliminary XMCD measurements on the anisotropic MnAl-C bulk samples taken along longitudinal direction are presented in Figure. 4.10, and it is obvious that the XMCD signal at Mn $L_{2,3}$ edges is extremely small compared to what was observed in LTP-MnBi. In addition, there are two satellite peaks (indicated with green arrows) and doublet structure on L_3 and L_2 edges, respectively. These features remain in the XAS spectra after the sample surface was polished a few times, implying that the surface grains were still covered with non τ-MnAl phases. In addition, the existence of oxidized layers should be also considered due to the high absorption intensity of O K-edge (see Figure 4.2).

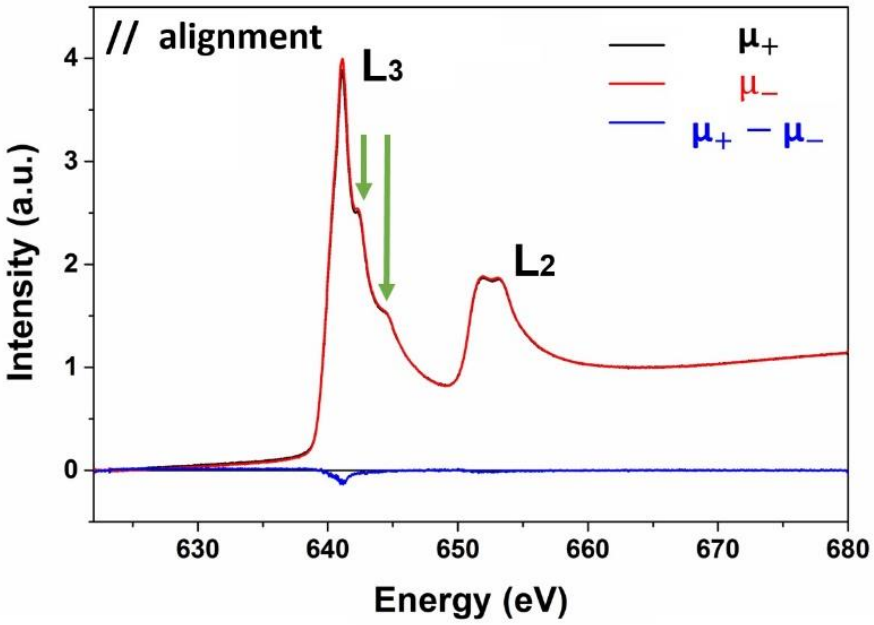

Figure 4.10 Mn $L_{2,3}$ XAS edgess and XMCD spectra of anisotropic MnAl-C bulk magnets measured parallel to field aligment at 300 K.

Figure 4.11(a) indicates that the level of L_3 satellites and L_2 doublet structure seems to vanish while the measurement is taken along the direction perpendicular to magnetic alignment. The reason could be that it is easier to clean the τ-MnAl grains, which surface normal is perpendicular to alignment direction, as seen in the corresponding SEM images presented in Figure 4.7. However, the observed XMCD signals are both weak no matter

which direction the measurement was performed along (see Figure 4.11(b)). The average $m_{\text{eff-spin}}$ and m_{orb} of Mn 3d electrons are listed in Table 4.1; not surprisingly, all values are too small to be reliable. Compared to the SQUID data ($\geq 1.2\ \mu_B$/Mn) and theoretical value ($\sim 2.4\ \mu_B$/Mn in Ref. [34]), the evaluated magnetic moments is apparently obscured by such weak XMCD signal. The same measurements were repeated on different pieces of τ-MnAl bulk samples, however, the problem has not been solved yet.

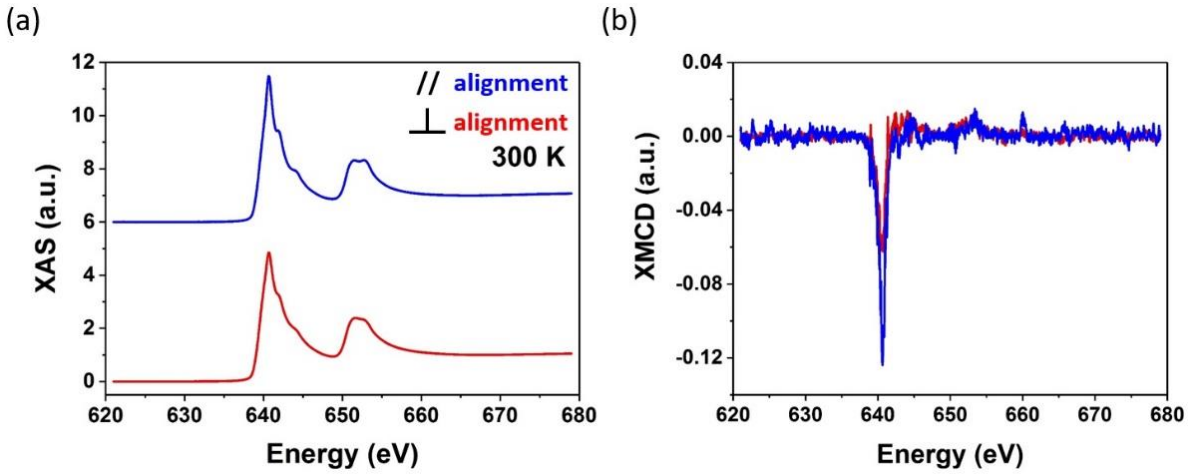

Figure 4.11 Anisotropic MnAl-C bulk magnets: (a) parallel and (b) perpendicular to magnetic direction.

Table 4.1 Magnetic moments of anisotropic MnAl-C magnet at 300 K. Noted that these values were estimated by assuming Mn 3d configuration is $d^{6.5}$.

Direction	$m_{\text{eff-spin}}$ [μ_B]	m_{orb} [μ_B]	m_{total} [μ_B]	$\frac{m_{\text{orb}}}{m_{\text{eff-spin}}}$	m_{spin}^{Cal} [μ_B]
Easy-like	0.05094	0.01648	0.06741	0.32345	2.4
Hard-like	0.02489	0.00293	0.02782	0.11785	

For this unexpected result, we suggest that this could be associated with the real microstructure of the compacted bulk system. As mentioned

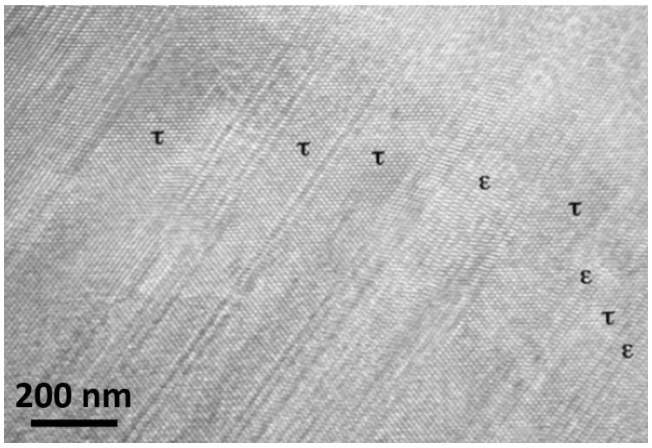

Figure 4.12 High resolution elecron microsope (HREM) image of the cross section near the plate-like τ-phase region in MnAl alloys. [38]

above, the usual methods to obtain τ-phase is to post-anneal ε-phase at moderate temperature range (450~650 °C). This means that the crystal growth of τ-phase is located near the edge of ε-phase in MnAl alloys. Therefore, it was found the τ-MnAl grains are always surrounded by parent ε-phase in the real texture as supported, for example, by the HRTEM image in Ref. [38] (see Figure 4.12). Furthermore, τ-MnAl is metastable so that it does partially decompose into nonmagnetic γ_2- and β-MnAl after hot consolidation. Due to the inevitable existence of these secondary phases enclosing τ-MnAl grains, it is not possible to study τ-MnAl bulk magnets by XMCD spectroscopy.

5. Characterization of α´-Fe_8N

5.1. Thin film preparation

This research work was inspired by Dr. Imants Dirba, while he was studying PhD in Prof. Oliver Gutfleisch's laboratory in TU Darmstadt. Our preliminary XMCD investigation on his samples shows that $m_{\text{eff-spin}}$ and m_{orb} of Fe atoms in a Fe-N system increase with increasing nitrogen doping. This phenomena could be related to the enhanced c/a ratio; unfortunately, we could not complete it systematically due to some technical problem with the UHV preparation chamber. Afterwards, the iron nitride samples were mainly provided from Mr. Dominik Gölden who is the PhD student in Prof. Lambert Alff's group also in TU Darmstadt. Dirba's and Gölden's samples were grown by magnetron sputtering and MBE, respectively. The substrate used for this study is MgO(001) by Dirba and Al_2O_3(0001) by Gölden, which were supplied from CrysTec. High-purity α-Fe and a series of α´-Fe_8N_x films were fabricated in ultra-high vacuum chamber at a base pressure of about 10^{-9} mbar. Prior to deposition, all substrates were subjected to a 30 min heat treatment (above 600 °C) to remove adsorbates from the surface. A Ta or Al capping layer (99.95% purity) was in situ deposited at the end, in order to prevent oxidation and potential decomposition of the phases. Structural characterization was determination by XRD and XRR using a Rigaku SmartLab system. The thickness for all samples is around 40 nm, and all films were grown without additional buffer layer. Hysteresis loops were measured at 300 K and 10 K using a SQUID magnetometer (MPMS 3). More detailed information can be found in Ref. [48] and [49].

5.2. Structural and magnetic properties

In Dirba et al.'s paper, it was proved that a gradual increase of the nitrogen incorporation in crystal unit transforms the bcc α-Fe into bct α'-Fe_8N. This structure expansion occurs along the [001] direction (c-axis), accompanied by an enhancement in magnetic moment to 2.61 ± 0.06 μ_B/Fe as well as considerable increase in magnetic anisotropy.[49] As depicted in Figure 5.1(a), it is clear that the magnetic moments of α'-Fe_8N_x compounds go up

steadily as a function of the estimated c-axis constant. Compared to α-Fe, Figure 5.1(b) shows a positive correlation between the in-plane saturation field (easy axis) of α'-Fe_8N_x films and corresponding c-lattice constants, in agreement with the previous theoretical prediction for α"-$Fe_{16}N_2$.[47] This leads to the conclusion that the magnetic easy axis shifts to the tetragonally distorted c-axis direction. Based on his finding, Dirba et al. suggested that the increase of the in-plane saturation field is associated with an increase in the intrinsic magnetocrystalline anisotropy induced by lattice expansion, since all other factors contributing to magnetic anisotropy are constant.

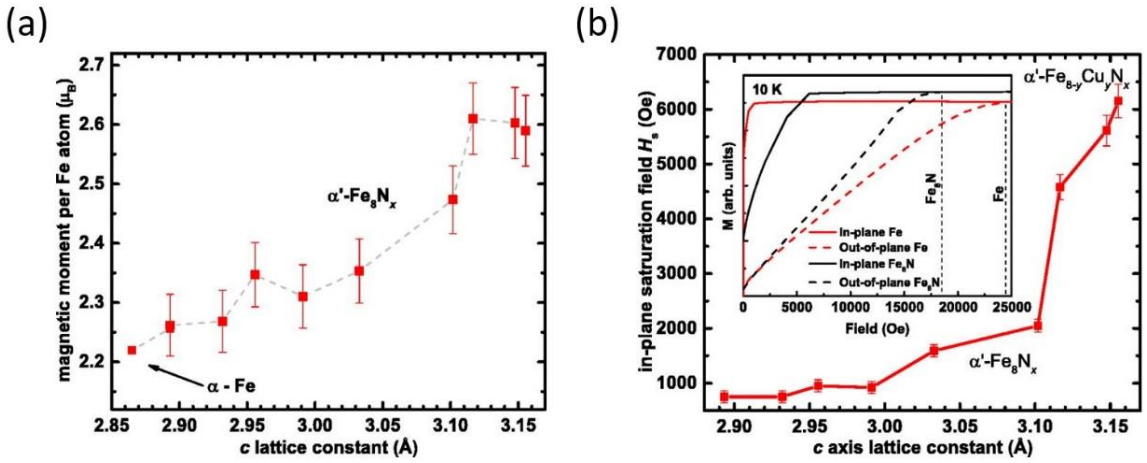

Figure 5.1 (a) Magnetic moment per Fe atom in α'-Fe_8Nx in dependence of the lattice constant. (b) In-plane saturation field in dependence of the c-axis lattice constant in α'-Fe_8Nx. In the inset, the in-plane and out-of-plane magnetization, M, is shown for both α-Fe and α'-Fe_8N_x. [47]

Following Dirba et al.'s work, Gölden has done a more comprehensive investigation on iron nitride system by MBE. He successfully achieved highly pure Fe_8N_x thin films with out-of-plane easy axis, which is important for practical application. In Figure 5.2(a) quoted from Ref. [48], Gölden showed that the X-ray diffracted peak of the α'-Fe_8N_x shifts with increasing rf power towards the expected position, indicating the elongation of the c-axis caused by introduction of nitrogen interstitials. The observed shift of the (004) reflection peak of α'-Fe_8N_x saturated at rf power of 145W, showing no further change upon further increase of the rf power. This variation

of lattice constant is consistent with that of Dirba et al.'s sputtered thin films.

The important result in Figure 5.2(b) is that the extracted anisotropy field (H_a) of the α'-Fe_8N_x films increases from ~370 Oe for the sample synthesized at lowest rf power to a maximum of ~1450 Oe for the one using rf power of 145W. Through the tetragonal distortion, the hard axis of original α-Fe unit structure tilts into the film plane, and an increase of the magnetic anisotropy occurs as c/a ratio increases (not shown). It is noted that the inset out-of-plane (c-axis) data showing magnetic hard-axis feature, which should be caused by strong shape anisotropy.

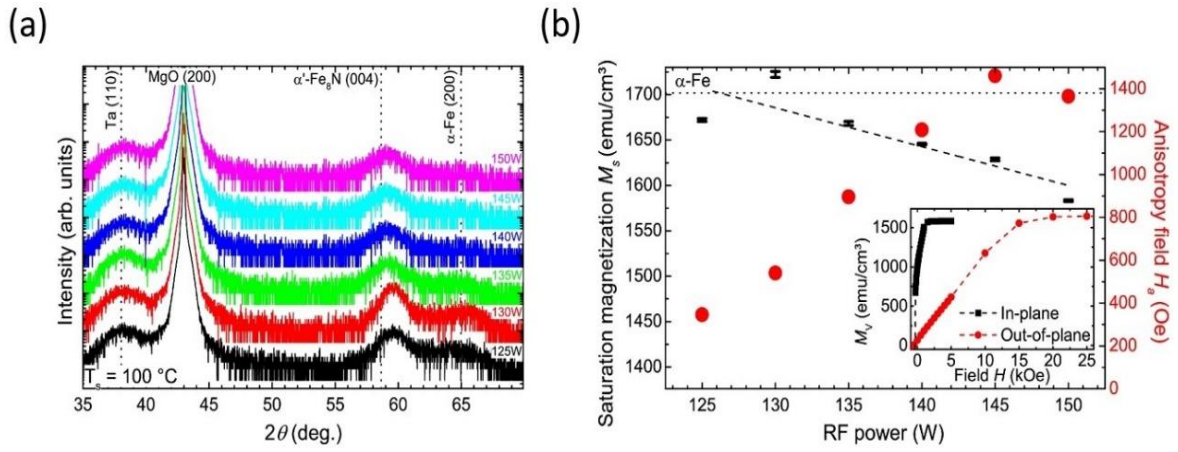

Figure 5.2 (a) XRD patterns of Fe-N thin films in the vicinity of the composition α'-Fe_8N_x of varying rf powers. (b) Saturation magnetization (black errorbars) and anisotropy field Ha of α'-Fe_8N_x as a function of the rf power applied to the nitrogen radical source. The indicated error of Ms is less than 3 emu/cm³. The inset shows the M_V-H curves of α'-Fe_8N_x grown with 150 W rf power along the in-plane and out-of-plane directions. [48]

In summary, both Dirba and Gölden proved that the evaluated magnetic moments per Fe atom continuously increases with increasing c lattice constants as well as c/a ratios. However, there is no evidence of a 'giant' magnetic moment reported previously for α"-$Fe_{16}N_2$ compound observed in their systematically experimental investigation.

5.3. XMCD measurements

In order to provide more convincing experimental support for Dirba's and Gölden's experimental results, corresponding XMCD measurements were performed systematically in ANKA synchrotron center. Our purpose is to see if there is actually consistent variation in spin and orbital moments on Fe $L_{2,3}$ edges as a function of nitrogen content. Both N K-edge and Fe $L_{2,3}$-edges were measured at about 10 K under a field of 7 Tesla, while the specimens are glued onto the Tantalum holders. The origin of magnetic anisotropy was investigated by angle-dependent measurements (17°, 40°, and 90°) under saturation condition.

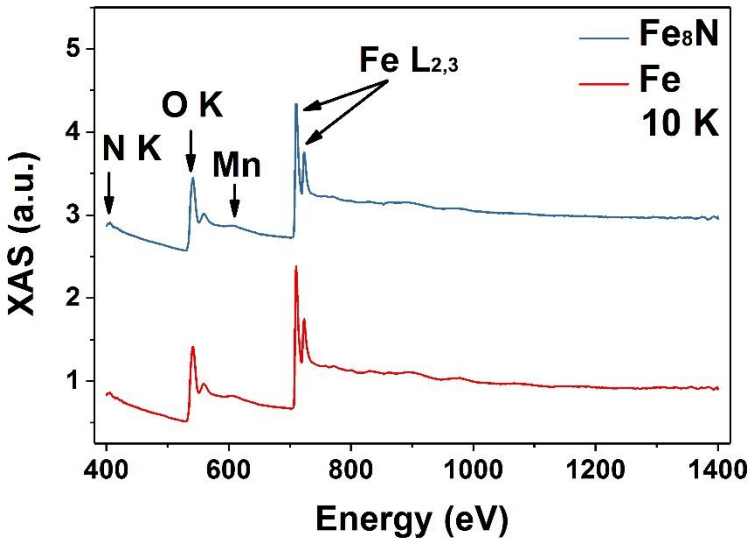

Figure 5.3 Overview XAS scans of α-Fe and α'-Fe_8N_x at 10 K. The spectrumof Fe_8N was shifted upward for clarity.

Prior to detailed XAS scans on each edge, survey spectra were done again to monitor the level of oxidation and chemical composition. As shown in Figure 5.3, it is proved that the specimens (ex. α-Fe and α'-Fe_8N) have negligible extrinsic contamination except Mn particles probably from scratched powders. Additionally, the signal intensity of $L_{2,3}$ edges is sufficient for quantitative investigation even though Fe-N specimens are protected with 2-3 nm Al or Ta capping layers.

5.4. Results and discussions

As mentioned above, it is not possible to perform systematic investigation on Dirba's samples because parts of them were heavily oxidized. Therefore, only the magnetic properties of Gölden's samples are discussed here, which are denoted hereafter as Fe, $Fe_{24}N$, $Fe_{12}N$ and Fe_8N, respectively. XRR technique was applied to determine the chemical stoichiometry and multilayer structure of each specimen. Detailed information is summarized in Table 5.1.

Table 5.1 Structural properties of four specimens.

Specimen	Thickness [nm]	Density [g/cm^3]	Capping layer thickness [MJ/m^3]	Structure
Fe	44.057	7.85	3.017	BCC
$Fe_{24}N$	44.423	7.52	3.286	BCT
$Fe_{12}N$	44.186	7.40	3.477	BCT
Fe_8N	43.894	7.17	3.295	BCT

5.4.1. Magnetic anisotropy

Gölden mentioned that the crystalline c-axis of the MBE samples is perpendicular to sample plane for all Fe-N thin films in his paper [48]. To clarify this assumption that the observed magnetic anisotropy is dominated by shape anisotropy, angle-dependent SQUID measurements were carried out at a step of 10° with respect to sample surface using our MPMS 3 magnetometer. In Figure 5.4, it is clear that the in-plane magnetization of α-Fe and Fe_8N, measured at 15 K under 550 Oe, shows more or less the highest magnetic moments, while the out-of-plane value is roughly the lowest (at around 90°). Both two curves indicate that the magnetization of the specimens decline gradually from in-plane to out-of-plane directions.

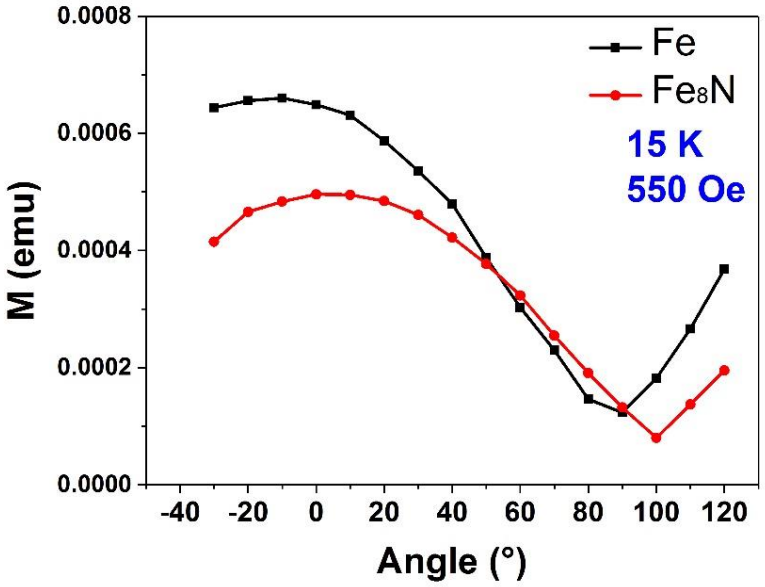

Figure 5.4 Angle-dependent magnetization of Fe and Fe_8N.

The shape anisotropy energy (MAE_{shape}) and total magnetic anisotropy energy (MAE_{total}) were further estimated by saturation magnetization and the difference between in-plane (maximum) and out-of-plane (minimum) magnetization curves respectively, as mentioned in the section 2.1.4. The evaluated values listed in Table 5.2 demonstrate that the observed total MAE is actually dominated by shape anisotropy as suggested in Ref. [48]. For Fe film, the experimental MAE_{shape} of 1.7×10^6 J/m^3 is very close to the reference value of 1.92×10^6 J/m^3 in Ref. [17]. Assuming that the difference between MAE_{shape} and MAE_{total} is only caused by corresponding magnetocrystalline energy (MAE_K), the experimental MAE_K values are 1.4×10^5 and 8.3×10^5 J/m^3 for Fe and Fe_8N respectively. These results are comparable to the reference 'bulk' values given in Refs. [17, 137]. Nevertheless, it is noted that "area method" can not give precise MAE. Looking at the ratio of MAE_{total} to MAE_{shape}, it can be concluded that the magnetocrystalline energy remarkably increases via lattice expansion from bcc Fe to bct Fe_8N. Moreover, it is obvious that the c-axis of Fe_8N film indeed points out-of-plane according to this rough examination; however, the magnetocrystalline energy is too small to compete with its large shape anisotropy.

Table 5.2 Detailed analysis on magnetic anisotropy. The reference values are quoted from the published reports: [137] and [17]. Noted that the out-of-plane direction is defined as reference axis.

Material	MAE_{total}	MAE_{shape}	$\frac{MAE_{total}}{MAE_{shape}}$	MAE_K (exp)	MAE_K (ref)
	[J/m^3]	[J/m^3]		[J/m^3]	[J/m^3]
Fe	-1.56×10^6	-1.70×10^6	0.92	1.4×10^5	5.4×10^4
Fe_8N	-1.18×10^6	-2.01×10^6	0.59	8.3×10^5	6.0×10^5

5.4.2. XMCD investigation

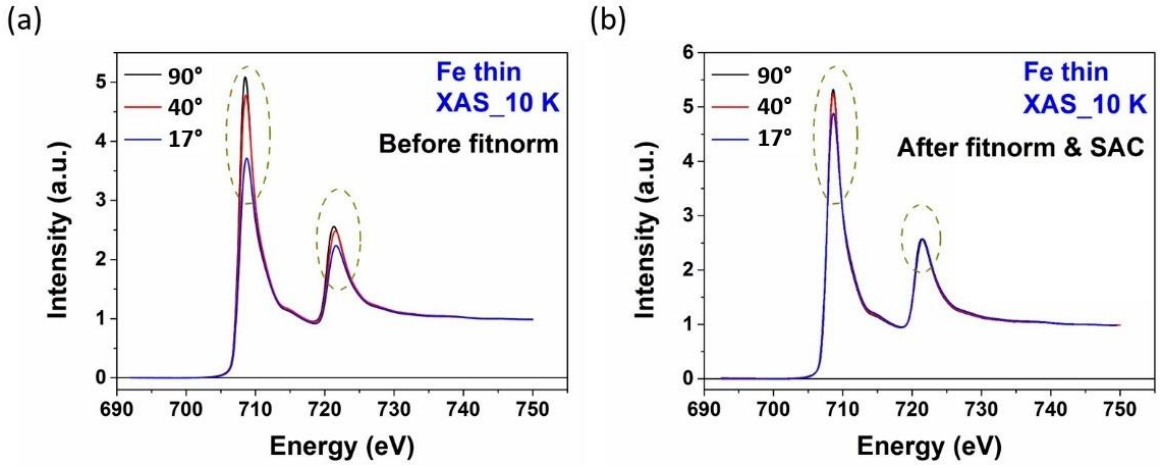

Figure 5.5 Angle-dependent normalized XAS curves (μ_0) of α-Fe at Fe $L_{2,3}$ edges: (a) before and (b) after fit-normalization and surface effect correction.

Since the series of Fe-N specimens are all in the form of thin films, it is necessary to carefully check if self-absorption effect exists in the analyzed data before applying sum rules to extract the values of magnetic moments. Taking Fe film for example, it is clear that the intensities of Fe $L_{2,3}$ peaks differ a lot at different angles in uncorrected normalized spectra, as shown in Figure 5.5(a). Because the thickness of all polycrystalline specimens is more than 40 nm (namely like a bulk compared to Fe effective electron escape

length of 1.7 nm),[68] it is necessary to make sure the μ^0 XAS spectra have the same intensities at three angles within non-resonant region. Before applying self-absorption correction, all linearly polarized spectra were rescaled to make sure that the background signal is at the same level. Following the discussions given in subchapter 2.3.4, the saturation effect correction was then carried out for all angle-dependent spectra of each specimen simultaneously using Eq. 2.28. The appropriate correction leads to the same L_2 peak intensities in the normalized angular nonmagnetic XAS spectra (see Figure 5.5(b)). Although there is still little deviation in L_3 peak intensities due to its stronger absorption coefficient, the corrected spectra would provide more reliable tendency compared to uncorrected ones.

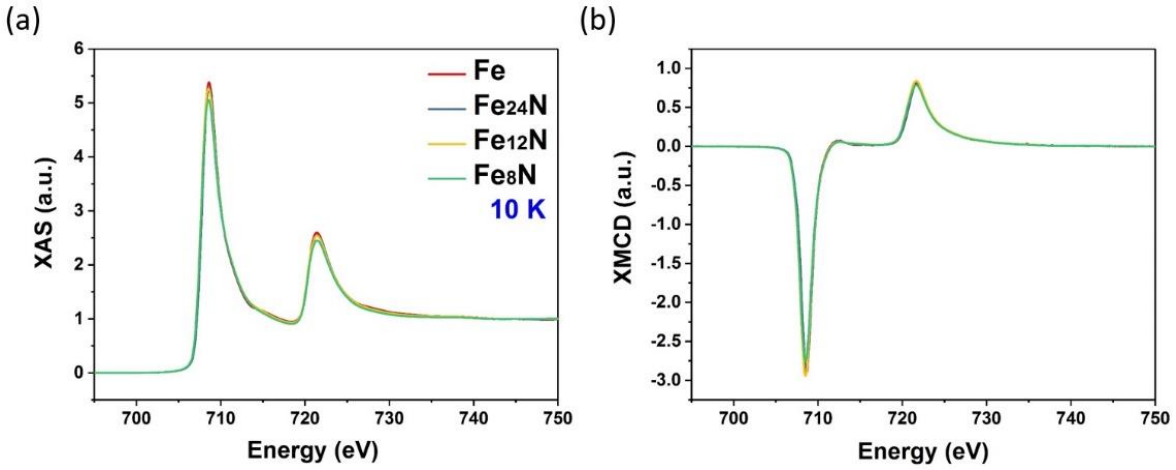

Figure 5.6 The normalized nonmagnetic XAS (a) and corresponding XMCD (b) curves for Fe, $Fe_{24}N$, $Fe_{12}N$, and Fe_8N films measured at 10 K along out-of-plane direction.

The fitting parameters obtained from the data correction were eventually used to modify corresponding μ_+ and μ_- spectra. Figure 5.6 shows the corrected μ_0 and XMCD curves of Fe-N thin films recorded at 10 K along out-of-plane direction. The peak intensities in XAS and XMCD profiles are very close for all specimens, but it still can be seen that the Fe_8N sample exhibits relatively smaller XAS and XMCD signals at resonance edges. The effective-spin and orbital moments evaluated by Eq. 2.26 and 2.27 from both uncorrected and corrected XMCD curves along out-of-plane direction (c-axis) are summarized in Figure 5.7. It is obvious that both effective-spin and orbital

moments are enhanced systematically along i.e. c-axis, namely larger saturation magnetization and anisotropy field. This tendency is in good agreement with the observed SQUID data (μ_B/Fe). Conversely, only effective-spin moments indeed increase as increased N doping along in-plane direction (see Figure 5.8). The invisible enhancement in orbital moments exactly matches the unchanged coersivity values of corresponding angular SQUID curves and Gölden's conclusion in Ref. [48].

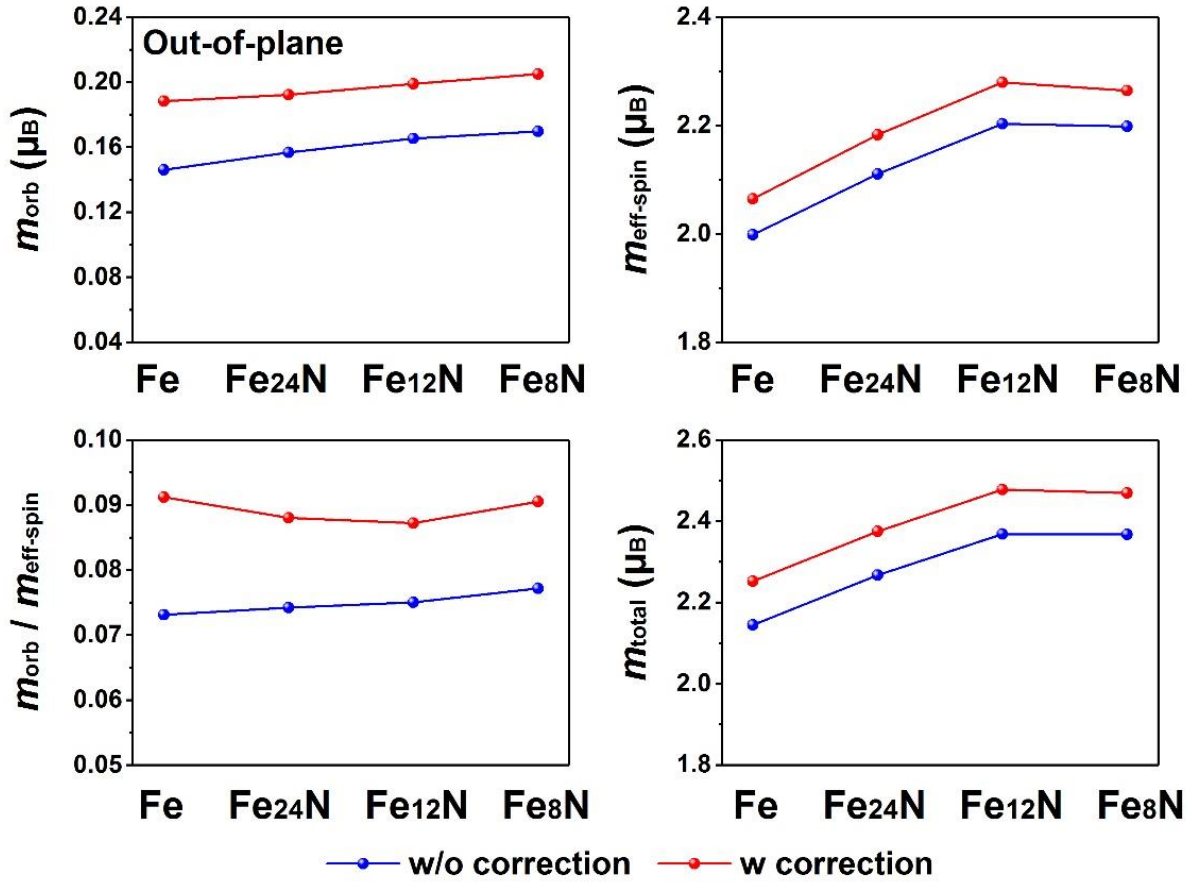

Figure 5.7 Dependence of orbital moment (m_{orb}), effective spin moment ($m_{eff\text{-}spin}$), $m_{orb}/m_{eff\text{-}spin}$ ratio, and total magnetic moment (m_{total}) at Fe site as a function of N doping along out-of-plane direction (c-axis).

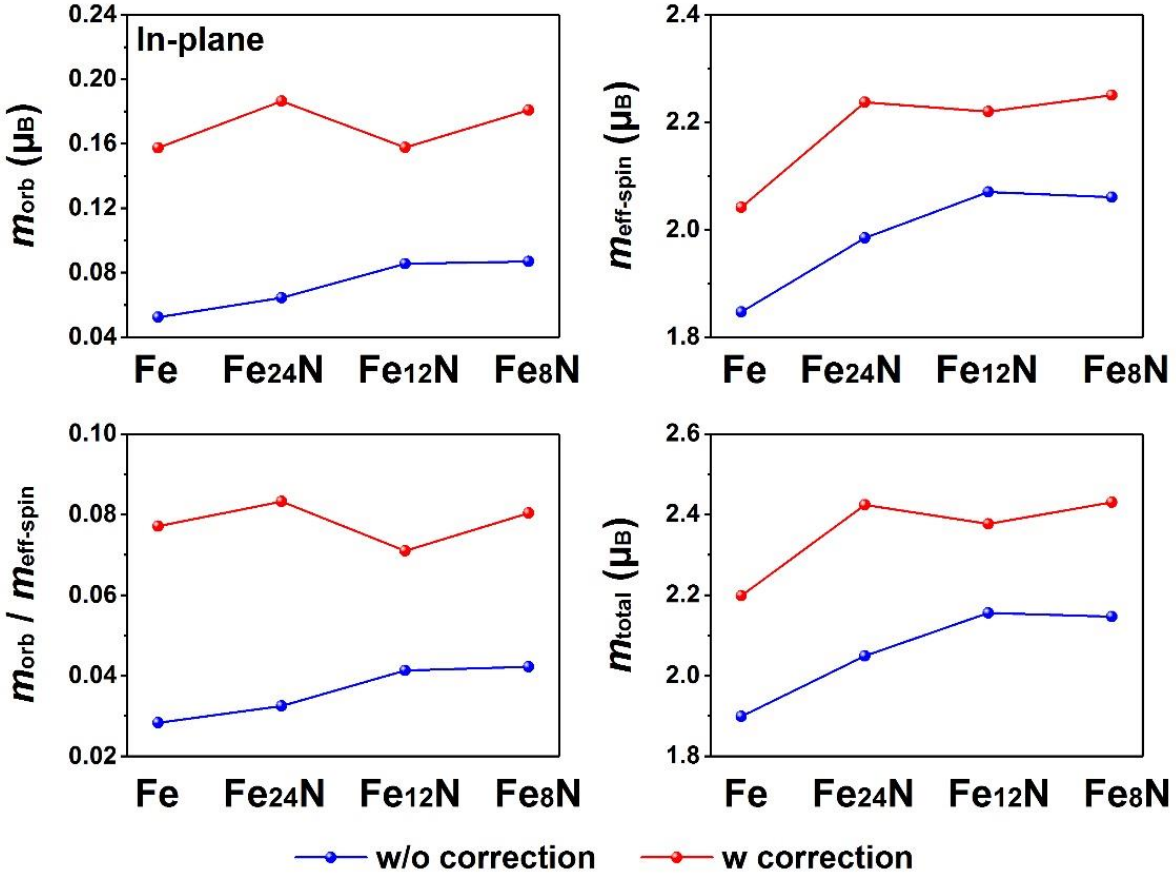

Figure 5.8 Dependence of orbital moment (m_{orb}), effective spin moment ($m_{eff-spin}$), $m_{orb}/m_{eff-spin}$ ratio, and total magnetic moment (m_{total}) at Fe site as a function of N doping along in-plane direction.

The detailed information of sum rule values from corrected XAS spectra are listed in Table 5.3 for clear comparison. Except $Fe_{24}N$, the variation in $m_{\mathrm{eff-spin}}$ and m_{orb} indicates that out-of-plane direction is easy-axis for all specimens. Due to the more than half-filled 3d states ($3d^{6.5\pm0.03}$ configuration),[138] both $m_{\mathrm{eff-spin}}$ and m_{orb} show the largest values along easy-axis in consistent with Bruno's model.[127] As mentioned above, α´-Fe_8N_x has a gradually distorted tetragonal unit structure. Hence T_z term may partially play a crucial role in the spin sum rule. Again, the estimation of T_z contribution is done by angle averaging spin sum rule provided that the spin-orbital coupling constant of Fe is much smaller than the exchange interaction.[17, 118, 128] The expectation values of Fe 3d T_z, m_{spin} and m_{orb} are

evaluated and summarized in Table 5.4. $Fe_{24}N$ is not discussed here because its angular data do not show systematical variation. It is found that the T_z could be still ignored in our study because the T_z/m_{spin} ratios are ~5% and ~3% for Fe and Fe_8N films, respectively. The average m_{spin} values of Fe and Fe_8N are 2.05 and 2.25 μ_B, which are close to the theoretical results of 1.98~2.2 and 2.4 μ_B respectively.[72, 138] However, the m_{orb} values are far larger than the theoretical prediction, which give 0.04~0.08 and 0.07 μ_B for Fe and Fe_8N respectively.[72, 137] The reason for this contradictory is not clear, but it could result from a large number of growth defects during the low-temperature synthesis or inappropriate orbital polarization treatment in DFT calculation.[49, 137] Nevertheless, the important result here is that both the average spin and orbital magnetic

Table 5.3 Detailed comparison of spin and orbital moments per Fe atom for Fe-N thin films. Noted that ξ_e-=1.3 nm and ξ_e-=1.4 nm are used for the saturation correction for Fe and Fe-N samples respectively. The average number of 3d electrons per Fe atom was set to 6.5 electrons for sum rum calculation.

Sample	angle	$m_{eff-spin}$ [μ_B]	m_{orb} [μ_B]	m_{total} [μ_B]	$\frac{m_{orb}}{m_{eff-spin}}$
Fe	90°	2.0646	0.1884	2.2530	0.0913
	40°	2.0466	0.1707	2.2173	0.0834
	17°	2.0419	0.1575	2.1994	0.0772
$Fe_{24}N$	90°	2.1832	0.1922	2.3754	0.0881
	40°	2.1724	0.1839	2.3563	0.0847
	17°	2.2377	0.1864	2.4240	0.0833
$Fe_{12}N$	90°	2.2795	0.1989	2.4784	0.0873
	40°	2.2453	0.1801	2.4254	0.0802
	17°	2.2197	0.1577	2.3774	0.0711
Fe_8N	90°	2.2647	0.2051	2.4698	0.0906
	40°	2.2416	0.1698	2.4113	0.0757
	17°	2.2503	0.1809	2.4312	0.0804

moments of Fe atoms do increase with an enlarged lattice expansion induced by the nitrogen incorporation in the Fe-N system.

Table 5.4 The experimental and theoretical magnetic moments of Fe atoms in Fe-N films. The m_{spin} term is defined as $m_{\mathrm{spin}} = (m_{\mathrm{spin}}^{0^\circ} + 2 \times m_{\mathrm{spin}}^{90^\circ})/3$. Hence $7m_{\mathrm{T}}^{\mathrm{x,y\ or\ z}} = m_{\mathrm{eff-spin}} - m_{\mathrm{spin}}$.

Sample	angle	$m_{\mathrm{T}}^{\mathrm{x,y\ or\ z}}$ [μ_B]	m_{orb} [μ_B]	m_{spin} [μ_B]	$m_{\mathrm{total}}^{XMCD}$ [μ_B]	m_{spin}^{Cal} [μ_B]	m_{orb}^{Cal} [μ_B]
Fe	90°	−0.0152	0.1884	2.0494	2.2379	2.22	0.05
	17°	0.0076	0.1575	2.0494	2.2070		
$Fe_{12}N$	90°	−0.0399	0.1989	2.2396	2.4385		
	17°	0.0199	0.1577	2.2396	2.3973		
Fe_8N	90°	−0.0096	0.2051	2.2551	2.4698	2.36	0.066
	17°	0.0048	0.1809	2.2551	2.4312		

Finally, we attempt to explain the origin of the enhanced magnetocrystalline anisotropy from Fe to Fe_8N. Similarly, the physics behind this phenomenon could be ascribed to the variation in orbital anisotropy proposed by Bruno's simple picture as discussed previously. Because the T_z contribution was obtained from angular dependent XMCD data, it is better to utilize van der Laan's MAE_K formula (Eq. 3.2) for this issue here again. The required parameters are listed in Table 5.5, and the spin-orbital coupling constant (ξ), exchange interaction (ΔE_{ex}) and MAE_K^{Cal} values are quoted from Refs. [139], [140] and [17, 137]. For Fe case, it is clear that the MAE_K^{exp} values (w or w/o T_z contribution) are much larger than the reference one by about two orders of magnitude. This result is absolutely not reasonable because α-Fe is well-known as a soft material with relatively low MAE_K. Therefore, it is not possible to have orbital variation of 0.03 μ_B

between two principle axes for α-Fe. Besides, ΔT_Z value is also too huge for us to believe. The big difference between our MAE_K^{exp} and MAE_K^{Cal} is most likely caused by insufficient or inappropriate saturation effect correction because there is still some gap in L_3 peak intensities between the corrected angular μ_0 spectra (see Figure 5.6). Additionally, the influence of defects should be taken into account in this issue too. Moreover, it seems that the T_Z contribution for Fe film must be deleted due to its cubic structure. For the tabulated data, it is found that the experimental MAE_K is much closer to the theoretical one without addition of T_Z component.

Table 5.5 Understanding of magnetic anisotropy energy of Fe-N_x compounds at atomic scale. Noted that $\widehat{\boldsymbol{S}}$ is set to 1 due to the saturated condition.

Sample	ξ [meV]	ΔE_{ex} [eV]	$\widehat{\boldsymbol{S}}$	ΔL	ΔT_Z	MAE_K^{exp} [μeV/atom]	MAE_K^{Cal} [μeV/atom]
Fe	50	1.2	1	−0.031	−0.023	883	4.02
	50	1.2	1	−0.031	0	385	4.02
Fe_8N	50	1.2	1	0.024	−0.0145	617	775

In contrast, our experimental MAE_K is in good agreement with the MAE_K^{Cal} value for Fe_8N. Noted that the observed orbital anisotropy of 0.024 μ_B from XMCD analysis is very close to the theoretical prediction, 0.03 μ_B given in Ref. [137]. Hence, it can be concluded that the magnetocrystalline energy of Fe_8N is determined mainly by the electronic configuration of Fe atoms. Both MAE_K and orbital variation of α'-Fe_8N are larger than those of α-Fe, so it is easier to identify the magnetic properties of Fe_8N at atomic scale within our experimental uncertainty.

Besides Fe $L_{2,3}$ edges, N K-edges of α'-Fe_8N_x specimens were measured multiple times to check if there is any reasonable XMCD effect at N atom. Although several DFT calculations predict a tiny spin moment (ex. −0.02

μ_B given in Ref. [44]) at N site antiparallel to that of Fe element, no clear XMCD curve were obtained in our 10 K measurements, as shown in Figure 5.9. Therefore, we can not address any comments on the role of N atoms in the observed magnetic properties.

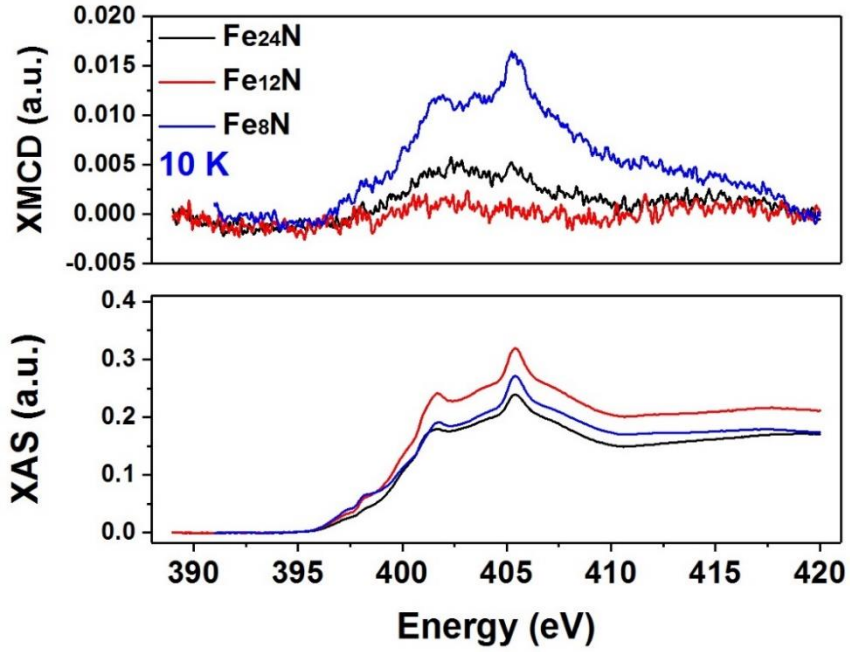

Figure 5.9 XMCD (top) and nonmagnetic XAS (bottom) curves for Fe-N thin films recorded at 10 K. The shapes of XMCD profiles are just from XAS offset.

6. Summary

In this thesis, three rare-earth-free magnetic compounds, LTP-MnBi, τ-MnAl and α'-Fe_8N, have been intensively studied from both theoretical and practical viewpoints. The former two materials are the main research targets of our G8 project. Besides the achievement in sample preparation, the magnetic properties of LTP-MnBi and τ-MnAl related samples were characterized by either phenomenological approach (microstructural analysis) or fundamental methodology (XMCD analysis). Fe-N system is another interesting topic because it was reported that the ordered phase, α''-$Fe_{16}N_2$, could shows giant saturation magnetization. A systematic investigation was carried out on α´-Fe_8N_x to clarify the evolution of magnetic response caused by corresponding structural deformation. Detailed experimental results and discussions are described briefly as following.

6.1. LTP-MnBi

It was demonstrated that high-purity LTP-MnBi powder and bulk magnets can be achieved using conventional metallurgical methods. In this study, the purified 2h-BM $Mn_{55}Bi_{45}$ powder exhibits remarkable room-temperature magnetic properties: M_r = 71 Am^2/kg and nominal $(BH)_{max}$ of 120 kJ/m^3, which are the highest record values for ball-milled powders so far. In addition, anisotropic bulk magnets with high remanence were also realized by both fast hot-compaction and spark-plasma-sintering techniques. It is worth noting that the $Mn_{45}Bi_{55}$ hot-compacted samples shows higher energy product value at above 500 K in comparison with NdFeB compound. This is the first experimental evidence that bulk LTP-MnBi can actually exhibit higher energy product than that of NdFeB above 450 K, as proposed by the theoretical prediction. The change of the room-temperature coercivity was investigated systematically using a phenomenological approach for all bulk magnets. A comprehensive microstructure analysis indicates that the observed coercive fields of bulk MnBi generally are enhanced with increasing area fraction of Bi residue, while it declines as corresponding grain size distribution and mean size goes up. Unlike NdFeB, the grain-

boundary phases between adjacent LTP-MnBi grains seem not to have an important impact on coercive field. Furthermore, the significant deviation of observed coercive fields ($\mu_0 H_c$) from the anisotropy fields ($2K_1/\mu_0 M_s$) is discussed using the microstructural parameters in Kronmüller's nucleation model. It was also proved that the unusual temperature-dependent coercivity behavior is strongly connected to corresponding temperature-dependent MAE_K due to the linear relation between $\mu_0 H_c/J_s$ vs $2K/M_s J_s$.

The thermal stability test reveals that all bulk samples retain the same magnetic properties after repeating heat treatment up to at least 500 K. This result is rather important from practical point of view. A careful DSC analysis confirms the remarkable thermal stability of the bulk magnets in this study compared to other reports in combination with reported phase diagrams. It is a pity that external field was unavailable throughout DSC measurements, hence thermodynamic characterization can not be carried out to clarify the unique thermal stability of the isotropic SPS-compacted specimens. Nevertheless, it was demonstrated that the magnetic properties of bulk MnBi are significantly tailored due to diverse microstructural modification. In light of above-mentioned experimental results, we suggest that LTP-MnBi based materials actually have a great potential to fill the gap of energy products between the best ferrite and NdFeB magnets.

Except microstructural effects on magnetic performance, the intensive XMCD measurements indicate that the magnetic anisotropy of LTP-MnBi is strongly associated with both the orbital moment anisotropy and anisotropic charge distribution of Mn 3d electrons. The angular XAS spectra (Mn $L_{2,3}$ edges) combined with van der Laan's generalized MAE_K model gives first experimental support for the theoretical DFT prediction, which shows smaller orbital moment along easy-axis. The evaluated values of magnetic moments suggest that the existence of unoccupied Mn 3d spin-up band could be responsible for this unusual phenomenon even though the Mn 3d states are more than half-filled. This assumption is further confirmed by the temperature-dependent XAS spectra, in which we observed more vacancies are present in 3d spin-up band along easy-axis of LTP-MnBi.

In addition to Mn 3d states, Bi 6p shell was also studied to identify its magnetic contribution. Although the intensities of XAS signals at Bi $M_{4,5}$ and $N_{4,5}$ edges are extremely small, clear XMCD effect was observed and confirms that the spin and orbital moments of Bi 6p states are anti-parallel to those of Mn 3d ones. To our knowledge, this is also the first experimental finding that strong spin polarization is present in a large element like Bi. Although the expectation values of magnetic moments can not be obtained due to the undetermined nonmagnetic XAS spectra, the large difference in orbital to spin moment ratio between easy- and hard-axes implies that the Bi atoms also have strong anisotropic magnetic properties. Unfortunately, the studies on angular and temperature-dependent variation on Bi sites have not been completed successfully yet since the signals in current results are drastically influenced by thermal leakage current. We still believe that related work could be done if more beamtime can be assigned for this research topic. Finally, it is noted that the observed XMCD effect on Bi 6p states can not be achieved without the successful work in sample fabrication.

6.2. τ-MnAl

τ-MnAl is indeed a very promising material for future permanent magnet applications because it is a low-cost material with high saturation magnetization. However, it is a big challenge task to approach the theoretical prediction of its magnetic performance due to the serious phase degradation caused by long-term particle size reduction. Another problem is the introduction of significant amount of defects during the milling process, which has have a negative impact on the magnetization of τ-phase MnAl.

In addition, it is known that the phase diagram of Mn-Al system is quite complicated. This feature leads to low purity of τ-phase in the ball-milled powders and sintered magnets since other non-ferromagnetic phases are always present in the real system. These non-magnetic phases enclose the τ-MnAl grains, so exchange coupling could not exist in the nanostructured material, which explains why the reported remanence ratios are usually

close to 0.5. In my opinions, a novel fabrication method is required to overcome these technical limitations, otherwise τ-MnAl based permanent magnets can be not realized in near future.

The XMCD spectra of the hot-compacted MnAl-C specimens show 'large' orbital moment, which is very unusual for 3d transition metals. However, it is not possible to clarify its origin because the texture is far too complicated (namely four different phases). Again, it is necessary to enhance the area fraction of τ-phase in the studied samples in order to obtain reasonable information for understanding the phenomenon at microscopic scale.

6.3. α´-Fe_8N

A systematic XMCD investigation shows that the evaluated orbital moments could explain the observed increasing coercive fields as a function of nitrogen incorporation. The magnetocrystalline anisotropy energy of α´-Fe_8N can be predominately determined by the orbital anisotropy of Fe atom in terms of Bruno's model. Besides, the expected increase in magnetic moments per Fe atom is also confirmed by corresponding enhanced spin moments. Although the mystery of giant magnet moment reported for α"-$Fe_{16}N_2$ is not observed in this study, we unambiguously demonstrated that the α´-Fe_8N_x films could be a great example for the idea of Bethe-Slater curve.

Although the magnitude of orbital moments at Fe site is not consistent with that of first principle calculation values, the tendency is still obvious for the FeN thin films. The discrepancy could originate from the defects during the low-temperature synthesis or surface effect because the theoretical estimation is based on perfect and bulk-like periodic structure. Moreover, it is not clear how much influence could be induced by the capping layer in the case of TEY measurements. Therefore, detailed and systematic DFT calculation is required to be done for further discussions. Furthermore, the XMCD intensities are too weak to be resolved at N K-edge within our technical limit. Therefore, it is not possible to make any comments on the

contribution of doped N atom inside the α-Fe bcc unit structure, for example, the p-d hybridization between N atom and its the nearest 6 iron neighbors.

7. Zusammenfassung

Die drei magnetischen Verbindungen ohne Seltene Erden LTP-MnBi, τ-MnAl und α'-Fe_8N wurden im Rahmen dieser Studie sowohl theoretisch als auch praktisch untersucht. Im Besonderen stehen LTP-MnBi und τ-MnAl im Fokus unseres G8 Projekts. Neben den erreichten Erfolgen in der Probenherstellung wurden außerdem die magnetischen Eigenschaften dieser zwei Materialien entweder durch einen phänomenologischen Ansatz (mikrostrukturelle Analyse) oder mit Hilfe grundlegender Methoden (XMCD Messungen) charakterisiert. Ein weiteres interessantes Material ist Fe-N da für die geordnete α''-$Fe_{16}N_2$ Phase sehr hohe Sättigungsmagnetisierungen beobachtet wurden. Um die Entwicklung der magnetischen Reaktion durch strukturelle Verformung zu verstehen wurden systematische Untersuchungen an α'-Fe_8N_x durchgeführt. Im Folgenden werden die experimentellen Ergebnisse kurz umrissen.

7.1. LTP-MnBi

Es wurde gezeigt, dass sowohl hochreines LTP-MnBi Pulver als auch Volumenmagnete mit herkömmlichen metallurgischen Methoden hergestellt werden können. Das in dieser Arbeit beschriebene, reine 2h-BM $Mn_{55}Bi_{45}$ Pulver zeigt außergewöhnlich gute magnetische Eigenschaften bei Raumtemperatur. Eine Remanenzmagnetisierung von M_r = 71 Am^2/kg und ein Energieprodukt von $(BH)_{max}$ = 120 kJ/m^3 stellen einen Rekordwert für mittels einer Kugelmühle gemahlenen Pulver dar. Zudem wurden anisotrope Volumenmagnete mit hoher Remanenzmagnetisierung mittels Heißverdichtung und Funkenplasmasintern präpariert. Erwähnenswert ist, dass durch Heißverdichtung hergestellte $Mn_{45}Bi_{55}$ Proben über 500 K ein höheres maximales Energieprodukt haben als NdFeB Verbindungen. Dies ist der erste experimentelle Beleg der theoretischen Prognose, dass LTP-MnBi über einer Temperatur von 450 K ein höheres Energieprodukt als NdFeB haben kann. Die Änderung der Koerzitivfeldstärke der Volumenmagnete bei Raumtemperatur wurde systematisch mit einem phänomenologischen Ansatz untersucht. Eine umfassende Mikrostrukturanalyse legt nahe, dass

die beobachtete Erhöhung des Koerzitivfeldes in MnBi Volumenmagneten durch größere Flächenanteile von Bi Ablagerungen hervorgerufen wird. Dagegen verschlechtern sich diese durch eine breitere Korngrößenverteilung und größere mittlere Korngrößen. Im Gegensatz zu NdFeB scheint die Korngrenzenphase zwischen benachbarten Körnchen keinen wesentlichen Einfluss auf das Koerzitivfeld zuhaben. Die beträchtliche Abweichung des gemessenen Koerzitivfeldes ($\mu_0 H_c$) vom Anisotropiefeld ($2K_1/\mu_0 M_s$) wird mit Hilfe der mikrostrukturellen Parameter in Kronmüllers Nukleationmodell dikutiert. Es konnte gezeigt werden, dass das ungewöhnliche, temperaturabhängige Koerzitivfeldverhalten von MnBi stark mit der Temperaturabhängigkeit der magnetischen Anisotropieenergie in Verbindung steht, da es einen linearen Zusammenhang zwischen $\mu_0 H_c/J_s$ und $2K/M_s J_s$ gibt.

Wiederholte Wärmebehandlung bei Temperaturen von mindestens 500 K um die thermische Stabilität der Volumenmagnete zu testen führen zu keinen Veränderungen der magnetischen Eigenschaften, was für die praktische Anwendung von großer Bedeutung ist. Die bemerkenswert hohe thermische Stabilität der untersuchten Volumenmagnete, verglichen mit anderen Studien und Phasendiagrammen, wurde durch eine sorgfältige DSC Analyse bestätigt. Während DSC Messungen war es nicht möglich externe Felder anzulegen um mit Hilfe einer thermodynamische Charakterisierung die hohe thermische Stabilität der mittels Funkenplasmasintern hergestellten Proben zu erklären. Nichtsdestotrotz konnte gezeigt werden, dass die magnetischen Eigenschaften von MnBi Volumenmagneten durch mikrostrukturelle Modifikationen maßgeschneidert werden können. Die experimentellen Ergebnisse zeigen, dass LTP-MnBi basierte Materialien das Potential haben die Lücke in erreichbaren Energieprodukten zwischen den besten Ferrit- und NdFeB-Magneten zu schließen.

Neben dem Einfluss der Mikrostruktur auf die magnetischen Eigenschaften von LTP-MnBi legen die umfangreichen XMCD Messungen Nahe, dass das magnetische Moment dieser Proben stark mit der Bahndrehimpuls Anisotropie und der anisotropen Ladungsverteilung der Mn 3d Elektronen zusammenhängt. Das XAS Winkelspektrum (Mn $L_{2,3}$ Kanten) zusammen

mit van der Laan's verallgemeinertem MAE_K Model bestätigt erstmals experimentell die theoretische Vorhersage, dass das Bahndrehmoment entlang der leichten Richtung kleiner ist. Die mit Hilfe der Summenregeln berechneten Werte deuten die Existenz eines unbesetzten Mn 3d spin-up Bandes an welches Verantwortlich für das ungewöhnliche Phänomen von mehr als halb gefüllten Mn 3d Zuständen sein könnte.

Neben der Mn 3d Zustände wurden auch die Bi 6p Zustände untersucht um ihren Beitrag zu den magnetischen Eigenschaften zu bestimmen. Trotz der niedrigen Intensität des XAS Signals an den Bi $M_{4,5}$ und $N_{4,5}$ Kanten konnte ein eindeutiger XMCD Effekt gemessen werden. Dieser bestätigt, dass die Bi 6p und Mn 3d Bahndrehmomente antiparallel ausgerichtet sind. Erstmals konnte damit experimentell gezeigt werden, dass es eine starke Spinpolarisation in großen Elementen wie Bi geben kann. Die Erwartungswerte der magnetischen Momente konnten durch die fehlenden nichtmagnetischen XAS Spektren nicht bestimmt werden. Trotzdem zeigt die große Differenz des Bahn- zu Spindrehmoment Verhältnisses zwischen leichter und schwerer Richtung, dass Bi Atome stark anisotrope magnetische Eigenschaften haben. Winkel und Temperatur abhängige Veränderungen an den Bismutatomen konnten wegen des starken Einflusses von thermischen Leckströmen auf das Signal bisher noch nicht erfolgreich gemessen werde. Wir sind allerdings davon überzeugt, dass diese Probleme in kommenden Strahlzeiten behoben werden können. Abschließend muss erwähnt werden, dass beobachteten XMCD Effekte an den Bi 6p Zuständen nicht möglich gewesen wäre ohne die Erfolgreich Probenpräparation.

7.2. τ-MnAl

τ-MnAl ist ein vielversprechendes Material im Anwendungsbereich von Permanentmagneten, das sich besonders durch niedrige Materialkosten und eine hohe Sättigungsmagnetisierung auszeichnet. Aufgrund der langfristigen Reduktion der Korngrößen und die damit einhergehende „phase degradation" können die von der Theorie vorhergesagten Eigenschaften

nicht ohne weiteres komplett ausgeschöpft werden. Dies zu verbessern stellt eine wichtige Aufgabe dar. Des Weiteren werden während des Mahlens eine signifikante Anzahl an Fehlstellen in das Material eingebracht, was ebenfalls einen negativen Effekt auf die Magnetisierung der τ-phase von MnAl haben kann.

Hinzu kommt, dass das Phasendiagramm des MnAl-Systems recht komplex ist. Dies führt dazu, dass in den gesinterten und pulverförmigen Materialien neben der τ-Phase noch andere nicht ferromagnetische Phasen präsent sind. Diese nicht ferromagnetischen Bereiche umschließen die τ-MnAl Körnchen, sodass in den nanostrukturierten Materialien keine Austauschwechselwirkung auftreten kann. Dies kann die Remanenz-Verhältnisse, die nahe bei 0.5 liegen, erklären. Meiner Meinung nach bedarf es einer neuen Herstellungsmethode um diese technischen Schwierigkeiten zu überwinden. Davon abgesehen könnten τ-MnAl basierte Permanentmagnete bereits in naher Zukunft realisiert werden.

Die XMCD-Spektren der unter erhöhter Temperatur verdichteten MnAl-C Proben zeigen, anders als bei 3d Übergangsmetallen zu erwarten, „große" Bahnmomente. Aufgrund der komplexen Struktur, bestehend aus den vier unterschiedlichen Phasen, ist es nicht ohne weiteres möglich den Ursprung dieser erhöhten Bahnmomente zu klären. An dieser Stelle sei noch einmal erwähnt, dass der Oberflächenanteil der τ-Phase in den zu untersuchenden Proben erhöht werden muss um zuverlässige Informationen über die auf mikroskopischer Ebene zugrundeliegenden Effekte zu gewinnen.

7.3. α´-Fe_8N

Eine systematische Untersuchung mittels XMCD zeigt, dass die so ermittelten Bahnmomente die beobachtbare Erhöhung des Koerzitivfelds durch Inkorporierung von Stickstoffatomen erklärt werden kann. Die magnetokristalline Anisotropieenergie von α'-Fe_8N kann, in Bezug auf „Brunos Modell", vorwiegend als Anisotropie der Fe-Orbitale verstanden werden. Die zu erwartende Erhöhung des magnetischen Moments pro Eisenatom ist durch die erhöhten Spin momente begründet. Obwohl die rätselhafte

Eigenschaft von α''-$Fe_{16}N_2$, besonders große magnetische Momente zu besitzen, in dieser Studie nicht beobachtet werden konnte, konnte eindeutig gezeigt werden, dass die α'-Fe_8N-Filme ein gutes Beispiel für die Anwendung der Bethe-Slater-Kurve darstellen.

Obwohl der Betrag der Bahnmomente an den Eisenatomen nicht mit den Werten von „first principle"-Rechnungen übereinstimmt, so ist die Tendenz bei dünnen FeN Filmen doch klar zu erkennen. Diese Abweichungen könnten darauf beruhen, dass das theoretische Modell von einer perfekt periodischen Anordnung des Systems ausgeht. Im echten System hingegen können Oberflächeneffekte und Fehler bei der Herstellung eine Rolle spielen. Zudem ist es nicht klar, welchen und wie viel Einfluss der „capping layer" auf die TEY-Messungen hat. Darum werden detaillierte und systematische DFT-Kalkulationen benötigt, um eine weitere Diskussion zu ermöglichen. Zudem sind die Intensitäten des XMCD-Signals nicht hoch genug, um sie mit den derzeitigen technischen Hilfsmitteln an der N K-Kante aufzulösen. Darum ist es nicht möglich irgendwelche Aussagen über die Verteilung von dotierten Stickstoffatomen innerhalb der α-Fe bcc Einheitszelle zu treffen, zum Beispiel die p-d-Hybridisierung zwischen einem Stickstoffatom und den 6 benachbarten Eisenatomen.

Bibliography

1. Kramer, M.J., et al., *Prospects for Non-Rare Earth Permanent Magnets for Traction Motors and Generators.* JOM, 2012. **64**(7): p. 752-763.
2. Gutfleisch, O., et al., *Magnetic Materials and Devices for the 21st Century: Stronger, Lighter, and More Energy Efficient.* Advanced Materials, 2011. **23**(7): p. 821-842.
3. Skomski, R. and D.J. Sellmyer, *Anisotropy of rare-earth magnets.* Journal of Rare Earths, 2009. **27**(4): p. 675-679.
4. Zeng, Q., et al., *Structural and magnetic properties of nanostructured Mn–Al–C magnetic materials.* Journal of Magnetism and Magnetic Materials, 2007. **308**(2): p. 214-226.
5. Humphries, M., *Rare Earth Elements:The Global Supply Chain*. 2013, U.S. Department of Energy.
6. Coey, J.M.D., *Hard Magnetic Materials: A Perspective.* IEEE Transactions on Magnetics, 2011. **47**(12): p. 4671-4681.
7. *Critical Materials Strategy December 2011*, U.S.D.o. Energy, Editor. 2012, U.S. Department of Energy: USA.
8. Coey, J.M.D., *Permanent magnets: Plugging the gap.* Scripta Materialia, 2012. **67**(6): p. 524-529.
9. Coey, J.M.D., *New permanent magnets; manganese compounds.* Journal of Physics: Condensed Matter, 2014. **26**(6): p. 064211.
10. B. D. Cullity, C.D.G., *Introduction to Magnetic Materials*. 2008: Wiley-IEEE Press.
11. O'Handley, R.C., *Modern Magnetic Materials Principles and Applications*, ed. 1. 2000: John Wiley & Sons.
12. Skomski, R., *Simple Models of Magnetism*. 2012: Oxford University Press.
13. Blundell, S., *Magnetism In Condensed Matter*. 2000: Oxford University Press.
14. Shanavas, K.V., Z.S. Popović, and S. Satpathy, *Theoretical model for Rashba spin-orbit interaction in d electrons.* Physical Review B, 2014. **90**(16): p. 165108.
15. Coey, J.M.D., *Magnetism and Magnetic Materials*. Cambridge University Press.
16. Michael, M., et al., *Open shells and multi-electron interactions: core level photoionization of the 3d metal atoms.* Journal of Physics B: Atomic, Molecular and Optical Physics, 2006. **39**(5): p. R79.

17. Bruno, P., *Physical origins and theoretical models of magnetic anisotropy*. Magnetismus von Festkörpern und Grenzflächen. Vol. 24. 1993: Forschungszentrum Jülich.
18. Jiles, D.C., *Introduction to Magnetism and Magnetic Materials*. 3 ed. 2015: Apple Academic Press Inc.
19. Bertotti, G., *Hysteresis in Magnetism: For Physicists, Materials Scientists, and Engineers*. 1998.
20. Kronmüller, H., *Theory of Nucleation Fields in Inhomogeneous Ferromagnets.* physica status solidi (b), 1987. **144**(1): p. 385-396.
21. Kronmüller, H., K.D. Durst, and G. Martinek, *Angular dependence of the coercive field in sintered Fe77Nd15B8 magnets.* Journal of Magnetism and Magnetic Materials, 1987. **69**(2): p. 149-157.
22. Kronmüller, H., K.D. Durst, and M. Sagawa, *Analysis of the magnetic hardening mechanism in RE-FeB permanent magnets.* Journal of Magnetism and Magnetic Materials, 1988. **74**(3): p. 291-302.
23. Widmer, J.D., R. Martin, and M. Kimiabeigi, *Electric vehicle traction motors without rare earth magnets.* Sustainable Materials and Technologies, 2015. **3**: p. 7-13.
24. Oikawa, K., et al., *Thermodynamic Assessment of the Bi-Mn System.* MATERIALS TRANSACTIONS, 2011. **52**(11): p. 2032-2039.
25. Chinnasamy, C., et al., *Mn-Bi Magnetic Powders With High Coercivity and Magnetization at Room Temperature.* IEEE Transactions on Magnetics, 2012. **48**(11): p. 3641-3643.
26. Cui, J., et al., *Thermal stability of MnBi magnetic materials.* Journal of Physics: Condensed Matter, 2014. **26**(6): p. 064212.
27. Köhler, J. and J. Kübler, *Calculated magneto-optical properties of pure and doped MnBi.* Journal of Physics: Condensed Matter, 1996. **8**(44): p. 8681.
28. Park, J., et al., *Electronic Structure and Maximum Energy Product of MnBi.* Metals, 2014. **4**(3).
29. Yang, J.B., et al., *Crystal structure, magnetic properties and electronic structure of the MnBi intermetallic compound.* Journal of Physics: Condensed Matter, 2002. **14**(25): p. 6509.
30. Yang, Y.B., et al., *Temperature dependences of structure and coercivity for melt-spun MnBi compound.* Journal of Magnetism and Magnetic Materials, 2013. **330**: p. 106-110.
31. Pasko, A., et al., *Hard magnetic properties of melt-spun Mn-Al-C alloys.* EPJ Web of Conferences, 2013. **40**: p. 06008.

32. Kim, Y.J. and J.H. Perepezko, *Formation of a metastable ferromagnetic τ phase during containerless melt processing and rapid quenching in Mn-Al-C alloys.* Journal of Applied Physics, 1992. **71**(2): p. 676-680.
33. Nie, S.H., et al., *Perpendicularly magnetized τ-MnAl (001) thin films epitaxied on GaAs.* Applied Physics Letters, 2013. **102**(15): p. 152405.
34. Park, J.H., et al., *Saturation magnetization and crystalline anisotropy calculations for MnAl permanent magnet.* Journal of Applied Physics, 2010. **107**(9): p. 09A731.
35. Jian, H., K.P. Skokov, and O. Gutfleisch, *Microstructure and magnetic properties of Mn–Al–C alloy powders prepared by ball milling.* Journal of Alloys and Compounds, 2015. **622**: p. 524-528.
36. Anurag, C., Y. Rumana, and B. Ian, *A comparison of τ -MnAl particulates produced via different routes.* Journal of Physics: Condensed Matter, 2014. **26**(6): p. 064201.
37. Jiménez-Villacorta, F., et al., *Exchange anisotropy in the nanostructured MnAl system.* Applied Physics Letters, 2012. **100**(11): p. 112408.
38. Wiezorek, J.M.K., et al., *Grain Boundary Mediated Displacive–Diffusional Formation of τ-Phase MnAl.* Metallurgical and Materials Transactions A, 2011. **42**(3): p. 594-604.
39. Saito, T., *Magnetic properties of Mn–Al system alloys produced by mechanical alloying.* Journal of Applied Physics, 2003. **93**(10): p. 8686-8688.
40. Zeng, Q., I. Baker, and Z.-c. Yan, *Nanostructured Mn–Al permanent magnets produced by mechanical milling.* Journal of Applied Physics, 2006. **99**(8): p. 08E902.
41. Geng, Y., et al., *Phase transformation and magnetic properties of rapidly solidified Mn-Al-C alloys modified with Zr.* Journal of Applied Physics, 2015. **118**(3): p. 033905.
42. Madugundo, R., O. Koylu-Alkan, and G.C. Hadjipanayis, *Bulk Mn-Al-C permanent magnets prepared by various techniques.* AIP Advances, 2016. **6**(5): p. 056009.
43. Wang, J.P., et al., *Fabrication of Fe16N2 Films by Sputtering Process and Experimental Investigation of Origin of Giant Saturation Magnetization in Fe16N2.* IEEE Transactions on Magnetics, 2012. **48**(5): p. 1710-1717.
44. Matar, S., *The magnetic properties of iron nitride: Fe8N.* Zeitschrift für Physik B Condensed Matter, 1992. **87**(1): p. 91-96.
45. Tomoyuki, O., et al., *Challenge to the Synthesis of α''-Fe 16N2 Compound Nanoparticle with High Saturation Magnetization for Rare Earth Free New Permanent Magnetic Material.* Applied Physics Express, 2013. **6**(7): p. 073007.

46. Sugita, Y., et al., *Magnetic and Mössbauer studies of single-crystal Fe16N2 and Fe-N martensite films epitaxially grown by molecular beam epitaxy (invited).* Journal of Applied Physics, 1994. **76**(10): p. 6637-6641.
47. Ke, L., et al., *Effects of alloying and strain on the magnetic properties of Fe16N2.* Physical Review B, 2013. **88**(2): p. 024404.
48. Gölden, D., E. Hildebrandt, and L. Alff, *Thin film phase diagram of iron nitrides grown by molecular beam epitaxy.* Journal of Magnetism and Magnetic Materials, 2017. **422**(Supplement C): p. 407-411.
49. Dirba, I., et al., *Increased magnetic moment induced by lattice expansion from α-Fe to α′-Fe8N.* Journal of Applied Physics, 2015. **117**(17): p. 173911.
50. Wang, H., P.-W. Ma, and C.H. Woo, *Exchange interaction function for spin-lattice coupling in bcc iron.* Physical Review B, 2010. **82**(14): p. 144304.
51. Willmott, P., *An Introduction to Synchrotron Radiation: Techniques and Applications*. 2011: John Wiley & Sons.
52. *BOREAS soft X-ray beamline*. Available from: https://www.cells.es/en/beamlines/bl29-boreas.
53. *WERA soft x-ray beamtine*. Available from: https://www.anka.kit.edu/766.php.
54. O'Brien, W.L., et al., *Experimental investigation of dichroism sum rules for V, Cr, Mn, Fe, Co, and Ni: Influence of diffuse magnetism.* Journal of Applied Physics, 1994. **76**(10): p. 6462-6464.
55. Schütz, G., et al., *Absorption of circularly polarized x rays in iron.* Physical Review Letters, 1987. **58**(7): p. 737-740.
56. Chen, C.T., et al., *Soft-x-ray magnetic circular dichroism at the L2,3 edges of nickel.* Physical Review B, 1990. **42**(11): p. 7262-7265.
57. Thole, B.T., et al., *X-ray circular dichroism as a probe of orbital magnetization.* Physical Review Letters, 1992. **68**(12): p. 1943-1946.
58. Carra, P., et al., *X-ray circular dichroism and local magnetic fields.* Physical Review Letters, 1993. **70**(5): p. 694-697.
59. Stöhr, J., *Exploring the microscopic origin of magnetic anisotropies with X-ray magnetic circular dichroism (XMCD) spectroscopy.* Journal of Magnetism and Magnetic Materials, 1999. **200**(1): p. 470-497.
60. van der Laan, G. and A.I. Figueroa, *X-ray magnetic circular dichroism—A versatile tool to study magnetism.* Coordination Chemistry Reviews, 2014. **277-278**(Supplement C): p. 95-129.
61. Groot, F.d., *Multiplet effects in X-ray spectroscopy.* Coordination Chemistry Reviews, 2005. **249**(1): p. 31-63.

62. Cowan, R.D., *The Theory of Atomic Structure and Spectra*. Los Alamos Series in Basic and Applied Sciences.
63. Agarwal, B.K., *X-Ray Spectroscopy: An Introduction*. 1991: Springer.
64. Hidekazu, I., et al., *Multiplet calculations of L 2,3 x-ray absorption near-edge structures for 3d transition-metal compounds.* Journal of Physics: Condensed Matter, 2009. **21**(10): p. 104208.
65. Macke, S. and E. Goering, *Magnetic reflectometry of heterostructures.* Journal of Physics: Condensed Matter, 2014. **26**(36): p. 363201.
66. Goering, E., et al., *X-ray magnetic circular dichroism — a universal tool for magnetic investigations.* Journal of Alloys and Compounds, 2001. **328**(1): p. 14-19.
67. de Groot, F.M.F., et al., *Fluorescence yield detection: Why it does not measure the X-ray absorption cross section.* Solid State Communications, 1994. **92**(12): p. 991-995.
68. Nakajima, R., J. Stöhr, and Y.U. Idzerda, *Electron-yield saturation effects in L-edge x-ray magnetic circular dichroism spectra of Fe, Co, and Ni.* Physical Review B, 1999. **59**(9): p. 6421-6429.
69. Goering, E., et al., *Non-symmetric influences in the total electron yield X-ray magnetic circular dichroism signal in applied magnetic fields.* Journal of Synchrotron Radiation, 2001. **8**(2): p. 434-436.
70. Gota, S., M. Gautier-Soyer, and M. Sacchi, *Fe 2p absorption in magnetic oxides: Quantifying angular-dependent saturation effects.* Physical Review B, 2000. **62**(7): p. 4187-4190.
71. Goering, E., et al., *Element specific x-ray magnetic circular dichroism magnetization curves using total electron yield.* Journal of Applied Physics, 2000. **88**(10): p. 5920-5923.
72. Chen, C.T., et al., *Experimental Confirmation of the X-Ray Magnetic Circular Dichroism Sum Rules for Iron and Cobalt.* Physical Review Letters, 1995. **75**(1): p. 152-155.
73. Vogel, J. and M. Sacchi, *Experimental estimate of absorption length and total electron yield (TEY) probing depth in dysprosium.* Journal of Electron Spectroscopy and Related Phenomena, 1994. **67**(1): p. 181-188.
74. Thole, B.T., et al., *3d x-ray-absorption lines and the 3d94fn+1 multiplets of the lanthanides.* Physical Review B, 1985. **32**(8): p. 5107-5118.
75. Goering, E., et al., *Vanishing Fe 3d orbital moments in single-crystalline magnetite.* EPL (Europhysics Letters), 2006. **73**(1): p. 97.
76. *ANKA Instrumentation Book 2012*. 2013: ANKA Synchrotron Radiation Facility, Karlsruhe Institute of Technology.
77. Rainer Pöttgen, D.J., *Intermetallics: Synthesis, Structure, Function*. 2014: De Gruyter.

78. *Arc melting system*. Available from: http://swlee.engr.uconn.edu/research/advanced-metal-intermetallic-composites/.
79. Upadhyaya, G.S., *Powder Metallurgy Technology*. 2002: Cambridge International Science Publishi.
80. Baláž, P., *Mechanochemistry in Nanoscience and Minerals Engineering*. 2008: Springer Berlin Heidelberg.
81. Subramanian, P.C.A.R., *Powder Metallurgy: Technology and Applications*. 2008.
82. Schreyer, P., *Direct Hot-pressing Makes Sintering of Near-net-shape Parts Quick and Easy*. Dr. Fritsch Sondermaschinen GmbH.
83. Hungría, T., J. Galy, and A. Castro, *Spark Plasma Sintering as a Useful Technique to the Nanostructuration of Piezo-Ferroelectric Materials.* Advanced Engineering Materials, 2009. **11**(8): p. 615-631.
84. Guillon, O., et al., *Field-Assisted Sintering Technology/Spark Plasma Sintering: Mechanisms, Materials, and Technology Developments.* Advanced Engineering Materials, 2014. **16**(7): p. 830-849.
85. Robert Ernst Dinnebier, S.J.L.B., *Powder Diffraction: Theory and Practice*. 2008: Royal Society of Chemistry.
86. John Clarke, A.I.B., *The SQUID Handbook: Fundamentals and Technology of SQUIDs and SQUID Systems*. 2004: Wiley-VCH.
87. Aharoni, A., *Demagnetizing factors for rectangular ferromagnetic prisms.* Journal of Applied Physics, 1998. **83**(6): p. 3432-3434.
88. Alex Hubert, R.S., *Magnetic Domains: The Analysis of Magnetic Microstructures*. 2008: Springer.
89. Horst Czichos , T.S., Leslie Smith, *Springer Handbook of Materials Measurement Methods*. 2006: Springer.
90. Günther Höhne, W.F.H., *Differential Scanning Calorimetry*. 2 ed. 2003: Springer.
91. Gill, P., T.T. Moghadam, and B. Ranjbar, *Differential Scanning Calorimetry Techniques: Applications in Biology and Nanoscience.* Journal of Biomolecular Techniques : JBT, 2010. **21**(4): p. 167-193.
92. *AccuPycTM 1330 Pycnometer Operator's Manual*. 2001.
93. Webb, P.A. *Volume and Density Determinations for Particle Technologists*. 2001. 16.
94. Moore, G.L., *Introduction to Inductively Coupled Plasma Atomic Emission Spectrometry*. 2012: Elsevier Science.
95. Thompson, M., *Handbook of Inductively Coupled Plasma Spectrometry*. 2013: Springer.

96. website, F.G.-M.a.S. *Planetary Mono Mill PULVERISETTE 6*. Available from: http://www.fritsch-international.com/sample-preparation/milling/planetary-mills/details/product/pulverisette-6-classic-line/.
97. Ko, K.Y., et al., *MnBi magnets fabricated through spark plasma-sintering process.* Journal of Magnetism and Magnetic Materials, 2007. **310**(2, Part 3): p. e887-e889.
98. Pasko, A., et al., *Spark plasma sintering of Mn–Al–C hard magnets.* Journal of Physics: Condensed Matter, 2014. **26**(6): p. 064203.
99. Zhang, D.T., et al., *Structural and magnetic properties of bulk MnBi permanent magnets.* Journal of Applied Physics, 2011. **109**(7): p. 07A722.
100. Cui, J., et al., *Effect of composition and heat treatment on MnBi magnetic materials.* Acta Materialia, 2014. **79**: p. 374-381.
101. Yang, J.B., et al., *Anisotropic nanocrystalline MnBi with high coercivity at high temperature.* Applied Physics Letters, 2011. **99**(8): p. 082505.
102. Rao, N.V.R., A.M. Gabay, and G.C. Hadjipanayis, *Anisotropic fully dense MnBi permanent magnet with high energy product and high coercivity at elevated temperatures.* Journal of Physics D: Applied Physics, 2013. **46**(6): p. 062001.
103. Yang, J.B., et al., *Magnetic properties of the MnBi intermetallic compound.* Applied Physics Letters, 2001. **79**(12): p. 1846-1848.
104. Kronmüller, H., J.B. Yang, and D. Goll, *Micromagnetic analysis of the hardening mechanisms of nanocrystalline MnBi and nanopatterned FePt intermetallic compounds.* Journal of Physics: Condensed Matter, 2014. **26**(6): p. 064210.
105. Hozumi, T., et al., *Magnetic and structural properties of MnBi multilayered thin films.* Journal of Applied Physics, 2014. **115**(17): p. 17A737.
106. Luborsky, F.E., *Development of Elongated Particle Magnets.* Journal of Applied Physics, 1961. **32**(3): p. S171-S183.
107. Chen, Y.-C., et al., *Unique high-temperature performance of highly condensed MnBi permanent magnets.* Scripta Materialia, 2015. **107**: p. 131-135.
108. Liu, Y., et al., *Microstructure, crystallization, and magnetization behaviors in MnBi-Bi composites aligned by applied magnetic field.* Physical Review B, 2005. **72**(21): p. 214410.
109. Toshiyuki, K., *Phase-field modeling of microstructure evolutions in magnetic materials.* Science and Technology of Advanced Materials, 2008. **9**(1): p. 013006.

110. Tu, C. and W. Stutius, *The phase transformation and physical properties of the MnBi and Mn1.08Bi compounds.* IEEE Transactions on Magnetics, 1974. **10**(3): p. 581-586.
111. Antropov, V.P., et al., *Magnetic anisotropic effects and electronic correlations in MnBi ferromagnet.* Physical Review B, 2014. **90**(5): p. 054404.
112. Muralidhar, S., et al., *Temperature-dependent first-order reversal curve measurements on unusually hard magnetic low-temperature phase of MnBi.* Physical Review B, 2017. **95**(2): p. 024413.
113. Goll, D., M. Seeger, and H. Kronmüller, *Magnetic and microstructural properties of nanocrystalline exchange coupled PrFeB permanent magnets.* Journal of Magnetism and Magnetic Materials, 1998. **185**(1): p. 49-60.
114. Guo, X., et al., *Magnetic properties of MnBi prepared by rapid solidification.* Physical Review B, 1992. **46**(22): p. 14578-14582.
115. Liu, J., et al., *Grain size dependence of coercivity of hot-deformed Nd–Fe–B anisotropic magnets.* Acta Materialia, 2015. **82**(Supplement C): p. 336-343.
116. Roberts, B.W. and C.P. Bean, *Large Magnetic Kerr Rotation in BiMn Alloy.* Physical Review, 1954. **96**(6): p. 1494-1496.
117. Coehoorn, R. and R.A.d. Groot, *The electronic structure of MnBi.* Journal of Physics F: Metal Physics, 1985. **15**(10): p. 2135.
118. Stöhr, J. and H. König, *Determination of Spin- and Orbital-Moment Anisotropies in Transition Metals by Angle-Dependent X-Ray Magnetic Circular Dichroism.* Physical Review Letters, 1995. **75**(20): p. 3748-3751.
119. Weller, D., et al., *Microscopic Origin of Magnetic Anisotropy in Au/Co/Au Probed with X-Ray Magnetic Circular Dichroism.* Physical Review Letters, 1995. **75**(20): p. 3752-3755.
120. Goering, E., et al., *Strong Anisotropy of Projected 3d Moments in Epitaxial CrO2 Films.* Physical Review Letters, 2002. **88**(20): p. 207203.
121. Goering *, E., *X-ray magnetic circular dichroism sum rule correction for the light transition metals.* Philosophical Magazine, 2005. **85**(25): p. 2895-2911.
122. Wu, R. and A.J. Freeman, *Limitation of the Magnetic-Circular-Dichroism Spin Sum Rule for Transition Metals and Importance of the Magnetic Dipole Term.* Physical Review Letters, 1994. **73**(14): p. 1994-1997.
123. Edmonds, K.W., et al., *Ferromagnetic moment and antiferromagnetic coupling in (Ga,Mn)As thin films.* Physical Review B, 2005. **71**(6): p. 064418.

124. Piamonteze, C., P. Miedema, and F.M.F. de Groot, *Accuracy of the spin sum rule in XMCD for the transition-metal L edges from manganese to copper.* Physical Review B, 2009. **80**(18): p. 184410.
125. Wu, R., D. Wang, and A.J. Freeman, *First principles investigation of the validity and range of applicability of the x-ray magnetic circular dichroism sum rule.* Physical Review Letters, 1993. **71**(21): p. 3581-3584.
126. van der Laan, G., *Magnetic Linear X-Ray Dichroism as a Probe of the Magnetocrystalline Anisotropy.* Physical Review Letters, 1999. **82**(3): p. 640-643.
127. Bruno, P., *Tight-binding approach to the orbital magnetic moment and magnetocrystalline anisotropy of transition-metal monolayers.* Physical Review B, 1989. **39**(1): p. 865-868.
128. Gerrit van der, L., *Microscopic origin of magnetocrystalline anisotropy in transition metal thin films.* Journal of Physics: Condensed Matter, 1998. **10**(14): p. 3239.
129. Shanavas, K.V., D. Parker, and D.J. Singh, *Theoretical study on the role of dynamics on the unusual magnetic properties in MnBi.* Scientific Reports, 2014. **4**: p. 7222.
130. Zarkevich, N.A., L.-L. Wang, and D.D. Johnson, *Anomalous magneto-structural behavior of MnBi explained: A path towards an improved permanent magnet.* APL Mater., 2014. **2**(3): p. 032103.
131. Wei, J.Z., et al., *τ-MnAl with high coercivity and saturation magnetization.* AIP Advances, 2014. **4**(12): p. 127113.
132. Bohlmann, M.A., J.C. Koo, and J.H. Wise, *Mn-Al-C for permanent magnets (invited).* Journal of Applied Physics, 1981. **52**(3): p. 2542-2543.
133. Fang, H., et al., *Directly obtained τ-phase MnAl, a high performance magnetic material for permanent magnets.* Journal of Solid State Chemistry, 2016. **237**(Supplement C): p. 300-306.
134. Zhang, C., et al., *Anisotropic single-variant of (Mn54Al46)97C3.* Scripta Materialia, 2018. **143**(Supplement C): p. 72-76.
135. Thielsch, J., F. Bittner, and T.G. Woodcock, *Magnetization reversal processes in hot-extruded τ-MnAl-C.* Journal of Magnetism and Magnetic Materials, 2017. **426**(Supplement C): p. 25-31.
136. Lu, W., et al., *Low-energy mechanically milled τ-phase MnAl alloys with high coercivity and magnetization.* Journal of Alloys and Compounds, 2016. **675**(Supplement C): p. 163-167.
137. Zhang, H., et al., *Engineering perpendicular magnetic anisotropy in Fe via interstitial nitrogenation: N choose K.* APL Materials, 2016. **4**(11): p. 116104.
138. *Private communication*, J. Hong, Editor. 2017: TU Darmtstadt.

139. Bennemann, K.H., *Non-linear Optics in Metals*. International Series of Monographs on Physics. 1999: Clarendon Press. 504.
140. Mankey, G.J., R.F. Willis, and F.J. Himpsel, *Band structure of the magnetic fcc pseudomorphs: Ni(100), Co(100), and Fe(100).* Physical Review B, 1993. **48**(14): p. 10284-10291.

List of publications

1. **Yu-Chun Chen**, Eberhard Goering, Lars Jeurgens, Zumin Wang, Fritz Phillipp, Johannes Baier, Thomas Tietze, and Gisela Schütz, "Unexpected room-temperature ferromagnetism in bulk ZnO", ***Appl. Phys. Lett.*** 103, 162405 (2013).
2. Thomas Tietze, Patrick Audehm, **Yu–Chun Chen**, Gisela Schütz, Boris B. Straumal, Svetlana G. Protasova, Andrey A. Mazilkin, Petr B. Straumal, Thomas Prokscha, Hubertus Luetkens, Zaher Salman, Andreas Suter, Brigitte Baretzky, Karin Fink, Wolfgang Wenzel, Denis Danilov, and Eberhard Goering, "Interfacial dominated ferromagnetism in nanograined ZnO: a μSR and DFT study", ***Sci. Rep.*** 5, 8871 (2015).
3. **Yu-Chun Chen**, Giuliano Gregori, Andreas Leineweber, Fei Qu, Chia-Chin Chen, Thomas Tietze, Helmut Kronmüller, Gisela Schütz, and Eberhard Goering, "Unique high-temperature performance of highly condensed MnBi permanent magnets", ***Scripta Mater.*** 107, 131 (2015).
4. **Yu-Chun Chen**, Zumin Wang, Andreas Leineweber, Johannes Baier, Thomas Tietze, Fritz Phillipp, Gisela Schütz, Eberhard Goering, "Effect of surface configurations on the room-temperature ferromagnetism of pure ZnO", ***J. Mater. Chem.*** **C** 4, 4166 (2016).
5. **Yu-Chun Chen**, Simon Sawatzki, Semih Ener, Hossein Sepehri-Amin, Andreas Leineweber, Giuliano Gregori , Fei Qu, Shreyas Muralidhar, Tadakatsu Ohkubo, Kazuhiro Hono, Oliver Gutfleisch, Helmut Kronmüller, Gisela Schütz, Eberhard Goering, "On the synthesis and microstructure analysis of high performance MnBi", ***AIP Advance*** 6, 125301 (2016).
6. Shreyas Muralidhar, Joachim Gräfe, **Yu-Chun Chen**, Martin Etter, Giuliano Gregori, Semih Ener, Simon Sawatzki, Kazuhiro Hono, Oliver Gutfleisch, Helmut Kronmüller, Gisela Schütz, Eberhard Goering, "Temperature-dependent first-order reversal curve measurements on unusually hard magnetic low-temperature phase of MnBi", ***Phy. Rev.*** **B** 95, 024413 (2017).

Danksagung

The realization of my PhD study and related research work would not have been possible without the help and professional support of many people.

Firstly, I would like to express my sincere gratitude to my advisor, PD Dr. Eberhard Goering, for giving me the chance of working in his subgroup and completing the G8 project “High Performance Permanent Magnets sustainable for Next Generation”. His guidance and patience helped me in all the time of research and writing of this thesis.

Besides my direct advisor, I would like to thank my big chef, Prof. Dr. Gisela Schütz, for giving me the opportunity of studying my PhD in her department at Max-Planck-Institut für Intelligente Systeme. She gave me 100 % degree of freedom to do whatever I wanted to try in my phD life.

My sincerest thanks also goes to Prof. Dr. Helmut Kronmüller because he is one of the G8 project proposers. Without his great effort, I would not have had this extraordinary opportunity of doing this international scientific cooperation. Additionally, his valuable comments were very beneficial to my research work.

To Prof. Dr. Sebastian Loth and Prof. Dr. Hans Büchler, I deeply thank you for agreeing to act as external referees of my thesis, as well as your precise corrections.

In terms of sample preparation, I would like to thank
– Mr. Thomas Meisner and Mr. Arnold Weible for arc- and induction-melting service to prepare alloy ingots used for the powder preparation.
– Mrs. Therese Dragon for sample cutting and polishing.
– Dr. Giuliano Gregori for the SPS-compaction of numerous MnBi bulk magnets and valuable suggestions on sample preparation and paper writing.
– Dr. Simon Sawatzki, Dr. Semih Ener, and Prof. Dr. Oliver Gutfleisch for

close internal cooperation, including hot-compaction and Kerr measurements of the MnBi bulk magnets, as well as detailed discussions.

In terms of sample characterization, I would like to thank
– Dr. Qu Fei, Dr. Chen WenWen, and Dr. Huang Wenting for SEM measurements.
– Prof. Dr. Andreas Leineweber for XRD characterization and detailed discussions.
– Dr. Hossein Sepehri-Amin, Prof. Tadakatsu Ohkubo, and Prof. Kazuhiro Hono for SEM/EDS measurements, microstructure analysis, and detailed discussions.
– Dr. Bastian Rheingans for careful DSC measurements as well as detailed discussions about phase transition and thermodynamics.
– Stephen Ruoß and Claudia Stahl for prompt arrangement and maintenance of SQUID measurement schedule.

In terms of XMCD studies, I would like to thank
– Mr. Bernd Ludescher and Dr. Thomas Tietze for the expert technical assistance to maintain the slef-built XMCD instrument.
– Dr. Huang Meng-Jie, Dr. Peter Nagel, and Dr. Stefan Schuppler, who are WERA beamline scientists of ANKA synchrotron center, for expert technical assistance to the XMCD measurements.
– Dr. Hari Babu Vasili and Dr. Manuel Valvidares, who are BOREAS beamline scientists of ALBA synchrotron center, for expert technical assistance to the XMCD measurements.

Finally, I do have to thank all of my colleagues in Department of Schütz for the wonderful and sweet atomosphere here, especially the members in Subgroup of Goering. I will never forget the help from Daniela Nolle (office 3E2), Joachim Gräfe (office 3E2), Kwanghyo Son, Mathias Schmidt, Patrick Audehm (office 3E2), Sapana Tripathi, and Thomas Tietze (office 3E2). It was my pleasure to know them and spend my daily life with them during my PhD study. It is emphasized that the chapeter, Zusammenfassung, was finished with the help of Sven Ilse and Frank Schulz. In addition, thanks to our nice secretary, Monika Kotz, for her huge patience and effective assitence on taking care of the bureaucratic part of my phD work.

Very special thanks are due to the prompt and comprehensive support from Prof. Takao Suzuki (University of Alabama) and Prof. George Hadjiapanayis (University of Delaware), including internal cooperation and G8 project management.

Finally, I would like to appreciate the constant love and encouragement from my family (wife, two sons, and parents) and practical support from Taiwan government during my PhD program.

Erklärung

Hiermit erkläre ich, Yu-Chun Chen, dass ich diese Arbeit selbständig verfasst und keine anderen als die angegebenen Quellen und Hilfsmittel benutzt habe. Die aus anderen Quellen oder indirekt übernommenen Daten und Konzepte sind unter Angabe der Quelle gekennzeichnet.

Stuttgart, den 9. Februar 2018

Yu-Chun Chen